Modeling Spatially and Spectrally Resolved Observations to Diagnose the Formation of Elliptical Galaxies

Modeling Spatially and Spectrally Resolved Observations to Diagnose the Formation of Elliptical Galaxies

A dissertation presented

by

Gregory Frantz Snyder

to

The Department of Astronomy

in partial fulfillment of the requirements

for the degree of

Doctor of Philosophy

in the subject of

Astronomy and Astrophysics

Harvard University

Cambridge, Massachusetts

May 2013

Dissertation Advisor: Professor Lars Hernquist Gregory Frantz Snyder

Modeling Spatially and Spectrally Resolved Observations to Diagnose the Formation of Elliptical Galaxies

Abstract

In extragalactic astronomy, a central challenge is that we cannot directly watch what happens to galaxies before and after they are observed. This dissertation focuses on linking predictions of galaxy time-evolution directly with observations, evaluating how interactions, mergers, and other processes affect the appearance of elliptical galaxies. The primary approach is to combine hydrodynamical simulations of galaxy formation, including all major components, with dust radiative transfer to predict their observational signatures

The current paradigm implies that a quiescent elliptical emerges following a formative starburst event. These trigger accretion onto the central supermassive black hole (SMBH), which then radiates as an active galactic nucleus (AGN). However, it is not clear the extent to which SMBH growth is fueled by these events nor how important is their energy input at setting the appearance of the remnant.

This thesis presents results drawing from three phases in the formation of a typical elliptical: 1) I evaluate how to disentangle AGN from star formation signatures in mid-infrared spectra during a dust-enshrouded starburst, making testable predictions for robustly tracing SMBH growth with the *James Webb Space Telescope* ; 2) I develop a model for the rate of merger-induced post-starburst galaxies selected from optical spectra, resolving tension between their observed rarity and merger rates from other

estimates; and 3) I present results from *Hubble Space Telescope* imaging of elliptical galaxies in galaxy clusters at $1 < z < 2$, the precursors of present-day massive clusters with $M \sim 10^{15} M_{\odot}$, demonstrating that their stars formed over an extended period and ruling out the simplest model for their formation history.

These results lend support to a stochastic formation history for ellipticals driven by mergers or interactions. However, significant uncertainties remain in how to evaluate the implications of galaxy appearance, in particular their morphologies across cosmic time. In the final chapter, I outline an approach to build a "mock observatory" from cosmological hydrodynamical simulations, with which observations of all types, including at high spatial and spectral resolutions, can be brought to bear in directly constraining the physics of galaxy formation and evolution.

Contents

Acknowledgments

I owe the opportunity to produce this dissertation to my family: my wife Stephanie for her thoughtfulness and dedication throughout this adventure; my parents, Drew Snyder and Deb Frantz, and grandparents for encouraging me to follow my passion, work hard, and obtain as much education as possible; and my in-laws Gregory, Beverly, and Charlotte Jacobs for treating me like one of their own.

I am immensely grateful to Lars Hernquist for supervising and supporting this thesis. Lars offered timely, salient advice about my science and my career, and permitted me significant independence to work on a broad range of topics at the interface between observational and theoretical astronomy, which was my primary goal in obtaining the PhD. Moreover, my thesis advisory committee Daniel Eisenstein, Giovanni Fazio, and Doug Finkbeiner provided constant help, support, and curiosity. This dissertation relied on the many postdoctoral fellows at the Harvard-Smithsonian Center for Astrophysics (CfA) with whom I have had the pleasure to collaborate, especially TJ Cox, Patrik Jonsson, Mark Vogelsberger, Debora Sijacki, Shy Genel, Desika Narayanan, and Mark Brodwin. In particular, Mark Brodwin pitched me a side project that grew into a significant portion (Chapter 5) of this thesis. I thank Anna Sajina for guidance during Chapter 3, Ann Zabludoff for graciously offering significant scientific advice early in my graduate career, and Lisa Kewley for hosting a very productive visit to the University of Hawaii Institute for Astronomy. I am grateful for scientific collaboration, mentorship, and friendship from current and former students affiliated with Lars' group: Stephanie Bush, Chris Hayward, Phil Hopkins, Dylan Nelson, Paul Torrey, Gurtina Besla, Joshua Suresh, Vicente Rodriguez-Gomez, and Laura Blecha.

This thesis owes much to the support of my officemate, Zach Berta, for five years of advice on life, computers, and astronomy. I thank Diego Muñoz, Robert Harris, Ragnhild Lunnan, and Sarah Rugheimer for countless snack and coffee breaks; Wen-fai Fong and Nick Stone for leading camping trips and throwing amazing parties; and all of my fellow CfA students for their friendship over the years. I thank the Institute for Theory and Computation (ITC) and the CfA for organizing such a vibrant group of scientists. It was a joy to write this thesis with the assistance of Jean Collins, Donna Adams, Peg Herlihy, Robb Schofield, Peg Hedstrom, Nina Zonnevylle, and Uma Mirani, who run the Department of Astronomy and the ITC so smoothly.

While writing this thesis, I was thrilled to participate in a number of activities to build professional experience in the fields of science education and policy. I am grateful to the Cambridge Citywide Senior Center for the opportunity to volunteer to teach astronomy to their members, and Doug Finkbeiner for mentoring my first semester as a Teaching Fellow. Assisting *Astronomy 130: Cosmology* was one of my most satisfying experiences during graduate school. The American Astronomical Society and the American Association for the Advancement of Science offered many policy advocacy and outreach programs in which I have been pleased to participate. I thank Professor Philip Sadler and the Science Education Department at CfA for their work in science learning and for teaching *Astronomy 302: Scientists Teaching Science*, one of my most valuable course experiences. I am grateful for support from the Center for Astronomy Education, with funding from NSF and NASA, to participate in the Kohala Coast Workshop, an intense two-day teaching workshop for Earth and space science graduate students on Hawaii's Big Island.

Much of this dissertation is published in *The Astrophysical Journal*, and so I thank

the staff of this and all other astronomical journals for their efforts to keep this vibrant field moving forward. Finally, this thesis relies on the work of thousands of individuals who conceived, built, and operated state-of-the-art astronomical instruments and scientific computing hardware and software, so I gratefully acknowledge the staffmembers of numerous research facilities, some of which are noted below.

Computations in Chapters 3, 4, and 6 were run on the Odyssey cluster supported by the Science Division Research Computing Group in the Faculty of Arts and Sciences at Harvard University. Additional computational resources and support were provided by the ITC and the Computing Facilities at the Harvard-Smithsonian CfA. This thesis made extensive use of the *matplotlib* Python plotting library (Hunter 2007). Chapter 5 is based on observations made with the NASA/ESA *Hubble Space Telescope*, obtained at the Space Telescope Science Institute (STScI), which is operated by the Association of Universities for Research in Astronomy, Inc., (AURA) under NASA contract NAS 5-26555. This work is also based in part on observations made with the *Spitzer Space Telescope*, which is operated by the Jet Propulsion Laboratory, California Institute of Technology under a contract with NASA. This work is also based in part on data obtained at the W.M. Keck Observatory, which is operated as a scientific partnership among the California Institute of Technology, the University of California and NASA. The Observatory was made possible by the generous financial support of the W.M. Keck Foundation. NASA's Astrophysics Data System was used nearly every day during this thesis.

In loving memory of

Beverly Faye Canzater Jacobs

Chapter 1

Introduction

1.1 Background

A complete picture of the evolution of the universe is beginning to emerge. Today, stars and planets form in cooling, contracting clouds of gas and dust in the interstellar medium (ISM) of galaxies, clumps of matter denser than the universal average by roughly 30 orders of magnitude. Compact remnants such as black holes form in the aftermath of stellar evolutionary processes and merge into supermassive black holes (SMBH) at the centers of, so far as we know, every massive galaxy. However, the universe did not begin in such a heterogeneous fashion. Instead, 13.8 billion years ago, the distribution of matter was nearly perfectly uniform, with only tiny fluctuations that grew under the influence of gravity to form the structure of galaxies we see today.

Analytical and observational work confirmed and expanded this picture over the past several decades. The majority of gravitating matter in the universe is invisible, the

so-called "dark matter", clumps of which grew from seed perturbations in the matter distribution; visible matter ("baryons") in the form of gas cooled and collapsed into the centers of these dark matter halos, and subsequently formed stars and thus luminous galaxies. Individual dark matter haloes and their subhaloes attract to other structures, eventually merging and forming more massive systems. This growth of structure from smaller pieces is known as the "heirarchical" model of galaxy formation.

Heirarchical structure growth is part of the highly successful paradigm known as the Lambda Cold Dark Matter (LCDM) universe model, whose success was affirmed by comparing numerical simulations to experiments on the cosmic microwave background radiation and large-scale distribution of galaxies. However, by itself the LCDM model does not explain the present appearance of galaxies. Roughly half are star-forming spiral galaxies like our Milky Way, while the rest are "bulge-dominated" or "elliptical" galaxies, spheroidal clumps of stars that contain little cold gas and thus are not actively forming stars. In addition, spiral galaxies often contain a central bulge component of varying mass that is similar in structure to elliptical galaxies.

Under the heirarchical story, this diversity of galaxy structure may arise naturally from differences in assembly history. However, since the ramifications of this assembly are connected tightly to baryon content (gas and stars), and hence the complex processes that act on them, a complete physical understanding of galaxy formation remains elusive.

1.2 Galaxy Formation and Evolution

1.2.1 Basic Results

A primary goal in observational cosmology is to understand what leads to such differences in appearance. Expanding on initial classification based on visual morphology (Hubble 1926), a number of observational characteristics, such as the motions, ages, and chemistry of stellar populations, have been used to trace the history of their components. Highly radial motions of old stars in the Milky Way imply the gas from which they formed "collapsed" from large galactic distances up to 10 billion years ago (Eggen et al. 1962), broadly consistent with the theory of galaxy formation by gas cooling in gravitational potential wells seeded by initial fluctuations (e.g., Silk 1968; Fall & Efstathiou 1980). The optical spectral shape ("color") of galaxies can shed light on the formation history of their stars: elliptical galaxies are comprised mainly of old, red stars, while spiral galaxies often contain young, blue stars. By extrapolating these stellar populations back in time, it was deduced that quiescent elliptical galaxies must have been much brighter and bluer during their formative periods (Tinsley 1968). The simplest model consistent with the present appearance of ellipticals is that they formed in a single episode ("monolithic collapse"), leading to a single short but intense burst of star formation at high redshift ($z > 1$) with little or no star formation since that time. However, a natural alternative is posited by the "merger hypothesis" (Toomre 1977), in which ellipticals are the evolutionary descendents of spiral galaxies, in which stars form over an extended period, that collide and merge, disrupting their stellar disks and forming an elliptical.

The rapid technology-driven expansion of galaxy surveys (e.g., Huchra et al.

1983) has revolutionized our ability to diagnose galaxy formation. Today, photometric surveys have measured the colors and shapes of tens of millions of galaxies, and large spectroscopic surveys have measured the large- and small- scale spatial distribution, as well as more details of the metal content and star formation history, of over a million galaxies (Ahn et al. 2012). Following Tinsley (1968), pre-computed stellar population synthesis (SPS) models (e.g., Leitherer et al. 1999; Bruzual & Charlot 2003; Conroy et al. 2009) allow efficient construction of galaxy spectral energy distribution (SED) models and inference regarding the star formation histories of observed sources (although perhaps with high uncertainty, e.g., Conroy et al. 2010). This has permitted the quantification of galaxy properties, for example in "color-magnitude diagrams" (CMD) describing the color distributions of galaxy populations as a function of their brightness or mass, in which the striking bimodality of galaxies was confirmed (e.g., Strateva et al. 2001). Figure 1.1 shows the number density of galaxies in an example CMD using data from the Sloan Digital Sky Survey (SDSS) presented by Blanton et al. (2003). Key features are the "red sequence", an overdensity of objects in a relatively tight, sloped line at the top center of the diagram, and the "blue cloud" at the lower left. The study of galaxy formation and evolution is often cast as attempting to understand the build-up of these two populations, including possibly movement between the classes.

1.2.2 Galaxy Demographics and Evolution

From such data, it is apparent that the most massive galaxies are commonly red, having very little ongoing star formation, and therefore are said to be "quenched". Subsequent work showed that galaxies in groups and clusters also tend to be quenched, regardless

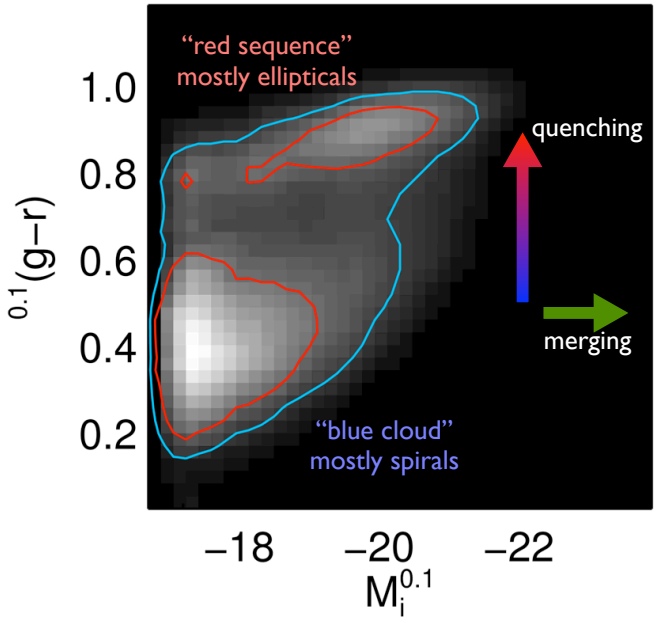

Figure 1.1.—: Logarithm of galaxy number density in the ${}^{0.1}(g-r)$ vs. ${}^{0.1}i$ color-magnitude diagram from the Sloan Digital Sky Survey published by Blanton et al. (2003). The photometry has been corrected to reflect the SED of each galaxy assuming it is at $z = 0.1$, near the middle of the redshift range of galaxies shown. The contours subtend 68% and 95% of objects, respectively. The "red sequence" and "blue cloud" are labeled; explaining this bimodality and its development over cosmic time is a primary goal in the field of galaxy formation and evolution. Arrows show heuristic examples of how a galaxy might evolve in this diagram: "quenching" represents the ending of star formation by some process, in which a blue cloud galaxy might evolve onto the red sequence, and "merging" represents mass growth through heirarchical assembly.

of their mass (Peng et al. 2010b). Beyond explaining the features of the galaxy CMD, quenching processes are required to reconcile the difference in shape between the inferred dark matter halo mass function and observed stellar mass functions (e.g., Moster et al. 2010). This helped establish the current paradigm that the efficiency of star formation is reduced in low-mass galaxies by the input of energy into the ISM from supernovae (e.g., Rees & Ostriker 1977), a direct result of star formation, and also in high-mass galaxies by another source of energetic "feedback". However, the exact nature and trigger of

these processes, as well as how they affect the formation of galaxy structures like disks and bulges, remain undetermined.

Over the past several decades, supermassive black holes (SMBHs) were appreciated as a potentially important new ingredient in the formation of galaxies. It is now well established that most, if not all, galaxies host a SMBH of $\sim 10^5$ to $10^{10} M_\odot$ in their centers (Kormendy & Richstone 1995). Numerous lines of circumstantial evidence suggest an evolutionary link between galaxies and their SMBHs, including tight correlations between bulge and SMBH mass (e.g., Gültekin et al. 2009) as well as unusually energetic emission in compact regions classified as "active galactic nuclei" (AGN, e.g., Rees 1984). A consequence is thought to be that heating of the ISM by feedback owing to SMBH growth can impede star formation in the host galaxy (e.g., Page et al. 2012), a direct physical coupling between SMBHs and galaxies. This prediction implies the existence of an observable connection between quasar and/or starburst activity and the transition of galaxies from a star-forming phase to a quiescent spheroid via galaxy merger activity (Sanders et al. 1988; Hopkins et al. 2008c). However, this connection is implemented by the extraordinarily complex interstellar medium (ISM), which is depleted, enriched, heated, expelled, and otherwise altered by depositions of energy and matter (feedback) from stars and black holes. Further, triggers of SMBH accretion such as galaxy-galaxy mergers can dramatically reshape galaxies by tidally disrupting original stellar disks (Toomre & Toomre 1972; Toomre 1977) and fueling star formation in gas-rich and potentially dust-enshrouded starbursts (Barnes & Hernquist 1991, 1996). Therefore the extent to which quenching and merging are coupled is uncertain.

To determine the true causal relationship between galaxies, their stars and gas, and SMBHs, it is essential to test predictions for how they evolved over the course of

cosmic time. In addition to necessitating understanding the consequences of galaxy interactions, it requires a robust accounting for the effects of dust, another intrinsically complex astrophysical phenomenon, which preferentially obscures short-wavelength light characteristic of emission by SMBHs and star formation and radiates a diversity of SED shapes across a wide range ($\lambda > 3\mu m$) of wavelengths (Rees et al. 1969; Draine 2003). This has lead to significant interest in objects such as quasars and other AGN, luminous and ultraluminous infrared galaxies (ULIRGs, Houck et al. 1984; Sanders et al. 1988; Sanders & Mirabel 1996), poststarburst galaxies (Dressler & Gunn 1983; Zabludoff et al. 1996), mergers, and galaxies between the peaks in the bimodal color distribution, so-called "green valley" (GV) galaxies (Strateva et al. 2001; Mendez et al. 2011).

1.2.3 Observations Across Cosmic Time

Deep multi-wavelength sky surveys trace the appearance of galaxies in the distant past, opening new avenues to address these questions. The *Hubble Space Telescope* (*HST*) has taken the highest resolution images of the most distant galaxies ever recorded ($z \gtrsim 11$, e.g., Coe et al. 2013; Ellis et al. 2013), and projects such as the *HST* Ultra Deep Field uncovered the emergence of star-forming galaxies during the first few billion years during and after reionization over small areas of the sky (Beckwith et al. 2006; Oesch et al. 2013). At nearer distances, high-resolution *HST* surveys have estimated the galaxy-galaxy merger rate (e.g., Conselice et al. 2003; Jogee et al. 2009; Lotz et al. 2011), a quantity with deep ramifications for bulge and elliptical formation. Additionally, deep wide-area surveys have found evidence for significant growth in the number and mass density of massive red galaxies (near $\sim M^*$, the characteristic stellar mass at the

knee of the mass function) with time since $z \sim 1$, while the corresponding mass density of the star-forming population has remained roughly constant (Bell et al. 2004; Faber et al. 2007; Brammer et al. 2011). These studies (e.g., Faber et al. 2007) inferred that a complex mix of quenching and merging is required to explain the build-up of the red sequence in the present-day color-magnitude diagram of Figure 1.1. Further, the size of the most massive ellipticals are believed to grow by a factor of ~ 3 since $z \sim 2$ (van Dokkum et al. 2008), raising the question of how physical processes such as minor merging could explain such growth (e.g., Oser et al. 2012). When corrected for dust, very few galaxies are found to occupy the green valley, implying that any process driving transformations between the blue cloud and red sequence must act on a very short ($\lesssim 10^9$ yr) timescale (Brammer et al. 2009). One challenge for interpreting data of galaxies over cosmic time is the issue of "progenitor bias" (van Dokkum & Franx 2001), a term originally referring to biases resulting from transformations of galaxy morphological type over time that add or remove them from selected samples in unpredictable ways. Biases of this type can apply to any study attempting to trace galaxy populations over cosmic time and any selection criterion.

The advent of pan-chromatic studies of distant galaxies has greatly augmented our ability to understand their formation. High-spatial resolution X-ray studies with, for example, the *Chandra X-ray Observatory* have yielded a comprehensive accounting of AGN emission in galaxies, and far-infrared surveys have traced the emission by dust heated by star formation and AGN over billions of years. Infrared and submillimeter telescopes such as the *Spitzer Space Telescope* and the *Herschel Space Observatory*, operating at $3\mu m < \lambda \lesssim 700\mu m$, have revolutionized our ability to, for example, trace star formation over cosmic time (e.g., Magnelli et al. 2011), to estimate galaxy stellar

masses (e.g., Marchesini et al. 2009), and robustly separate AGN-heated from star formation-heated dust emission (e.g., Stern et al. 2005; Donley et al. 2012; Kirkpatrick et al. 2013). Combined with optical surveys, a number of studies challenge the picture that mergers are a primary triggering mechanism for AGN or starburst activity in distant galaxies (Kocevski et al. 2012; Targett et al. 2012; Aird et al. 2012). In addition, integral field unit observations have spatially resolved galaxy kinematics, line emission, and dust attenuation (e.g., Förster Schreiber et al. 2009; Rich et al. 2010; Swinbank et al. 2011), providing additional rich constraints on their formation processes.

Several key uncertainties remain. The essential physics – multi-phase gasdynamics at a wide range of scales – is intrinsically complex, and the processes of star formation, stellar winds and supernovae feedback, SMBH accretion and feedback, are notoriously difficult to constrain observationally or to calculate from first principles. Luckily, the amount and quality of such data will continue to grow. *HST* Legacy surveys such as CANDELS, 3D-HST, CLASH, and the Frontier Fields, will continue obtaining high-quality optical and near-IR imaging and spectroscopy for $\gtrsim 10^5$ galaxies during the first half of the universe, the *Atacama Large Millimeter/Submillimeter Array* (*ALMA*) will begin to reveal the state and content of gas in galaxies over the past 10 billion years, and by $\sim$ 2020, the *Large Synoptic Survey Telescope* is expected to begin imaging tens of millions of distant galaxies. Moreover, the *James Webb Space Telescope* (*JWST*), expected to be operating by $\sim$ 2020, will unveil with unprecedented sensitivity the optical SEDs of the most distant galaxies and the mid-IR SEDs of galaxies since $z \sim 3$.

However, a fundamental limitation common to these surveys is the inability to follow directly the evolution of individual galaxies over time. Therefore it is difficult to assign causality for any statistical trend in observed galaxy properties, and progenitor

bias can obfuscate true evolutionary paths. For these reasons, the implications of many observations can be interpreted as supporting very different models of galaxy formation. This has led to the development of numerical simulations of galaxy formation and evolution, with which models for galaxy physics can be evolved in concert with each other, and that can predict as many observed galaxy properties as possible. Such calculations enable tighter theoretical constraints using the increasing wealth of precise data, and provide new ways of interpreting such data by opening the time domain with precise predictions for galaxy evolution.

1.2.4 Computational Methods

Simulations of structure formation have revolutionized our ability to predict the formation and evolution of galaxies. Dark matter-only calculations have exploded from individual galactic encounters (Navarro et al. 1987) or structure formation (White et al. 1987) with few mass elements to megaparsec-to-gigaparsec scale cosmological simulations with $\gtrsim 10^{10}$ (and growing) resolution elements (Springel et al. 2005c; Boylan-Kolchin et al. 2009; Klypin et al. 2011) that provide the best estimates of the structure of dark matter halos that would be occupied by millions of galaxies. Although dark matter-only simulations cannot follow directly all components such as star formation and SMBH growth, subsequent modeling of the galaxy population ("semi-analytic modeling", SAM, e.g., Cole et al. 2000; Benson 2012) has enabled the direct testing of theories regarding their formation. For example, such modeling has lent support to the canonical picture that AGN feedback is required to inhibit star formation by heating or expelling gas from massive galaxies (Croton et al. 2006). Sub-halo abundance matching, in which observed

galaxy clustering statistics are matched against simulated dark matter halo catalogs, allow the statistical derivation of the evolution of galaxy masses, star formation rates, and other properties (Wechsler et al. 2001; Behroozi et al. 2012). These approaches have led to not only more accurate models of galaxy formation and evolution in a LCDM universe, but also highly useful tools for interpreting observational data using these models, such as the Millennium Run Database (Lemson 2006) and Millennium Run Observatory (Overzier et al. 2012).

However, dark matter only simulations cannot directly exploit spatially resolved or multi-wavelength survey data. To do so requires evolving all components of the galaxy at small ($\lesssim 1$ kpc) spatial scales, including coupled processes such as gas heating and cooling, star formation, absorption and emission by dust, and SMBH evolution. Hydrodynamical simulations of galaxies accomplish this by combining a gravity solver with a treatment of gasdynamics, plus optional models for astrophysical processes. A commonly used method is smoothed-particle hydrodynamics (SPH, Lucy 1977; Gingold & Monaghan 1977), in which equations of motion are derived and evolved for a set of discrete particles that move with the flow. In their modern form (e.g., the GADGET code, Springel 2005), astrophysical SPH calculations naturally and adaptively improve their resolution in regions where mass accumulates, an extremely advantageous property for problems requiring a wide dynamic range, such as in cosmology. Another method in use is adaptive mesh refinement (AMR, e.g., Berger & Colella 1989), in which space is discretized into a set of cells on which the hydrodynamics equations are solved (e.g., the Enzo code, O'Shea et al. 2004). Recently, a hybrid method was developed (e.g., the AREPO code, Springel 2010) in which an adaptive mesh itself deforms and moves with the fluid. This approach seeks to combine the Lagrangian character of SPH

with the shock-capturing power of AMR, and has begun to be tested on cosmological hydrodynamics. For such problems, Arepo yields significant differences, believed to be improvements in accuracy, relative to earlier simulation techniques (e.g., Vogelsberger et al. 2012; Nelson et al. 2013).

On top of these hydrodynamics solvers, models of astrophysical processes such as star formation and feedback must be implemented to facilitate the study of their impact on galaxies' appearance. Such models serve two basic purposes: to encapsulate physics that we may not yet fully understand, and to limit the dynamic range of numerical simulations so that it feasible to run them on available computational resources. The basic result of prescriptions for star formation and stellar feedback is the ability to model the ISM, form stars that can be evolved under gravity thereafter, enrich the ISM with metals, and heat the ISM owing to supernova feedback. The star formation and ISM model implemented in several parts of this thesis treats the gas particles as containing a diffuse hot phase and cold star-forming clouds (Springel & Hernquist 2003). Simple empirically motivated equations for star formation and supernova feedback govern the thermodynamics and flow of mass between these phases. By design, such a model reproduces the observed correlations between galaxy star formation rate surface density and gas density (Kennicutt 1998). Similarly, prescriptions for SMBH growth (e.g., Springel et al. 2005b; Di Matteo et al. 2005) utilize an accretion model to grow the mass of SMBH seeds and return a fraction of the accreted mass-energy into the ISM, heating it and potentially quenching subsequent SMBH growth and star formation (Springel et al. 2005a), as required from the previously mentioned studies of SAMs. Hydrodynamical models with SMBH growth reproduce the slope of the observed BH-bulge relations and can be constrained to reproduce its normalization (Robertson et al. 2006b).

Subsequent modeling of the stars, SMBHs, and ISM can directly transform these hydrodynamical calculations into an observational frame. For example, such simulations have been used to model the kinematic (Cox et al. 2006a; Hoffman et al. 2010) and photometric properties (Hopkins et al. 2008b) of elliptical remnants of merger-induced starbursts, the co-evolution of quasars, ellipticals, and mergers (e.g., Hopkins et al. 2008c), and the metallicty evolution during galaxy encounters (Torrey et al. 2012a). An extension of this modeling can be used to predict the effects of dust (e.g., Witt et al. 1992), which can obscure essential components of galaxies (Gordon et al. 1997) while revealing additional information through IR observations. Dust radiative transfer methods have been developed to predict images and spectra from hydrodynamical simulations (e.g., Jonsson 2006) by propagating models for stellar, dust, and AGN populations through to their observational conclusions. A number of studies have evaluated the appearance of simulated galaxies at X-ray through optical wavelengths (Hopkins et al. 2005a; Wuyts et al. 2009a,b, 2010; Bush et al. 2010a; Scannapieco et al. 2010; Guedes et al. 2011) including the effects of dust attenuation. This technique has also been used to calibrate the galaxy-galaxy merger rate using morphological disturbances predicted from merger simulations (e.g., Lotz et al. 2008, 2010, 2011). Furthermore, by calculating the energy absorbed by dust grains, such techniques can also self-consistently estimate the spatially resolved IR emission by dust in the ISM (Jonsson et al. 2010; Chakrabarti et al. 2007; Li et al. 2008), from which analyses of the power sources in simulated IR-luminous galaxies have been conducted (e.g., Younger et al. 2009; Narayanan et al. 2010b; Hayward et al. 2013).

This generalization of stellar population synthesis has been enabled by the rapid expansion of available computing power, opening a new avenue for comparing data

directly to theory. By extending the original, standard stellar population synthesis techniques (Tinsley 1968; Leitherer et al. 1999; Bruzual & Charlot 2003) and the modeling of dark matter structure formation catalogs (Overzier et al. 2012) to include the three-dimensional evolution of stars, AGN, and dust, hydrodynamical simulations coupled with dust radiative transfer can form the foundation of a full "mock observatory" that can directly engage forthcoming data from *ALMA*, *JWST*, and *LSST*.

1.3 Applications to Elliptical Galaxy Formation

In this thesis, I apply these and other methods to infer the formation history of elliptical galaxies in a variety of contexts. Explaining structural diversity in present-day galaxies remains a key goal of observational cosmology, and comprehensive models are essential for disentangling intrinsically complex questions related to galaxy formation. The bulk of this thesis comprises making direct predictions of how simulated galaxies would be observed. The goal is to leverage the current best theoretical knowledge to create models that evolve in time and which can inform interpretation of diverse extragalactic datasets. The primary scientific content is the development of realistic diagnostics of AGN and merger activity which may ultimately be used to constrain models of galaxy physics processes.

In Chapter 2, I examine a newly found scaling relation in elliptical galaxies that takes advantage of high resolution imaging to measure the incidence of globular star clusters orbiting galaxies. Burkert & Tremaine (2010) discovered an unexpectedly tight correlation between the number of globular clusters and the mass of SMBHs, suggesting a direct causal link between the SMBH and globular clusters. However, we show that this

trend can be explained as an indirect consequence of other more physically motivated correlations, such as that between SMBH mass and bulge binding energy expected in models of feedback-regulated SMBH growth.

Chapters 3, 4, and 5 constitute the bulk of this thesis, and the focus of each is on a successive stage in the timeline of elliptical galaxy formation. Chapters 3 and 4 combine hydrodynamical simulations of mergers with dust radiative transfer to directly predict signatures of starburst and AGN activity. In Chapter 3, I examine the dust-obscured starburst phase thought to represent the formative stage of elliptical galaxies, suggesting a reliable method for the *James Webb Space Telescope* to disentangle AGN from star formation in galaxies using mid-infrared spectral energy distributions. In Chapter 4, I develop a model for merger-induced fossil remnants of starbursts, so-called "poststarburst" galaxies, building a catalog of optical absorption line diagnostics used to identify the signature of young stars in optical spectra ~ 1 Gyr after the starburst. I use this catalog to show that the commonly assumed ~ 1 Gyr duration of the poststarburst signature is too long for many major gas-rich mergers, leading to their signature being rarer than conventionally believed and reconciling this rarity with other estimates of the galaxy-galaxy merger rate. In Chapter 5, I construct rest-frame optical color-magnitude diagrams to identify and examine the stellar ages of ellipticals in galaxy clusters at $1 < z < 2$, finding that they formed their stars over an extended period, confirming previous evidence for vigorous galaxy formation at $z \gtrsim 1.5$ in the precursors to today's most massive clusters. This lends evidence for a stochastic formation process (i.e., possibly mergers) that involves ongoing formation of the red sequence, resulting in significant progenitor bias as more and more ellipticals enter the sample with time.

Chapter 6 examines *ab initio* cosmological simulations of galaxy formation from an

observational perspective. With such an approach it is possible to address, for example, the challenge in interpreting the evolving morphologies, colors, and spatial distributions of galaxies raised in Chapter 5. Given intrinsic limits and biases with available data, we explore how to exploit the growing volume and sophistication of numerical calculations to assist with both interpreting data and constraining theoretical models. We conclude with a summary and discussion of how approaches used in this thesis can serve as the backbone of a fully customizable "mock observatory" to create broad-based statistical comparisons between observations and theoretical calculations that will each continue to grow in size, precision, and expense.

Chapter 2

Relation Between Globular Clusters and Supermassive Black Holes in Ellipticals as a Manifestation of the Black Hole Fundamental Plane

G. Snyder, P. Hopkins, & L. Hernquist

The Astrophysical Journal Letters, Vol. 728, No. 24, 2011

Abstract

We analyze the relation between the mass of the central supermassive black hole (M_{BH}) and the number of globular clusters (N_{GC}) in elliptical galaxies and bulges as

a ramification of the black hole fundamental plane, the theoretically predicted and observed multi-variable correlation between M_{BH} and bulge binding energy. Although the tightness of the M_{BH}–N_{GC} correlation suggests an unlikely causal link between supermassive black holes and globular clusters, such a correspondence can exhibit small scatter even if the physical relationship is indirect. We show that the relatively small scatter of the M_{BH}–N_{GC} relation owes to the mutual residual correlation of M_{BH} and N_{GC} with stellar mass when the velocity dispersion is held fixed. Thus, present observations lend evidence for feedback-regulated models in which the bulge binding energy is most important; they do not necessarily imply any 'special' connection between globular clusters and M_{BH}. This raises the question of why N_{GC} traces the formation of ellipticals and bulges sufficiently well to be correlated with binding energy.

2.1 Introduction

There are now well-established correlations between the mass of supermassive black holes (SMBHs) and properties of their host galaxies, such as bulge luminosity, mass, light concentration, and velocity dispersion (Kormendy & Richstone 1995; Magorrian et al. 1998; Ferrarese & Merritt 2000; Gebhardt et al. 2000; Graham et al. 2001; Tremaine et al. 2002; Marconi & Hunt 2003; Gültekin et al. 2009). This suggests that the physical mechanism driving growth of the SMBH also plays a key role in forming the bulge (for spiral galaxies) or galaxy (for ellipticals). Analytical estimates (Silk & Rees 1998; Burkert & Silk 2001; Hopkins & Hernquist 2006), as well as numerical simulations (Di Matteo et al. 2005; Springel et al. 2005b; Cox et al. 2006a; Robertson et al. 2006b; Croton et al. 2006; Johansson et al. 2009) with simple prescriptions for SMBH accretion

have demonstrated the plausibility of this inference by matching the expected slopes of these correlations.

Regardless of the detailed feedback prescription, these models predict that SMBHs grow until reaching some critical mass, where the energy and/or momentum released by feedback expels material from the nucleus. As such, they robustly predict that the "true" correlation should be between SMBH mass and a quantity such as the binding energy or potential well depth of material in the bulge. Hopkins et al. (2007a) show that the observed correlations with different variables, and importantly their scatter and systematic deviations from the relations, can be understood as the projections of a single fundamental dependence. This relation is approximated closely by a multi-variable correlation, a black hole fundamental plane (BHFP). Aller & Richstone (2007) confirmed this in a sample of ellipticals and spiral bulges using dynamical models of bulge potentials, and Feoli & Mancini (2009) did so with simple proxies such as $M_{BH} \propto E_b \sim M_* \sigma^2$.

Additional correlations have been found between SMBH mass and dark matter halo mass, as well as the number N_{GC} of globular clusters (GC) in the host galaxy (Spitler & Forbes 2009; Burkert & Tremaine 2010; Harris & Harris 2011). In particular, Burkert & Tremaine (2010, hereafter BT10) argued that N_{GC} is a better predictor of M_{BH} than the velocity dispersion σ, citing a smaller intrinsic scatter and a residual correlation between N_{GC} and M_{BH} in elliptical galaxies even after accounting for the median $M_{BH} - \sigma$ correlation, suggesting a fundamental link between the accretion of gas by the SMBH and the formation of a galaxy's globular cluster system. Harris & Harris (2011, hereafter HH10) extended the sample by making reasonable estimates of N_{GC} from the literature in galaxies with M_{BH} measurements.

In this letter, we illustrate that the above link can be understood as a consequence of the BHFP relation combined with a residual correlation between N_{GC} and the bulge's stellar mass M_* at fixed σ. Rather than suggesting a single "best" correlation between M_{BH} and a single galaxy parameter, the BHFP implies that the best predictor of SMBH mass is some combination thereof. For example, M_{BH} has a positive correlation with the bulge's stellar mass even at fixed σ. Although the number of globular clusters in a particular galaxy, like M_{BH}, is a complex function of the galaxy's formation history, there exists a similar positive residual correlation between N_{GC} and M_*, so that the resulting N_{GC}–M_{BH} residuals (fixing σ) will be positively correlated.

In §5.2 we describe a sample of 32 elliptical galaxies from Peng et al. (2008) with auxiliary data compiled in Hopkins et al. (2008b, and subsequent papers). In §2.3 we fit separately the relations M_*–σ and N_{GC}–σ in these galaxies to establish the residual correlation between N_{GC} and M_*. Then we combine this residual slope with knowledge of the M_{BH}–M_* correlation at fixed σ from the BHFP, and calculate the residual correlation and scatter expected between N_{GC} and M_{BH}. We summarize and conclude in §5.7.

2.2 The Data

To determine the dependence of N_{GC} on M_* at fixed σ, we cross-match objects compiled in Hopkins et al. (2008b) and subsequent works with the ACS Virgo Cluster Survey (VCC, Côté et al. 2004), from which Peng et al. (2008) determined globular cluster counts (N_{GC}) and uncertainties. Following BT10, we obtained N_{GC} for several additional galaxies from Spitler et al. (2008).

We obtained stellar masses and uncertainties from Peng et al. (2008) and Hopkins et al. (2009a,c), who compiled photometric data from several authors (e.g. Bender et al. 1988; Rothberg & Joseph 2004; Lauer et al. 2007; Kormendy et al. 2009, and references therein). We use velocity dispersions as compiled by Hopkins et al. (2009a,c). The latter quantity is the one best-determined for nearby massive galaxies, so we assume a log-uniform uncertainty in σ of 0.02 dex, consistent with literature values. This approach yields 33 galaxies for which we will determine the residual correlation between N_{GC} and M_*. We discard the known recent merger remnant NGC1316 because its nuclear velocity dispersion is unrelaxed and the globular cluster system is actively evolving (Schweizer 1980). The galaxy properties used to analyze this 32-galaxy sample are provided in Table 2.1.

In addition, we will utilize the M_{BH}, N_{GC}, and σ data directly from Table 1 of BT10 (compiled mostly from Gültekin et al. (2009)), and the M_{BH}, N_{GC} data from Table 1 of HH10. For the latter, we use the mean σ values from the Hyperleda database (Paturel et al. 2003; McElroy 1995). These two sources yield a 21 galaxy combined comparison sample (Table 2.2) for our derived M_{BH}–N_{GC} residual correlation. We note that BT10 and HH10 use slightly different, but statistically consistent, values for N_{GC} where the samples overlap. The differing values of M_{BH} may make a larger difference in cases where multiple measurements exist; here, we follow BT10 and give half weight to each in our fits. Furthermore, different studies provide different values for the velocity dispersion of a given galaxy; for example, Hyperleda returns σ values $\sim$10-20 km/s smaller than the ones from BT10, and the papers by Hopkins et al. provide values that differ by $\sim \pm$10-20 km/s. We computed the observed residual N_{GC}–M_{BH} correlation using these alternate sources of σ, and find that this leaves our conclusions completely unchanged.

Table 2.1. Galaxy properties for Figure 2.1

Galaxy	N_{GC}	M_* ($10^9 M_\odot$)	σ (km/s)
NGC0821	320 ± 45[a]	229 ± 57	209 ± 10
NGC1399	5800 ± 700[a]	363 ± 91	359 ± 18
NGC3377	266 ± 66[b]	26.3 ± 6.6	141 ± 7
NGC3379	270 ± 68[a]	107 ± 27	221 ± 11
NGC4318	18 ± 6.1	5.0 ± 1.7	101 ± 5
NGC4365	3246 ± 598	226 ± 52	269 ± 13
NGC4374	4301 ± 1201	236 ± 61	287 ± 14
NGC4382	1110 ± 181	186 ± 44	196 ± 10
NGC4387	69.5 ± 9.8	13.7 ± 3	84 ± 4.2
NGC4406	2660 ± 129	289 ± 60	250 ± 12
NGC4434	141 ± 34	21.4 ± 4	118 ± 6
NGC4458	72 ± 12	8.7 ± 2	85 ± 4.3
NGC4459	218 ± 28	77.9 ± 14	168 ± 8
NGC4464	25.3 ± 9.2	7.1 ± 1.4	120 ± 6
NGC4467	-6 ± 13	1.8 ± 0.6	67 ± 3.4
NGC4472	7813 ± 830	531 ± 110	287 ± 14
NGC4473	76 ± 97	53.5 ± 12	178 ± 9
NGC4476	20.1 ± 7.3	3.7 ± 2	41 ± 2.1
NGC4478	58 ± 11	22 ± 4	149 ± 7
NGC4486	14660 ± 891	302 ± 79	360 ± 18
NGC4489	31 ± 9	6.98 ± 1.7	49 ± 2.4
NGC4515	81 ± 10	7.7 ± 1.5	90 ± 4.5
NGC4551	47 ± 11	11.6 ± 2.4	100 ± 5
NGC4552	984 ± 198	95 ± 16.9	261 ± 13
NGC4564	213 ± 31	26 ± 6	153 ± 8
NGC4621	803 ± 355	83.9 ± 19	237 ± 12
NGC4649	4745 ± 1099	339 ± 50	341 ± 17
NGC4660	205 ± 28	23.8 ± 4	191 ± 9
VCC1199	-9 ± 14	0.58 ± 0.16	69 ± 3.5
VCC1440	26.7 ± 6.8	1.2 ± 0.44	59 ± 3
VCC1627	3.6 ± 3.7	1.0 ± 0.32	47 ± 2.4
VCC1871	10.4 ± 5	2.3 ± 0.58	51 ± 2.6

[a]Spitler et al. (2008)

[b]Kundu & Whitmore (2001)

Note. — Properties of ellipticals used to determine the correlation of N_{GC} with M_* at fixed velocity dispersion σ (Figure 2.1). Values of N_{GC} and M_* are from Peng et al. (2008) unless otherwise noted. Values of σ are from Hopkins et al. (2009a,c) and assumed to have a log-uniform uncertainty of 0.02 dex.

Table 2.2. Galaxy properties for Figure 2.2

Galaxy	M_{BH} ($M_\odot$)	+1-sigma ($M_\odot$)	-1-sigma ($M_\odot$)	N_{GC}	σ (km/s)	ΔN_{GC}	ΔM_{BH}
Burkert & Tremaine (2010)							
NGC0821	4.2×10^7	2.8×10^7	8×10^6	320 ± 45	209 ± 10	-0.39	-0.79
NGC1316	1.5×10^8	8×10^7	8×10^7	1173 ± 240	226 ± 9	0.05	-0.37
NGC1399	1.3×10^9	5×10^8	7×10^8	5800 ± 700	337 ± 16	0.11	-0.13
	5.1×10^8	7×10^7	7×10^7			0.11	-0.54
NGC3377	1.1×10^8	1.1×10^8	1×10^7	266 ± 66	145 ± 7	0.11	0.27
NGC3379	1.2×10^8	8×10^7	6×10^7	270 ± 68	206 ± 10	-0.44	-0.31
	4×10^8	1×10^8	1×10^8			-0.44	0.22
NGC4374	1.5×10^9	1.1×10^9	6×10^8	4301 ± 1201	296 ± 14	0.19	0.16
NGC4459	7.4×10^7	1.4×10^7	1.4×10^7	218 ± 28	167 ± 8	-0.20	-0.15
NGC4472	1.8×10^9	6×10^8	6×10^8	7813 ± 830	310 ± 10	0.37	0.16
NGC4486	6.4×10^9	5×10^8	5×10^8	14660 ± 891	375 ± 18	0.34	0.38
NGC4564	6.9×10^7	4×10^6	1×10^7	213 ± 31	162 ± 8	-0.17	-0.13
NGC4594	5.5×10^8	5×10^7	5×10^7	1900 ± 189	240 ± 12	0.16	0.09
NGC4649	4.5×10^9	1×10^9	1×10^9	4745 ± 1099	385 ± 19	-0.19	0.18
NGC5128	3×10^8	4×10^7	2×10^7	1550 ± 390	150 ± 7	0.82	0.65
	7×10^7	1.3×10^7	3.8×10^7			0.82	0.01
Harris & Harris (2011)							
NGC2778	1.6×10^7	9×10^6	2×10^5	50 ± 30	162 ± 8	-0.80	-0.76
NGC4261	5.5×10^8	1.1×10^8	1.2×10^8	530 ± 100	309 ± 14	-0.79	-0.35
NGC4473	1.3×10^8	5×10^7	9.4×10^7	376 ± 97	180 ± 8	-0.08	-0.03
NGC4552	4.8×10^8	8×10^7	8×10^7	1200 ± 250	253 ± 12	-0.12	-0.06
NGC4621	4×10^8	6×10^7	6×10^7	800 ± 355	225 ± 11	-0.11	-0.06
NGC4697	2×10^8	2×10^7	2×10^7	229 ± 50	171 ± 8	-0.22	0.24
NGC5813	7×10^8	1.1×10^8	1.1×10^8	1650 ± 400	237 ± 11	0.12	0.22
NGC5846	1.1×10^9	2×10^8	2×10^8	4700 ± 1200	239 ± 11	0.56	0.40

Note. — Properties of elliptical galaxies used to calculate the correlation of N_{GC} with M_{BH} at fixed velocity dispersion σ (Figure 2.2), following BT10. Data for N_{GC} and M_{BH} are compiled from BT10 and HH10. Values of σ are as presented in BT10 for those galaxies, and values of σ for the HH10 ellipticals are taken as the mean value recorded in the HyperLeda database (Paturel et al. 2003; McElroy 1995).

2.3 Correlations

Both the BHFP and M_{BH}–N_{GC} relation appear to perform better than the M_{BH}–σ relation because they explain its residuals and hence have a smaller intrinsic dispersion. Rigorously, this can be restated as follows: at fixed σ, the residuals in M_{BH} correlate tightly with the residuals in N_{GC} and in M_* for the BHFP.

The question then arises: does N_{GC} directly explain the residuals in M_{BH}, or could the latter be attributed to other variables already proposed? Specifically, we examine whether the observed N_{GC}–M_{BH} relation is predicted as an indirect consequence of the BHFP relation. This is motivated by the BHFP prediction that at fixed σ, good tracers of the bulge binding energy correlate tightly with the residuals in M_{BH}. (Interestingly, a similar relation was shown for the binding energies of individual Milky Way globulars by McLaughlin (2000).) An approximation to the bulge binding energy in ellipticals is a quantity like $M_*\sigma^2$, so that at fixed σ, galaxies with larger M_* will have a greater binding energy. Thus, if N_{GC} adequately traces M_* at fixed σ, as might be natural given the observed N_{GC}–galaxy correlations, then the tightness of the N_{GC}-M_{BH} relation is expected.

In this work, we focus on a particular projection of the BHFP that uses the bulge binding energy as the driving parameter. However, we note that the general BHFP, and also the corresponding salient relation for GCs (e.g. Harris & van den Bergh 1981; McLaughlin 1999, and subsequent works) depends on galaxy formation history in a more complicated way (Hopkins et al. 2009d). Thus while the bulge binding energy serves adequately for our purposes, a more detailed accounting of, for example, the total baryon mass may lead to an even tighter expected correspondence.

As follows, we calculate the expected residuals in N_{GC}–M_{BH} assuming that this relation is a consequence of the BHFP and no other physics. As an expression of the BHFP correlation, we use the relation between the mass of the SMBH and bulge binding energy from Hopkins et al. (2007a),

$$\log M_{BH} = \eta + \beta \log(M_* \sigma^2),$$

where $\eta = 8.23 \pm 0.06$, and $\beta = 0.71 \pm 0.06$. We will denote this quantity as predicted from the other observed variables as $\log\langle M_{BH}|\mathrm{BHFP}\rangle$. Then we subtract from this the logarithm of M_{BH} as predicted solely from M_{BH}–σ, denoted by $\log\langle M_{BH}|\sigma\rangle$, to obtain the BHFP-predicted residual correlation between M_{BH} and M_*. We will signify this difference in logarithmic quantities as ΔM_{BH} (ΔM_*, ΔN_{GC}):

$$\begin{aligned}\Delta M_{BH} &= \log\langle M_{BH}|BHFP\rangle - \log\langle M_{BH}|\sigma\rangle = \\ &= \beta \log(M_* \sigma^2) - \beta \log(\langle M_*|\sigma\rangle \sigma^2) \\ &= \beta(\log M_* - \log\langle M_*|\sigma\rangle) = \beta \Delta M_*. \end{aligned} \tag{1}$$

This is just the statement that at fixed σ, $M_{BH} \propto M_*^{\beta}$.

If there exists a relation between ΔN_{GC} and ΔM_*:

$$\Delta N_{GC} = \gamma \Delta M_*, \tag{2}$$

this will therefore result in a correlation between ΔN_{GC} and ΔM_{BH}:

$$\Delta N_{GC} = \frac{\gamma}{\beta} \Delta M_{BH} = \alpha \Delta M_{BH}. \tag{3}$$

To test this, we first calculate γ from the existing data to establish a correlation between N_{GC} and M_* at fixed velocity dispersion σ (Figure 2.1), and then combine it

with the BHFP to create a prediction for the N_{GC}–M_{BH} residuals. Then, in Figure 2.2, we compare this prediction to the observed residual correlation between N_{GC} and M_{BH} from BT10 and HH10.

Specifically, we begin by determining the observed best-fit linear correlations between $\log N_{GC}$ and $\log \sigma$, and $\log M_*$ and $\log \sigma$. The resulting fits are shown in the top two panels of Figure 2.1. We undertake all fits using two methods: the χ^2-minimization methods of Tremaine et al. (2002) (hereafter, T02), and the bivariate correlated errors and intrinsic scatter (BCES) estimators of Akritas & Bershady (1996). For the former, we account for intrinsic scatter in the Y axis by adding a uniform scatter in quadrature with the measurement errors such that the reduced-χ^2 value of the fit is 1. For the latter, we choose the regression line that bisects the BCES(Y|X) and BCES(X|Y) curves. Altering these choices leads to small changes in the residual values, but does not change the residual slope in a statistically significant way. One-sigma uncertainties in the fitted slopes are calculated using paired nonparametric bootstrap simulations (Babu & Rao 1993).

For each object, we then use the fitted relation to compute the expected value of $\log N_{GC}$ ($\log M_*$) given its observed value of σ, and subtract it from the observed value of $\log N_{GC}$ ($\log M_*$) to obtain ΔN_{GC} (ΔM_*). In the lower left panel of Figure 2.1, as expected we see a clear positive correlation between ΔN_{GC} and ΔM_*, indicating that at a fixed σ, elliptical galaxies with more globular clusters also have a larger total stellar mass. We note that the values of ΔN_{GC} and ΔM_{BH} calculated using BCES or χ^2-minimization on the direct correlations are the same to within 0.1 dex. Subsequent estimates of the residual slope are unaffected by this choice.

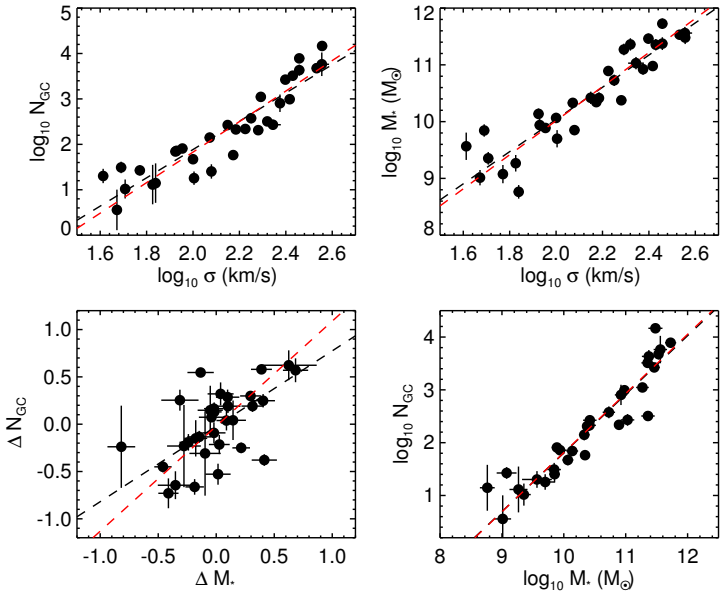

Figure 2.1.—: *Top:* Observed correlations of N_{GC} and M_* with velocity dispersion σ for the 32-galaxy sample described in §5.2. *Lower Left:* Correlation between N_{GC} and M_* at fixed σ: ΔN_{GC} (ΔM_*) is the difference between the observed logarithm of N_{GC} (M_*) and the expected value of the logarithm of N_{GC} (M_*) given the linear relation in the top left (top right) panel. The lines are our regression curves fitted to the data. The dashed black curves are fitted using a χ^2 technique accounting for intrinsic scatter (Tremaine et al. 2002), while the dashed red curves use an alternative maximum-likelihood technique from Akritas & Bershady (1996). There is a clear positive correlation between ΔN_{GC} and ΔM_*. If the BHFP is the true underlying relation, then this observed residual correlation will lead to a correlation between N_{GC} and M_{BH}, even at fixed σ and with no other physics linking M_{BH} to the globular cluster systems. *Lower Right:* The observed correlation between N_{GC} and M_*.

However, the two fitting methods obtain somewhat different estimates for the slope of the resulting residual correlation, γ, which we will use to estimate the expected N_{GC}–M_{BH} residual slope $\alpha = \gamma/\beta$. As plotted in Figure 2.1, we find

$$\gamma_{T02} = 0.79 \pm 0.25$$

$$\gamma_{BCES} = 1.11 \pm 0.21,$$

and correspondingly,

$$\alpha_{T02} = 1.11 \pm 0.36$$

$$\alpha_{BCES} = 1.56 \pm 0.32.$$

In Figure 2.2, we compare this predicted slope with the one observed in the comparison sample of BT10 and HH10. Again, we compute the residuals against σ in both N_{GC} and M_{BH}; note that for consistency, this is slightly different than the quantities plotted in BT10's Figure 3 where the N_{GC} residual was computed against the bulge luminosity, not velocity dispersion. We plot a region in light gray to highlight the extremes of the predicted slopes, corresponding to the range bounded by the 1-sigma uncertainties in the slope given by our two regression methods. In darker gray we simply plot the range bounded by our two slope estimates.

As in Figure 2.1, we fit the data directly and find that the observed residual slope between N_{GC} and M_{BH} is

$$\hat{\alpha}_{T02} = 0.78 \pm 0.24$$

$$\hat{\alpha}_{BCES} = 1.33 \pm 0.34,$$

in good agreement with the BHFP predictions above.

The detection of this residual correlation by BT10 quantitatively demonstrates that N_{GC} is a better predictor of M_{BH} than is σ. Such a comparison can be alternatively phrased as a reduction in the intrinsic scatter of the correlation. In BT10, the intrinsic scatter of M_{BH}–σ was found to be $\epsilon \sim 0.3$ dex, while the intrinsic scatter in N_{GC}–M_{BH} is $\epsilon \sim 0.2$ dex. The magnitude of this dispersion can be predicted by combining the BHFP relation with the observed correlations with N_{GC}. From Hopkins et al. (2007a),

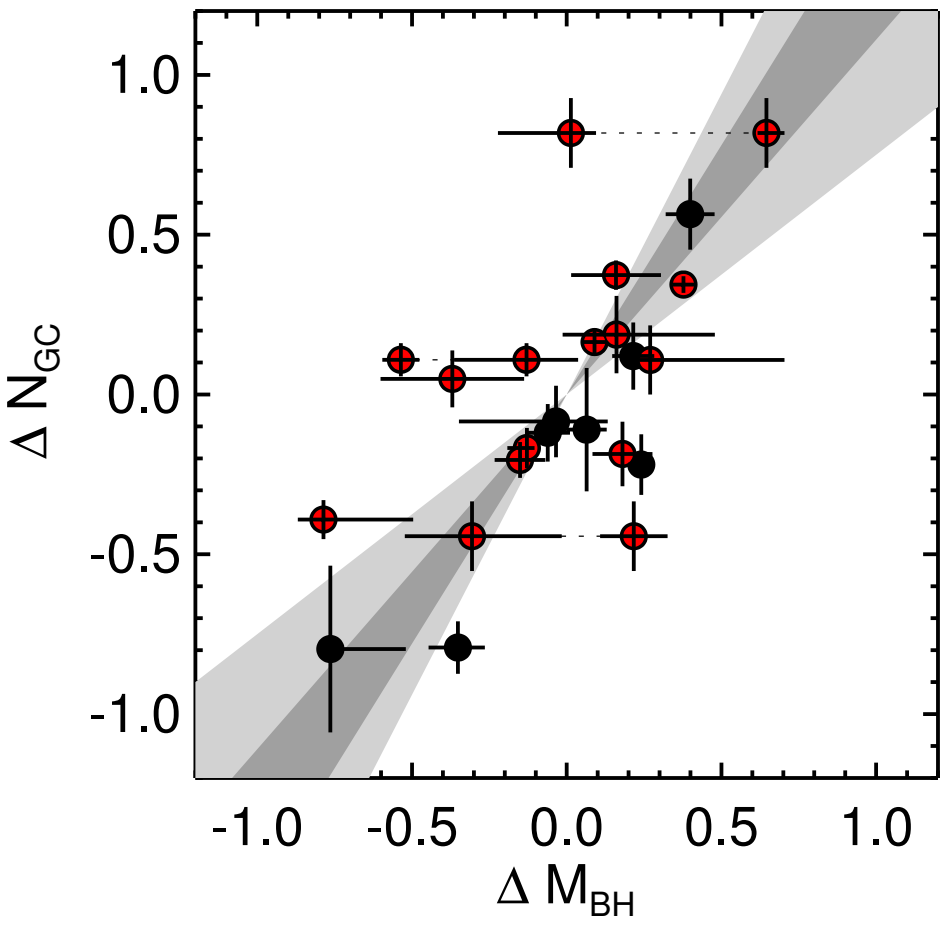

Figure 2.2.—: Residual correlation between N_{GC} and M_{BH} at fixed velocity dispersion σ. The points are data from BT10 and HH10; we follow BT10 where multiple M_{BH} measurements exist by assigning each measurement half weight in any fits. Red points correspond to the BT10 sample; their positions here and in BT10's Figure 3 differ slightly because we take N_{GC} residuals with respect to σ instead of bulge luminosity, but the residuals here have roughly the same slope and span a similar range of ΔN_{GC} as compared with BT10. The eight points added by the elliptical sample of HH10 reinforce this residual correlation and expand its range. The dark gray shaded region is the *predicted* residual correlation (with associated 1-sigma uncertainty in lighter shade) assuming that M_{BH} is determined only by the BHFP, combined with the observed correlation between N_{GC} and M_* at fixed σ determined by fitting the data in Figure 2.1. We see that the observed residual slope is in good agreement with this expected slope. Thus the apparent additional predictive power of N_{GC} for M_{BH} can be entirely accounted for by the predicted correlation of M_{BH} and the observed correlation of N_{GC} with the bulge binging energy.

we see that the M_{BH}–E_b correlation has an intrinsic scatter $\sim$ 0.2-0.25 dex, and from the present data, we find the scatter of E_b–N_{GC} is 0.22 ± 0.04 dex. By propagating these as measurement uncertainties to the M_{BH}–N_{GC} relation, we predict that the measured N_{GC}–M_{BH} intrinsic scatter should be $\epsilon = 0.23 \pm 0.03$ dex, consistent with the measurement by BT10. It is also consistent with the combined dataset of BT10 and HH10, for which we find $\epsilon = 0.21 \pm 0.04$ dex.

2.4 Conclusions

We have shown that the number of globular clusters in elliptical galaxies exhibits a residual dependence on M_* at fixed σ, implying that the bulge binding energy ($\sim M_*\sigma^2$) is a better indicator of N_{GC} than σ or M_* alone. The same was shown to be true for M_{BH} by Hopkins et al. (2007a), as these parameters constitute a formulation of the BHFP. Thus the apparent power of M_{BH}–N_{GC} versus M_{BH}–σ owes to the fact that N_{GC} and M_{BH} are both tracers of the same fundamental property such as the bulge binding energy.

This resolves several puzzling aspects of the previous interpretation of the data. As BT10 themselves point out, there cannot be a direct causal correlation between N_{GC} and M_{BH}, since most of the GC mass is at very large radii and has never had any interaction with the galaxy nucleus. Moreover, while most GCs likely formed at very high redshift, the final mass of the SMBH is sensitive to its growth via gas accretion at $z \lesssim 2$ (e.g. Hopkins & Hernquist 2006; Hopkins et al. 2007c, 2008a). However, this naturally predicts that N_{GC} should serve reasonably well as a mass tracer, so that the dependence of M_{BH} on M_* and formation time leads to a surprisingly tight but expected

N_{GC}–M_{BH} correlation. The same arguments explain the result in Hopkins et al. (2009d), who show that the observed M_{BH} is sensitive to the entire galaxy baryonic mass – i.e. perhaps the mass traced by N_{GC} is the same as the mass that actually sets the escape velocity and potential well depth at $R = 0$, rather than just the stellar mass enclosed in a small radius around the BH, which can vary widely in systems of similar M_{BH}. Such a relation between N_{GC} and global galaxy mass or luminosity has been demonstrated (e.g. Harris & van den Bergh 1981; McLaughlin 1999), and this trait supports the idea that N_{GC} and M_{BH} are connected indirectly by a more fundamental galaxy property.

This also naturally explains why HH10 find that the relation breaks down for S0 galaxies. These galaxies are structurally different than ellipticals and may have different formation histories (Larson et al. 1980), so N_{GC} and the total stellar mass may not faithfully trace the bulge binding energy. Since S0's are not particularly discrepant in M_{BH}–σ (e.g. Gültekin et al. 2009, and previous works), this suggests that the N_{GC}–bulge relation is the connection that weakens for these systems. HH10 also find no statistically significant correlation in spirals: although three out of the four spirals from HH10 lie on the N_{GC}–M_{BH} relation, there simply isn't yet enough data to know for sure if this relation persists for spiral bulges. However, the underlying BHFP relation ties M_{BH} to the binding energy and explains its residual correlations with bulge parameters, even for these disky galaxies where N_{GC} possibly deviates. This alone suggests that the BHFP, not M_{BH}–N_{GC} or M_{BH}–σ, is the 'more fundamental' correlation.

Hopkins et al. (2007b) showed that the existence of a black hole fundamental plane is a robust prediction of numerical simulations of gas-rich mergers that include the effects of gas dissipation, cooling, star formation, and black hole accretion and feedback. The present work shows that this local and widely expected correlation between supermassive

black hole mass and bulge binding energy in feedback-regulated scenarios, combined with a similar correlation for N_{GC}, can account for the observed N_{GC}–M_{BH} relation and its scatter. The interesting question raised by such a correlation is *not* why N_{GC} correlates tightly with M_{BH}, since this is indirect, but why N_{GC} correlates tightly with galaxy binding energy/potential well depth. Some such correlation is expected and observed (McLaughlin 1999; Blakeslee 1999; Peng et al. 2008): an example is that systems at fixed velocity dispersion with higher stellar mass have accreted or formed more stars, likely including globular clusters. But that the N_{GC}–bulge relation should be so tight, and include both metal-rich and metal-poor populations, may support the inferences by BT10 and HH10 (and references therein) that the formation of globular cluster systems and growth of supermassive black holes in elliptical galaxies are driven by a common galaxy property.

Chapter 3

Modeling Mid-Infrared Diagnostics of Obscured Quasars and Starbursts

G. Snyder, C. Hayward, A. Sajina, P. Jonsson, T. J. Cox, L. Hernquist, P. Hopkins, L. Yan

The Astrophysical Journal, Vol. 768, No. 168, 2013

Abstract

We analyze the link between active galactic nuclei (AGN) and mid-infrared flux using dust radiative transfer calculations of starbursts realized in hydrodynamical simulations. Focusing on the effects of galaxy dust, we evaluate diagnostics commonly used to disentangle AGN and star formation in ultraluminous infrared galaxies (ULIRGs). We examine these quantities as a function of time, viewing angle, dust model, AGN

spectrum, and AGN strength in merger simulations representing two possible extremes of the ULIRG population: one is a typical gas-rich merger at $z \sim 0$, and the other is characteristic of extremely obscured starbursts at $z \sim 2$ to 4. This highly obscured burst begins star-formation-dominated with significant PAH emission, and ends with a $\sim 10^9$ yr period of red near-IR colors. At coalescence, when the AGN is most luminous, dust obscures the near-infrared AGN signature, reduces the relative emission from polycyclic aromatic hydrocarbons (PAHs), and enhances the $9.7\mu m$ absorption by silicate grains. Although generally consistent with previous interpretations, our results imply none of these indicators can unambiguously estimate the AGN luminosity fraction in all cases. Motivated by the simulations, we show that a combination of the extinction feature at $9.7\mu m$, the PAH strength, and a near-infrared slope can simultaneously constrain the AGN fraction and dust grain distribution for a wide range of obscuration. We find that this indicator, accessible to the *James Webb Space Telescope*, may estimate the AGN power as tightly as the hard X-ray flux alone, thereby providing a valuable future cross-check and constraint for large samples of distant ULIRGs.

3.1 Introduction

Understanding the link between supermassive black holes (SMBHs) and their host galaxies is essential for deciphering the formation and evolution of galaxies. Galaxy/SMBH co-evolution is expected given the observed correlations between SMBH mass and galaxy properties (e.g., Kormendy & Richstone 1995; Magorrian et al. 1998; Ferrarese & Merritt 2000; Tremaine et al. 2002; Gültekin et al. 2009) and theoretical arguments that SMBH growth is self-regulated by feedback (e.g., Silk & Rees 1998; Springel et al. 2005b;

Hopkins et al. 2007a,b).

A key prediction from this framework is that a galaxy experiencing rapid inflow of cold gas can evolve through various classes of starbursts and active galactic nuclei (AGN), such as ultra-luminous infrared galaxies (ULIRGs) and quasars (QSOs), and that these phases are connected in an evolutionary sequence (e.g., Sanders et al. 1988). With such a model, both a starburst and a heavily obscured AGN can co-exist (Hopkins et al. 2006a).

Testing this picture requires not only finding signatures of obscured AGN activity within starburst galaxies, but also interpreting them in the context of galaxy/SMBH co-evolution. Locally, the most extreme starbursts are the ULIRGs ($L_{\rm IR} > 10^{12} L_{\odot}$; Sanders et al. 1988), which are almost exclusively the result of a recent/ongoing major merger (Sanders & Mirabel 1996), which triggers both starburst and obscured AGN activity. To evaluate SMBH growth and the role of feedback during this critical phase, it is necessary to robustly estimate the AGN power during all observed phases. A primary challenge to determine the fraction of flux attributable to the AGN is the reprocessing of its photons by the host galaxy's interstellar medium (ISM). In essence, most diagnostics focus on finding signatures that are directly associated with the AGN output: narrow-line region (NLR) emission, X-rays, torus emission, or radio emission.

A popular approach to study, in particular, dust-obscured AGN utilizes the mid-infrared (mid-IR) regime, loosely defined as 3-30μm, where typical starbursts have a spectral energy distribution (SED) with a minimum in continuum emission, while continuum emission from dust surrounding AGN rises toward longer wavelengths owing to hot dust emission, potentially from a torus (e.g., Pier & Krolik 1992; Stern et al. 2005;

Hönig et al. 2006; Nenkova et al. 2008).

This idea led to the construction of diagnostic diagrams separating starburst from AGN dominated sources, based on Infrared Space Observatory (*ISO*) data of local IR-luminous sources (Lutz et al. 1996, 1998; Genzel et al. 1998; Rigopoulou et al. 1999; Laurent et al. 2000; Tran et al. 2001). The sensitive Infrared Spectrograph (IRS; Houck et al. 2004) aboard the *Spitzer* Space Telescope (Werner et al. 2004) enabled the expansion of this approach to larger samples covering a wider range of physical properties (e.g., Smith et al. 2007; Brandl et al. 2006; Schweitzer et al. 2006; Wu et al. 2006; Dale et al. 2006; Armus et al. 2006, 2007; Sturm et al. 2006; Spoon et al. 2007), and permitted mid-IR diagnostic work on objects at higher redshifts. In particular, mid-IR diagnostics have been applied to galaxies at $z \sim 1$ to 3 (e.g. Houck et al. 2005; Yan et al. 2007; Pope et al. 2008), the epoch of peak star-formation rate density (e.g., Bouwens et al. 2007) and peak quasar number density (e.g., Richards et al. 2006b), which makes it a period crucial for evaluating the co-evolution of galaxies and SMBHs. It is also when LIRGs and ULIRGs (see Sanders & Mirabel 1996, for a review) make a significant contribution to the global averaged luminosity density and to the cosmic infrared background (Le Floc'h et al. 2005; Dole et al. 2006; Caputi et al. 2007; Hopkins et al. 2010a).

Other findings on high-z IR-luminous galaxies suggest that high-redshift ULIRGs may be unlike local ULIRGs in that they may not all be late-stage mergers. For example, $z \sim 2$ sources tend to be more starburst-dominated than $z \sim 0$ sources of comparable mid-IR luminosity (Fadda et al. 2010). Differences in both the spectral energy distributions (SEDs) and morphologies of high redshift ULIRGs, as compared with local ($z \lesssim 0.1$) sources, do suggest that they are not analogous (e.g., Sajina et al. 2012, hereafter S12). Furthermore, submillimetre galaxies, a subset of high-redshift ULIRGs,

may be a mix of early-stage quiescently star-forming mergers, late-stage merger-induced starbursts, and isolated disk galaxies (Hayward et al. 2012, 2013). The typically greater gas fractions (Tacconi et al. 2010) imply that fueling both star-formation and black hole accretion is relatively easier, and therefore not necessarily analogous to what we see in local ULIRGs.

In both the local and high-redshift work, it is not clear to what extent common diagnostics miss the crucial evolutionary stage when the AGN is most deeply obscured. It is possible that we can only detect the presence of an AGN once sufficiently many unobscured lines of sight to the AGN exist. Moreover, while IR diagnostics generally follow the expected AGN/starburst fractions, the evolution of IR SED properties reflects a complex mix of these components which may be difficult to interpret for individual sources or samples (Veilleux et al. 2009, hereafter V09). Therefore it is desirable to search for signposts of AGN powering that may suffer minimally from these complexities.

To analyze this issue, numerical calculations have been used to capture the complex geometries and radiation sources relevant for disentangling AGN activity from star formation. Originally restricted to simplified geometries (e.g., Witt et al. 1992), calculations of dust attenuation and reprocessing are now tenable for three-dimensional dynamical simulations on galactic scales including starbursts and SMBH emission (e.g., Chakrabarti et al. 2007). Studies of hydrodynamical simulations with dust radiative transfer in postprocessing have found that AGN signatures, such as a power-law SED or warm IR colors in ULIRGs, are generally associated with SMBH activity (Younger et al. 2009) but may also be caused by intense starbursts (Narayanan et al. 2010b). Analyzing the predicted far-IR emission from such simulations, Hayward et al. (2011a) and Hayward et al. (2012) found that the IR signatures of star formation vary depending

on whether the activity occurs in a quiescent or bursty mode, potentially complicating discriminators of AGN and star formation activity. One challenge raised by this body of work is how to interface the modeled SMBH with the host galaxy when it is not feasible to model the central engine fully self-consistently, a problem similar to the one described by, e.g., Jonsson et al. (2010) for modeling young star clusters.

In this paper we combine the high diagnostic power of mid-IR features, such as PAH emission and the $9.7\mu m$ silicate feature (e.g., Siebenmorgen et al. 2005; Levenson et al. 2007), with three-dimensional hydrodynamical galaxy merger simulations to better understand existing *Spitzer* IRS data, and to prepare for future data from the *James Webb Space Telescope*. In this novel approach to AGN diagnostics, we calculate infrared SEDs from simulations using dust radiative transfer, including a simple model for AGN accretion and emission. We then use mid-IR diagnostics to gain insight regarding AGN activity when dust in the host galaxy may be important, and also to highlight areas in which such modeling techniques might be improved. In Section 3.2 we describe simulations of two representative starbursts meant to bracket the level of obscuration in ULIRGs, from which we compute and analyze the mid-IR SEDs as described in Section 3.3. In Section 4.3, we show how these features depend on AGN power, evolutionary stage, viewing direction, intrinsic AGN SED, and assumptions about the dust and ISM. In Section 3.5 we construct commonly used diagnostic diagrams and evaluate their ability to estimate the AGN luminosity fraction. We consider implications of this work for future AGN modeling and studies of the evolution of IR-luminous galaxies in Section 3.6, and we conclude in Section 5.7. We explore a toy model for our indicators in Appendix 3.7.

3.2 Simulations

We combine high-resolution GADGET-2 (Springel 2005) 3-D N-body/smoothed-particle hydrodynamics (SPH) simulations of equal-mass galaxy mergers with the SUNRISE (Jonsson 2006; Jonsson et al. 2010) polychromatic Monte Carlo dust radiative transfer (RT) code to examine commonly-applied mid-infrared (mid-IR) AGN signatures. We focus on two representative mergers, a "highly obscured" hyper-LIRG analogue, and a "less obscured" marginal ULIRG example. The highly obscured simulation analyzed here is the same one focused on in Hayward et al. (2011a).

3.2.1 Hydrodynamical simulations

GADGET-2 is a TreeSPH (Hernquist & Katz 1989) code that conserves both energy and entropy (Springel & Hernquist 2002). The simulations include radiative heating and cooling as in Katz et al. (1996), which assumes ionization equilibrium with an ultraviolet background (Faucher-Giguère et al. 2009) and no metal line cooling. Star formation (SF) is modeled to reproduce the global Kennicutt-Schmidt law (Kennicutt 1998) via the volumetric relation $\rho_{\rm SFR} \propto \rho_{\rm gas}^{1.5}$ with a minimum density threshold $n \sim 0.1$ cm^{-3}. The star formation law employed should be considered an empirically and physically motivated prescription to summarize physics we do not resolve. We do not track the formation of molecular gas or resolve individual molecular clouds, and this limitation is a key uncertainty in our radiative transfer step (see Section 3.2.3).

The structure of the ISM is modeled via a two-phase sub-resolution model in which cold, star-forming clouds are embedded in a diffuse, hot medium (Springel & Hernquist

2003) pressurized by supernova feedback that heats the diffuse ISM and evaporates the cold clouds (Cox et al. 2006b). All supernova energy is assumed to thermally heat the hot ambient medium, and no kinetic stellar wind kicks are used. Metal enrichment is calculated by assuming each gas particle behaves as a closed box with a yield $y = 0.02$. Supermassive black hole (SMBH) particles accrete via Eddington-limited Bondi-Hoyle accretion and deposit 5% of their luminosity to the nearby ISM as thermal energy (Springel et al. 2005b; Di Matteo et al. 2005). The luminosity is computed from the accretion rate assuming 10% radiative efficiency, $L_{\rm bol} = 0.1\dot{M}c^2$.

In this paper, we focus on two merger simulations, summarized in Table 3.1, that represent starbursts with different characteristics. Our "highly obscured" simulation is a very massive, gas-rich merger meant to mimic very luminous starbursts at $z \sim 2$ to 4, while the "less obscured" simulation is more representative of typical gas-rich mergers at $z \sim 0$. In each case, we use two identical progenitor galaxies. The progenitors of the highly obscured merger are composed of an exponential disk with baryonic mass $4 \times 10^{11} M_\odot$ (60% of which is gas) and dark matter halo of mass $9 \times 10^{12} M_\odot$ described by a Hernquist (1990) profile. The galaxy properties are scaled to $z \sim 3$ following

Table 3.1. Properties of Merger Simulations

Name	$M_{\rm halo}/M_\odot$	$M_{\rm disk}$	$f_{\rm gas,0}$	$M_{\rm BH}(t=0)$	$M_{\rm BH}(t_4)$	$N_{\rm halo}$[a]	$N_{\rm disk}$[a]
Highly Obscured[b]	9×10^{12}	4×10^{11}	0.6	1.4×10^5	9.6×10^8	6×10^4	8×10^4
Less Obscured[c]	2.6×10^{12}	1.1×10^{11}	0.4	1.4×10^5	8.7×10^7	1.2×10^5	8×10^4

[a]Number of SPH particles in each progenitor. Gravitational softening lengths are 200 h^{-1} pc for the dark matter particles, and 100 h^{-1} pc for the disk particles

[b]Galaxy properties scaled to $z \sim 3$ following Robertson et al. (2006b)

[c]Galaxy properties assumed typical for $z \sim 0$

Robertson et al. (2006b). The orbital parameters are identical to those of the 'e' orbit of Cox et al. (2006a). In contrast, the progenitors of the weakly obscured example have lower mass ($M_* \sim 10^{11} M_\odot$), are less gas-rich (40%) than the highly obscured example, and are scaled to $z \sim 0$. Each progenitor galaxy is seeded with one SMBH particle.

In this work we focus on signatures of AGN activity that normalize out the galaxy's mass or total luminosity, and therefore the salient difference between these two cases are the relative extents to which the merger triggers star formation, AGN activity, and obscuration. A disadvantage with this approach is we are restricted in the range of ULIRG scenarios we can probe, owing in part to limited computational resources. In this paper we have chosen to explore two merger simulations that potentially reflect the extremes of IR-luminous galaxies, and we discuss further consequences of this limitation in Section 3.2.4.

3.2.2 Radiative transfer

We use SUNRISE[1] Version 3 in post-processing to calculate the SED observed from seven cameras distributed isotropically in solid angle every 10 Myr. For a full description of SUNRISE see Jonsson (2006) and Jonsson et al. (2010), and for a summary of components essential for this work and a description of other specific choices, see Hayward et al. (2011a). We describe specific choices for some of the radiative transfer parameters in Section 3.2.3.

[1]see http://code.google.com/p/sunrise/ for the project source code and documentation

Sources

SUNRISE calculates the emission from the stars and AGN in the GADGET-2 simulations and the attenuation and re-emission from dust. STARBURST99 (Leitherer et al. 1999) SEDs are assigned to star particles according to their ages and metallicities, and SMBH particles emit the luminosity-dependent templates of Hopkins et al. (2007d) by assuming the formula above for $L_{\rm bol}$. At mid-IR wavelengths this template emits the mean SED of Richards et al. (2006a). In Section 3.4.4, we vary the AGN source SED, applying two clumpy torus models by Nenkova et al. (2008) that span their modeled properties. Our templates follow typical bright AGN in that only $\lesssim 10\%$ of their flux is emitted at X-ray wavelengths

Recently formed star particles ($t < 10^6$ yr) are assigned the MAPPINGSIII HII region sub-grid SED models of Groves et al. (2008). These models include a dusty photodissociation region (PDR) with a tunable covering fraction ($f_{\rm PDR}$). With a non-zero $f_{\rm PDR}$, the dust re-emission from such regions is included in the emission template. In these models, a fraction of the carbon grains are assumed to be PAH molecules whose absorption is calculated from the cross sections by Draine & Li (2001). Their emission is modeled to follow a fixed template of Lorentzian profiles designed to match *Spitzer* IRS observations of PAH emission (Dopita et al. 2005; Groves et al. 2008). We use $f_{\rm PDR} = 0$ for the "highly obscured" simulation owing to concerns about the applicability of these templates to the extreme ISM densities and pressures found in this merger ; see Section 2.2.1 of Hayward et al. (2011a) for a full discussion of these issues.

ISM Structure, Metals, and Dust

To initialize the galaxy dust radiative transfer calculation, SUNRISE projects the GADGET-2 gas-phase metal density onto a three dimensional cartesian adaptive grid. To construct this grid, the code bounds the simulation volume with a $(200\ \mathrm{kpc})^3$ cube and divides this initial cube into 125 equally sized subregions for the first level of refinement. Subsequent refinement is based on an estimate for the dust optical depth in each cell from the GADGET metal density. In this work, nine further refinement steps were undertaken, in which cells targeted for refinement are split into eight sectors by dividing each spatial dimension in half. This leads to a minimum cell size of $(200\ \mathrm{kpc}/5)/2^9 = 80\ \mathrm{pc} = 55\ \mathrm{h}^{-1}\ \mathrm{pc}$, roughly half of the softening length ($100\ \mathrm{h}^{-1}\ \mathrm{pc}$) used for the hydrodynamical simulations, or $\sim 1/4$ of the SPH resolution. For the fixed resolution of the hydrodynamical simulations, this level of refinement ensures that the SEDs are converged to within 10% (Hayward et al. 2011a), indicating that our radiative transfer grid settings are satisfactory for the simulations we use here.

The galaxy stars and gas were assumed to have an initial mass fraction in metals of $Z = 0.01$. During the mergers presented here, the mean gas-phase mass fraction of metals increases to $Z \sim 0.018$ just after the merger coalescence. Here we assume 40% of these metals are in dust (Dwek 1998). We consider the Milky Way $R_V = 3.1$ (MW) and SMC bar (SMC) dust models of Weingartner & Draine (2001) updated by Draine & Li (2007). These models are comprised of populations of carbonaceous and silicate dust grains inferred from observations along lines of sight to stars in the two regions. The SMC dust grain model we apply differs from the MW model in part by having a factor of ~ 10 fewer small carbonaceous grains (including, e.g., the PAHs), leading to a much

weaker 2175 Å absorption feature. In active regions, small grains are expected to be depleted by a number of processes (e.g., Laor & Draine 1993) on short timescales, and it has been found that galactic dust appears to vary continuously between properties that are MW-like and those that are SMC-like owing to the influence of star formation activity (e.g., Gordon et al. 2003, and references therein). Draine et al. (2007) found that typical nearby spirals tend to have dust properties similar to those that give rise to the MW dust model, while bright AGN are believed to be depleted of small grains (Laor & Draine 1993). Hopkins et al. (2004) found that an SMC-like dust model better matches reddening of the optical colors in quasars. Observations of nearby starburst galaxies were found to lack a strong 2175 Å extinction feature, also resembling SMC dust (Gordon et al. 1997; Gordon & Clayton 1998). Likewise, Vijh et al. (2003) found that the SEDs of $z \sim 3$ starbursts (e.g., Lyman break galaxies) indicate SMC-like dust.

Therefore, the observed dust properties are correlated with the evolutionary stage of the galaxy, as SF and AGN activity affect the creation and destruction of grains. We limit ourselves to specifying the dust model by hand to these MW and SMC models, but in principle an evolving model could be developed and tested against observations using a suite of simulations like those we analyze here.

Radiative Transfer

With the dust distribution and grain models set, SUNRISE then performs Monte Carlo radiative transfer through the galaxy dust by emitting photon packets from the sources and drawing interaction optical depths from the appropriate probability distribution as the packets traverse the ISM. For each grid cell, the temperature of each dust

species (with the exception of polycyclic aromatic hydrocarbons; PAHs) is calculated assuming the dust is in thermal equilibrium, and the dust re-emits the absorbed energy as a modified blackbody. PAH molecules are treated using a method similar to the MAPPINGSIII models. A fixed fraction, f_t, of the carbon grains with size $a < 100$ Å are assumed to emit radiation thermally. The remaining fraction, $1 - f_t$, are assumed to be PAH molecules which emit the template spectrum from (Groves et al. 2008). f_t is a free parameter that we set to $f_t = 0.5$ following Jonsson et al. (2010), roughly matching the $8\mu m$-$24\mu m$ flux ratios from the *Spitzer* Infrared Nearby Galaxies Survey (Dale et al. 2007). In high-density regions, the dust can be opaque to its own emission, so the contribution of the dust emission to dust heating must be considered. SUNRISE computes this self-consistently by iteratively performing the transfer of the dust emission and the temperature calculation using a reference field technique.

SUNRISE calculates energy absorption by dust from radiation at wavelengths 912 Å$< \lambda < 1000\ \mu m$, neglecting dust heating by radiation at energies above the Lyman limit. This may neglect some amount of energy absorbed from X-ray radiation ($h\nu > 0.5$ keV) by atoms in dust grains. However, since our AGN template emits $\lesssim 10\%$ of its energy at these wavelengths, and the dust may not thermalize effectively under radiation at these wavelengths, we expect that the contribution to thermal dust emission we ignore from this regime can comprise only a few percent of the bolometric luminosity (Laor & Draine 1993). Additionally, SUNRISE neglects the effects of thermal fluctuations in stochastically heated galaxy dust grains.

Our focus herein is the mid-IR portion of the rest-frame SEDs, $1\mu m < \lambda < 30\mu m$, a regime in which dust grains heated to a wide range of temperatures ($T \sim 100$ to 1500 K) emit thermal radiation. Arbitrary dust temperature distributions are possible during

a gas-rich galaxy merger, owing to the complex and chaotically-evolving multi-phase structure of the ISM induced during a global starburst and feedback-regulated SF and SMBH growth. Thus the accurate dust heating calculations employed by SUNRISE, including treatments of multiple dust species, are essential for understanding this key phase of galaxy evolution.

Since we will make extensive use of the 9.7 μm silicate absorption feature, we stress that the depth of the feature is determined self-consistently via the radiative transfer. The strength of the feature depends on the amount of dust and the geometry of sources (stars and AGN) and dust. For reasonable galaxy geometries we expect the AGN to be more obscured than the bulk of the stars; this differential extinction is inherently ignored when one assumes a foreground screen dust geometry, so our simulations provide an excellent way to test the uncertainties caused by this assumption.

The results of the SUNRISE calculation are spatially resolved, multi-wavelength SEDs observed from seven directions. The success of this approach at modeling diverse galaxy populations—both local (e.g., Younger et al. 2009; Bush et al. 2010b; Snyder et al. 2011a) and high-redshift (e.g., Wuyts et al. 2010; Narayanan et al. 2010a,b; Hayward et al. 2012, 2013)—lends credibility to its application here.

3.2.3 Alternate Radiative Transfer Models

In order to gain additional physical insight, we consider different sets of assumptions for the radiative transfer stage, including two sub-resolution models for the dust distribution on scales below that resolved by the GADGET-2 simulation. For our highly obscured simulation, we will focus on the ISM treatment referred to in Hayward et al. (2011a)

as "multi-phase off". This choice assumes that the dust mass contained in both phases of the Springel & Hernquist (2003) ISM model is distributed uniformly across each resolution element, which is likely appropriate for gas-rich mergers in which the central regions are are composed of dense, almost exclusively molecular gas. Throughout this work we refer to this model as our "default ISM" treatment.

Alternatively, we can assume that gas in the cold, dense clouds of the Springel & Hernquist (2003) model has negligible volume filling factor. This alternate choice distributes dust mass that corresponds to the diffuse gas phase of the Springel & Hernquist (2003) model uniformly across each resolution element, but assumes no attenuation from the dust occupying the dense, cold clouds. In this case we neglect attenuation and emission from both the cold clouds in which stars are formed and from other clouds photons encounter along the line-of-sight. This assumption thus gives a lower limit on the amount of attenuation. We refer to this assumption as our "alternate ISM" treatment, and apply it to both our highly and weakly obscured simulations.

The fraction of gas in the cold phase, and therefore the amount of dust ignored by the alternate ISM model, varies with time and position during our simulations. For the highly obscured merger, the amount of mass in the cold phase is $\sim 38\%$ ($\sim 27\%$) at the peak of the starburst (AGN). For the less obscured merger, this fraction is $\sim 28\%$ at the peak starburst and $\sim 15\%$ at peak AGN power. Gas which is at higher densities contains a larger fraction in the cold phase, and so during merger coalescence gas in the central few kpc achieves a cold phase fraction of $\sim 90\%$. Thus the alternate ISM assumption, discarding this fraction of dust in the cold clouds, more strongly affects the central regions than the galaxy as a whole. Our radiative transfer calculation implicitly assumes that this dust does not absorb any energy, and therefore it is not included in the

IR emission calculation. This dust emission would primarily affect far-IR wavelengths, and so it should not affect the analysis presented here.

The two treatments of subresolution dust structure we employ should be considered two plausible and physically-motivated, yet uncertain, ISM models that encapsulate unresolved processes. With current simulations it is only possible to parameterize our ignorance in this way. However, *any* model used to interpret ULIRG SEDs is limited by this uncertainty. These simulations are thus particularly useful for their ability to quantify the uncertainty caused by dust clumpiness.

For both mergers, we perform the RT calculations after multiplying the SMBH luminosity at all times by zero (AGNx0), one (AGNx1), and ten (AGNx10), allowing us to manually adjust the AGN contribution to the SEDs. Note that the effect of AGN feedback, the thermal heating of the ISM surrounding the SMBH particles, is kept fixed at the fiducial level of Section 3.2.1. The AGN contribution to the mid-IR SED arises from separate self-consistent RT calculations with each of our assigned AGN luminosities, dust grain models, and ISM assumptions. This enables us to cleanly test how a given indicator depends on AGN luminosity for fixed geometry and galaxy ISM conditions. At each of these AGN strengths, we apply both ISM assumptions to the highly obscured merger and the "alternate ISM" treatment for the less obscured case. For these three sets of three simulations, we perform the RT using both the MW and SMC bar dust models.

3.2.4 Galaxy models

Although the "high obscuration" and "low obscuration" simulations are meant to mimic gas rich starbursts in massive major mergers at $z \sim 3$ and $z \sim 0$, respectively

(Table 3.1), these cases do not necessarily accurately reflect the real ULIRG population at a given redshift. The "high obscuration" example is, by choice, a particularly massive and gas-rich merger, and thus becomes a luminous hyper-LIRG that reaches a peak $\log L_{IR} \sim 13$ briefly, having $\log L_{IR} > 12$ for ~ 1 Gyr. This merger is consistent with extreme starbursts such as sub-millimeter galaxies (SMGs) and hot-dust ULIRGs at $z \sim 2$ to 4 (Hickox et al. 2012; Hayward et al. 2012, 2013), and therefore reflects a typically observed source at these redshifts (note: this does not mean it is a typical galaxy). By contrast, the "weakly obscured" example is marginally a ULIRG, briefly reaching $L_{IR} \sim 10^{12} L_{\odot}$ at merger coalescence under our default assumptions, consistent with the idea that local ULIRGs are almost exclusively ongoing mergers (Sanders & Mirabel 1996). Note that the initial gas fractions assigned in our progenitors, 60% and 40%, are high compared to comparable star-forming galaxies at these two epochs — this is to account for our neglecting cosmological accretion and gas recycling, and a fairer comparison is to the gas fractions at the time of merger, which are $\sim 30\%$ and $\sim 20\%$.

Of course, real IR-luminous galaxy samples at a given redshift will draw from a wide range of scenarios. Therefore we cannot hope to fully represent the ULIRG population in the present study. However, we will focus primarily on the goal of separating AGN from SF activity in a small set of experiments defined by our two mergers with the radiative transfer variants described in Section 3.2.3, whose properties may more broadly span plausible situations. As an example, at $z \sim 3$, there are some mergers with the same stellar mass as our highly obscured simulation but a lower gas fraction. In the Eddington-limited phase, such mergers may have higher AGN-to-SF fractions than our fiducial highly obscured calculation, so the AGNx10 model may more accurately represent such cases. Similarly, our simulations at $z \sim 0$ may not be a close match to the

conditions in all local ULIRGs. Moreover, while the final mass of our accreting SMBHs depends primarily on the fraction of feedback energy coupled to the ISM (e.g., Springel et al. 2005b), the growth history of SMBH, and hence its luminosity at a given time, can depend sensitively on the adopted sub-resolution model.

Given these uncertainties, the goal of our experiments — in particular the AGNx0, AGNx1, and AGNx10 models — is to cover our bases and controllably boost the luminosity so that we span a wide enough range in the ratio of AGN to SF activity, and not to comprehensively predict the behavior of observed ULIRGs. In the future, a more realistic treatment of the population may be possible as large suites of high-resolution simulations become more common. However, many uncertainties remain not only in the physical models of the ISM and AGN accretion on sub-resolution scales, but also in how to interface emission and dust attenuation from the central engine with the host galaxy in the radiative transfer stage (e.g., Jonsson et al. 2010). Therefore we begin with an exploration of these few numerical experiments in a first attempt to explore the applicability of this modeling technique.

In Figure 3.1 we summarize the predicted SEDs of our mergers. We focus on four times during each merger spanning ~ 500 Myr, and present the total mid-IR SEDs emerging in a particular direction. In the left SED columns we show the results of our fiducial ISM assumption, but artificially vary the total luminosity of the two (and eventually one) SMBH particles. In the right SED columns we explore our assumptions about the ISM and dust, a study that we analyze in more detail below in Section 3.4.2 (see also Section 3.2.3).

Figure 3.1.—: An overview of the SEDs of our merger simulations. First we show false-color rest-frame U-V-J and IRAC composite images of the highly obscured merger at each of four example times, as seen from the same direction as the SEDs that follow are measured, and utilizing our default RT model and AGN strength. On the next page we show total rest-frame SEDs of the highly obscured merger from this example viewing direction at each of four times labeled in the left-most panel. SEDs have the same arbitrary flux normalization. Different curves in the left column represent our fiducial dust model, but the input AGN spectrum has been multiplied by 0, 1, and 10. Curves in the second column show our fiducial AGN level, but different ISM assumptions. Finally, we demonstrate the SEDs of the less obscured merger.

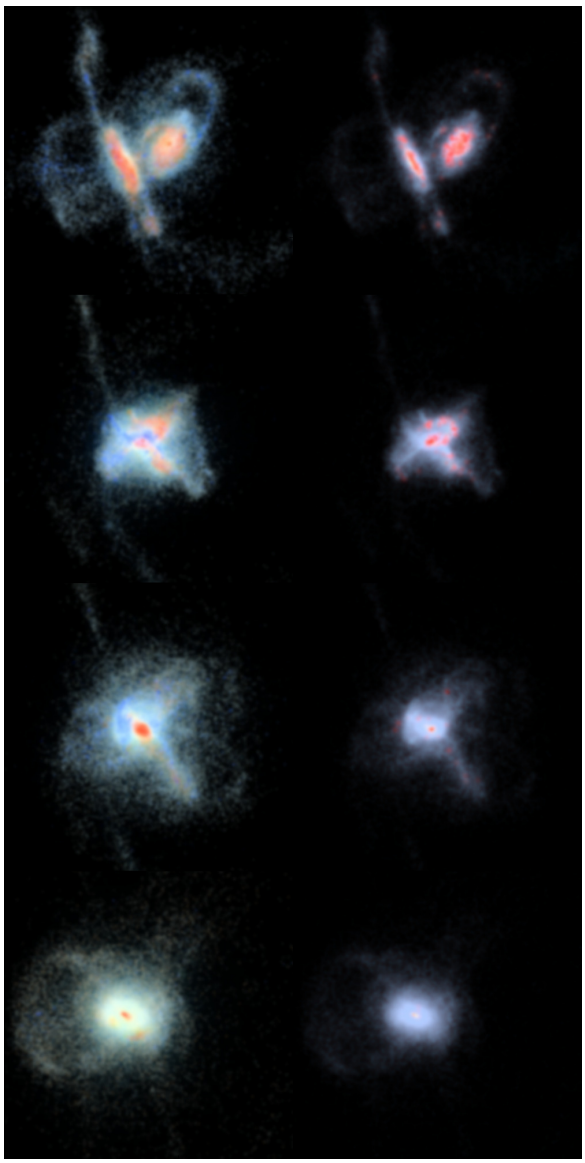

Figure 3.1.—: (Continued)

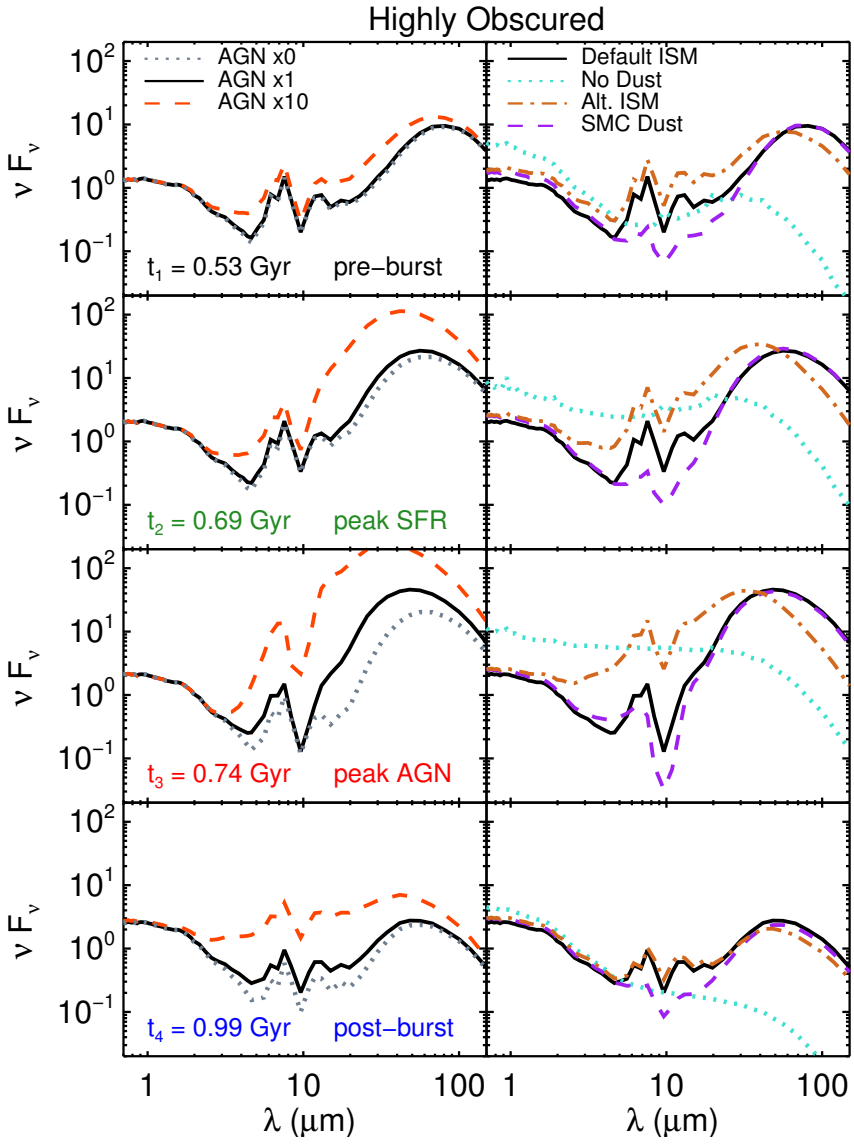

Figure 3.1.—: (Continued)

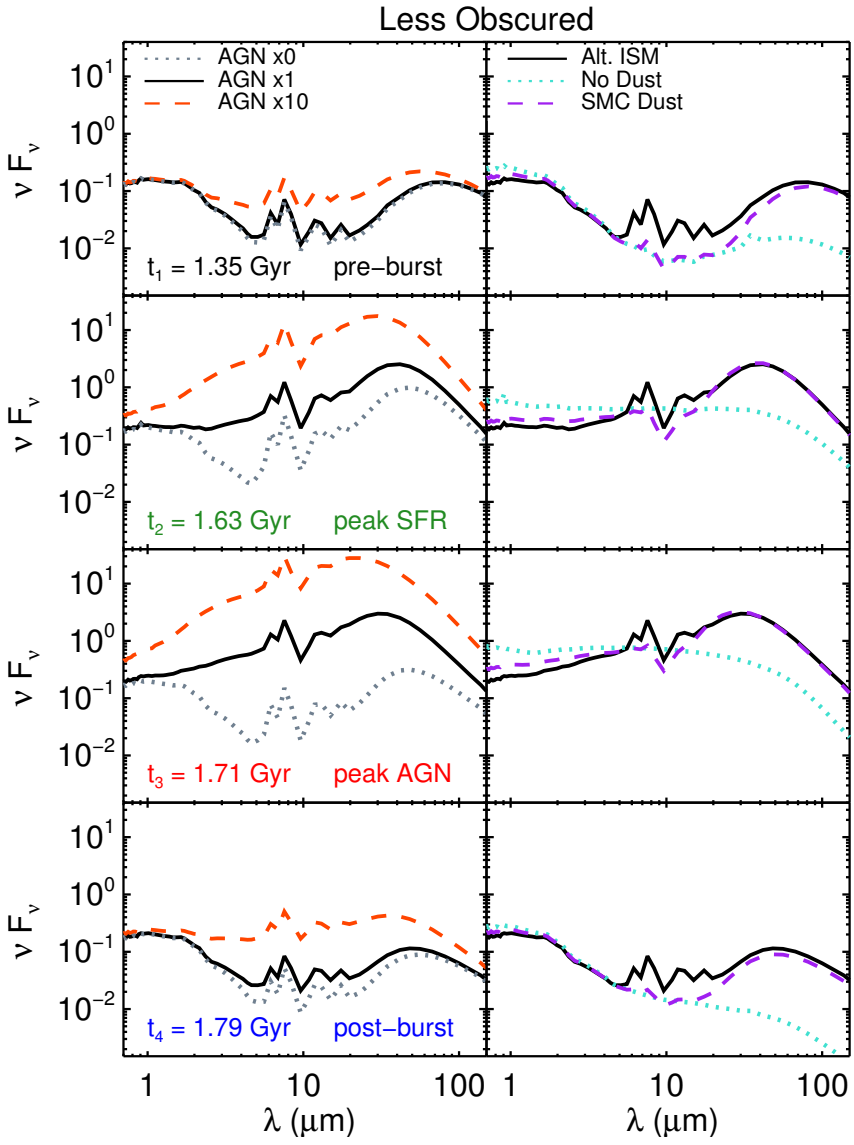

Figure 3.1.—: (Continued)

Alongside the SEDs we show high-resolution false-color composite images corresponding to the same viewing direction as the highly obscured SEDs. The left images present the system in the U, V, and J bands (Johnson & Morgan 1953), and the second in the 3.6, 4.5, and $8\mu m$ channels of the *Spitzer* Infrared Array Camera (IRAC; Fazio et al. 2004). These images provide some insight into how these systems might be classified in terms of a merger-stage diagnostic – if this system is observed at high redshift, then the only time it is obviously a merger is at $t \lesssim t_1$. This precedes the SMBH's peak luminosity and therefore the times at which it makes an obvious contribution to the mid-IR SED, a period spanning ~ 1 Gyr.

3.2.5 X-ray Calculations

We compute X-ray fluxes from SMBH particles and subsequent attenuation by the ISM following the approach described by Hopkins et al. (2005a) and Hopkins et al. (2006a). This method uses the intrinsic quasar SED (Section 3.2.2 and Hopkins et al. 2007d), and calculates its extinction at X-ray wavelengths by applying the photoelectric absorption cross sections of Morrison & McCammon (1983), as well as Compton scattering cross sections, each scaled by metallicity.

A key difference between Hopkins et al. (2005a) and the present work is their assumptions correspond to the "alternate ISM" treatment we described in Section 3.2.3, where the cold clumps in the ISM, and hence often a significant fraction of the dust mass, are assumed to have a small volume filling factor. This may be true under many conditions, but may not be applicable to extremely gas-rich ULIRGs with abundant supplies of molecular gas. Therefore we choose to use the same assumptions for X-ray

attenuation that we use for the IR calculations described in Section 3.2.3. For our highly obscured merger simulation we calculate the column densities that attenuate the X-ray flux both ways: by discarding the cold phase mass ("alternate ISM"), and by keeping the cold phase mass ("default ISM"). For our less obscured merger simulation, we use only the "alternate ISM" model, discarding the cold phase mass.

3.2.6 AGN Fraction

For this paper, we focus on the AGN fraction, which we define as the ratio of SMBH luminosity to total luminosity across the wavelength range used by SUNRISE: 0.09 to $10^3 \mu m$. We denote this quantity $L_{\rm agn}/L_{\rm bol}$. Our definition uses the intrinsic AGN power regardless of how it appears in the final observed SED (i.e., it is insensitive to the amount of attenuation), but it does not include AGN emission at X-ray wavelengths. This quantity, $L_{\rm agn}/L_{\rm bol}$, is not normally available for a given observed sample. Here, the SMBH accretion rate and $L_{\rm agn}/L_{\rm bol}$ are available directly from the GADGET and SUNRISE calculations. Thus we can evaluate directly the effectiveness of observed indicators, defined in Section 3.3, at estimating the AGN contribution utilizing self-consistent calculations of the galaxy's stars, dust, and SMBH.

3.3 Mid-Infrared Spectral Diagnostics

3.3.1 From Simulations

We compute mid-infrared diagnostics based on the rest-frame spatially integrated SUNRISE SEDs, which we store as specific luminosities, i.e., the energy through the camera per unit time and per unit frequency (or wavelength) interval: L_ν or L_λ. For simplicity and for analogy with observable quantities, we denote these as $f_\lambda \equiv L_\nu(\lambda)$, where λ is in microns. Owing to computational constraints, these SEDs have very low spectral resolution ($\lambda/\Delta\lambda \sim 10$), so we limit consideration to approximations of several observationally-motivated estimators. We focus on two spectral dust features, $r_{9.7}$, $r_{7.7}$, defined by

$$r_{9.7} = \frac{f_{9.7}}{c_{9.7}}$$
$$r_{7.7} = \frac{f_{7.7}}{c_{7.7}},$$

where c_λ is the continuum level estimated by interpolating linearly between $f_{5.7}$ and f_{15}. The remaining indicators are ratios of f_λ at 1.6, 5.7, 15, and 30 μm. These points were chosen to match common mid-IR colors, in which a point is often chosen just below $6\mu m$ to avoid the $6.2\mu m$ PAH and $6\mu m$ water ice features. Unless otherwise specified, we present all SEDs and their derived quantities in the source's rest frame.

In Figure 3.2 we present an example rest-frame SED in the mid-IR and highlight the spectral features that we will consider here. In addition to the final SED, we plot the intrinsic SMBH SED that we assume, which exhibits a generally flat shape with an "IR bump". If this source were observed unobscured, or obscured only by an optically thin (at several μm) dust column, then this would resemble a "power-law-like" AGN

source with red near- and mid-IR colors. We see this situation in the t_2 and t_3 panels for the less obscured merger (right side) of Figure 3.1: the $f_{4.5}/f_{1.6}$ slopes depend strongly on the AGN strength, and a comparison of the "no dust" and "alternate ISM" cases indicates that dust attenuation is insignificant at wavelengths longer than a few microns. Furthermore, a near-IR slope (such as $f_{4.5}/f_{1.6}$) has been used to select AGN in wide-field IR surveys (see, e.g., Stern et al. 2005, 2012). Thus we will keep this feature in mind while analyzing the mid-IR properties of more highly obscured sources.

By contrast, the starburst SED falls as lambda increases at $1\mu m < \lambda < 10\mu m$, but also exhibits distinctive features from dust grains identified as polycyclic aromatic hydrocarbons (PAHs) superimposed at 3.3, 6.2, 7.7, 8.6, 11.3, 12.6, and $17\mu m$. For example, SEDs characterstic of starbursts are seen in the first row of SEDs in Figure 3.1 (i.e., the black curves at time t_1) .

3.3.2 From Observations

Observationally, weaker PAH and stronger continuum (i.e., lower PAH equivalent width (EW)) effectively indicate a higher relative contribution from the AGN in dusty galaxies, especially ULIRGs (e.g., Laurent et al. 2000; Sturm et al. 2000; Tran et al. 2001). This diagnostic is supported by mid-IR fine structure line diagnostics implying an AGN-like radiation field in sources of lower PAH EW (Genzel et al. 1998; Armus et al. 2007).

More recently, such mid-IR diagnostic studies discovered sources that have a small PAH EW but a deep $9.7\mu m$ silicate absorption feature (e.g., Houck et al. 2005), which seems to require a deeply embedded, centrally concentrated source (Levenson et al. 2006). These sources are believed to represent Compton-thick AGN (Bauer et al. 2010;

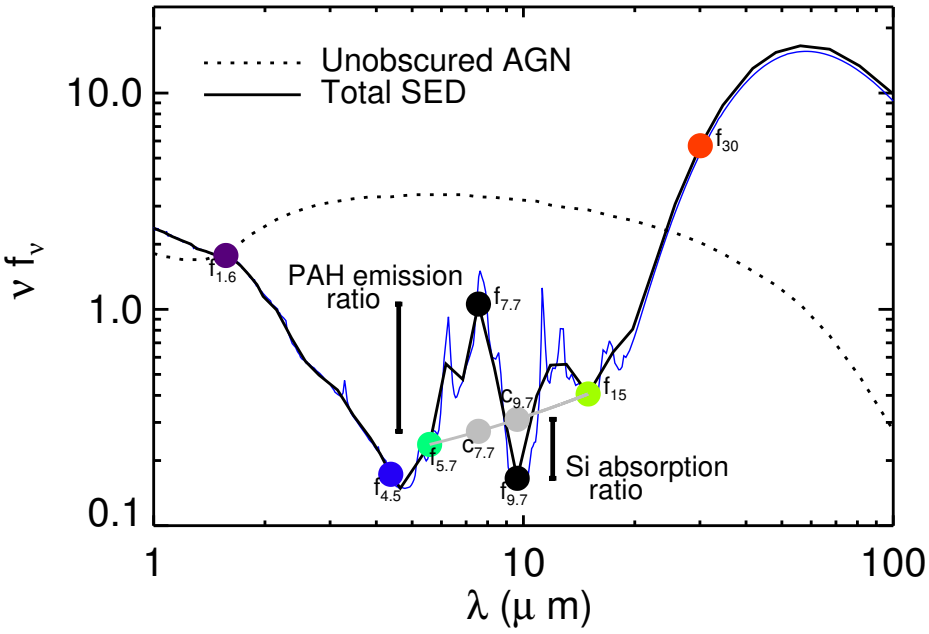

Figure 3.2.—: In the solid black line we show an example SED output from SUNRISE in the source's rest frame. For all subsequent analysis we use this low-resolution version, but here we plot in blue a higher-resolution calculation that demonstrates the validity of the continuum estimation that we show in gray (see Section 3.3). In the dashed black curve we show the intrinsic AGN spectrum used by SUNRISE as a light source from the SMBH particles. This SED occurs between the peak of the starburst and the peak of the AGN's bolometric contribution to the SED (between times t_2 and t_3 shown in Figure 3.1). Note that during this time the intrinsic AGN emission (attributed to the torus) at $2\mu m < \lambda < 10\mu m$ is completely absorbed and reprocessed into the far-infrared.

Georgantopoulos et al. 2011), although there is at least one known star forming dwarf without an AGN whose mid-IR spectrum fits the above criteria (Roussel et al. 2003).

In Section 3.5, we will compare our predictions with data for local and high-z starbursts with available low-resolution *Spitzer* IRS spectra. Specifically, we use the ULIRG sample of V09 and a sample of 192 $24\mu m$-selected $z \sim 0.3-3$ starbursts and obscured quasars. The redshifts and IRS spectra of the $24\mu m$-bright sample are presented

in Yan et al. (2007) and Dasyra et al. (2009), while the full IR SEDs are compiled in Sajina et al. (2012) (S12).

Using the IRS spectra for both ULIRG samples, we estimate $r_{7.7}$, $r_{9.7}$, f_6, f_{15}, and f_{30} in the same manner as for the simulated SEDs. However, the observed spectra have a more limited spectral coverage. The observed coverage of the IRS spectra varies between 5.2 and 38μm, or 14 – 38μm if only the LL modules are used, as is the case for most of the higher-z sample. This means that for the local ULIRG sample, the required rest-frame 6-30μm is covered by the available IRS spectra, while for the 24μm-bright sample, the 15μm and 30μm continuum points are outside the IRS coverage above $z \sim 1.5$. Below $z \sim 1.5$, the 6μm continuum point is often outside the IRS coverage (depending on whether or not the SL module is available), and even the 7.7μm point can be outside the IRS coverage below $z \sim 0.8$. We compensate using the empirical SED model fits from Sajina et al. (2012), which necessarily introduces additional systematic uncertainty. These extrapolations are constrained below or above the IRS spectral coverage with IRAC 3.6, 4.5, 5.8, and 8μm, and MIPS 70μm photometric points, ensuring that the mid-IR colors obtained are reasonably accurate.

We choose to exclude the $z \lesssim 0.9$ sources from this sample in order to avoid all cases where the 7.7μm PAH feature is not covered by the IRS spectra. This step also removes all sources whose overall IR luminosities (L_{3-1000}) place them in the LIRG rather than ULIRG category. We also exclude the $z > 2.5$ sources, for which the 9.7μm silicate absorption feature is too poorly defined, being only partially covered by the IRS spectra. This leaves a total of 118 sources. We explore determining the above quantities with and without interpolating the IRS spectra onto the much lower resolution simulated SED wavelength array,c and we find no significant difference in the overall results.

Lastly, in 4 cases, the silicate feature is saturated making the measured $r_{9.7}$ value a lower limit. The saturation flag is triggered when the mean of the IRS spectra between 9.0 and 10.4μm is less than or equal to the standard deviation in the same region.

In Section 3.6 we discuss the rest-frame near-IR as another means of diagnosing AGN power. For observational comparisons in this regime, we use *Spitzer* IRAC photometry for the high-redshift sample, and for the low-redshift ULIRGs, we interpolate from 2MASS H and K band photometry (using total magnitudes). The unknown aperture corrections add some uncertainty here; however, ULIRGs are typically compact enough in the near-IR relative to the ~ 2.5 arcsecond 2MASS beam that aperture effects should be small (Surace & Sanders 1999; Surace et al. 2000). For several sources, we use 2.5 to 5μm spectra (Imanishi et al. 2008; Sajina et al. 2009) from AKARI for more accurate near-IR fluxes.

3.4 Simulation Results

3.4.1 Time Evolution

In Figure 3.3, we explore how the mid-IR diagnostics vary with time for our two fiducial simulations: "highly obscured" and "less obscured". We show spectral diagnostics along with quantities of interest such as the overall IR luminosity, the star formation rate (SFR), and the AGN fraction, $L_{\rm agn}/L_{\rm bol}$. We assume our default ISM model and default AGN torus model, but we show the effect of varying these choices in Section 3.4.2 and Section 3.4.4, respectively. All curves shown are the median over the viewing angle. The scatter introduced by the uncertainty in the viewing angle is addressed in Section 4.3.4.

To guide the discussion, we indicate the four times from the panels in Figure 3.1 with vertical lines for the highly obscured (left column) and less obscured (right column) mergers. The progenitors are still separated at time t_1, which precedes the period of final coalescence and peak L_{IR} by $\sim$ 200 Myr. The maximum SFR and AGN power occur at $t \sim t_2$ to t_3, after the galaxies have merged, but the central sources are still largely obscured by dust. At t_4, up to $\sim$ 300 Myr later, the SFR has plummeted but the AGN fraction is still elevated, and the remnants are on their way to being ellipticals.

Qualitatively, we find that our simulated mid-IR diagnostics behave largely as expected, but not always. Below we address each of the diagnostics in turn.

The PAH strength, $r_{7.7}$, drops at the time of coalescence (t_2 to t_3), reaching its lowest values at t_3 when the AGN fraction is highest. Pre-coalescence, the PAH strength is weakest for the model with strongest AGN (AGN$\times$10). Post-coalescence, the PAH strength again increases but does not return to its pre-coalescence levels. No significant "coalescence" dip in the PAH strength is seen in the less obscured case. The level of absorption by silicate grains, $r_{9.7}$, is greatest when the AGN is most luminous, which is also when the relative strength of the PAH emission is weakest. These extrema are relatively sharp and confined to the period of final coalescence at $\sim t_2$-t_3, although the AGN luminosity fraction remains elevated for $\approx$ 1 Gyr. Overall, the shape of the PAH strength curve in both the highly obscured and less obscured cases does not bear a strong resemblance to the AGN fraction curve nor to the SFR curve.

In the highly obscured case, the $f_{15}/f_{5.7}$ slope is reddest when the AGN is most luminous, a somewhat counter-intuitive result since the $6\mu m$ continuum is generally believed to be enhanced by AGN torus emission. This result likely owes to the fact

that the time when the AGN fraction is greatest corresponds to the time of greatest obscuration, when the $9.7\mu m$ silicate absorption feature is deepest. This obscuration would lead to significant absorption of the observed $6\mu m$ continuum, reddening the $f_{15}/f_{5.7}$ color. However, this may result from the simulations not having sufficiently clumpy ISM to allow for lines of sight directly to the AGN torus. This slope is also reddened at t_2, the time of peak SFR activity, as expected due to enhanced HII-region type emission. For the less obscured case, the $f_{15}/f_{5.7}$ color is reddened throughout the merger (t_1 to t_4), likely the result of the enhanced SFR, but lacks a sharper reddening at the time of coalescence. This supports our view that the "coalescence" reddening seen in the "highly obscured" case is a direct result of galaxy dust attenuation.

Similarly, the f_{30}/f_{15} slope is effectively constant for the duration of the merger for the less obscured case, but is significantly reddened at the time of coalescence in the highly obscured case. At a given time, this slope is bluer when the AGN source is more luminous (e.g., AGN$\times$10), and in contrast to $f_{15}/f_{5.7}$, f_{30}/f_{15} does not experience a sharp peak at t_3 for the most powerful AGN in the highly obscured merger.

Overall, our simulations indicate that the dependence of any of these mid-IR spectral diagnostics on the AGN fraction is time-dependent and non-linear and is affected by the properties of the host galaxy. The dependence on the overall level of obscuration, as parametrized by the silicate absorption depth, is to some degree stronger. For example, these indicators vary much less when there is less obscuration.

Figure 3.3.—: We compare various rest-frame mid-IR quantities as a function of time for our highly obscured (left) and less obscured (right) starburst simulations. At each time, we plot the median over viewing angle of each quantity. Vertical lines highlight the four characteristic times t_1 to t_4 from Figure 3.1, corresponding to pre-burst, peak starburst, peak AGN, and post-burst. The three curves in each panel represent the same models shown in the left column of Figure 3.1: we multiply the AGN luminosity deduced from the simulation by 0, 1, or 10. In several rows, the gray solid (lined) bands subtend the 25-75% range in the distribution of local ULIRGs (quasars) compiled by Veilleux et al. (2009). In the highly obscured case, the AGN is most dominant and most obscured at the time t_3, when the PAH emission ($r_{7.7}$) and Si absorption ($r_{9.7}$) ratios are minimized, in agreement with previous reasoning. The mid-infrared colors f_{30}/f_{15} and $f_{15}/f_{5.7}$ also exhibit a weaker signal around this time, but this signal can be confused with the starburst phase (t_2) for $f_{15}/f_{5.7}$, and depends non-linearly or not at all on the AGN strength with f_{30}/f_{15}. The more typical starburst represented in the right column is a marginal ULIRG, and its mid-infrared SED is relatively insensitive to the presence of the AGN which dominates at $1.4 < t/\mathrm{Gyr} < 1.8$.

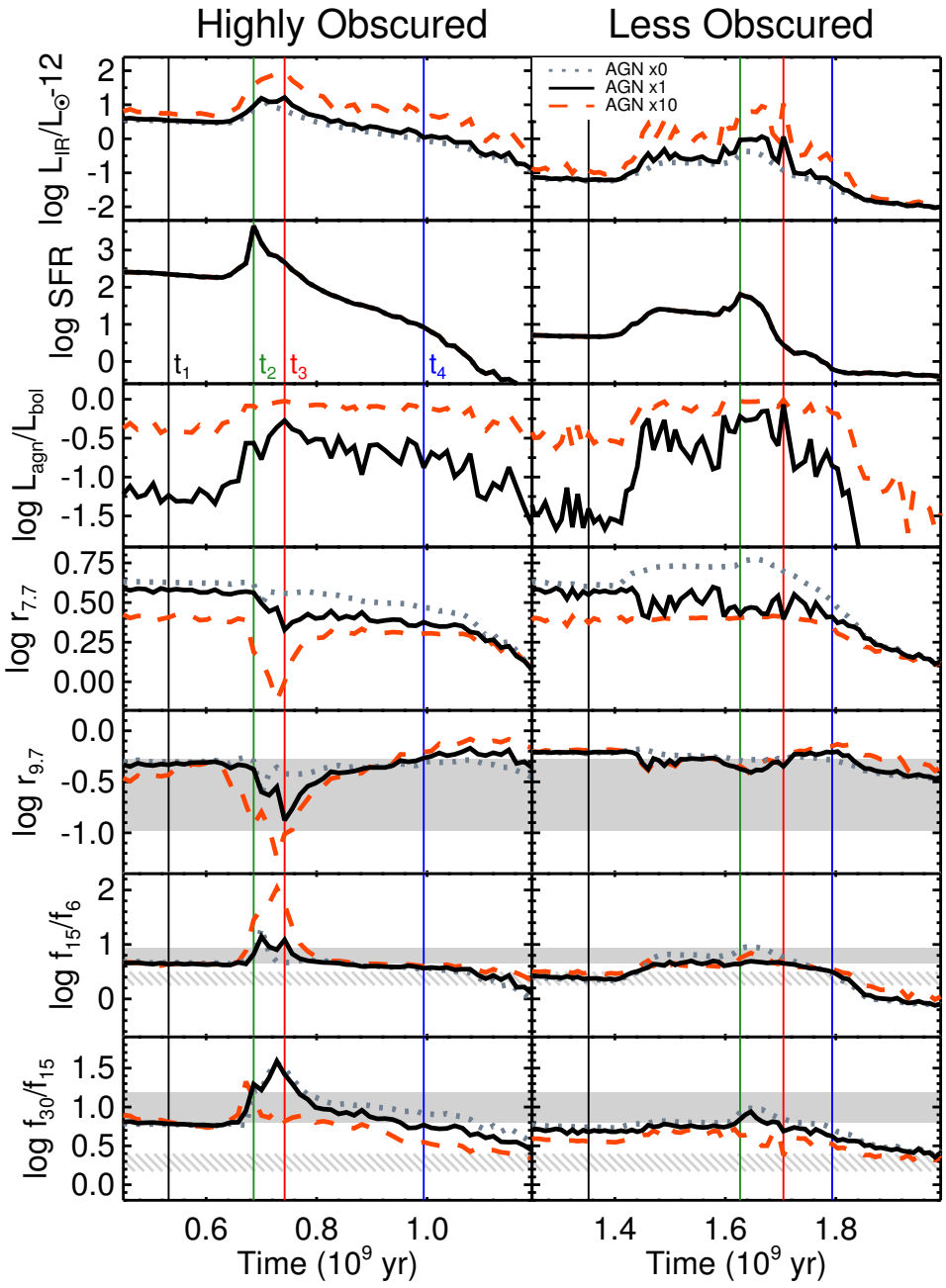

Figure 3.3.—: (Continued)

When the highly obscured and less obscured simulations have the same AGN fraction, the highly obscured case shows much sharper coalescence-stage SED reddening and deepening of the silicate feature. These effects on the SED are therefore the direct result of the host galaxy dust attenuation. This supports earlier observational evidence (Lacy et al. 2007; Sajina et al. 2007; Juneau et al. 2011) that in at least some AGN-dominated, deep silicate absorption sources, the absorption could arise in the host galaxy rather than the AGN torus.

3.4.2 Dust Model Dependence

In this section, we address the effect of varying both the dust structure in the ISM (clumpy vs. smooth) and its composition (Milky Way-like vs. SMC-like). In Section 2.4, we described the two ISM treatments we apply to the highly obscured merger. Broadly speaking, the "default ISM" case assumes the dust and gas associated with both hot and cold ISM phases are smoothly distributed. The "alternate ISM" assumes the cold phase gas is in clumps sufficiently dense to have a negligible volume filling factor, so that the dust it contains does not contribute to the overall attenuation. In Figure 3.4, we explore these effects on the mid-IR SEDs.

When switching to the alternate ISM assumption for the highly obscured simulation, the magnitude of $r_{9.7}$ is reduced by ~ 0.3 dex, and the color f_{30}/f_{15} by ~ 0.7 dex, while $r_{7.7}$ and $f_{15}/f_{5.7}$ are mostly unchanged. In addition, the total IR luminosity (first row of Figure 3.4) is negligibly affected by this change. Therefore the differences from this ISM structure assumption arise only because the source energy is redistributed in a different way, and not to changes in the total amount of energy that is attenuated.

Figure 3.4.—: We compare the dust models in the same simulations and quantities as Figure 3.3. For both bursts, we show our fiducial models in solid black curves, the SMC dust grain model in the dashed purple curves, and the fiducial models without galaxy dust in the light blue curves. Vertical lines highlight the four characteristic times t_1 to t_4 from Figure 3.1, corresponding to pre-burst, peak starburst, peak AGN, and post-burst. In the deeply obscured case, we also plot two alternate models: the SMC dust grain model and the clumpy ISM structure model. The powerful AGN signal in $r_{9.7}$ and $r_{7.7}$ at t_3 (Figure 3.3) can be replicated, at normal AGN strength, with the silicate-heavy SMC dust grain distribution. In several rows, the gray solid (lined) bands subtend the 25-75% range in the distribution of local ULIRGs (quasars) compiled by Veilleux et al. (2009).

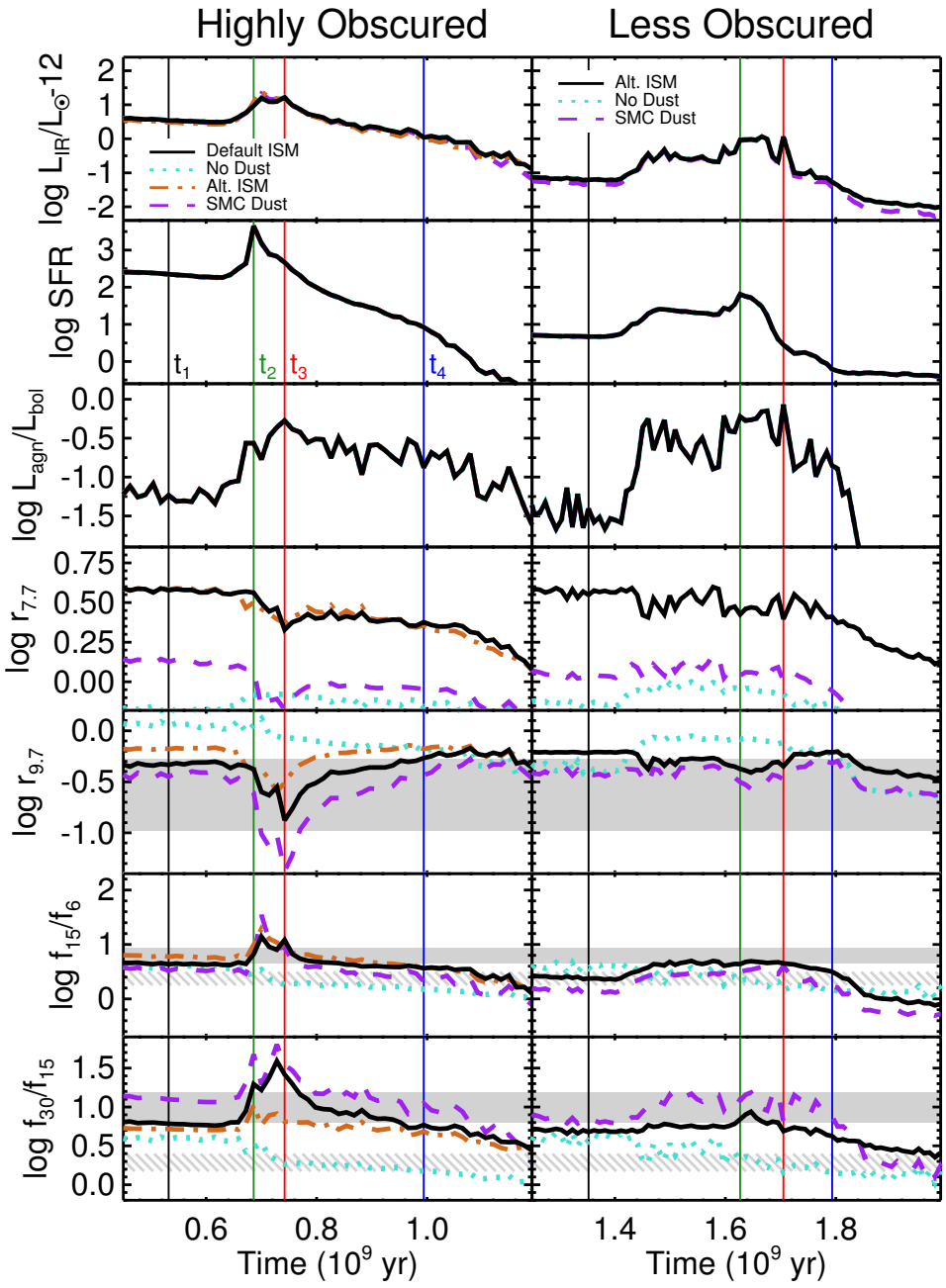

Figure 3.4.—: (Continued)

This implies that there is less dust self-absorption in the alternate ISM model, which typically experiences less attenuation than the default case, so the source radiation that is reprocessed into the near-IR and mid-IR is not as often reprocessed again to longer wavelengths.

With SMC or MW dust, the IR SEDs at a given time during the starburst have similar slopes f_{30}/f_{15} and $f_{15}/f_{5.7}$ (see also, Figure 3.1). Furthermore, L_{IR}, a measure of the amount of attenuated light, is nearly identical in these cases. By contrast, the SEDs show very different spectral characteristics $r_{7.7}$ and $r_{9.7}$, reflecting the difference between MW and SMC grain composition. The SMC dust is assumed to contain relatively more silicate than carbonaceous grains, leading to virtually non-existent PAH emission $r_{7.7}$ and correspondingly stronger silicate absorption $r_{9.7}$.

3.4.3 Viewing Perspective Dependence

In addition to the (evolving) source SEDs, the observed SED depends on the evolving relative distributions of sources and dust. This evolution changes the relative obscuration of AGN and stellar sources, affecting the behaviors of mid-IR indicators depending on whether the luminosity is dominated by star formation or AGN, because the AGN is generally much more highly obscured than the stellar component. In Appendix 3.7, we use toy models to confirm and further examine the behavior of the simulated diagnostics.

Figure 3.5 shows the time-dependence of variation in the mid-IR quantities with viewing angle, focusing on the highly obscured merger. The camera angle scatter is much lower (median $S < 0.05$ dex) for the less obscured merger. We show the same assumptions regarding AGN strength and ISM models from Figure 3.4, and we plot

the scatter S, in dex, of the mid-IR quantities as a function of time. We define S(q) to be the normalized median absolute deviation (MAD, e.g., Mosteller & Tukey 1977; Beers et al. 1990) of the quantity q among the seven SUNRISE viewing directions at a particular time during the simulation. First we calculate the median M_q of q, and then the seven values $|q - M_q|$, the median of which we define to be the MAD of q. We define S(q) = MAD/0.67 so that if q is drawn from a Normal distribution with standard deviation σ, then S is an unbiased estimator of σ.

At $t \lesssim t_2$, $S < 0.1$ dex for all models, so the SED shape and spectral features are similar in all directions. Generally speaking, the scatter S reaches a maximum ($\sim$ 0.2 to 0.4 dex) for conventional AGN diagnostics during t_3 to t_4. These times are also when the AGN luminosity fraction and IR luminosity are highest. Thus the increased viewing-angle scatter implies a large AGN contribution to the IR SED. This is because the AGN is effectively a point source, so the observed SED is sensitive to attenuation along a single LOS, which can vary widely. Moreover, the sudden change in the extinction curve at $9.7\mu m$ causes $r_{9.7}$ to have an exagerrated dependence on the line of sight attenuation. $r_{7.7}$ experiences much less viewing angle scatter than $r_{9.7}$, $S(r_{7.7}) \sim 0.0$ versus $S(r_{9.7}) \sim 0.2$ dex, because the extinction is the same for both the PAH features and $7.7\mu m$ continuum. Turning off AGN emission leads to essentially no viewing angle variation in either quantity.

Figure 3.6 presents the SED from seven viewing angles at time t_3 (peak AGN) for our highly obscured merger, with AGN $\times$ 1 and fiducial ISM models. This gives us a clearer physical picture of what is driving changes to the mid-IR diagnostics during coalescence. The generally higher level of obscuration at these times leads to the enhanced silicate absorption, causing the dip in median $r_{9.7}$ at t_3 (Figure 3.3). However, at a fixed time

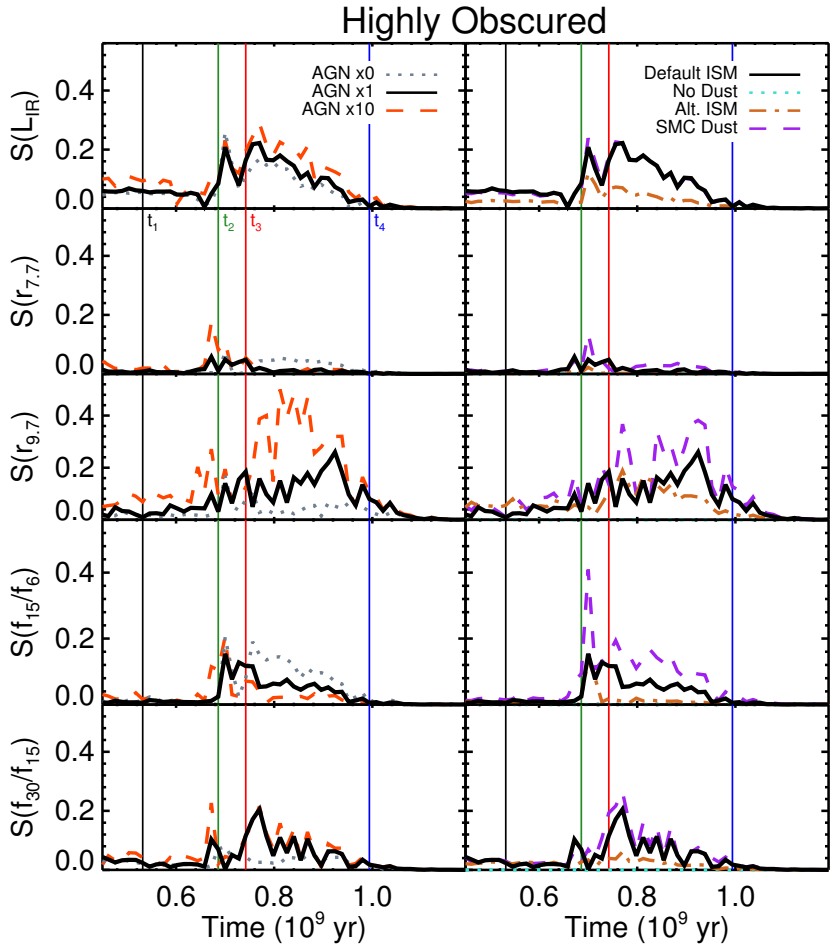

Figure 3.5.—: Scatter S, in dex, between viewing angles for the infrared quantities of the highly obscured case from Figures 3.3 and 3.4. S is defined in the text of Section 4.3.4. Vertical lines highlight the four characteristic times t_1 to t_4 from Figure 3.1, corresponding to pre-burst, peak starburst, peak AGN, and post-burst. The scatter S is largest when the AGN is strongest, $\sim t_3$ to t_4, because the obscuration varies significantly among the different sightlines to the AGN. The camera angle scatter for the less obscured burst (not shown) is much smaller, with S always below 0.1 dex, and its median value below 0.05 dex.

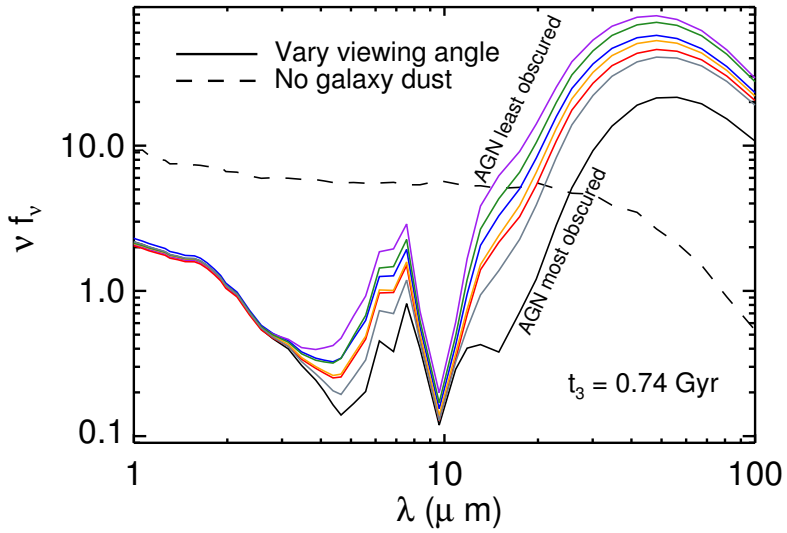

Figure 3.6.—: Infrared SEDs of the AGN × 1 highly obscured burst simulation at time t_3 (AGN peak) observed from each of the seven viewing angles. The IR spectrum varies owing to the anisotropy of extremely optically thick material surrounding the central engine (starburst or AGN). Along a given direction, this dust absorbs IR light and reemits it into other lines of sight.

during this period of very high attenuation, like the one shown in Figure 3.6, the silicate absorption feature is stronger along lines of sight in which the AGN is less obscured. In other words, the silicate feature only correlates positively with AGN attenuation until the level of attenuation is so extreme that the emergent stellar SED dominates the mid-IR emission associated with the AGN. This phenomenon is derived in Appendix 3.7 for a toy model of $r_{9.7}$.

3.4.4 Intrinsic AGN Emission Dependence

In Figure 3.7 we consider the effect of intrinsic mid-IR AGN SED shape on the final observed SED. We show the manually boosted model (AGN×10) in order to maximize the possible effect. We demonstrate that the intrinsic AGN mid-IR spectrum has no

impact on the observed mid-IR SED at t_2 to t_3 of the highly obscured merger, during the starburst and AGN peak at final coalescence when the central densities are highest. We use our default AGN SED, the template by Hopkins et al. (2007d), as well as two templates by Nenkova et al. (2008). These templates reflect obscuration by clumpy tori inclined by $i = 0°$ and $i = 90°$, spanning the range of derived mid-IR torus SED shapes.

With our default ISM assumption, dust obscures this central source at wavelengths as long as $\lambda \sim 20$ to $50\mu m$. Thus the flux at $\lambda \sim 2 - 5\mu m$, conventionally attributed to AGN tori, only indicates direct AGN emission when the central source is sufficiently unobscured (e.g., t_1 and t_4). In the less obscured simulation, the AGN torus SED has a large effect throughout the merger, as seen by the near-IR slopes of the SEDs in the left column of the "Less Obscured" panels in Figure 3.1.

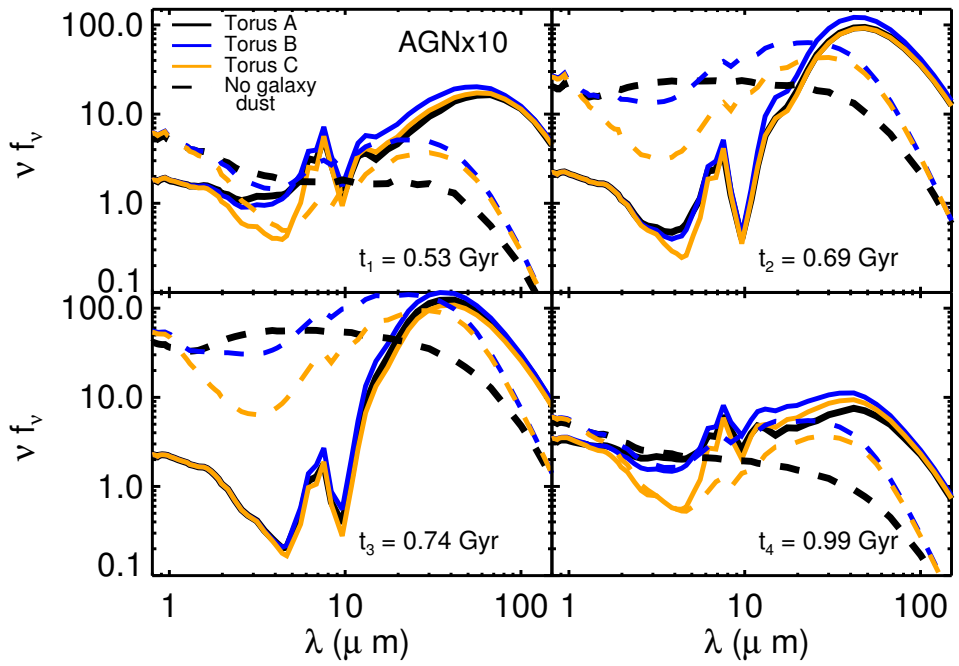

Figure 3.7.—: We explore the sensitivity of the final infrared SED to the assumed intrinsic AGN (or AGN+torus) spectrum, focusing on the highly obscured simulation. In this figure we use the manually boosted AGN (x10) input SED, and so the effect sizes shown here should be considered upper limits. Solid lines show the emergent SED from an example viewing direction with three assumptions about the intrinsic AGN SED. Dashed lines show the intrinsic stellar+AGN source emission before the dust RT calculation. Black lines use the mean templates from Richards et al. (2006a), while blue and yellow lines use $i = 0°$ and $i = 90°$ clumpy torus models from Nenkova et al. (2008), respectively. The choice of intrinsic AGN SED matters least at t_3, when the SMBH's contribution to the total luminosity is largest. The AGN fraction at times t_2 to t_4 are all $\gtrsim 70\%$ and yet the appearance of the mid-IR SED changes dramatically over these several 10^8 yr. The influence of the intrinsic AGN spectrum on the final SED at $5\mu m$ increases from ~ 0 dex at t_3 to ~ 1 dex at t_4.

3.5 Observational Comparison

3.5.1 2-Dimensional Diagnostics

In Section 4.3, we presented the time evolution of the observed mid-IR indicators and noted that their dependence on $L_{\rm agn}/L_{\rm bol}$ is both time-dependent and non-linear. We showed that our mid-IR spectral diagnostics strongly depend on the dust model and can be highly scattered as a function of veiwing angle. How could we hope to observationally discern the level of AGN in a given galaxy based on its mid-IR spectrum, given that typically no information on the merger stage is available, the dust model is even less constrained, and we will never have more than one viewing perspective? Here we attempt to do just that by using the simulation results as a diagnostic tool.

In Figure 3.8, we present mid-IR diagnostic diagrams that have been used in the literature for the purpose of disentangling the role of AGN and starburst activity in dusty galaxies. Specifically, using our definitions of the PAH strength, silicate feature depth, and mid-IR colors, we present slightly modified versions of the "Laurent" diagram (Laurent et al. 2000), the "Spoon" diagram (Spoon et al. 2004), the "Veilleux" diagram (Veilleux et al. 2009), and the "Lutz" diagram (Lutz et al. 2004). The last diagram presents the relation between the $6\mu m$ luminosity and X-ray luminosity for unobscured or mildly obscured AGN. The left-hand column of Figure 3.8 presents the highly obscured simulation, the middle column presents the less obscured simulation, and the right-hand panel presents real galaxy data that we discuss in more detail in the following section.

Figure 3.8.—: We compare the two simulations to observed samples of ULIRGs. The four rows each present an example diagnostic diagram that has been examined in the literature. Within each row, the left plot shows the "highly obscured" model points colored according to the median AGN fraction $L_{\rm agn}/L_{\rm bol}$ within each grid cell: see the text for a description of this procedure, and refer to the colorbar at the left. The middle panel of each row shows the same mapping for the "less obscured" simulation. We employ the fiducial ISM settings for these panels, in particular MW dust, and include all points between t_1 to t_4 from the AGNx10, AGNx1, and AGNx0 models as a means of exploring the sensitivities of these SEDs to changes in modeled AGN strength. We show a histogram around the edges of the first three columns to highlight the relative amount of time spent by the simulations in each region. We find that dark squares span almost the entire y axis in the left column of the top three rows, implying that powerful AGN can occupy any value of these diagnostics in our two merger models. The right panel in each row plots observed local V09 and high-z S12 ULIRGs. When the $r_{9.7}$ feature is saturated, we plot a brown asterisk. In the "Lutz diagram" in the bottom row, the gray shaded region shows the 1σ range of intrinsic X-ray-to-mid-IR ratio for Type 1 AGN from Bauer et al. (2010).

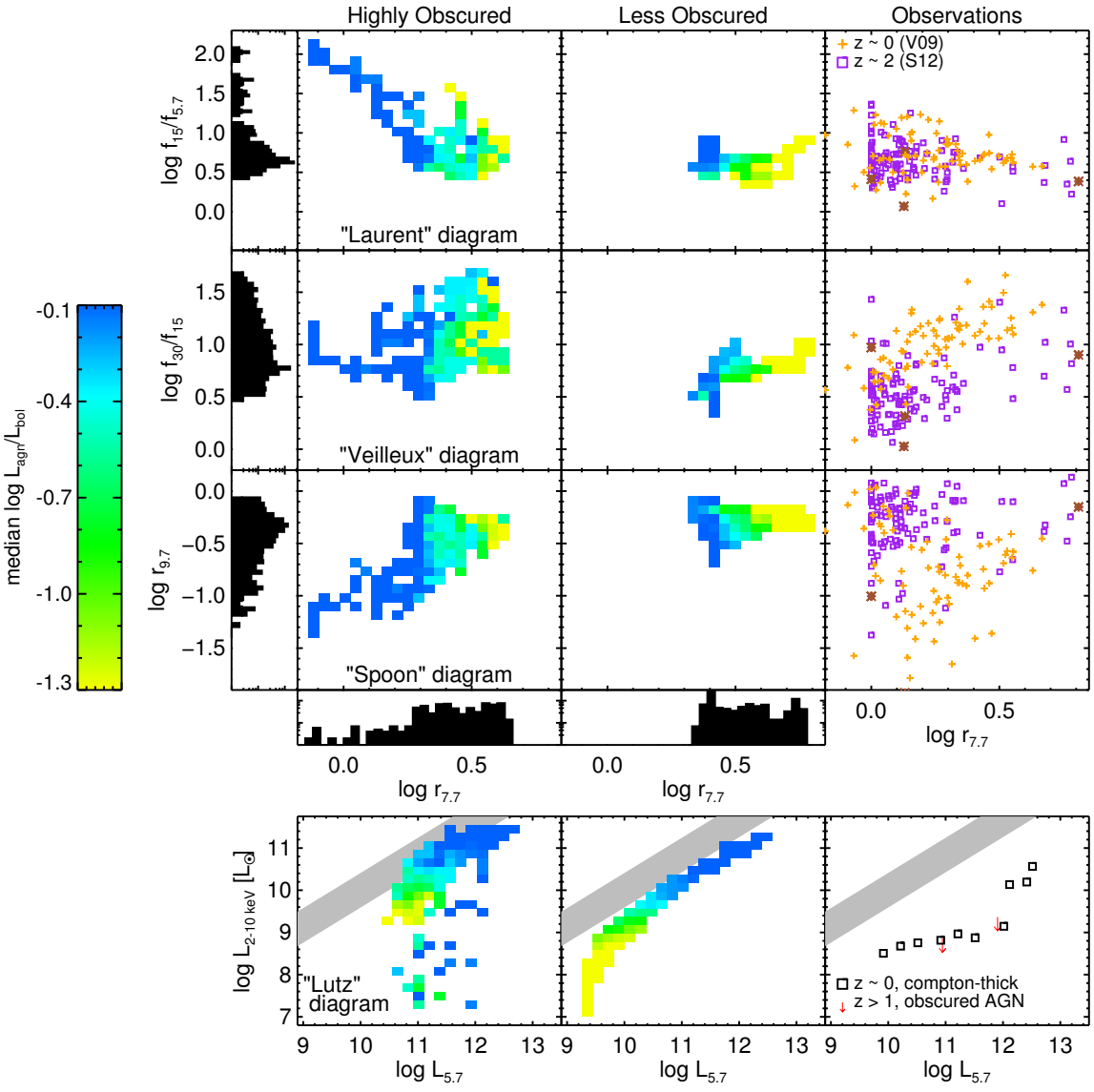

Figure 3.8.—: (Continued)

For the simulation columns in Figure 3.8, we plot the IR quantities in the following way. Each panel is divided into a grid of 25x25 bins, each of which contains zero or more simulated points. These points include all seven viewing angles at each timestep in t_1 to t_4, which are sampled every 10^7 years. We use our fiducial ISM settings and plot the three AGN strengths (x10, x1, and x0) in order to span a full range of $L_{\rm agn}/L_{\rm bol}$ in our experiments. Bins containing zero of these points are white, and bins with one or more point are shaded according to the median value of $L_{\rm agn}/L_{\rm bol}$ among the points it contains, as indicated by the colorbar: darker/blue regions have $L_{\rm agn}/L_{\rm bol} \sim 1$, while lighter/yellow regions have $L_{\rm agn}/L_{\rm bol} \lesssim 0.1$. We plot histograms (on a logarithmic scale) along the edges of the first three rows to show the relative timescales of the model populations giving rise to these diagrams.

We caution that our plotting and selection here are not meant to directly characterize the observed populations of ULIRGs that we plot in the right column; these are included primarily as a reference and plausibility check. Instead, from this coding we seek to identify which regions, if any, isolate powerful AGN during these mergers, regardless of the length of time the observed properties may be visible. A larger sample of models will be needed in order to fully constrain the expected observed distribution of $L_{\rm agn}/L_{\rm bol}$ at each location in these diagrams, but we can begin to highlight some basic trends implied by the simulations.

3.5.2 Comparison Between Models and Data

Veilleux et al. (2009) analyzed the standard evolutionary scenario for ULIRGs (Sanders et al. 1988), which broadly speaking proceeds through three stages. In "Stage 1", the

IR emission of a gas-rich merger is dominated by star formation, leading to large PAH EWs and relatively small silicate absorption EW. As the merger proceeds to "Stage 2", $r_{9.7}$ increases as the central source is buried in the gas-rich starburst, and the PAH emission decreases relative to the IR continuum that is boosted by the AGN, which remains sub-dominant to the starburst. Finally, at "Stage 3", the silicate absorption and PAH emission both subside as the starburst fades, the obscuring medium is cleared or consumed, and the ULIRG is completely or nearly AGN dominated. Overall, Veilleux et al. (2009) concluded that AGN contribute $\sim 35-40\%$ to the IR luminosity of ULIRGs, and that ULIRGs experience significant scatter from this general pattern.

In Figure 3.8, the highly obscured model points roughly fill the space spanned by observed sources. Our procedure does not mandate such consistency, and so we interpret this as one important check of the modeling technique. In particular, ignoring other diagnostics (such as SED slopes), this simulation reproduces the observed spread in $r_{9.7}$ and $r_{7.7}$. In Table 3.2, we summarize a few numerical results of our deeply obscured simulation. We divide the merger into three stages, t_1 to t_2 (pre-coalescence), t_2 to t_3 (coalescence), and t_3 to t_4 (post-coalescence), and report the median values of $L_{\rm agn}/L_{\rm bol}$, $r_{9.7}$, and $r_{7.7}$ calculated in those periods.

Generally, the SED properties along the model timeline follow those of the merger stages by V09, albeit with an expectedly high amount of scatter. Local ULIRGs have a large amount of silicate absoprtion ($r_{9.7} \sim 0.7$), suggesting they may correspond to the modeled points at $t_2 < t < t_3$ where $r_{9.7}$ peaks. However, the AGN fractions in models depend sensitively on the dust model and AGN strength choices, and so it is unclear how well they may correspond to the $\sim 30\%$ reported in V09. This value is consistent with our AGN $\times$ 1, MW dust simulation, but is much lower than the $\sim 70\%$ from the

Table 3.2. Selected Diagnostics, Deeply Obscured Case

time range[a]	$\log r_{7.7}$[b]	$\log r_{9.7}$[b]	$\log L_{\rm agn}/L_{\rm bol}$[b]
AGN x0, MW dust			
$t1 < t < t2$	0.62	−0.31	0.00
$t2 < t < t3$	0.56	−0.40	0.00
$t3 < t < t4$	0.52	−0.37	0.00
AGN x1, MW dust			
$t1 < t < t2$	0.57	−0.33	0.06
$t2 < t < t3$	0.46	−0.62	0.33
$t3 < t < t4$	0.39	−0.43	0.26
AGN x1, SMC dust			
$t1 < t < t2$	0.12	−0.44	0.06
$t2 < t < t3$	−0.13	−1.09	0.33
$t3 < t < t4$	−0.03	−0.70	0.26
AGN x10, MW dust			
$t1 < t < t2$	0.40	−0.37	0.43
$t2 < t < t3$	0.04	−0.95	0.86
$t3 < t < t4$	0.30	−0.40	0.81
Combined, MW dust			
$t1 < t < t2$	0.57	−0.32	0.36
$t2 < t < t3$	0.45	−0.65	0.70
$t3 < t < t4$	0.39	−0.38	0.58

[a]These time ranges are 0.154, 0.056, and 0.252 $\times 10^9$ yr long, respectively

[b]Median values

"combined" model set, in which each of the AGN strengths are given equal weight. The more realistic choice is uncertain, but the AGN $\times$ 1 case has trouble reproducing observed objects with $r_{9.7} < -1$. However, SMC dust with lower AGN strengths can also provide that feature, and observations suggest that SMC-like dust may be more appropriate during bright starburst or AGN phases, as small grains are preferentially depleted (Gordon et al. 1997; Hopkins et al. 2004). This may imply that SMC dust is more appropriate to use in this situation; in any case, it highlights the difficulty in determining the path of the AGN fraction in such objects if their dust grain populations are changing significantly.

In Figure 3.8, swaths of strong and weak AGN exist, but most of these projections do not isolate AGN in simple ways. For example, while it is true that sources with strong starbursts and weak AGN typically have stronger PAH emission and redder f_{30}/f_{15} as discussed in Veilleux et al. (2009), strong AGN occupy all values of f_{30}/f_{15}, $f_{15}/f_{5.7}$, and $r_{9.7}$. Furthermore, the PAH strength depends sensitively on the dust model we assumed (see Figure 3.4), and the $r_{7.7}$ values of low $L_{\rm agn}/L_{\rm bol}$ points depend on the obscuration level of the simulation.

In addition, we compare the relative fluxes emerging at hard X-ray and mid-IR wavelengths in the bottom row of Figure 3.8. We compute model X-ray fluxes as in Section 3.2.5. Bauer et al. (2010) found that $z > 1$ ULIRGs that are otherwise thought to be AGN-dominated (with low $r_{7.7}$) are undetected at X-ray wavelengths, suggesting that they are at least mildly Compton-thick. Moreover, they presented Compton-thick examples from the literature at $z \sim 0$, which lie ~ 2 dex below the relation for less obscured AGN (c.f., Hönig et al. 2010). Many model galaxies with powerful AGN lie in the same region of this diagram, and are reflected in the dark blue squares mixed in with

the lighter squares at $L_6 \sim 10^{11}$–$10^{12} L_\odot$. These are the same sources in the low-$r_{7.7}$ (high $r_{9.7}$) tail of dark points in the upper panels, implying that this class of Compton-thick sources is a short-lived phase of our highly obscured model. The bulk of the simulation points have X-ray fluxes ~ 0.5 dex below the gray Type 1 AGN band, reflecting our choice to not analyze completely unobscured models.

There are some properties for which the model values are not realized by observed sources. Generally speaking, the differences are most apparent in the mid-IR SED slopes f_{30}/f_{15} and $f_{15}/f_{5.7}$. The most AGN-dominant model points are ≈ 0.5 dex redder in $f_{15}/f_{5.7}$ than any observed object. In bulk, the model f_{30}/f_{15} values are larger by ≈ 0.3 dex than the observed distribution. And there are few model galaxies with $\log r_{9.7} \sim 0$ *and* $\log r_{7.7} \sim 0$, in contrast to those observed. However, this is sensitive to our dust grain model (Section 3.6.2), and may also reflect our not having modeled AGN with no galaxy obscuration. Our calculations are necessarily uncertain, so in Section 3.6.3 below, we summarize some of these theoretical limitations and potential implications of these mismatches.

As we have seen in Section 4.3, when sufficiently obscured, a powerful AGN has an SED shape the same as a dusty pure starburst (see also Younger et al. 2009; Narayanan et al. 2010b). Figure 3.8 shows high $L_{\rm agn}/L_{\rm bol}$ squares occupying a large fraction of the $r_{7.7}$, $r_{9.7}$, f_{30}/f_{15}, and $f_{15}/f_{5.7}$ values. We also saw that the model SEDs can change drastically on timescales $\sim 10^8$ yr. A further challenge is that the implied $L_{\rm agn}/L_{\rm bol}$, given a set of SED properties, depends sensitively on assumptions about the dust model and AGN strength. An ideal indicator is one that identifies powerful AGN regardless of the host galaxy's content or state. An example is hard X-ray emission which can penetrate even very large optical depths, and in Section 3.6, we use our simulations to

suggest other ideal indicators that have not been easily accessible with current data, but may be useful for future mid-IR studies with the *James Webb Space Telescope* (*JWST*).

3.6 Implications

3.6.1 An Ideal Indicator of $L_{\rm agn}/L_{\rm bol}$

Ultimately, we seek an indicator that can be used to determine the AGN contribution to IR-luminous galaxies across the full range of obscuration by galaxy dust. Such a tool could simplify efforts to accurately track the growth of SMBHs and assess their impact on the ISM in diverse and evolving host galaxies.

Near-infrared colors effectively identify AGN when their IR SED resembles a power-law, leading to enhanced emission beyond the stellar bump at $\gtrsim 2\mu m$. This yields a high value of our example near-IR color $f_{4.5}/f_{1.6}$, for which the numerator is a proxy for torus emission and the denominator is a proxy for stellar mass. Such techniques have been used to successfully identify high-redshift AGN-dominated ULIRGs using Wide-field Infrared Survey Explorer (WISE) photometry (e.g., Stern et al. 2012; Eisenhardt et al. 2012; Wu et al. 2012). This near-IR reddening operates in powerful AGN for a wide variety of attenuation. However, as we saw in Figure 3.7, on short timescales the near-IR SED shape can change from a power-law AGN to one that resembles a starburst-dominated ULIRG when the obscuration increases drastically. In these high-obscuration situations, $r_{9.7}$ is sensitive to the AGN power, and so combining these indicators into a generic diagnostic may be feasible.

In Figure 3.9, we plot two-dimensional diagrams with our near-IR color $f_{4.5}/f_{1.6}$ on the y-axis and $r_{9.7}$ on the x-axis. We have included our fiducial ISM assumptions for each mergers and all three AGN strengths: AGNx10, AGNx1, and AGNx0. We note that these settings are chosen by hand in order to more broadly span the range of $L_{\rm agn}/L_{\rm bol}$ produced by our calculations, and are justified by the uncertainty inherent in the simulation methods and limited range of cosmologically motivated models we consider (see e.g., Section 3.2.4). Therefore, these model diagrams do not directly correspond with any realistic ULIRG populations; we plot two samples in the right panel primarily as a reference.

The light/yellow shaded region corresponds to low AGN emission ($L_{\rm agn}/L_{\rm bol} \lesssim 0.1$) and is confined to a small region (~ 0.4 by 0.4 dex) of this parameter space centered at $(\log r_{9.7}, \log f_{4.5}/f_{1.6}) \approx (-0.32, -0.5)$. In both the highly and less obscured simulations, the value $\log f_{4.5}/f_{1.6} \sim -0.5$ corresponds to the SED shape of purely stellar emission, which can be seen in the gray dotted curves in Figure 3.1 at $1\mu m < \lambda < 5\mu m$. The value $\log r_{9.7} \sim -0.32$ appears to be the typical SED produced by ordinary (non-bursting) star formation in our simulations. Numerically, this value may be set by our simplistic continuum estimate (Section 3.3.1), which is likely affected to some extent by the nearby PAH features. Both of these "zeropoints" do not depend strongly on the dust model, and are roughly the same in the highly and less obscured mergers.

Away from this point, the median AGN fraction varies in a semi-regular pattern. Redder $f_{4.5}/f_{1.6}$ implies a contribution at $4.5\mu m$ from the relatively brighter AGN source, as expected from conventional hot dust/torus interpretations. The absorption diagnostic $r_{9.7}$ does not vary strongly in the less obscured case, as we have seen in Section 3.4.1, and so the locus of increasing $L_{\rm agn}/L_{\rm bol}$ traces roughly a vertical line in the second column of

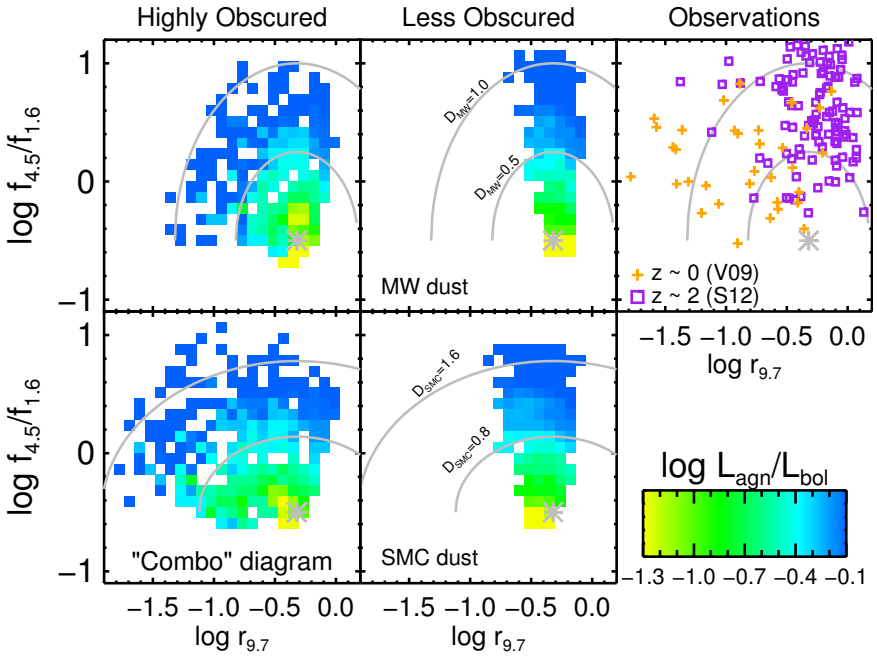

Figure 3.9.—: Following Figure 3.8, we plot panels motivating the diagnostic D: see text for definitions of $D_{\rm MW}$ and $D_{\rm SMC}$. The left two columns are our simulated points, colored by $L_{\rm agn}/L_{\rm bol}$, for our two representative levels of obscuration. For this plot we include the AGNx10, AGNx1, and AGNx0 strengths. The top row assumes MW dust, and the bottom assumes SMC dust. In contrast to the other quantities from Figure 3.8, diagnostic D straightforwardly estimates $L_{\rm agn}/L_{\rm bol}$ for both low and high optical depth, assuming we know the dust model. We note that diagnostic D requires information at rest-frame wavelengths 1 to 10μm, rendering it somewhat impractical to measure using any single current instrument. However, diagnostic D will be accessible to the *James Webb Space Telescope* for sources at $z \lesssim 1$.

Figure 3.9.

By contrast, in the highly obscured simulation, a significant area of the $\log r_{9.7} \lesssim -0.5$ regions of the diagram is occupied by squares with $L_{\rm agn}/L_{\rm bol} \gtrsim 0.1$. In the lower left quadrant of each panel in the left column of Figure 3.9, the dust column is large enough to produce a significant silicate absorption feature and to attenuate the near-IR continuum associated with AGN-heated dust, leading to $\log f_{4.5}/f_{1.6} \lesssim 0$. In the upper

left quadrant, there are several squares with both a strong silicate feature and a red near-IR continuum. At a fixed $L_{\rm agn}/L_{\rm bol}$, these two quantities are correlated in the sense that increased silicate absorption implies more attenuation of the near-IR AGN-heated continuum relative to the starlight, giving a bluer $f_{4.5}/f_{1.6}$, leading to the slanted or semi-elliptical pattern in the areas of constant shading ($L_{\rm agn}/L_{\rm bol}$) in Figure 3.9. These qualities are the same when switching to the "alt. ISM" model for the highly obscured merger (not shown).

We seek to summarize these trends and estimate $L_{\rm agn}/L_{\rm bol}$ directly from these variables. Visually, the areas of constant $L_{\rm agn}/L_{\rm bol}$ form a semi-elliptical pattern that can be approximated by an analytic formula to potentially estimate $L_{\rm agn}/L_{\rm bol}$ with low scatter. For MW dust, we consider the formula

$$D_{\rm MW} = \sqrt{(\log r_{9.7} + 0.32)^2 + \left(\left[\log \frac{f_{4.5}}{f_{1.6}} + 0.5\right] \frac{2}{3}\right)^2}.$$

The effectiveness of combination D_{MW} is evident in the top row of Figure 3.9: the map between color/shading ($L_{\rm agn}/L_{\rm bol}$) and these axes, $f_{4.5}/f_{1.6}$ and $r_{9.7}$, appears to be a well defined and slowly varying function of few parameters. In Appendix 3.7, we confirm the rough behavior of this diagnostic from toy models.

We caution that we have analyzed only a handful of specially chosen models: AGNx10, AGNx1, and AGNx0 in two mergers that likely occupy two very different extremes of the ULIRG population. Therefore the shaded points in Figures 3.8 and 3.9 are likely to change with a larger and more representative sample of models. Nevertheless, it is encouraging that a clear trend in the $f_{4.5}/f_{1.6}$–$r_{9.7}$ plane exists for both our highly and less obscured mergers (in contrast to the diagrams in Figure 3.8), and for either the default or alternate ISM model in the highly obscured merger. This can

be understood as a result of the relatively simple ways that the two axes of Figure 3.9 reflect AGN-associated emission and its obscuration. In Section 3.6.2, we show that this visual trend we identify in Figure 3.9 defines a tight relationship between $L_{\rm agn}/L_{\rm bol}$ and $D_{\rm MW}$ at all times t_1 to t_4 when the dust model is constrained.

3.6.2 Constraining Dust Properties

However, we note that shape of the trend in the $f_{4.5}/f_{1.6}$–$r_{9.7}$ plane depends on our dust model: the bottom row of Figure 3.9 shows the same simulation using SMC dust instead of MW dust. Importantly, a nice mapping in the above sense still exists, it is just skewed toward higher values of $r_{9.7}$. Therefore we can define a similar diagnostic,

$$D_{\rm SMC} = \frac{5}{8}\sqrt{(\log r_{9.7} + 0.32)^2 + \left(\left[\log\frac{f_{4.5}}{f_{1.6}} + 0.5\right]\frac{5}{4}\right)^2},$$

centered around the same point as $D_{\rm MW}$, but with a different axis ratio and scaling.

In order to select between these estimators, we must first constrain the dust properties; in other words, we must jointly constrain the dust and $L_{\rm agn}/L_{\rm bol}$. One option is to use the PAH emission: assuming SMC dust, $r_{7.7} \sim 0$ for all model points instead of ~ 0.3 for MW dust (see Figure 3.4). We demonstrate this procedure in Figure 3.10: while $D_{\rm MW}$ does not yield a low-scatter predictor of $L_{\rm agn}/L_{\rm bol}$ when applied to a system with SMC dust, it does broadly select stronger AGN. Moreover, at $D \gtrsim 0.2$, sources with these different dust models separate based on their PAH strength, $r_{7.7}$, permitting either a direct choice between the formulae for $D_{\rm MW}$ and $D_{\rm SMC}$ or an intermediate case. This suggests the following procedure:

1. Estimate $D_{\rm MW}$.

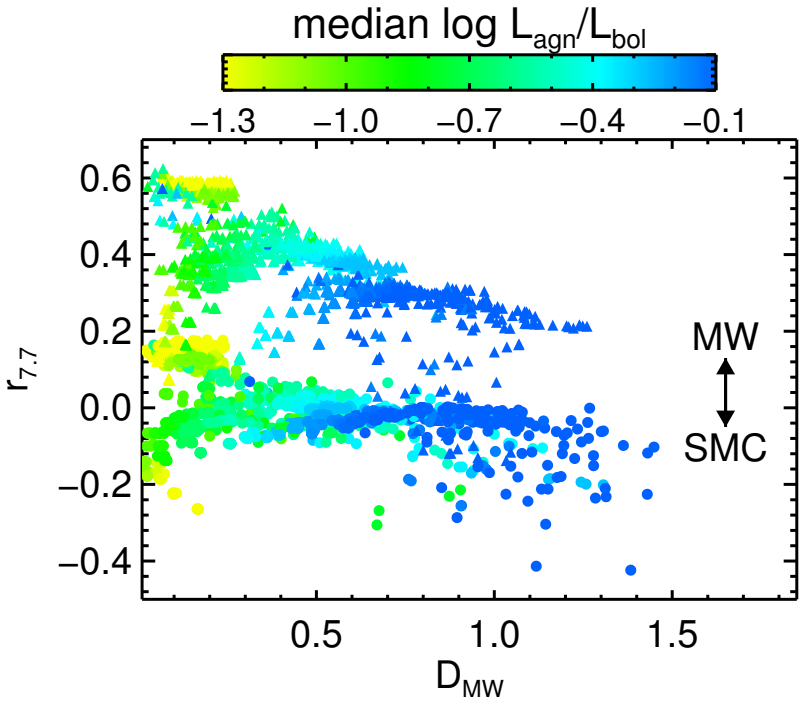

Figure 3.10.—: PAH strength versus our combination diagnostic $D_{\rm MW}$, which contains information about obscuration $r_{9.7}$ and near-IR color, providing a rough estimate of $L_{\rm agn}/L_{\rm bol}$ at both low and high mid-IR optical depths. If we have incorrectly assumed MW dust when the appropriate model is more like the SMC dust, then Figure 3.9 implies that the $D_{\rm MW}$ to $L_{\rm agn}/L_{\rm bol}$ relation will be skewed and have a large scatter. However, at fixed high $D_{\rm MW}$, the PAH strength can roughly select the appropriate dust model, and therefore the appropriate predictor of $L_{\rm agn}/L_{\rm bol}$: $D_{\rm MW}$, $D_{\rm SMC}$, or an interpolation. For this plot we have included the AGNx1 and AGNx10 strengths for the default ISM model of the highly obscured merger.

2. Estimate the PAH strength (here, $r_{7.7}$).

3. Select dust model X based on the value obtained in step 2, by e.g., checking whether at the $D_{\rm MW}$ value, $r_{7.7}$ lies closer to the MW or SMC points.

4. Calculate $D_{\rm X}$ and use it to estimate $L_{\rm agn}/L_{\rm bol}$.

With a known dust model, diagnostic D robustly predicts $L_{\rm agn}/L_{\rm bol}$ regardless of

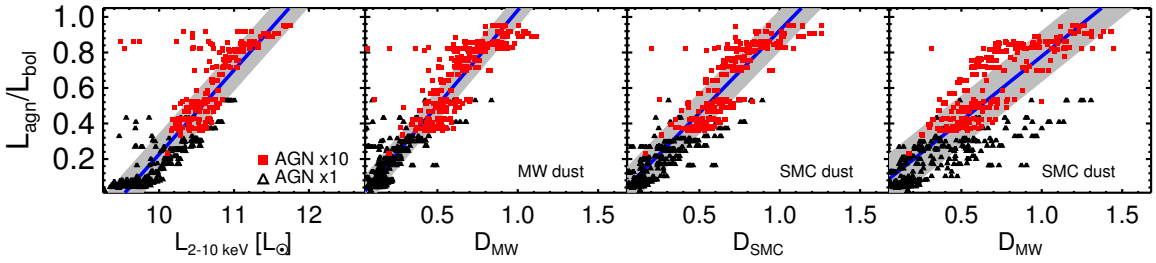

Figure 3.11.—: We show how diagnostic D correlates with $L_{\rm agn}/L_{\rm bol}$ in our simulations in the right three panels. We show here only the highly obscured merger with our default ISM model, but the trends are similar for the alternate ISM model and the less obscured merger, as summarized in Table 3.3. As a comparison, we plot the hard X-ray flux through the $2-10$ keV band in the left panel. If the correct dust model is used, D accurately predicts $L_{\rm agn}/L_{\rm bol}$ as well as $L_{2-10\ \rm keV}$. In the rightmost panel, we apply $D_{\rm MW}$ when the source has SMC dust instead, demonstrating that the scatter increases by $\sim 70\%$. This issue can be mitigated by using, for example, Figure 3.10 to choose the appropriate indicator D.

the physical conditions of the ULIRG source. We compare the ability of diagnostics $D_{\rm MW}$ and $D_{\rm SMC}$ to predict $L_{\rm agn}/L_{\rm bol}$ to that of hard X-ray fluxes in Figure 3.11.

Using a least absolute deviation method, we fit the relation $L_{\rm agn}/L_{\rm bol} = a + bQ$ for three quantities Q ($D_{\rm MW}$ with MW dust, and both $D_{\rm MW}$ and $D_{\rm SMC}$ with SMC dust) and each of our two ISM models for the highly obscured simulation, and compile the results in Table 3.3. To measure the scatter in the correlations' residuals, we used the same scale estimator S defined in Section 4.3.4, which is generally insensitive to outliers. In both cases, $L_{2-10\ \rm keV}$ and each D predict $L_{\rm agn}/L_{\rm bol}$ with roughly the same median scatter, $S \sim 10\%$. However, we find that $L_{2-10\ \rm keV}$ experiences a failure rate ($> 3\sigma$) two to three times higher than D in the highly obscured calculation. Both quantities predict $L_{\rm agn}/L_{\rm bol}$ equally well under the alternate ISM treatment and for the less obscured candidate (not shown), with $S < 10\%$ and failure rates $< 1\%$.

Several simulated points at $L_{\rm agn}/L_{\rm bol} \approx 0.8$ fail in both $L_{2-10\ \rm keV}$ and $D_{\rm MW}$. In these cases, corresponding to the most highly obscured lines of sight in our AGN $\times$ 10 calculation from Figure 3.6, the mid-IR is so heavily attenuated that no $r_{9.7}$ signature from the central source survives in the observed SED (see also Section 4.3.4).

Diagnostic D requires information about the galaxy's stellar mass (rest-frame $\lambda \sim 1$ to $2\mu m$), limiting its immediate application to large new samples. However, the rest-frame wavelength range D requires will be covered by the *James Webb Space Telescope* (*JWST*), an observatory whose Mid-Infrared Instrument (MIRI) (e.g., Wright et al. 2004) permits measurements of $r_{7.7}$ and $r_{9.7}$ for sources at $z \lesssim 1$. The tight correlation we find between D and $L_{\rm agn}/L_{\rm bol}$ reflects the possible benefit in combining information about $r_{9.7}$ and $r_{7.7}$ with near-IR color diagnotics from *JWST* itself (e.g., Messias et al. 2012), or by matching to sources from other IR surveys (e.g., Stern et al. 2005, 2012). For the two example SEDs in Figure 3.12, whose known AGN fractions are both $L_{\rm agn}/L_{\rm bol} = 0.33$, this procedure estimates $L_{\rm agn}/L_{\rm bol} = 0.33 \pm 0.09$ and $L_{\rm agn}/L_{\rm bol} = 0.38 \pm 0.09$ (uncertainties are from the minimum theoretical scatter in the correlations) for the high and low obscuration examples, respectively.

Table 3.3. Ability to Predict $L_{\rm agn}/L_{\rm bol}$

Quantity, Q[a]	scatter, S[b]	intercept, a	slope, b	Failure %[c]
Default ISM				
$\log L_{2-10\ \rm keV}/L_\odot$	0.12	−4.51	0.47	6.1
$D_{\rm MW}$, MW dust	0.09	−0.04	1.07	2.6
$D_{\rm SMC}$, SMC dust	0.12	−0.01	0.93	0.5
$D_{\rm MW}$, SMC dust	0.14	0.05	0.72	0.8
Alternate ISM				
$\log L_{2-10\ \rm keV}/L_\odot$	0.09	−4.59	0.47	0.8
$D_{\rm MW}$, MW dust	0.10	−0.04	0.96	0.9
$D_{\rm SMC}$, SMC dust	0.09	0.00	0.86	0.0
$D_{\rm MW}$, SMC dust	0.10	0.00	0.98	1.3

[a] $L_{\rm agn}/L_{\rm bol} = a + b\,(Q)$

[b] $S = {\rm MAD}/0.67$, see Section 4.3.4.

[c] Percentage of points with $L_{\rm agn}/L_{\rm bol}$ further than 3σ away from the fitted relation. In practice, for these cases the indicator predicts an $L_{\rm agn}/L_{\rm bol}$ smaller than the true value owing to extreme attenuation.

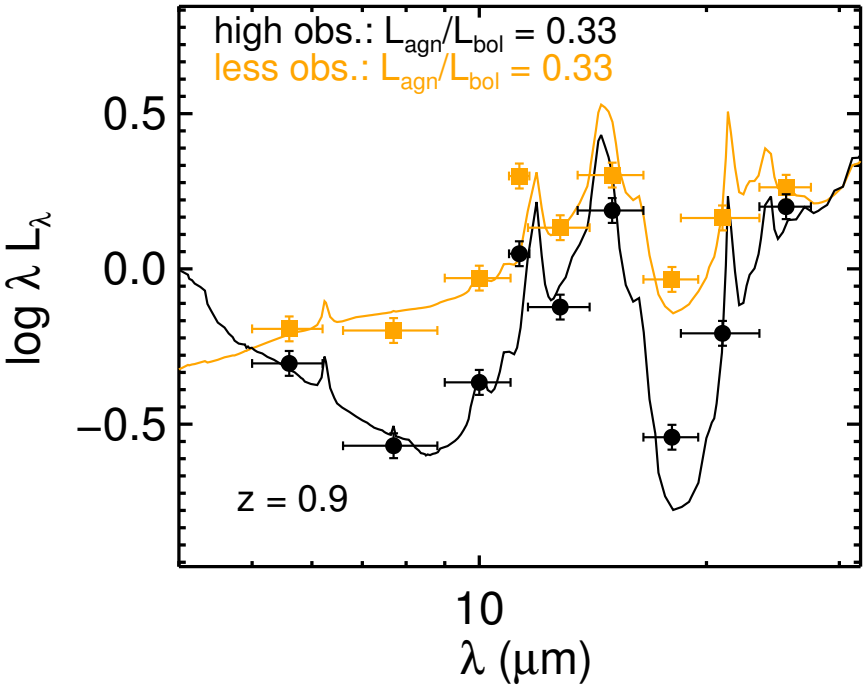

Figure 3.12.—: Synthetic photometric observations by MIRI on *JWST*, demonstrating the ability of future mid-IR technology to measure AGN power in systems with a wide range of obscuration. Here we assumed MW dust and $z = 0.9$.

3.6.3 Limitations and Improvements

A concern with the present method is that we cannot be sure how our few idealized simulations fit into a cosmological context. We have mitigated this issue by presenting two rather different ULIRG candidates, by varying the relative power between the AGN and star formation, and by varying the assumptions acting on dust obscuration and emission. We are planning to build a library of model SEDs for a much wider variety of systems, enabling more robust studies across IR-luminous galaxy populations. Moreover, we have focused here on AGN signatures at mid-infrared wavelengths, and information at longer wavelengths (c.f., Younger et al. 2009), such as the location of the far-IR peak, could further constrain the AGN fractions in such sources (e.g., S12). In an upcoming paper (E. Roebuck et al. in prep.), we include the far-IR peak predictions from these simulations in interpreting the properties of $z \sim 0.3 - 3$ starbursts and quasars (the S12 sample).

The simplest interpretation of Figure 3.8 is that analogues of our "highly obscured" and "less obscured" examples are both realized in observed sources, in addition to both MW and SMC dust: all four models are required to cover the wide observed distributions of mid-IR color, PAH emission, and silicate absorption. A higher ratio of silicate to carbonaceous dust grains increases $r_{9.7}$ while shrinking $r_{7.7}$ (Figures 3.4), without changing $f_{4.5}/f_{1.6}$ (Figure 3.9), permitting estimates of $L_{\rm agn}/L_{\rm bol}$ under a variety of physical conditions, dust models, and optical depths. Although different ISM or dust models can produce broadly similar mid-IR trends, a separate measure of the AGN power, such as X-ray flux, is essential to further constrain these models. Furthermore, the recent discovery of high-redshift, hyper-luminous, hot-dust ULIRGs (Eisenhardt et al.

2012; Wu et al. 2012) suggests that we may lack a key phase in these few simulations, in which feedback initiates a transition between scenarios represented by our "highly obscured" and "less obscured" SED models.

Several assumptions regarding the dust radiative transfer may lead to discrepancies between our model sources and real sources. In particular, from Figure 3.8 we have identified two failures to which these assumptions likely contribute: 1) the mid-IR colors of the most AGN-dominated highly obscured sources are redder than their real counterparts (although bluer at $\lambda \lesssim 5\mu m$; see Figure 3.9), and 2) we do not simulate enough sources with little signs of PAH emission or silicate absorption: $r_{9.7} \sim 0$ *and* $r_{7.7} \sim 0$.

The IR calculation in SUNRISE distributes the energy absorbed by small PAH grains equally between emission in thermal equilibrium and in modes giving rise to the distinctive mid-IR PAH lines (Jonsson et al. 2010). Therefore, any change to this assumption or more sophisticated calculation, such as thermally fluctuating small grains (e.g., Guhathakurta & Draine 1989), will affect the dust continuum shape and PAH strength. In addition, we do not currently model dust destruction, and our model for dust production is crude, both key areas where near-future progress may be tenable. By not allowing our radiation to destroy dust grains or alter the dust grain distribution (or changing more generally the gas distribution owing to realistic feedback), we may be preventing ourselves from obtaining truly "power-law" AGN SEDs with no mid-IR dust features that may arise after AGN feedback disrupts the ISM.

We have purposefully focused on how galaxy dust can affect the fixed SMBH source SED (with minor variations in Section 3.4.4), rather than how the physics on smaller

scales play out in observations of ULIRGs. While high levels of galaxy dust can reproduce a number of properties of obscured quasars, the evolution of the central regions during these times of maximum obscuration will depend on the behavior of gas structures very close to the SMBH. This behavior may set the minimum scatter to be observed in correlations between these indicators. Using multiscale simulations, Hopkins et al. (2012a) showed how gravitational instabilities propagate down to scales of $\sim$ 1 to 100 pc during large-scale gas inflows. They demonstrated that a number of properties of obscured AGN attributed to a torus are explained by such dynamically-evolving accretion structures. Furthermore, these simulations suggest that the angular momentum vector of the small-scale "torus" can often be misaligned with the angular momentum of gas on galaxy scales, and the relative orientations can vary significantly in time (Hopkins et al. 2012b). Thus, the attenuation from the host galaxy may vary more significantly than our current simulations suggest. Therefore we are motivated to develop methods of integrating knowledge of the impact of these different scales on the emergent SEDs as a means for further interpreting the evolution of IR-luminous galaxies.

Recent work on merger simulations at higher resolution (Hopkins et al. 2013) and with different hydrodynamics solvers (e.g., AREPO: Springel 2010, C. Hayward et al. in prep.) shows that the average global evolution in simulations like the ones we analyze here, and hence conclusions made based on them, are robust. However, such advances will enable more sophisticated treatments of feedback processes and hydrodynamics in gas with a complex phase structure and at smaller scales; therefore future SED modeling could exploit these improvements to produce ever more detailed comparison libraries.

3.7 Summary and Conclusions

In this work we used the detailed information contained in high-resolution hydrodynamical merger simulations to analyze the impact of galaxy-scale evolution of dust on interpretations of AGN power in ULIRGs derived from the mid-infrared. Using the dust radiative transfer code SUNRISE, we calculated the SED evolution during two model starbursts meant to represent possible extremes of observed ULIRG populations. One merger is characteristic of bright starbursts at $z \sim 2$ to 4, while the other is a typical gas-rich merger at $z \sim 0$.

Increasing computational resources will enable future analyses of many more galaxy and galaxy merger scenarios and more sophisticated modeling of the small-scale physics that are presently very uncertain. In this initial work, we studied the variation of the modeled mid-IR SEDs as a function of viewing angle, source SED, dust grain distribution, galaxy ISM clumpiness, and AGN power, and evaluated the ability of common mid-IR diagnostics to predict the AGN UV-IR luminosity fraction, $L_{\rm agn}/L_{\rm bol}$. We developed a possibly generic mid-IR estimator of $L_{\rm agn}/L_{\rm bol}$ that can be measured for new samples with next-generation instruments such as *JWST*.

Our main conclusions are:

1. Our modeling technique broadly reproduces the observed span of common mid-IR diagnostics used to disentangle AGN and starburst activity.

2. Although generally consistent with previous interpretations, none of the indicators straightforwardly predict $L_{\rm agn}/L_{\rm bol}$ because they depend non-linearly on the galaxy's properties, which can vary rapidly on timescales $\sim 10^8$ yr.

3. Highly obscured sources can be more AGN-dominated than realized, even when the shape of their SED resembles a pure starburst. A large enough column density reprocesses all of the direct AGN light into longer wavelengths.

4. The mid-IR SEDs of sources with a powerful, highly obscured AGN depend strongly on the direction from which the source is observed. Along some lines of sight, significant dust self-absorption attenuates the IR flux and obscures the mid-IR signatures of the buried AGN.

5. Sources with a deep $9.7\mu m$ silicate absorption feature can be reproduced by models either with an extremely luminous AGN and MW galaxy dust, or with an average-strength AGN and SMC galaxy dust.

6. It is possible to construct an idealized mid-IR indicator utilizing future *JWST* data to cleanly estimate $L_{\rm agn}/L_{\rm bol}$ while simultaneously constraining the dust grain model.

Appendix: Toy Models for Qualitative Diagnostic Behavior

Here we make plausibility arguments based on a simple toy model to validate the simulated behavior of the diagnostics we analyzed. We assume a point source AGN that has an SED composed of direct AGN emission and dust re-emission from the torus. We label this flux $c_{\rm A}$. This is attenuated by a foreground screen such that the flux at infinity is $c_{\rm A}e^{-\tau}$. For the starburst component, $c_{\rm S}$, energy is absorbed by dust and re-emitted

at IR wavelengths. Then, this dust emission is attenuated at larger scales with some effective optical depth.

The presence of silicate grains causes a sharp increase in the dust opacity near $\lambda = 9.7\mu m$. Suppose that the attenuation curve is such that the attenuation on either side of the deep silicate feature is $e^{-\tau_{9.7}}$, but in the feature, the attenuation is $e^{-R\tau_{9.7}}$ where $R > 1$. R represents the ratio of the peak of the full extinction curve at $9.7\mu m$ to that arising without the silicate absorption; here we analyze $R = 6$, which roughly matches the behavior we see in the simulations as expected with an extinction curve for MW-like dust (Li & Draine 2001).

As in Section 3.3.1, $r_{9.7} = f_{9.7}/c_{9.7}$. We define the intrinsic monochromatic AGN fraction $F_{\rm A} = c_{\rm A}/(c_{\rm A} + c_{\rm S})$. This quantity is closely related to, but not directly proportional to, the bolometric AGN fraction $L_{\rm agn}/L_{\rm bol}$ used throughout the rest of this paper and defined in Section 3.2.6. We estimate the conversion between these quantities in Equation 3.4. By deriving toy diagnostics as a function of F_A we can controllably analyze their behavior in much the same way that we explored the simulations in Sections 4.3, 3.5, and 3.6 using the AGNx0, AGNx1, and AGNx10 models defined in Sections 3.2.3 and 3.2.4. Expanding $r_{9.7}$, we find,

$$r_{9.7} = \frac{f_{9.7}}{c_{9.7}} = \frac{c_{\rm A}e^{-R\tau_{9.7}} + ac_{\rm S}}{c_{\rm A}e^{-\tau_{9.7}} + c_{\rm S}} = \frac{F_{\rm A}e^{-R\tau_{9.7}} + a(1-F_A)}{F_{\rm A}e^{-\tau_{9.7}} + (1-F_A)}, \tag{3.1}$$

where a is a new parameter that characterizes the silicate absorption feature imprinted on the IR energy emitted from star formation. In the RT calculations, we obtain $a \sim 0.5$ since $\log_{10} r_{9.7} \sim -0.3$ when $F_{\rm A} \sim 0$ (Figure 3.3); this corresponds to an effective optical depth to the star forming regions of $\tau_{9.7,{\rm SF}} \sim 0.13$. Since the SF gas is spatially extended, $\tau_{\rm SF}$ will change less with viewing angle than $\tau_{\rm A}$, allowing us to keep this parameter a

fixed.

The PAH fraction $r_{7.7}$ is defined to be $r_{7.7} = f_{7.7}/c_{7.7}$. Add new variables $p_{\rm A}$ and $p_{\rm S}$ for the PAH emission luminosity, and assume that the PAH emission is some fixed factor P times the continuum emission for either AGN or star formation. We expand to find,

$$r_{7.7} = \frac{(c_{\rm A}+p_{\rm A})e^{-\tau_{7.7}}+(c_{\rm S}+p_{\rm S})}{c_{\rm A}e^{-\tau_{7.7}}+c_{\rm S}} \approx \frac{(1+P)c_{\rm A}e^{-\tau_{7.7}}+(1+P)c_{\rm S}}{c_{\rm A}e^{-\tau_{7.7}}+c_{\rm S}} \sim 1+P. \qquad (3.2)$$

The true behavior is somewhat more complex than this, since in Figure 3.3 we see that $r_{7.7}$ varies quickly at high AGN fractions and obscuration levels, but since both the numerator and denominator have a similar dependence on $\tau_{7.7}$, there is minimal scatter with viewing angle at all times.

Now, if we ignore SF by setting $F_{\rm A} = 1$, we get $r_{9.7} = e^{-(R-1)\tau_{9.7}}$, or $\ln r_{9.7} = -(R-1)\tau_{9.7}$ for all $\tau_{9.7}$. The magnitude of this pre-factor ($R - 1 > 1$) implies that the depth of the silicate feature varies more strongly with optical depth, and thus viewing angle and time, than does the continuum. Its negative sign gives rise to the intuitive behavior that the silicate absorption feature becomes more apparent ($r_{9.7}$ shrinks) with increasing optical depth. However, this trend fails in, e.g., Figure 6, and the D points scattered low in Figure 3.11.

For simplicity, in the case of mixed SF and AGN, let $a = 0.5$ and $F_{\rm A} = 0.9$, but let τ vary. When τ is very small, then the AGN terms dominate, yielding $\ln r_{9.7} \sim -(R-1)\tau, \quad \tau \ll 1$, the same behavior as the no-SF case. When τ is large enough that the AGN term in the numerator of Equation 3.1 can be safely ignored, then we have $r_{9.7} \approx 0.5/(9e^{-\tau}+1)$. This simplifies depending on τ:

$$\ln r_{9.7} \approx -\ln 9 + \tau, \quad \tau \sim 1, \qquad \ln r_{9.7} \approx -9e^{-\tau}, \quad \tau \gg 1$$

Therefore, for powerful AGN, $r_{9.7}$ depends strongly on τ, until τ gets too far above 1, giving rise to the strong viewing-angle scatter we noticed in the simulations in Section 4.3.4. In Figure 3.13, we plot example curves showing how $r_{9.7}$ and $r_{7.7}$ depend on $F_{\rm A}$ and τ in this toy model, which generally match the behavior we find in the simulations.

The qualitative behavior of diagnostic $D_{\rm MW}$ can be derived in the same fashion. For this, we seek a similar type of model for $f_{4.5}/f_{1.6}$. Roughly speaking (Figure 3.2), the pure-AGN SED is such that $f_{4.5} = f_{1.6}\,(\nu_{1.6}/\nu_{4.5}) = 2.8 f_{1.6}$, and the stellar SED is $f_{4.5} = f_{1.6}\,(\nu_{4.5}/\nu_{1.6}) = f_{1.6}/2.8$. The added complication in this situation is the attenuation of the AGN source depends on wavelength, roughly speaking as $\tau(\lambda) \sim \tau(1\mu m) \times (\lambda/1\mu m)^{1.5}$ (e.g., Weingartner & Draine 2001). We can use the same correction when combining $r_{9.7}$ and $f_{4.5}/f_{1.6}$ to model the $D_{\rm MW}$ diagnostic. We get:

$$\frac{f_{4.5}}{f_{1.6}} \approx \frac{F_{\rm A} e^{-\tau_{4.5}} + (1 - F_{\rm A})}{(F_{\rm A}/2.8) e^{-\tau_{4.5} 2.8^{1.5}} + 2.8(1 - F_{\rm A})} \tag{3.3}$$

In Figure 3.13, we construct $f_{4.5}/f_{1.6}$ and $D_{\rm MW}$ analytically and plot their behavior as a function of $F_{\rm A}$ and τ (at $4.5\mu m$). A final difference between the simulated quantities and these toy models is that we derived these models as a function of a monochromatic AGN fraction, while the quantity $L_{\rm agn}/L_{\rm bol}$ used in the rest of this paper is the bolometric AGN fraction. The correction depends on the SED shape of the various components, which we parametrize as $P_{\rm A} = jP_{\rm A,bol}$, $P_{\rm SF} = kP_{\rm SF,bol}$. The AGN bolometric correction factor j is fixed since our input template has a fixed SED shape over the wavelengths used by SUNRISE, while the SF correction k varies; we find that $j/k \approx 5 \pm 2$ in our RT calculations, and so we derive:

$$F_{\rm A} = \frac{P_{\rm A}}{P_{\rm A} + P_{\rm SF}} = \frac{kP_{\rm A,bol}}{kP_{\rm A,bol} + jP_{\rm SF,bol}} = \frac{(k/j)F_{\rm A,bol}}{F_{\rm A,bol}(\frac{k}{j} - 1) + 1} \sim \frac{5F_{\rm A,bol}}{4F_{\rm A,bol} + 1}. \tag{3.4}$$

Figure 3.13 shows $r_{9.7}$, $f_{4.5}/f_{1.6}$, and $D_{\rm MW}$ from these idealized formulae for a sampling of AGN fractions and optical depths, confirming much of the behavior we observed in the results of the RT calculations.

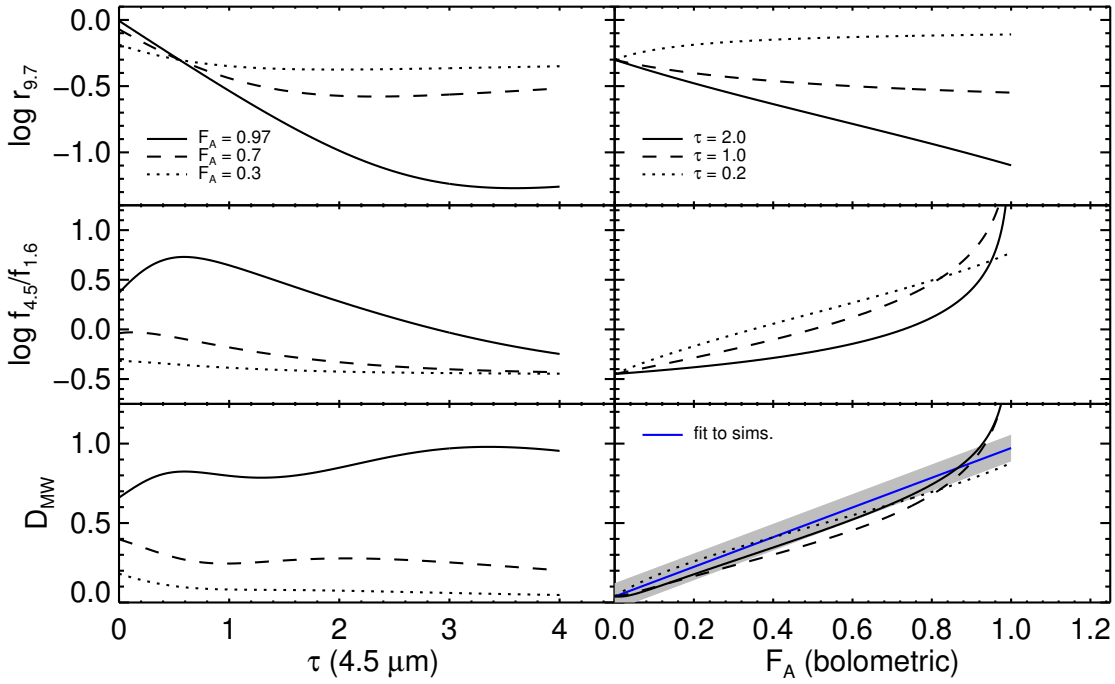

Figure 3.13.—: Behavior of toy models for $r_{9.7}$, $f_{4.5}/f_{1.6}$, and $D_{\rm MW}$ as a function of near-IR optical depth and AGN fraction. These simple models consist of an AGN source buried behind a simple obscuring screen ("galaxy dust"), plus an extended region of star formation that has a fixed spectral shape that does not depend on the optical depth to the AGN. In the upper left panel, $\log r_{9.7}$ has a strong dependence on τ, even at low levels of obscuration, giving rise to the large viewing angle scatter of $r_{9.7}$ in the simulations of Section 4.3.4: since the AGN is a point source, its final SED depends only on attenuation along a single line of sight, which can vary widely, while indicators of activity over a larger spatial region (such as $r_{7.7}$) have their attenuation averaged over many lines of sight. Several other phenomena from the simulations are demonstrated by these models: 1) Generally, the silicate feature is enhanced as the AGN fraction increases and as τ increases, up until the SF gas begins to dominate the attenuated AGN SED, at which point the dependence of $r_{9.7}$ on τ reverses; 2) The near-IR color $f_{4.5}/f_{1.6}$ effectively selects powerful AGN when τ is small enough (in our units, $\tau(4.5\mu m) \lesssim 1$ to 2); and 3) At larger τ, $\log f_{4.5}/f_{1.6}$ decreases and $|\log r_{9.7}|$ increases in such a way that the combination of these diagnostics, $D_{\rm MW}$, remains roughly constant for a fixed AGN fraction. This constancy is shown in the bottom left panel, and gives rise to the tight correlation between AGN fraction and $D_{\rm MW}$ in the bottom right panel. These simple arguments roughly verify the RT calculations and motivate the behavior of the empirically defined indicator $D_{\rm MW}$ (Section 3.6.1).

Chapter 4

K+A Galaxies as the Aftermath of Gas-Rich Mergers: Simulating the Evolution of Galaxies as Seen by Spectroscopic Surveys

G. Snyder, T. J. Cox, C. Hayward, L. Hernquist, & P. Jonsson

The Astrophysical Journal, Vol. 741, No. 77, 2011

Abstract

We construct models of poststarburst (or "K+A") galaxies by combining fully three-dimensional hydrodynamic simulations of galaxy mergers with radiative transfer

calculations of dust attenuation. We derive spectral line catalogs automatically from moderate-resolution optical spectra calculated as a function of merger progress in each of a large suite of simulations. By systematically varying the mass, gas fraction, orbital parameters, and mass ratio of the merging galaxies, we show that the lifetime and properties of the K+A phase are strong functions of the merger scenario. K+A durations are generally $\lesssim$ 0.1-0.3 Gyr, significantly shorter than the commonly assumed 1 Gyr, which is obtained only in rare cases, owing to a wide variation in star formation histories resulting from different orbital and progenitor configurations. Combined with empirical merger rates, the model lifetimes predict rapidly-rising K+A fractions as a function of redshift that are consistent with results of large spectroscopic surveys, resolving tension between the observed K+A abundance and that predicted when one assumes the K+A duration is the lifetime of A stars ($\sim$1 Gyr). These simulated spectra are spatially resolved on scales of about 1 kpc, and indicate that a centrally-concentrated starburst causes the Balmer absorption strengths to increase towards the central few kiloparsecs of the remnant. In some cases, the K+A features are longer-lived and more pronounced when AGN feedback removes dust from the center, uncovering the young stars formed during the burst. In this picture, the K+A phase begins during or shortly after the bright starburst/AGN phase in violent mergers, and thus offers a unique opportunity to study the effects of quasar and star formation feedback on the evolution of the remnant. We provide analytic fitting formulae for the estimates of K+A incidence as a function of merger scenario.

4.1 Introduction

Generally speaking, bright galaxies fall into two broad visible-spectrum categories: star-forming, blue spiral galaxies, and passively-evolving, red elliptical galaxies (Hubble 1926). Two long-standing questions for studying galaxy formation are: How does each type of galaxy form? Do galaxies transform from one type to another, and if so, how?

Early studies of the relationship between these classes as a function of lookback time focused on galaxy clusters. Oemler (1974) and Butcher & Oemler Jr. (1978) concluded that intermediate-redshift ($z \sim 0.5$) clusters have a much larger fraction of blue, star-forming galaxies than nearby clusters: the "Butcher-Oemler effect". Dressler & Gunn (1983) found that in one cluster, these blue cluster members were not "normal" spiral galaxies as we might see in the local Universe, but had spectra indicating either nuclear activity (e.g. Seyfert) or a recently quenched star-forming episode. The latter, so-called "E+A" galaxies, named as the combination of an early-type galaxy spectrum (E) with an A type stellar spectrum, were fitted best by an old stellar population plus a starburst component whose development ended within the last $\sim$ 1 Gyr; they have strong Balmer absorption features but weak or undetected nebular emission lines. Also known as "K+A" (for K type stars) or "poststarburst" galaxies, E+A galaxies were seen as occupying an important transitional state between the star-forming and passive populations. These objects are commonly selected from spectroscopic surveys as having Hδ equivalent width greater than some value (typically roughly 5Å) in absorption and [O II] emission equivalent width less than roughly 2Å. The latter limit corresponds to a cut in specific star formation rate at roughly $10^{-11}\mathrm{yr}^{-1}$, or a star formation rate below about 2 $\mathrm{M}_{\odot}\mathrm{yr}^{-1}$ for the most massive galaxies we consider in this work (Kennicutt Jr. 1998).

Numerous studies of K+A galaxies have been undertaken to explore this paradigm of galaxy evolution. K+A galaxies were found to be a significant fraction (~ 0.2) of rich cluster members at $0.2 \lesssim z \lesssim 0.6$ (Couch & Sharples 1987; Dressler & Gunn 1990; Fabricant et al. 1991; Belloni et al. 1995; Balogh et al. 1999; Poggianti et al. 1999), but are fewer than 1% of cluster members at $z < 0.1$ (Dressler 1987). Thus, a cluster-specific mechanism was thought to be responsible for quenching the star formation in these galaxies at intermediate redshifts, leaving fewer potential progenitors for the present time. Unbiased spectroscopic surveys revealed that although K+As seem to be a sizable fraction of cluster galaxies, they also exist in substantial numbers in lower density regions (Zabludoff et al. 1996; Blake et al. 2004; Goto 2007a; Yan et al. 2009; Vergani et al. 2010) out to $z \sim 1$. In fact, the majority of K+A galaxies in the local universe do not reside in clusters (Quintero et al. 2004). Thus, a cluster-specific mechanism cannot be the only way to make a K+A galaxy (also see Yan et al. 2009), and a systematic study of alternative mechanisms is warranted.

Detailed studies of the morphology, kinematics, and metal abundances of nearby poststarburst galaxies (primarily in the field) indicate that many of them are likely progenitors of bulge-dominated galaxies (Norton et al. 2001; Blake et al. 2004; Quintero et al. 2004; Goto 2007b; Yang et al. 2008). Thus, studying K+A galaxies may give clues to the evolution of galaxies from star-forming disks into quiescent ellipticals in a variety of environments at different cosmological times. Lavery & Henry (1988) proposed galaxy-galaxy interactions as a mechanism for driving K+A formation. A number of previously-mentioned studies of nearby K+As point out that a substantial fraction exhibit tidal features (Zabludoff et al. 1996; Chang et al. 2001) or companion galaxies (Yamauchi et al. 2008), suggesting that galaxy interactions or mergers indeed play a role

in K+A formation. In addition, hydrodynamic simulations (with simple star-formation laws, e.g. Mihos & Hernquist 1994b, 1996) of gas-rich galaxy mergers can lead to global star formation histories (SFH) characterized by strong, short bursts. Using simple stellar population synthesis (SPS), these bursts can lead to spectra with the lack of nebular star-formation indicators and strong Balmer absorption and that are found in poststarburst galaxies.

These studies and others led to proposed K+A formation mechanisms that fall broadly into two classes: (1) interaction of a star-forming disk with another galaxy, and (2) processes specific to massive clusters and halos. While a non-cluster-specific mechanism is required for K+As in the field, the relative inefficiency of major mergers in systems of galaxies with high relative velocities implies that mergers and galaxy-galaxy interactions may not be sufficient for creating the large number of K+As in the highest-mass halos.

Ram-pressure stripping (Gunn & Gott 1972), the removal of gas from disks traveling at high-speeds through a hot intracluster medium (ICM), is a likely candidate for reducing or ending the star formation in galaxies that fall into clusters. Although the gradual removal of low-density H I gas, presumably with a subsequent decline in the total gas reservoir and star formation, is unlikely to be violent enough to trigger a strong K+A phase, numerical work indicates that such galaxy-cluster interactions may lead to compression of the disk gas, offsets of the disk gas with respect to the galaxy's central potential, or infall of stripped gas that remained bound to the subhalo (e.g. see Schulz & Struck 2001; Vollmer et al. 2001; van Gorkom 2004). These may lead to enhancements of the star formation rate owing to torques and central infall, and thus a better chance of seeing strong Balmer lines in a galaxy's spectrum (Dressler & Gunn 1983). However,

these systems cannot dominate the population of moderate or bright K+A galaxies, because the vast majority of galaxies at these masses ($\gtrsim 10^9 M_\odot$) are centrals (e.g. Yang et al. 2009), so they undergo their transition from star-forming to passive as central galaxies.

In addition, for galaxies in halos above $\sim 10^{12} M_\odot$, cosmological accretion is likely to lead to virial shocks and heating (Rees & Ostriker 1977) that can shut down star formation in a manner that may produce K+As. Numerical simulations of this phenomenon (e.g. Kereš et al. 2005; Dekel & Birnboim 2006; Birnboim et al. 2007) indicate that galaxies in massive halos might experience a powerful burst-quench cycle suggestive of galactic evolution, perhaps through an obvious post-starburst phase. However, this mode is likely not a dominant contributor to the K+A population for several reasons. In particular, gas will continue to cool and rain down on the galaxy (Kereš & Hernquist 2009), so it is not certain that a complete (or fast enough) cessation of star formation will occur. In addition, it is not clear if this mode or transition can drastically alter galaxy morphology in a manner consistent with field K+A galaxies.

In this work, we focus on K+A formation via galaxy-galaxy interactions. Mergers have long been thought to be responsible for destroying stellar disks and turning them into dispersion-dominated ellipticals: the "merger hypothesis" (Toomre 1977). However, recent advances in numerical simulation methods have allowed the study of galaxy evolution via mergers in a significantly more quantitative way. For example, it has recently become possible to "age-date" the time since the starburst in K+A galaxies (e.g. Yang et al. 2008), and merger simulations can be used to test these methods by including a more sophisticated treatment of dust attenuation.

In particular, using physical models also allows the study of realistic SFH outcomes for a given set of mergers. Empirical models used in studies of K+A galaxies have often assumed very simple forms for the SFH induced by a merger. These SFHs imply "K+A lifetimes" of order the lifetime of an A type star, 0.5-1.5 Gyr. While it is true that for a given galaxy, the merger-induced burst can mimic this trivial single-aged stellar population (SSP), it is not clear if this is true for the "typical" merger involving a given disk. In fact, with fixed progenitors, variations in the orbital parameters of a merger can lead to an enormous variety of dynamical and SFH outcomes (Barnes 1992; Barnes & Hernquist 1996). The merger or event rate inferred by surveys of K+A galaxies are sensitive to this distribution of the K+A duration timescale. In the present work, we quantify this variation on the inferred K+A lifetimes of simulated mergers.

In addition, the mechanism for the rapid shutoff of star formation is not known precisely. Feedback from star formation and active galactic nuclei (AGN) activity, presumably leading to the expulsion of the remaining gas reservoir, has been inferred indirectly in a wide variety of observations (Kaviraj et al. 2007; Tremonti et al. 2007; Brown et al. 2009). By varying the feedback prescriptions and strengths in the numerical models, simulations can test a large variety of these processes in a systematic way. More generally, by studying poststarburst galaxies in the context of the extragalactic zoo and standard cosmology, we hope to study their implications for the role of mergers in driving galaxy evolution.

In this paper, we define and study a set of K+A galaxy models which are the remnants of simulated galaxy mergers. We have seen that the characteristic rapid inflow and consumption of gas during a major gas-rich merger is likely to be the cause of some K+A galaxies, and a recent study by Wild et al. (2009) used simulations from

Johansson et al. (2009) to perform a similar comparison of the models to poststarburst data; the reader is encouraged to see those papers for another detailed investigation of the characteristics of poststarburst galaxies in merger simulations. Our conclusions are broadly consistent with those reported in Wild et al. (2009).

The present work applies different spectrum synthesis and selection methods to a broad set of simulations by Cox et al. (2006a) to systematically quantify the variation of K+A properties with different merger parameters. In particular, we utilize three-dimensional radiative transfer to study the post-starburst stellar populations using standard line strength indicators. This procedure allows us to arbitrarily vary observing parameters such as the viewing angle and spectrograph fiber size and realistically measure the line strengths for a wide range of simulated mergers that include processes such as star formation, feedback, accretion onto a central supermassive black hole, and dust attenuation.

The primary goal of this work is to reconcile observed K+A numbers with realistic merger models and well-motivated merger rates. In §4.2, we outline in detail our methodology for generating spectral line catalogs from numerical simulations. Readers wishing to bypass these details can skip to the relevant parts of §4.3, §4.4, §4.5, or §4.6. In §4.3, we study the basic ramifications of our methods, highlighting the resulting variations owing to viewing angle, aperture bias, the presence of a bulge, and AGN feedback. In §4.4, we systematically calculate the lifetime of the K+A phase as a function of the input merger parameters, and summarize the results in §4.5, providing fitting formulae that can be used in semi-analytic modeling. In §4.6, we discuss the implications of our study by comparing observed K+A fractions to those inferred by our lifetime calculations. We summarize and discuss the implications of these studies in §5.6,

and conclude in §4.8.

4.2 Methods

We employ the GADGET 2 code (Springel 2005) to simulate galaxy merger scenarios. In §4.2.1 we describe the mergers studied in this work and the relevant physics included. Stellar light and dust extinction are modeled post-simulation using the three-dimensional polychromatic radiative transfer code SUNRISE (Jonsson 2006; Jonsson, Groves, & Cox 2010, hereafter J06, J10), with specific models discussed in §4.2.2. We produce spatially-resolved spectral energy distributions (SEDs) along multiple sight lines from 50x50 pixel cameras with each pixel spanning two physical kiloparsecs. To select K+A galaxies, we mimic the data of optical spectroscopic surveys (§4.2.3) and generate spectral line catalogs for each simulation. For this purpose, we use the following equivalent widths: the Balmer lines (Hβ, Hγ, Hδ) = (4861Å, 4341Å, 4101Å) and the [O II] λ = 3727Å transition (§4.2.4). In Figure 4.1 we demonstrate our aperture and spectrum fitting procedure.

4.2.1 Galaxy Simulations

This study is one in a series based on numerical simulations of gas-rich galaxy mergers. The calculations used here are essentially a subset of those employed by a number of other authors, for example Cox et al. (2006a), Hopkins et al. (2005b), Narayanan et al. (2010b,a), Robertson et al. (2006a), Wuyts et al. (2009a,b, 2010), Younger et al. (2008, 2009), Hoffman et al. (2009, 2010), and others. The focus of this work differs in that

we wish to generate and analyze mock spectral catalogs of merger remnants in order to quantify their observed poststarburst characteristics. Hence, most of the discussion in this section will be on the application of the radiative transfer code SUNRISE (J06, J10) to the extraction of realistic spectra. For a complete description of the physical models applied to the hydrodynamic methods in the context of this ongoing study, the reader is encouraged to see Springel, Di Matteo, & Hernquist (2005b) and Cox et al. (2006a).

GADGET 2 (Springel 2005) combines an accurate N-body gravity solver with a smoothed particle hydrodynamics (SPH) code that is fully conservative (Springel & Hernquist 2002) to perform cosmological or galaxy simulations. Gravity dominates on galactic scales, but hydrodynamics is essential in many applications and serves as the basis for treating a great deal of challenging baryon physics. Our simulations spawn star particles stochastically from the gas via a prescription designed to reproduce the Schmidt-Kennicutt law (Springel & Hernquist 2003). Each galaxy is seeded with a central massive black hole that undergoes Eddington-limited Bondi-Hoyle accretion. These processes inevitably inject energy back into the surrounding gas (supernovae, jets, winds, radiation, etc), so our simulations model this by thermally coupling some of this energy to nearby gas particles (Di Matteo, Springel, & Hernquist 2005; Springel 2005; Springel, Di Matteo, & Hernquist 2005b). The feedback efficiency parameters used are identical to those used in previous studies (e.g. Hopkins et al. 2005b; Cox et al. 2006a, and subsequent works): the radiative efficiency is 0.1, and the feedback energy couples dynamically to the surrounding gas with an efficiency of $\approx 5\%$.

Our star-forming disk galaxies consist of dark matter halos, stellar and gaseous disks, and stellar bulges. We place two disks on parabolic orbits with a variety of relative disk orientations. Generally speaking, the major mergers (two galaxies equal in mass)

proceed as follows. As the two disks approach for the first time, strong non-axisymmetric forces cause the disks to form a transient bar, driving some material into the center (Barnes & Hernquist 1991, 1996). How much material depends on the merger orientation as well as the properties of the original galaxy (Hopkins et al. 2009b,e). For example, Mihos & Hernquist (1994b, 1996) find that the presence of a stellar bulge can resist perturbations owing to this first passage.

Ultimately, the torques produced during this close passage transfer angular momentum from the halos' mutual orbit into their constituents, leading to a direct coalescence of the two disks. During this phase, the perturbing forces are so great that they completely disrupt the disks, sending much of the remaining gas into the center of the combined dark matter potential. As the gas density increases in the central regions, star formation and central black hole growth proceed rapidly.

In this study, we explore isolated binary mergers for which we vary galaxy mass, gas fraction, and bulge fraction, as well as their relative orientation and mass ratio.

4.2.2 Radiative Transfer

We generate mock optical observations of our galaxies in post-processing for all relevant times during each merger simulation. Roughly speaking, knowledge of the global star formation rate and approximate wavelength-dependent dust attenuation is sufficient to produce a reasonable prediction of the integrated galaxy spectrum. However, large spectroscopic surveys (in which poststarburst galaxies are identified) typically measure only a portion of the galaxy light in a spatially-biased way (fibers, slits), and we wish to explore how K+A selection varies with aperture size and viewing angle. Therefore,

we prefer a method that uses and preserves the information we get from the simulations about the locations of individual star particles and hence of distinct stellar populations, as well as the gas and dust. This requires knowing the complete spatially-resolved star formation history (SFH) of the system, which we can follow via the histories of the stochastically-spawned SPH star particles. We then must assign each particle a single-age stellar population (SPS) SED for a cluster of that mass, age, and metallicity. Moreover, the wavelength-dependent attenuation cannot be reliably predicted from integrated quantities, as it depends on the geometry of stars, AGN, and dust, as well as dust grain composition and sizes, and scattering of light into the line of sight. Thus we calculate the dust attenuation along each line of sight using knowledge of the surviving gas particles' spatial distribution and metallicity by assuming a dust-to-metals ratio.

To these ends, we employ the SUNRISE polychromatic Monte Carlo radiative transfer code (described in J06 and J10). This code performs all of the necessary steps above and allows us to conveniently vary important stellar modeling parameters for our study. Below we discuss the principle components used to compile our final spectra. In addition, we describe the modeling assumptions we make when limited by the finite resolution of the simulations. These choices were made to be reasonable for local merger remnants, and were set before making any of the conclusions in §4.3 or §4.6. In some cases (§4.2.5), we varied these assumptions to explore their effect on a small subset of our simulations. However, in this work we make no attempt to constrain or fit these modeling uncertainties, but rather treat them as a fixed set of inputs with which to test the overall picture.

1. *Normal stars.* To model stars of age $> 10^7$ years (10 Myr), we apply a high-optical-resolution ($\Delta\lambda/\lambda \approx 20,000$) STARBURST99 SED (Leitherer et al. 1999)

with metallicity closest to that of the star particle. We use the two-segment power-law initial mass function (IMF) of Kroupa (2001). It is from these models that Balmer-series absorption enters our SEDs, since stellar clusters of a certain age will be dominated by A stars, originally defined by such strong absorption features.

2. *Young stars.* For stars less than 10 Myr old, SUNRISE uses the SED templates of Groves et al. (2008). These models combine one-dimensional shock models for evolution of the H II and photodissociation regions (PDRs) around massive stars and clusters (Dopita et al. 2005; Groves et al. 2008), with the MAPPINGS dust and photoionization radiative transfer code (Binette et al. 1982; Sutherland & Dopita 1993; Groves et al. 2004; Allen et al. 2008) to calculate the SED that emerges from the HII region and, optionally, the PDR, which is the region where the gas surrounding young stars transitions from being fully ionized to fully molecular. These SEDs include nebular emission lines. An uncertain tunable model parameter of this component is the time-averaged fraction, $f_{\rm PDR}$, of each H II region that we assume to be surrounded by the birth cloud from which the cluster was born (the PDR). The dust in the PDR is a significant source of attenuation for young stars that are potentially the dominant contributor to the galaxy luminosity. Much observational and theoretical work is attempting to constrain this parameter, and a number of discussions about its impact and use for studying such simulations can be found in J10, Groves et al. (2008), Narayanan et al. (2009), and Younger et al. (2009).

Prior to running any simulations, we selected $f_{\rm PDR} = 0.3$ as a realistic value for the majority of K+A galaxies at low redshifts. This choice gives results that are identical to within 10% (in line fluxes) to when the fiducial value of 0.2 from J10 is used. These values of $f_{\rm PDR}$ correspond to molecular cloud clearing timescales of $\sim$1-2 Myr, which is

consistent with observational estimates (Groves et al. 2008, and references therein). As pointed out in J10, the MappingsIII particles contribute weakly to the galaxy SEDs when the specific star formation rates are at or below those of typical local galaxies, which is what we expect for the majority of K+A galaxies found in local surveys. See §4.2.5 for a discussion on the effect of $f_{\rm PDR} = 0.9$ on K+A selection.

Another source of noise tied to the treatment of young stars owes to the stochasticity of the star formation prescription in the simulation. Although it gives the expected overall star formation rates for each gas particle, the version of Gadget we use for this study generates actual star particles using a finite table of random numbers for the Monte Carlo step. This causes the formation of actual star particles to be somewhat more correlated than it ought to be, and the emission line star formation indicators reflect this by being highly variable from snapshot to snapshot even for smooth overall analytic star formation rate histories. For all of our measurements, we smooth the spectral line catalogs over a 50 Myr box to limit the noisiness of the lightcurves owing to this effect. This will add a comparable amount ($\sim$ 50 Myr) of uncertainty to our measurements, but this is a small effect and is likely to be random in nature.

3. *Dust attenuation.* To attenuate the light originating from the source particles, Sunrise performs Monte Carlo radiative transfer on an adaptively refined Cartesian grid. For complete details, see J06 and J10. We assume a dust-to-metals ratio of 0.4 (Dwek 1998) and Milky Way dust grain models from Weingartner & Draine (2001) with Draine & Li (2007) updates. Using the energy input into the dust by the source particles, Sunrise computes self-consistently absorption, scattering, and subsequent infrared re-emission from dust. The wavelength-dependent dust attenuation is calculated correctly from the assumed dust grain models, producing spectra for which the lines are

attenuated realistically.

The radiative transfer of dust attenuation by dense clumps requires subresolution considerations because the underlying hydrodynamic simulations do not have sufficient resolution to model the ISM on all scales. Under the ISM treatment that we use (Springel & Hernquist 2003), gas particles in GADGET should be thought of as containing both a diffuse "hot" component and a clumpy "cold" component where the total masses of each are estimated, but we have no information about their physical distribution. In this work we will assume that the covering fraction of the cold phase (which can contain $\sim 90\%$ of the gas mass) is small, and ignore it. Then we use the PDR model described above to treat the attenuation by clumpy, star-forming clouds. In this approach, we ignore non-star-forming dense clumps and simply treat the PDR model as the source spectrum for newly-spawned (< 10 Myr) star particles. This model is sometimes referred to as "multi-phase ON". We believe this choice is appropriate for the conditions of most local K+A galaxies, where large reservoirs of obscuring dust are not available. In §4.2.5 we briefly discuss an alternative choice.

4. *Galaxy properties.* We use [O II] as a star-formation rate indicator to select against poststarburst galaxies, so in order to capture the approximately correct metallicity dependence of this line, we assume the gas disks have an initial central stellar and gas-phase metallicity of $1.5 Z_\odot$ and gradient -0.03 dex kpc^{-1}, consistent with Zaritsky et al. (1994). We assume that the stars initially present in the disk were formed continuously over 14 Gyr and the bulge was formed in a single burst 14 Gyr ago.

5. *AGN.* This implementation of SUNRISE uses the black hole accretion rate from the GADGET simulation to estimate the bolometric luminosity of the central

AGN, $L = \epsilon \dot{M} c^2$, where we use $\epsilon = 0.1$. The code then inserts an unreddened luminosity-dependent broadband quasar SED from the templates in Hopkins et al. (2007c). This source is considered to be at the location of the central SMBH and its spectrum is treated in the same way as a star particle, meaning that it is subject to dust absorption and scattering. While the underlying AGN templates used for this work include emission from narrow-line regions (NLR), the coarse interpolation used in this work to create the broadband AGN spectrum makes it impossible to measure this component to the lines (it is treated as continuum). Thus the emission lines in our spectra solely owe to star formation, and are not contaminated by emission from NLRs.

4.2.3 Simulated Spectra

For the results we present here on the lifetimes of nearby poststarburst galaxies, we generate mock catalogs designed to mimic Sloan Digital Sky Survey (York et al. 2000) data. We fix the scale of our measurements by placing each galaxy at $z = 0.1$. The result of the SUNRISE procedure is, in general, a set of observations of the galaxy merger from several different camera angles. We choose seven viewing angles distributed uniformly in solid angle. One might think of each viewing angle for a given snapshot as a distinct measurement. Thus our sample consists of $N_{\rm cameras} \times N_{\rm snapshots} \times N_{\rm simulations}$ measurements. The mock data consist of the spectral flux density on a square grid of pixels for each camera. For the present work, our pixels are at most 2 kpc on a side, which is sufficient to resolve typical spectroscopic apertures at $z \approx 0.1$.

For a reasonable balance between spectral resolution and computation efficiency, we produce SEDs on an $R = \lambda/\Delta\lambda \approx 1000 - 1200$ wavelength grid for the range of interest,

3000-7000Å. However, owing to technical limitations at the time these calculations were made, we have used $R \approx 100$ for the MAPPINGS component of the galaxy SED (§4.2.2, component 2), oversampling it onto our R1200 grid. Thus the nebular emission lines are wider than they should be given the spectral resolution of the output wavelength grid, but the total flux of each line is conserved. This somewhat degrades the SEDs for which there is a substantial emission line component and renders impossible a two-component fitting of spectra in which there are comparably strong emission and absorption components. To avoid confusion, we stick to simple line strength indicators and do not try to fit both emission and absorption components.

We conserve the flux in the emission line component, so we still accurately measure the evolution of the total flux in the line during the ingress to the poststarburst phase as star formation/line emission turns off and A stars become dominant. During the E+A phase and egress (as the A stars dominate then fade), the low-resolution MAPPINGS model is sub-dominant and our ≈ R1200 sampling becomes meaningful and effective for measuring the Balmer absorption lines as they shrink and disappear. This means that we produce spectra (or sequences of spectra) in which the effective spectral resolution varies unrealistically in both time and wavelength. The K+A selection criteria we employ will be sensitive to this, because ordinary Balmer absorption line strengths are calculated by measuring the equivalent width without any emission lines present, because they have been subtracted out. However, we will apply an [O II] limit and use typically-observed metallicity profiles, so we expect any Balmer emission filling to be small for systems that we observe as having small [O II] emission fluxes. We have checked this by running several simulations without the emission line component. In these cases, our pipeline measures absorption equivalent widths that are the same to within $\sim 5\%$ for all snapshots

that satisfy the [O II] criterion.

We measure the simulated spectrum observed by each camera at every time in four ways. By doing this for all of our simulations, we hope to get a rough idea of how these different observing modes can affect the selection of poststarburst systems formed from a variety of merger scenarios.

(Spectrum A) Our default spectrum is measured by including the full radiative transfer model (elements 1-4 in the Section 4.2.2) *and by only using light that falls within a 3 arcsecond aperture*. We center the aperture on the peak of the optical surface brightness via centroiding and weight the pixels according to their intersection with a 3 arcsecond diameter circle centered on this point. For $z = 0.1$, this corresponds to a diameter of approximately 6 kpc. See Figure 4.1 for a graphical description.

(Spectrum B) We turn off element 3 of Section 4.2.2, the attenuation by diffuse dust, and use the exact same aperture as for measurement A. The attenuation in the Mappings subresolution model, item 2 in §4.2.2, is still included. Note that we do not re-center the aperture, so cases A and B measure an identical line of sight.

(Spectrum C) We measure the integrated spectrum of the square camera, which is 100 kpc on a side. We use this as a rough way to estimate the relative spatial concentration of the K+A component to the stellar populations.

(Spectrum D) We measure the integrated light as in C, but we turn off element 3 of Section 4.2.2, the attenuation by diffuse dust.

We point out that these methods generalize easily. Our pixel-weighting scheme can make spectra using arbitrary spectrograph aperture shapes (slits, etc), and we scale

the aperture consistently using the angular diameter distance to a given redshift and telescope properties. Where needed, we assume a flat cosmology with $\Omega_m = 0.3$ and $\Omega_\Lambda = 0.7$. In principle, it is feasible to mimic (in all but spectral resolution) any realistic observing mode.

4.2.4 Line Catalogs

Following a number of observational works, we use the rest-frame equivalent widths (W_{line}), and simple comparisons between them, as primary indicators of poststarburst activity. This equivalent width is defined (ideally) as

$$W_{\rm line} = \int_{\rm line} \frac{I_\lambda - C_\lambda}{C_\lambda} d\lambda, \tag{4.1}$$

where I_λ is the spectral flux in the line at wavelength λ, C_λ is the spectral flux in the continuum at wavelength λ, and the integral is taken separately over each spectral line in the galaxy's rest frame.

Thus, our goal is to generate catalogs of this quantity for each simulation snapshot, camera angle (0-6, Section 4.2.3), and measurement mode (A-D, Section 4.2.3). For the number of simulations, viewing angles, and observing modes we wish to test in this work, we must measure in total a few times 10^6 individual lines, so we require a robust, relatively quick way to automate these measurements. We describe our method in this section.

Like real spectra, we do not know ahead of time the continuum level C_λ. So for each spectrum, we must estimate C_λ on the wavelength range of interest. This

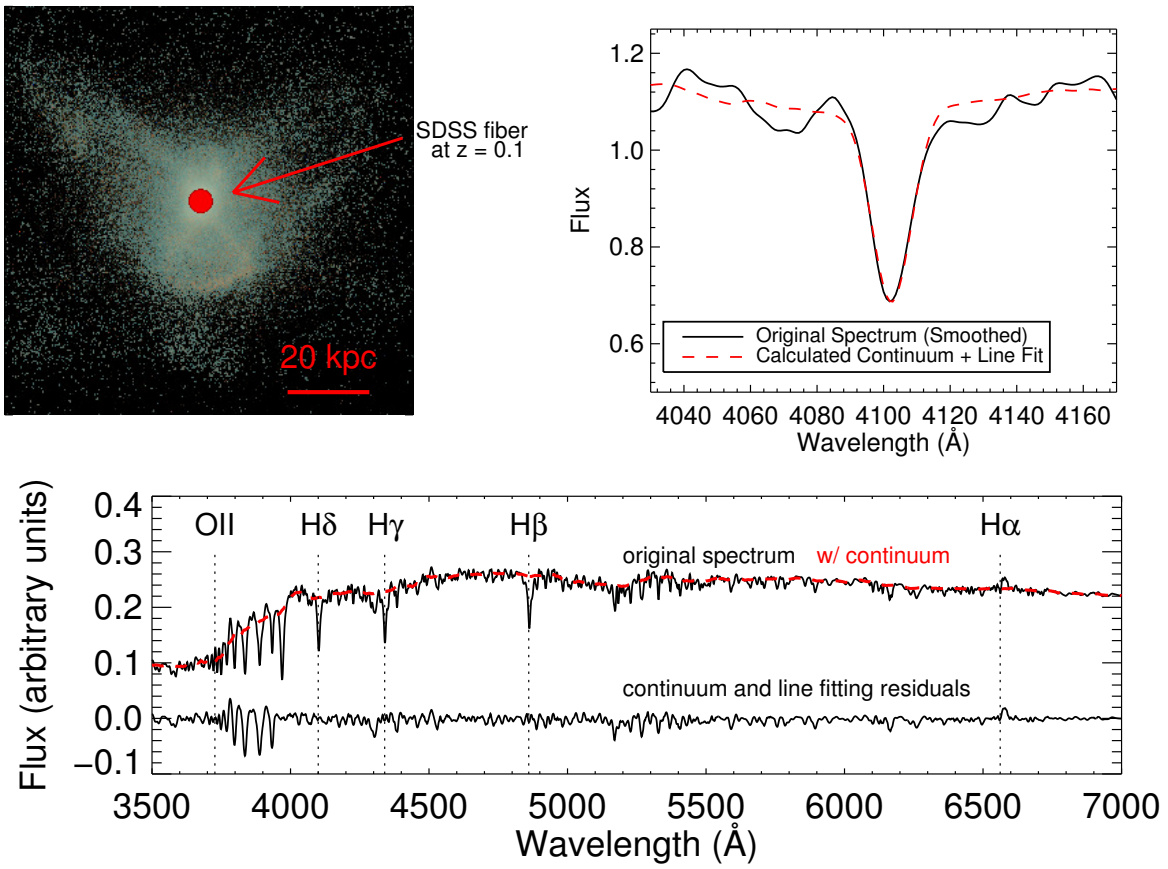

Figure 4.1.—: An overview of our selection method. Optical images are created for each of seven viewing angles for all simulation snapshots and scaled to z=0.1. The light falling within a chosen aperture is taken to be the galaxy's spectrum in our default model. A simple k-σ rejection filter is applied to estimate the continuum level, and the lines of interest are then fitted with individual Gaussians. The top left panel here shows the logarithm of the optical flux in g-r-i colors for one of our simulated K+A galaxies. We overlay the SDSS spectrograph fiber scaled appropriately: this is what our default spectrum A seeks to mimic. In the top right panel we show a zoom-in of our fit to the Hδ line in the resulting spectrum. In the bottom panel, we show the spectrum (black), our continuum fit (dashed red), and the residuals (black, arbitrary offset) after fitting for Hϵ, Hδ, Hγ, Hβ, Hα, and [O II]. This procedure allows us to create realistically-generated spectral line catalogs for a large number of simulations.

computation is a source of uncertainty for any equivalent width measurement and is especially problematic for the [O II] and Hδ lines because they sit in a portion of the spectrum which varies rapidly with wavelength, especially when Balmer-series absorption is prevalent. This makes any general continuum-fitting procedure difficult.

In an attempt to minimize this issue, we follow the approach of many catalogs and calculate C_λ using an iterative 2σ rejection filter with a window of width 200Å. Note that these continuum fitting parameters are somewhat arbitrary; we chose them so that the automatic measurement best resembles continua one might draw by hand near all our lines at all times during the simulation. It should be noted that this procedure somewhat underpredicts the true continuum level, since it is calculating an average of the flux near the lines while the true continuum level is unknown. Thus our absorption equivalent widths are slightly smaller than a more robust calculation might find. There are many choices of parameters for this procedure that give reasonable but different results for the continuum estimation, and we find that this introduces uncertainty in a relatively balanced way among the lines of interest near the 4000Å break, at the $\approx 10\%$ level.

We then convolve (smooth) the continuum with a normalized 100Å box and subtract it from the spectrum and convolve (smooth) the result with a normalized 15Å box to produce the input S_λ for the line measurement procedure. For each line, we approximate Equation (4.1) by fitting to S_λ a Gaussian curve with parameters A_λ, σ, and $\lambda_{\rm center}$ as the line amplitude, Gaussian width, and center, respectively. The equivalent width for the fitted curve is then

$$W_{\rm fit} \approx \frac{A_\lambda \sigma \sqrt{2\pi}}{C_\lambda(\lambda_{center})}. \tag{4.2}$$

This fitting procedure has several advantages over a direct application of

Equation (4.1). Most importantly, relative uncertainties to the fit parameters are readily estimated, allowing us to let the fit proceed with minimal preconditions. We simply throw out line measurements for which the line center is not sufficiently close to the catalog line center, the computed $W_{\rm fit}$ uncertainty is very large, or the Gaussian fit parameters are very highly correlated. Since we value speed for performing so many calculations, we apply a very simple MCMC procedure from Press et al. (1986). We find that a 1000-step burn-in followed by a 5000-step chain more than suffices to estimate the parameters and their relative uncertainties for lines that exist.

The pipeline was tested extensively by visually comparing the spectral lines to the automatically-calculated EW values. For lines that do not exist visually, the parameter uncertainties and/or correlations are tens of percent, and the center of the fitted Gaussian often does not match the line catalog, so we reject measurements that have these properties. Lines that exist visually have small residuals ($\lesssim 5\%$), and nearby/slightly overlapping lines can be separated effectively. This procedure takes approximately 1 second per spectral line on modern processors: this is adequately fast for our purposes. Although the uncertainties we measure are not real in the observational sense because our models do not produce measurement uncertainties, their relative magnitudes are very effective at quickly estimating the robustness of our line measurements. We will use $W_{\rm fit}$ as the primary line strength measurement throughout this paper.

In this work, for simplicity, we do not use Hα as a star formation rate indicator. This line enters our model spectra from all of the model components mentioned in § 4.2.2, and the resolution limitations for the emission components mentioned in § 4.2.3 are exacerbated by AGN contributions and the nearby Nitrogen lines.

Future work on these simulations will include the Hα line. It is useful as an additional observational discriminant against dust-obscured star-forming contaminants to the K+A population. Moreover, a number of different selection criteria have been applied to select poststarburst galaxies in different observational samples. In principle our models can mimic any of these, but here we do not consider more than simple EW cuts. This is sufficient to test K+A formation and discuss their properties, but not for complete comparisons to real samples. A full experiment on the merits and results of different selection methods is beyond the scope of this paper, but will be the subject of future work.

4.2.5 Modeling and Numerical Considerations

In §4.2.2 we described our default model and why we believe this choice to be reasonable for the galaxies considered here. However, we might expect poststarburst selection to depend sensitively on these assumptions in certain cases, so in this section we discuss briefly how our measurements are affected by different modeling assumptions and numerical resolution. These variations are motivated by the large uncertainties in modeling the dense, star-forming, obscuring ISM. Such uncertainties arise because many of the processes that drive the evolution of this medium exist on scales below our resolution or are computationally intractable for such kinds of simulations. Hence we are limited to using sub-grid models with parameter choices constrained to some degree by observations.

For example, the rapidly-varying physical conditions of late-stage mergers may imply that the appropriate $f_{\rm PDR}$ varies in a complicated way in both time and space.

Emission lines are strongly suppressed from regions with a high PDR fraction that may exist in extremely dense and massive molecular environments, leading to a situation in which the optical spectrum of a powerful starburst may imply instead a starburst relic. By contrast, emergent emission lines are strongest when the PDR fraction is low, shortening the length of time a given selection criterion will define a K+A galaxy.

Thus a value of $f_{\rm PDR}$ near 1.0 may be appropriate for specific galaxies, such as very gas-rich interactions at high redshift (e.g. Narayanan et al. 2009). We believe it is unrealistic for this work, since we will focus on times of the simulations that are not extreme starbursts. However, in order to test the sensitivity of K+A selection to high values of $f_{\rm PDR}$, a number of mergers were run with $f_{\rm PDR} = 0.9$. In general, the K+A lifetimes of these simulations were longer by up to a factor of two than those using smaller values, with a second K+A phase occurring immediately after first pericentric passage and prior to final coalescence (unlike the $f_{\rm PDR} = 0.3$ case). This can be understood because the first passage produces a weak starburst, but star formation continues; the Balmer absorption strength increases in both cases, but with $f_{\rm PDR} = 0.9$, the emission lines from the youngest stars are obscured enough to be considered quiescent by our [O II] emission line cut. We did not find any simulation with either choice of $f_{\rm PDR}$ where we selected as K+A a snapshot during the starburst.

Another way to deal with obscuration by dense clumps of gas is to turn off the PDR model and instead treat the entire gas mass as existing in the diffuse ISM phase (sometimes referred to as "multi-phase OFF"). In this case, SUNRISE treats the entire mass of each gas particle as having uniform density over an entire resolution element. We note that this choice does not necessarily maximize the attenuation of young (< 10 Myr old) stars versus the multi-phase ON model, though it does systematically increase the

attenuation for stars with ages > 10 Myr. Several simulations were undertaken with this choice, with the effect being to attenuate most of the light from young stars throughout the simulation, including A stars. Although this choice is unlikely to be justified during the relatively quiescent K+A phase of galaxies, this difference represents a significant modeling uncertainty.

These alternative choices may be appropriate for extreme environments. However, the duration of the K+A phase is commonly of order 100 Myr or more, significantly longer than the duration of the peak of the starburst where the modeling of dust attenutation is most uncertain. Thus, while our subresolution models are imperfect at following the ISM during these extreme conditions and should be treated as significant uncertainties, this minimal overlap cannot change general conclusions made about the poststarburst properties of these simulations. However, they may affect inferences made about specific times during the merger (e.g. the peak of the starburst or AGN activity), so more detailed comparisons may further constrain the sub-grid models. For example, the K+A pair fraction may rely on a combination of $f_{\rm PDR}$ and progenitor bulge properties (see §4.3.2), or the dynamics of K+A galaxies may depend on the feedback physics during the final merger coalescence.

Another important component to the model is the assumed ISM pressure support. Here, we follow (among others) Cox (2004), Springel et al. (2005b), Robertson et al. (2004, 2006a), and Hopkins & Quataert (2010) to apply an equation of state leading to a relatively stable ISM suggestive of local disk galaxies. We do not vary this model here, but recent studies have relaxed this assumption in order to simulate the clumpy, turbulent ISM observed in disk galaxies at high redshift (e.g. Elmegreen et al. 2007). The reader is encouraged to see Bournaud et al. (2011) and Teyssier, Chapon, & Bournaud

(2010) (and references therein) for results on how this can affect the evolution of the ISM in simulations of turbulent gas-rich disk galaxies and mergers.

Although we are unable to fully model the clumpy structure of the ISM, the above model variants serve to bracket the plausible extremes of attenuation. The default set described in §4.2.2 and used throughout the rest of this paper is observationally well-motivated, but it is useful to consider the effects of these different extreme assumptions. In summary, if we assume a maximal fraction by which young stars are attenuated by dust in their birth clouds ($f_{\rm PDR} = 1$), galaxies with a high star formation rate more commonly satisfy the K+A criterion. If instead we assume that all of the dust is distributed more diffusely throughout the ISM ("multi-phase OFF"), then there exists enough dust in our merger remnants to mostly obscure the A stars near the center of the remnant for a large fraction of their lifetimes. While we do not have a single precise appropriate description of the ISM structure, such false-K+As (Brown et al. 2009) or dust-obscured quiescent galaxies are observationally extremely rare at best, so we are assured that our choices are reasonable for the K+A phase of galaxies and should serve to encompass their real behavior.

In addition to the modeling parameter choices, we must also choose at what level to resolve the underlying SPH and radiative transfer simulations. Cox et al. (2006b) studied this for a suite of merger simulations that were identical in spatial resolution and equal to or worse in mass resolution than those considered here, but with a slightly different feedback model. They showed that the star formation histories of the GADGET merger simulations are the same to within 5% when the particle number is increased by factors of 2, 4, and 10. This indicates that our SPH particle number is sufficient to resolve the star formation history of the mergers. Small differences in the simulated

spectra are expected when varying the spatial resolution, because the star formation law we apply depends super-linearly on the gas density, and because the exact distribution of stars and gas will vary with resolution. However, the integrated quantities that will most directly affect the K+A features are typically unchanged at the same level as above.

The convergence properties of the SUNRISE radiative transfer approach were demonstrated for the integrated SEDs of isolated galaxies in J10. In the present work, we use similar grid refinement parameters, such as $\tau_{tol} = 1$, and a fiducial resolution setting that leads to $\approx$ 500k grid cells for simulations in which the gas fractions are less than or similar to, for example, the Sbc simulation from J10. During the parts of the merger that K+As could exist in the simulations with our choice of $f_{\rm PDR}$, gas fractions are only a few percent or less and star formation rates are at most a few $M_{\odot}{\rm yr}^{-1}$. In these cases, diffuse dust attenuation is negligible and the uncertainty in the output spectrum arises principally from the underlying stellar population methods and not the radiative transfer procedures. To verify similar convergence for our pipeline to produce the post-merger fiber spectra, we re-ran a simulation commonly presented in this work (40% initial gas, $10^{11}M_{\odot}$ baryonic mass, 1-1 merger) with different resolution settings, giving $\approx$ 250k and 2M grid cells for the same simulation snapshot quoted above. For these three cases, in Figure 4.2, we plot the viewing-angle averaged post-merger evolution of the mean EW of the Balmer absorption lines Hβ, Hγ, and Hδ, which we will use for K+A selection. The absolute difference in this quantity at our times of interest for K+A selection is less than 12% between the low resolution and our fiducial setting, and less than 2.5% between our fiducial and the high resolution setting. The K+A lifetime we calculate in all three cases is the same to within 0.5%.

In addition, the K+A selection criteria among different observations are not

identical, and the method we employ here (§5.3.2) is not a perfect match to any one observational scheme. Unlike many approaches, we do not fit stellar templates to our spectra, and owing to our spectral resolution limitations, we do not attempt to disentangle the absorption component of the Balmer lines from the emission component. Thus our EW measurements can be thought of as essentially the sum of the (signed) emission line flux with the absorption line flux, and differ in this fundamental way from those of, for example, Zabludoff et al. (1996), when emission is present. When the remnant becomes absorption dominated, as for poststarburst galaxies, our models capture the line evolution faithfully. Future enhancements to our input spectral models will be used to improve upon these measurements.

Another future improvement will be to include in the merger models a realistic treatment of gas recycling during stellar evolution. In the simulations presented here, a fixed fraction of gas (0.1, representing ejecta from Type II supernova) is returned instantaneously to the ISM as part of the stochastic mechanism used to form stars. However, the complexity and short timescales of gas infall in a merger imply that the evolution of star formation during and immediately after coalescence will be sensitive to the amount, rate, and temperature of gas returned to the ISM from stars formed during the burst. Moreover, a significant fraction of stellar mass is returned the ISM on long timescales via stellar winds, further motivating the use of accurate gas-recycling methods in studying merger remnants such as K+A galaxies.

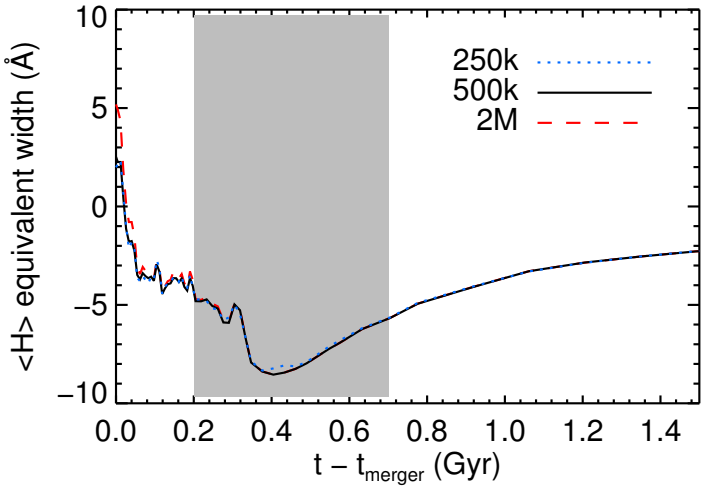

Figure 4.2.—: Here we demonstrate the relative invariance of our lifetime calculations to the resolution of the radiative transfer grid. We show the same simulation used for row a) of Figure 4.4 and row b) of Figure 4.5 using three different grid refinement settings. The black curve is the setting used throughout the rest of this paper, and we find that quadrupling the number of cells for a representative snapshot does not dramatically alter the line strength evolution during our times of interest; the gray box is where our fiducial cut might select this simulation as a poststarburst galaxy. The K+A lifetimes are the same to within a few percent (when all other parameters are fixed). Note that our definition of equivalent width has absorption as negative values.

4.3 Initial Studies

In this section we apply the above method to a variety of galaxy merger simulations to study their general properties. Our systematic study of merger parameters follows in §4.4.

In §4.3.1 and §4.3.3, we describe the basic output of our pipeline: the spectral line evolution of each simulation and the "K+A lifetime". We point out in §4.3.2 that stellar bulges stabilize some merging galaxies against K+A creation after their first passage. In §4.3.4, §5.6.3, and §4.3.6 we employ SUNRISE to study in detail the effects of viewing

angle, dust, and aperture size on K+A selection for several simulations. The influence of AGN feedback is discussed briefly in §4.3.7.

Note that in what follows, we take the convention that equivalent widths in absorption are negative.

4.3.1 K+A Light Curves

The fundamental output of our procedure in §4.2 is a catalog of line strengths at all times during a simulation. We keep catalogs for 7 viewing angles and for our 4 spectrum models as described in §4.2.3. An illustration of this output is shown in Figure 4.3, where we compare the evolution of these line strengths to the global star formation history in the GADGET simulation. We plot the data for a single camera angle and our default Spectrum A. In general, the star formation histories of our merger simulations range between those that look like row (a) and those that look like row (b). The only difference between these two simulations is the relative orientation of the merging disks at the start of the simulation. Thus, as we vary all merger parameters, we expect to see a wide variety in the strength and duration of the K+A spectral features.

This forms a key result that we will focus on in §4.4: a merger between a given pair of progenitor disks produces a "maximal" K+A galaxy only a fraction of the time, because the K+A features require a particular strength and shape to the star formation history.

For mergers that do not drive a substantial starburst, for example row (a) of Figure 4.3, obvious star formation continues well after the nuclei merge. In the spectra we measure, the [O II] emission line strength does not drop to zero even after $\sim$ Gyr

(and cosmological accretion may drive star formation at near-constant levels), and our average of the three Balmer lines ($\beta,\ \gamma,\ \delta$), $\langle H \rangle$, does not exceed 3Å in absorption. For mergers that drive a massive burst, e.g. row (b), the gas is efficiently funneled to the center, where it is either consumed into stars or thrown out by violent feedback. This sequence of events leads to a rapid decline in the [O II] and Balmer emission line strength, with a nearly simultaneous increase in the strength of the Balmer absorption features as the A stars become the luminosity-weighted dominant stellar component.

For comparison, in row (c), we artificially truncate an isolated star-forming disk (the same disks merged in the first two rows). As has been pointed out by other authors (e.g. Poggianti et al. 1999, and references therein), this demonstrates that a K+A galaxy as we have defined it is not necessarily a post-starburst system, but can instead be formed by rapidly shutting off the star formation starting from a specific star formation rate of $\approx 10^{-10}\mathrm{yr}^{-1}$ (a few $\mathrm{M}_{\odot}\mathrm{yr}^{-1}$ for the galaxy we tested). Other metrics, such as colors, have been used to distinguish the two scenarios (Couch & Sharples 1987), but we do not consider photometry in this work. The reader is encouraged to see Wuyts et al. (2009a), Scannapieco et al. (2010), and J10 for detailed discussions of common observables measured from merger simulations using SUNRISE.

4.3.2 Stellar Bulges

An unexpected property of these line catalogs is the strong effect produced by a stellar bulge. We naively expected that a simulation leading to a major starburst might pass through a single (or no) K+A phase. However, our simulations of mergers between disks with no stellar bulge component experience two significant phases of enhanced Balmer

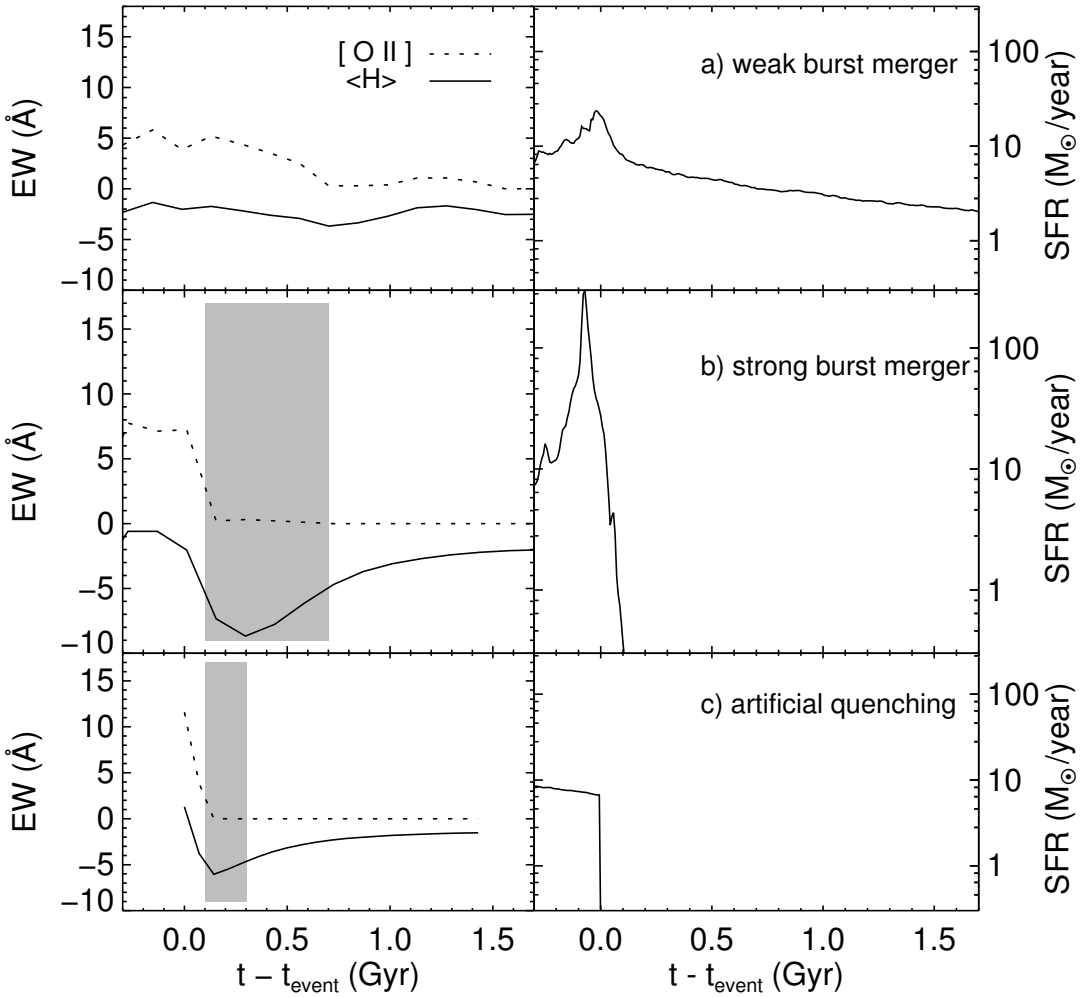

Figure 4.3.—: A summary of different outcomes. *Left:* The evolution of the K+A parameters as a function of time for three representative simulations. The dashed curve corresponds to the [O II] equivalent width measurement, and the solid curve indicates the <H> measurement, the average of the Balmer lines. Emission is positive in these figures. The gray box is where our fiducial cut (-5.5Å) selects these simulations as poststarburst galaxies. *Right:* The global star formation rate as a function of time corresponding to the lightcurves in the left column. *Row (a)* A merger that does not induce a major starburst/shutoff scenario. *Row (b)* A powerful merger-induced starburst leading to exhaustion of the gas supply. *Row (c)* An isolated disk with $f_{bulge} = 0.25,\ f_{gas} \approx 0.4,\ M_{baryons} \approx 5 \times 10^{10} M_{\odot}$, for which we have artificially shut off its star formation at $t = 0$. Scenarios (b) and (c) evolve through a K+A phase.

absorption strength along with reduced emission lines. The first occurs immediately after the first close passage of the two progenitors, and the second occurs where we expected it: after the two nuclei merge and produce a starburst.

Mihos & Hernquist (1994b, 1996) described the effect of a stellar bulge stabilizing the center of a gaseous disk against infall induced during close passages. Since our default measurement mode is to observe the central few kpc of the brightest galaxy in the image, we are particularly sensitive to differences in the star formation history of the central regions of our interacting galaxies. Without a bulge, a close passage of a gas disk to a major companion is enough to incite a transient bar and subsequent burst-quench cycle in its center, even though the galaxy continues to form stars at $\gtrsim 3 M_{\odot} yr^{-1}$. The bulge suppresses these perturbations and preserves more gas for star formation prior to the final burst. The torques experienced during the final coalescence of a major merger are sufficient to destroy the disk regardless of the bulge.

This effect is shown in Figure 4.4, where we merge two identical galaxies that have a moderate stellar bulge. In this case, we preserve the total mass (dark matter plus baryons), but add a stellar bulge equal to 25% of the resulting baryon mass. The dynamics of the two scenarios (different only in the presence of the bulge component) are similar enough that the nuclear gas infall and starburst at the final merger lead to very similar K+A lightcurves after coalescence. Thus, the K+A history of a merger between two disks with significant bulges can be approximated by ignoring the pre-merger lightcurves of a simulation between two bulgeless disks. This is true in all cases where we have mergers both with and without bulges (about 10% of our sample), and we will make use of this result for the sake of efficiency. We note that without bulges, the burst induced by this first passage is highly dependent on the choice of initial disk orientation

(see §4.4.1).

Although K+A galaxies have a slightly higher probability of having a visible companion galaxy ($\sim$ 10% vs. 5% for non-K+A field galaxies; Yamauchi et al. 2008) than ordinary field galaxies, these bulgeless simulations suggest that if all merger progenitors lack a dynamically important stellar bulge, then the companion fraction for K+As should be of order 20-50%. However, a fraction this high is not observed, consistent with the fact that spiral galaxies in the nearby Universe typically contain a bulge.

This companion fraction may increase at earlier times, where potential progenitors may have smaller bulge fractions. In addition, this prevalence of a K+A phase for our late-type mergers between first passage and coalescence supports the assertion that some poststarburst+companion systems are dynamically interacting and not all such systems are a superposition of an interloper with a merger remnant.

4.3.3 Selection Criteria and K+A Lifetimes

In this paper we adopt K+A selection criteria in the [O II] - $\langle H \rangle$ plane, where $\langle H \rangle$ is defined as the mean equivalent width of Hβ, Hγ, and Hδ. This is similar to the cuts used in, for example, Zabludoff et al. (1996). We parametrize our K+A lightcurves by the amount of time that we see a given simulation satisfying a particular set of selection cuts. For the K+A lifetimes presented in §4.3.4 and beyond, we require $W_{[OII]} < 2.0$Å in emission, and $W_{<H>} < x$Å in absorption, where x is an independent variable. In what follows we use $-7.5 < x < -3.5$, where negative values signify absorption. We will refer often to our fiducial cut, where we set $x = -5.5$.

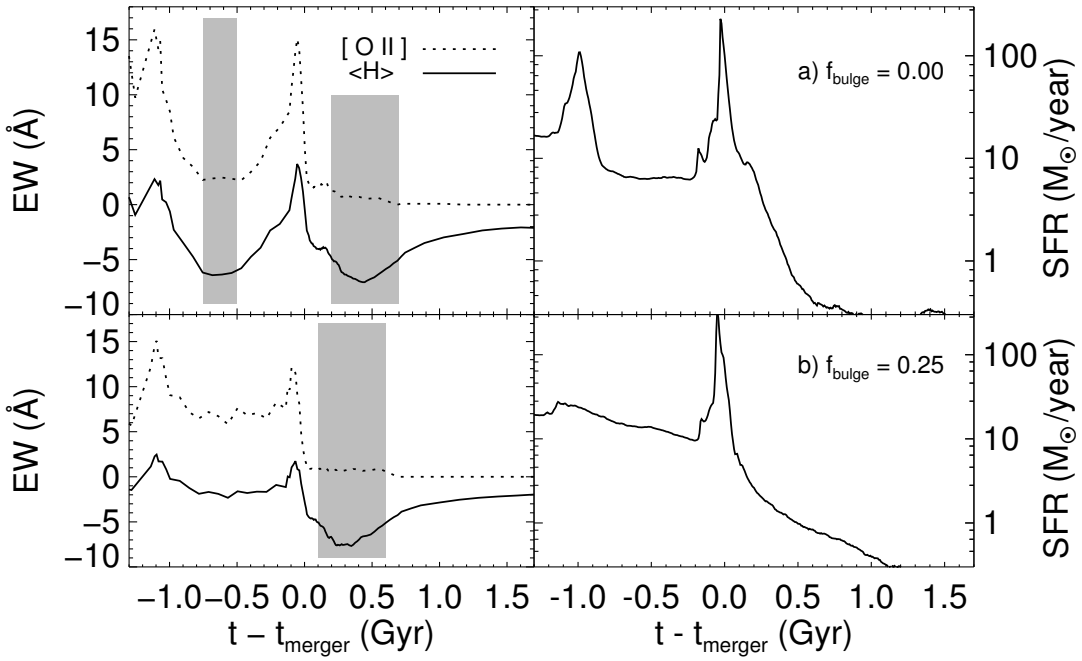

Figure 4.4.—: Demonstration of the effect of bulges on K+A dynamics. *Left:* The evolution of the K+A parameters as a function of time for two merger simulations identical except for the presence of a stellar bulge. The gray box is where our fiducial cut might select these simulations as poststarburst galaxies. The simulation was chosen to be of the "strong burst" type as shown in Figure 4.3, and we use our default Spectrum A as described in the text. *Right:* The global star formation rate as a function of time corresponding to the lightcurves in the left column. *Top:* $f_{bulge} = 0.0$. *Bottom:* $f_{bulge} = 0.25$. The bulgeless merger is a K+A galaxy for more than twice as long as the merger with bulges, inducing a "binary K+A" phase after first passage, at $t - t_{merger} \approx -0.7$ Gyr. Despite the global star formation rate being $\approx 6 M_{\odot} \mathrm{yr}^{-1}$ during this period, the nuclei of the galaxies experience an inflow/burst/quench cycle that happens to dominate the spectrograph aperture. When bulges are present, this inflow is suppressed, yet the final starburst and K+A phase are roughly identical; see Mihos & Hernquist (1994b, 1996) for a discussion of this phenomenon. In our simulations, this behavior of a bulge suppressing the first-passage K+A phase while leaving the post-coalescence phase intact is representative of all mergers that experience a significant burst owing to the first passage of the two disks.

4.3.4 Viewing Angle

A feature of the SUNRISE method that we employ is the ability to vary the viewing angle of our mock observations. Any one of our simulations may correspond to different observed galaxies owing to differing three-dimensional spatial distributions of dust, stellar populations, and AGN relative to the viewing angle.

The placement of our fiber depends solely on the optical flux, so changes in the dust distribution among differing lines of sight will shift the peak of this flux around the image as we vary the viewing angle. Thus the stellar populations intersected by the aperture vary, and the extent to which we see the galaxy as characteristic of a post-starburst will differ. In addition, when more gas is present, star formation may continue at higher levels in various parts of the merger remnant. By looking at images of the merging galaxies, it is clear that in some cases, our aperture intersects the outer regions (for example, a star-forming spiral arm) of one progenitor in front of or behind the center of the one on which we intended to put down the fiber. In other cases, the final burst simply does not exhaust the gas supply sufficiently rapidly, so star forming clumps continue to rain into the center well after the peak of the burst.

In the first column of Figure 4.5, we quantify this effect on the K+A lifetimes for two representative simulations, as well as our artificially truncated disk for comparison, as viewed through a typical aperture (our default Spectrum A). Recall that the different spectra A, B, C, and D are listed in Section 4.2.3 and are calculated simultaneously for every simulation. The uncertainty owing to viewing angle correlates most tightly to the gas mass of the disk. For our major mergers most typical of local spirals (initial $f_{gas} \lesssim 40\%$, or at the time of merger $\lesssim 15\%$), the dispersion owing to angle is of order 10^8

years or less. However, when the initial gas fraction is increased to 80%, this dispersion becomes of order 10^9 years. In Section 4.4 and beyond, we will demonstrate this effect for a wider sample of mergers by plotting this as a measurement uncertainty.

We also consider the isolated disk with its star formation artificially cut off to zero when SFR $\approx 6 M_{\odot} yr^{-1}$: row (c) of Figure 4.5. In this case, the post-starburst component of the galaxy is strongly obscured when looking along the plane of the galaxy, yet easily viewable from higher angles. Here, dust obscuration prevents the younger A star population from dominating the spectrum.

In the second column of Figure 4.5, we include all the light from the system (Spectrum C) to demonstrate that the magnitude of this dispersion owing to dust obscuration is strongly dependent on aperture size. This emphasizes the fact that the dust in these remnants is centrally concentrated owing to the global gas infall experienced during the interaction. We describe the effect of dust in more detail in §5.6.3, and further discuss discuss aperture bias in several simulations in §4.3.6.

We conclude that when considering merger remnants with small amounts of residual gas, viewing angle effects will not introduce significant errors to the inferred stellar populations. However, care must be taken when making conclusions about systems that potentially retain a significant gas reservoir.

Figure 4.5.—: Demonstration of the effect of viewing angle and dust attenutation on K+A selection, emphasizing the fact that the dust in these remnants is centrally concentrated. We measure the length of time we view a simulation as a K+A galaxy using our default selection cuts. Each color represents a single viewing angle that is constant across the panels. *Left:* Our default Spectrum A - measurements made from a spectrum falling within a 3 arcsecond fiber at $z = 0.1$. *Middle:* Our Spectrum C - measurements made with the integrated light of the entire system viewed from different angles. *Right:* Our Spectrum B - measurements made ignoring the effect of attenuation by dust in the diffuse ISM. Each row shows one simulation: (a) gas-rich major merger leading to a strong starburst; (b) identical to (a), except with half the initial gas content; (c) our isolated disk with artificially truncated star formation (the same simulation as row (c) in Figure 4.3). Thus we can measure the dispersion in K+A incidence with viewing angle for each of our simulations: we keep track of this scatter in Figures 4.8-4.11 by plotting its average magnitude as error bars along the top of each panel.

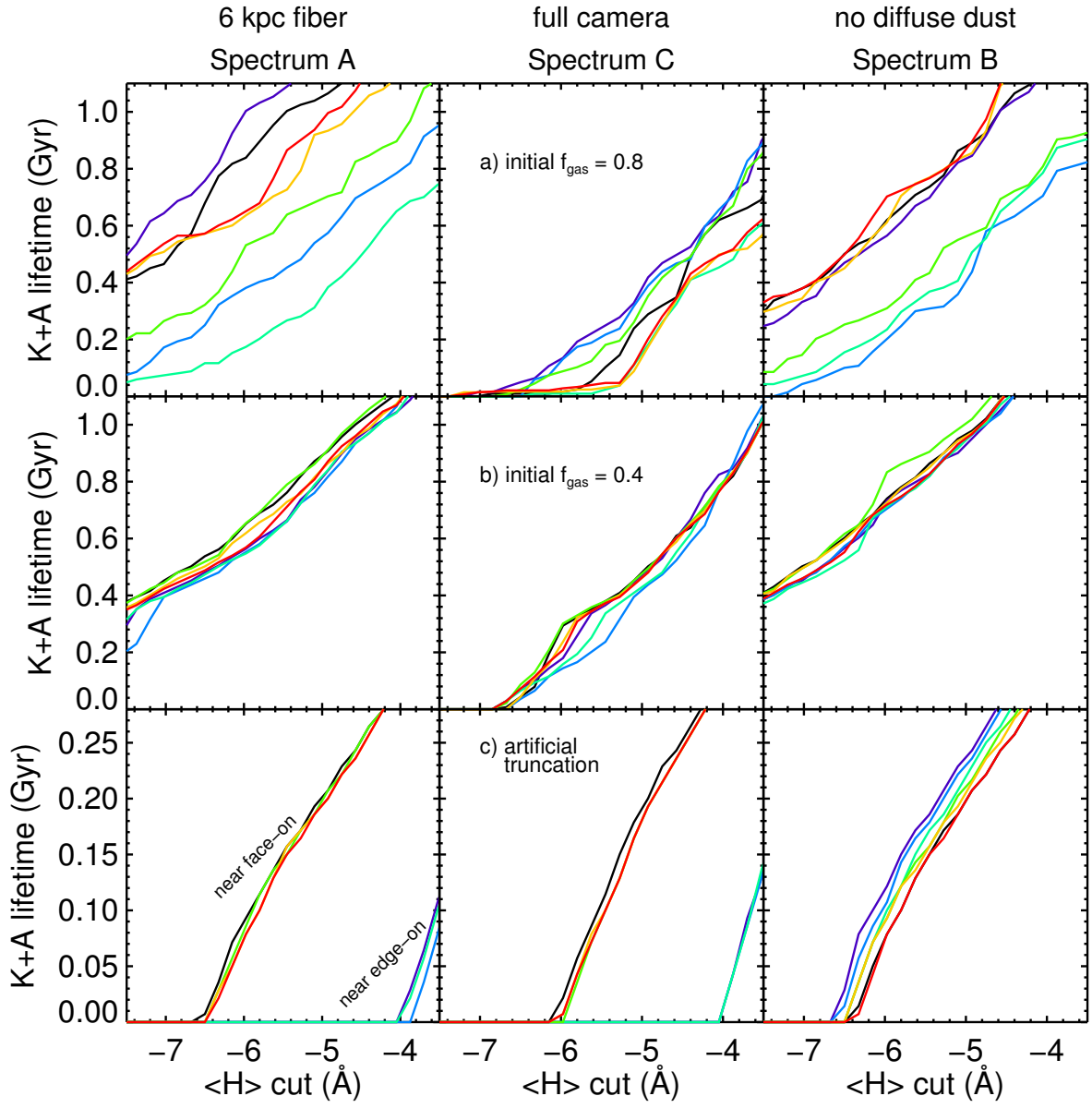

Figure 4.5.—: (Continued)

4.3.5 The Effects of Dust Attenuation

Here we briefly summarize the effect of dust attenuation on our K+A selection within the framework of our chosen subresolution models. See §4.2.2 and §4.2.5 for a more thorough discussion of the underlying ISM modeling and the treatment of dust in dense regions. Given that we track four separate spectra in each of our simulations (§4.2.3) in which we vary both the aperture size and presence of dust in the diffuse ISM, it is possible to make approximate conclusions regarding the impact and distribution of dust.

First off, note that dust influences most aspects of this study. When significant gas and dust is present, dust along a particular line of sight strongly affects the visible K+A lifetime. The pre-coalescence binary K+A phase (§4.3.2) occurs in systems where a gas disk is still intact, so the presence of such a phase is viewer-dependent, and the viewing angle dependence of §4.3.4 depends strongly on the gas (hence dust) content and central location. The visibility and slope of 2-D profiles in the stellar populations (4.3.6) will depend on the dust content and distribution. We argue in §4.3.7 that any poststarburst dependence on AGN feedback owes primarily to expulsion of the gas and dust from the central few kpc.

To see this more explicitly, we plot in the rightmost column of Figure 4.5 the same simulations described in the previous section, except we now ignore attenuation by diffuse dust along each line of sight (Spectrum B). For simplicity, we focus on this single set of simulations, but the same effect exists (though not shown in this work) for all studies of §4.4. In case (a) of Figure 4.5, the merger with a high starting gas fraction of 0.8, the K+A lifetimes are in general a few tens of percent longer for each viewing angle when diffuse dust is included (first column) versus ignored (third column). In these

cases dust serves to obscure [O II]-emitting star forming regions that otherwise disqualify the system as a poststarburst, extending the K+A lifetimes. In addition, we confirm that dust is responsible for the very large line of sight scatter in K+A lifetime seen in Spectrum A for this case. Note that the two separate groups in Spectrum B result from a particular feature in this merger: the true instrinsic scatters of each group are also much smaller than the first column.

However, in case (b) where the gas fraction begins at 0.4, the post-burst phases do not coexist with massive star-forming clumps, so the K+A phase cannot be dramatically extended by dust obscuration of these regions as in case (a). Essentially, the [O II] cut is satisfied with or without the presence of dust. Instead, the primary observable effect is that the diffuse dust obscures the A star population after the final burst and shrinks the K+A lifetimes by up to 10% for each line of sight. Note that this effect may also be present in case (a), but is overwhelmed by the effect of star-forming clumps intersecting the aperture. These tests illustrate that the magnitude and nature of the effect of dust in the diffuse ISM on K+A selection depends in detail on the three-dimensional distribution of the gas and dust with respect to the A star population and star-forming regions.

4.3.6 Radial Profiles and Aperture Bias

In §4.3.4, we showed that K+A lifetimes are shorter when a larger extent of the galaxy is subtended by the aperture, because the fraction of the luminosity falling on the aperture owing to A stars, which are more centrally concentrated than the older stars, is reduced. Thus, generally speaking, all of our simulations are consistent with K+As being the result of a starburst concentrated in the central few kpc.

In the top panel of Figure 4.6 we demonstrate this effect in more detail than is possible with the four types of spectra we will discuss in Section 4.4. We compute the spectrum for a wide range of spectrograph fiber apertures, and show the spatial variation in the poststarburst spectrum. The first (top panel) mimics the effect either of using instruments with differing fiber sizes or using the same fiber at a different distance. The second (bottom panel) mimics the data from multiple pixels available from integral field observations. The radial dependence of the Balmer absorption is not flat in any of the simulations presented here.

The curves in the top panel suggest that with a fixed spectrograph aperture, a K+A selection cut applied at $z < 0.1$ will identify a somewhat different class of object than when it is applied at $z = 0.5$ or higher. The difference in Hδ EW between $z = 0.1$ and 0.5 is ~ 1Å when measuring a strong-burst merger remnant with the SDSS fiber. For the merger simulations (neglecting possibly highly obscured contaminants), a constant EW criterion will typically select a more extreme population at higher redshifts. The effect is opposite for the artificially quenched disk, where an old stellar bulge dominates the spectrum in the very center.

In the bottom panel of Figure 4.6, we demonstrate the ability of SUNRISE to study the galaxy spectra in a spatially resolved way. We plot the spectra of seven 2 kpc-sized pixels along a line near the nucleus of one of our poststarburst galaxies (the one from the solid curve, above). This simulation snapshot is one of our "strong burst" mergers and clearly shows a decline in Hδ absorption as we look farther away from the center.

Figure 4.6.—: *Top:* The $H\delta$ equivalent width of single galaxies measured through different spectrograph apertures. Here we show measurements of two major gas-rich merger remnants (solid and dotted curves), as well as an artificially quenched stable star-forming disk with $f_{bulge} = 0.25$ (dashed curve). Each curve is calculated at a single time in the simulation by measuring the equivalent width of the line using a range of physical aperture sizes (listed in the lower x-axis), and averaging over the viewing angles that give a K+A spectrum. The upper x-axis, the galaxy's "corresponding redshift", is found by fixing the angular radius of the aperture to 1.5 arcseconds (corresponding to the SDSS fiber), and then computing the redshift for which this angle subtends the physical radius given by the lower x-axis. We note that the two merger remnants have similar trends with aperture size (signal weakens with larger diameter), while the truncated disk has the opposite trend at small radii. *Bottom:* We demonstrate the ability of SUNRISE to make integral field spectroscopy maps by plotting the spectrum from seven adjacent pixels in a line near the nucleus of the simulation studied with the solid black curve in the top panel. We can clearly see the strength of the Balmer absorption lines decreasing and older populations becoming dominant as we move away from the center.

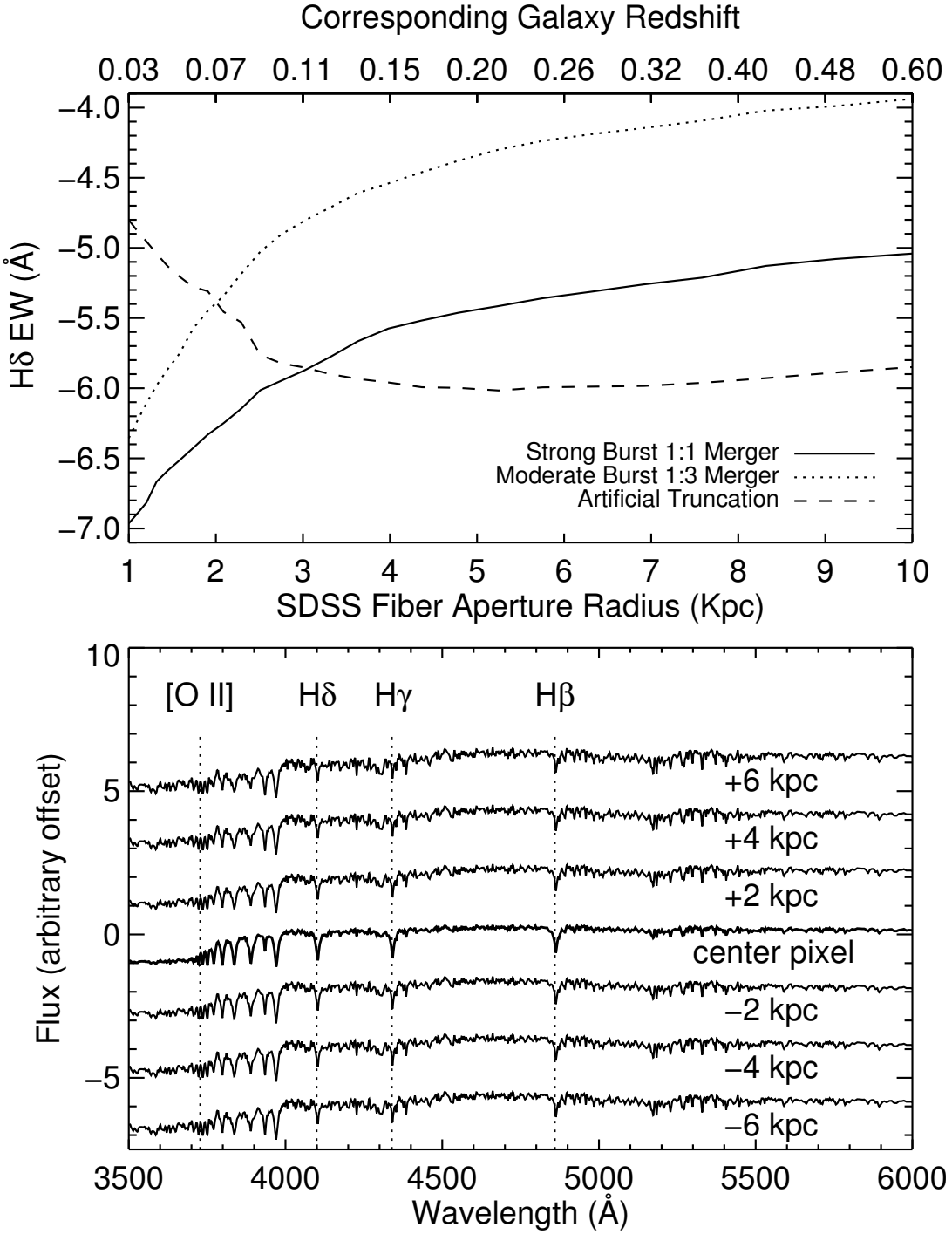

Figure 4.6.—: (Continued)

The gradient is steepest in the central few kpc for this simulated K+A galaxy and many of the ones presented in this paper. Several observational studies (e.g. Goto et al. 2008; Pracy et al. 2009) have used integral field unit (IFU) spectroscopy to study the radial profiles of the Hδ absorption line, with mixed conclusions regarding the presence of a gradient. While we have only studied several simulations in this way, our sample is consistent with a clear increase in Balmer absorption EW towards the center of the remnant. By studying a large number of such simulations, it is possible to estimate what the distribution of gradients is expected to be, and compare in detail with these sophisticated observations, but we leave this endeavor for a future paper.

4.3.7 AGN Feedback

Several studies, such as Wild et al. (2009) and Brown et al. (2009), have explored the connection between poststarburst galaxies and quasar activity. While it is thought that AGN-induced outflows carry relatively little gas mass, it is not clear what the effect of this energy deposition will be on the remaining cold gas and subsequent star formation. Obviously, we have chosen a specific model to approximate these processes, but we can test whether or not it predicts a difference in K+A lifetime from AGN-induced star formation quenching.

Here we briefly demonstrate that in certain cases, the K+A feature depends weakly on the presence or absence of AGN accretion and feedback. In the example we simulate here, the AGN feedback is responsible for dispersing the remaining gas from the central few kpc, reducing the optical depth to the young A star population, thus strengthening the Balmer absorption in the resulting spectrum. Dust-removal is the dominant effect:

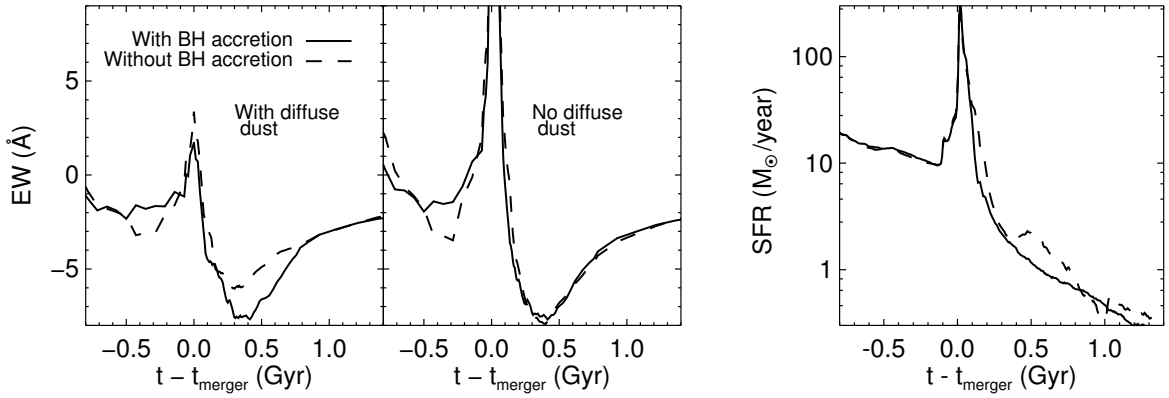

Figure 4.7.—: Here we demonstrate the effect of AGN feedback on the evolution of the Balmer absorption equivalent width. The solid line represents our default simulation (same as in Figures 4.4 and 4.6, 40% initial gas fraction, 25% initial bulge fraction, Milky Way- mass, one-to-one merger) with AGN accretion turned ON. The dashed curve is an identical simulation with AGN accretion turned OFF. We find that the presence of AGN accretion makes almost no difference to the evolution of the post-merger spectrum when obscuration by diffuse dust is not considered (middle panel). However, with a realistic treatment of the surviving dust content (left panel), we see that the case with AGN accretion experiences a longer K+A phase with stronger Balmer absorption than the one without this accretion. We interpret this as AGN feedback dispersing the surviving gas and dust, reducing the optical depth to the young stellar population in the nucleus. In the right panel we plot the global star formation histories of the merger.

the burst shutdown rate and total mass are not changed enough to affect the K+A lines. This result is consistent with Wild et al. (2009) that at least for mergers representative of the low-redshift Universe, the K+A feature is not dramatically affected by AGN feedback.

We repeat one of our commonly-used one-to-one merger simulations with AGN accretion turned off. This merger has 40% initial gas fraction, 25% bulge fraction, stellar mass of $\approx 4 \times 10^{10} M_{\odot}$, and is run on the "e" orbit (see below). In Figure 4.7 we plot the evolution of the Balmer equivalent width as a function of time through the merger, where the black solid line is our default setting, with AGN accretion turned on, and the black dashed line is with AGN accretion turned off completely. We show a single viewing angle that is identical in all cases and plot the global star formation rates for comparison. In the first panel, in which we include the obscuration from diffuse dust, we notice a small (~ 1Å) difference between the cases with and without AGN feedback, where the merger with feedback experiences stronger Balmer absorption lines. This suggests that AGN feedback may be contributing substantially to the star formation quenching.

However, in the second panel of the figure, we see that the unobscured stellar populations with or without AGN are nearly indistinguishable after the starburst. Thus, the slight difference in SFR between the two cases (third panel) is not, by itself, dramatic enough to influence the K+A phase. Instead of directly shutting down the star formation, the AGN feedback serves to remove obscuring dust from near the young stellar population, enhancing the Balmer absorption features. We note that this is only a single viewing angle of a single merger, so further study is needed in order to determine whether this effect has reliable observational consequences. In addition, we leave a systematic study of residual X-ray or LINER emission in simulated K+A galaxies to

future work.

4.4 Systematic Study of Merger Parameters

In the previous section, we analyzed a number of effects that are relevant for understanding the basic output of our radiative transfer simulations. In particular, we quantified the effect of stellar bulges, viewing angle, aperture bias, and AGN feedback. For our fixed choice of physical models, which we argued in §4.2.5 are appropriate for typical local mergers, these effects are dominated by the physical variation in K+A lifetime arising from the variety of late-stage SFHs produced by merging a given pair of disks.

In this section, we quantify this variation as a function of four parameters that define the initial physical setup of the mergers. The four parameters we vary are: (a) relative orientation of the disks: all else equal, this parameter determines how effectively the merger will drive gas to the center of the remnant; (b) total mass of the progenitor galaxies; (c) gas fraction at the start of the merger; and (d) the mass ratio between the progenitor galaxies. A note about gas fractions: real galaxies will accrete matter from the IGM and replenish gas formed into stars, a process we do not include. Therefore, our initial gas fractions must be set higher than observed gas fractions for typical local galaxies. The quantity that should be compared to observed gas fractions is the gas fraction at the time of merger; this ranges between 0-30% for the mergers we consider, consistent with starburst galaxies in the local Universe.

We point out that we have fixed the orbital parameters of the merger such that the

progenitors follow a roughly parabolic orbit with a first pericentric passage at ≈ 7 kpc. Changes to this orbit will likely lead to differing K+A lifetimes and line strengths, but for simplicity we limit our study to this initial condition.

We will assume for the purposes of forming the K+A signatures that the progenitor galaxies have a stellar bulge component that inhibits gas infall owing to a close passage, and consider only the times after final coalescence. From Yamauchi et al. (2008) we have seen that this correction can be as high as 5-10%, but it is within the uncertainties of the merger rates we will be using to estimate the K+A population. The early-type spiral approximation is reasonable for the majority of mergers in the local Universe, but is likely not correct for mergers at high redshift or specific systems that happen to have low bulge fraction at present times.

We present the full data from varying the merger parameters separately in the four Figures 4.8-4.11. In each case, we vary a single one of our four parameters while the other three parameters are held fixed. When a parameter is held fixed, we use the following values: (a) orientation "e" leading to a strong burst; (b) $M_{\rm baryons} = 4 \times 10^{10} M_{\odot}$; (c) $f_{\rm gas,0} = 0.4$; and (d) equal mass mergers. We summarize these trends and provide fitting functions in Section 4.5. For clarity, we focus only on our default spectrum model (Spectrum A).

As we have seen, the intrinsic scatter owing to viewing angle may be large: we plot the standard deviation of K+A lifetime owing to viewing angle, averaged over all simulations, as a function of $\langle H \rangle$ at the top of each figure, and find that it can be as high as 100 Myr. This scatter is a complicated function of both the selection cut and merger scenario. For mergers that produce shorter-lived K+As ($\lesssim 0.3$ Gyr), the scatter

is roughly a constant fraction of the K+A lifetime, and this can be understood as the effect of dust attenuating the lines by a multiplicative factor. The scatter for these short-lived K+A galaxies tends to be larger than for the long-lived ones because the magnitude of the viewing-angle scatter is directly related to the amount of gas (dust) in the system (Figure 4.5), and for cases considered here, mergers that are efficient at consuming gas tend to make longer-lived K+As. We point out that on average, the viewing-angle scatter is relatively low (less than $\sim$0.05 Gyr in all cases) when considering galaxies selected by our fiducial cut of $\langle H \rangle < -5.5$.

4.4.1 Disk Orientation

We assume that the relative orientation of disk galaxies in the Universe on large scales is essentially a random variable, as is the viewing angle for which we observe any given galaxy: the merger rates are not fundamentally different for any subset of these tests, and so our simulations here characterize the scatter in K+A lifetime for a given merger event. However, the merger rate does depend on total mass, mass ratio, and gas fraction (parameters b-c), so ultimately we will use the results from the orientation study to constrain the mean K+A incidence for the remaining parameters.

As shown in Figure 4.8, mergers between otherwise identical disks can produce a very wide range of K+A lifetimes, with a spread of over 500 Myr at our fiducial Balmer cut. These are the simulations in which we vary only the relative orientation of the progenitor spin vectors. These orientations are labeled as letters b-p at the top of Figure 4.8, and the exact parameters can be found in Table 1 from Cox et al. (2006a).

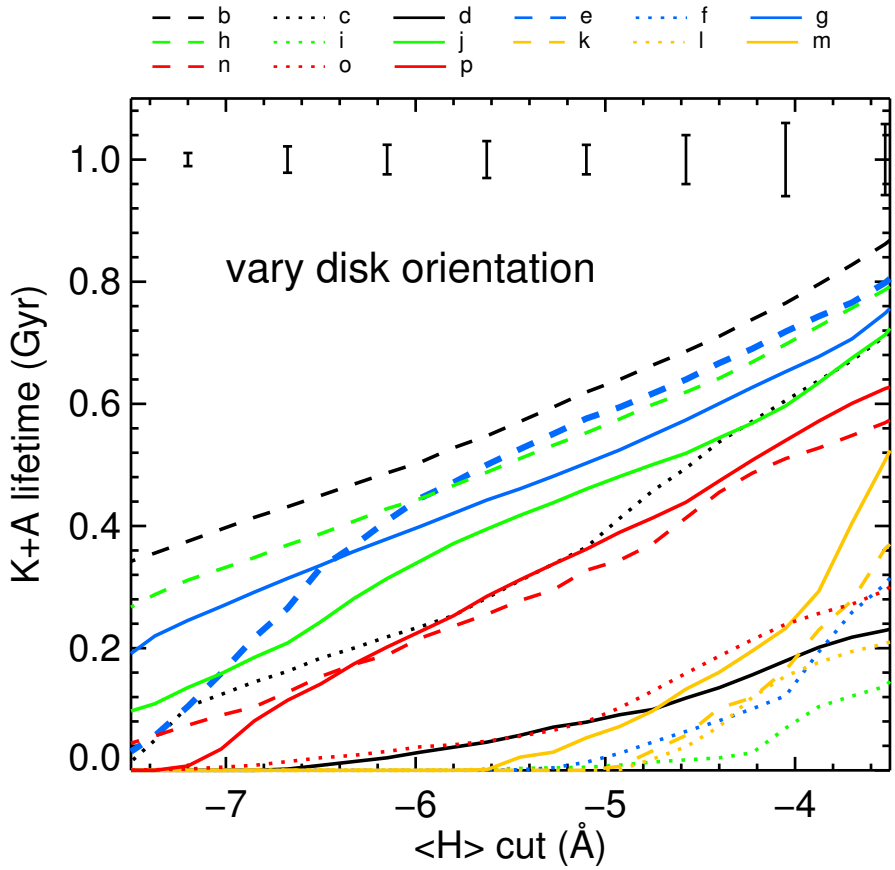

Figure 4.8.—: We plot K+A lifetime measurements using Spectrum A (the default) as described in the text, demonstrating the dramatic effect that different orbital configurations have on the duration of the ensuing K+A phase. Here we vary the initial disk orientation of the galaxies, while keeping fixed the mass of the progenitor galaxies ($M_{baryons} = 4 \times 10^{10} M_{\odot}$), the gas fraction ($f_{\rm gas,0} = 0.4$), and the mass ratio (1-1 mergers). We assume that all progenitor galaxies for major mergers have bulges that inhibit the binary K+A phase prior to final coalescence. Relaxing this assumption would lead to a set of simulations with an even larger spread in K+A lifetimes owing to the orbit-dependent nature of the burst after first passage. The bars along the top represent the standard deviation in K+A lifetime (total length = 2σ) owing to viewing angle, averaged over this set of simulations, as shown by Figure 4.5 for single cases. Note: these bars do not represent the scatter between the curves plotted here.

Orientations b-h are commonly found in the literature and include special ones like the "prograde-prograde" h merger, while orientations i-p are from Barnes (1992) and chosen so to be unbiased initial conditions. These vectors are expected to be broadly sampled by real galaxies, and we see from the spread in the figure that both of these orbit subsets span nearly the full range of K+A lifetimes. We conclude that a given otherwise identical pair of gas-rich progenitors can merge to produce a wide variety of K+A lifetimes.

In fact, the mean K+A lifetime inferred by this study is $\approx 0.2 \pm 0.05$ Gyr, roughly a factor of 5 smaller than the 1 Gyr typical of canonical estimates! For mergers of the disks presented in Figure 4.8, our fiducial cuts find K+A lifetimes longer than 0.3 Gyr only about 50% of the time.

In general, the long-lived K+As are ones in which a rapid, strong burst occurred, consuming much of its gas and producing an A-star dominated spectrum. The short-lived K+As experienced a relatively less violent burst, preserving more gas throughout the merger and creating a weaker signature in the remnant stellar population. The dust column will be higher in these galaxies and will tend to more strongly obscure the K+A signal. This gives a shortened observed lifetime and contributes to the separation between classes suggested by Figure 4.8a. This can also be seen by comparing Figure 4.11a to 4.11b.

4.4.2 Progenitor Mass

To isolate the mass dependence, five simulations were run with a single disk orientation (the "e" orbit in Figure 4.8), and with a single initial gas fraction (0.4), but with a total mass spanning a factor of ~ 100. One complication is that in real galaxies, properties

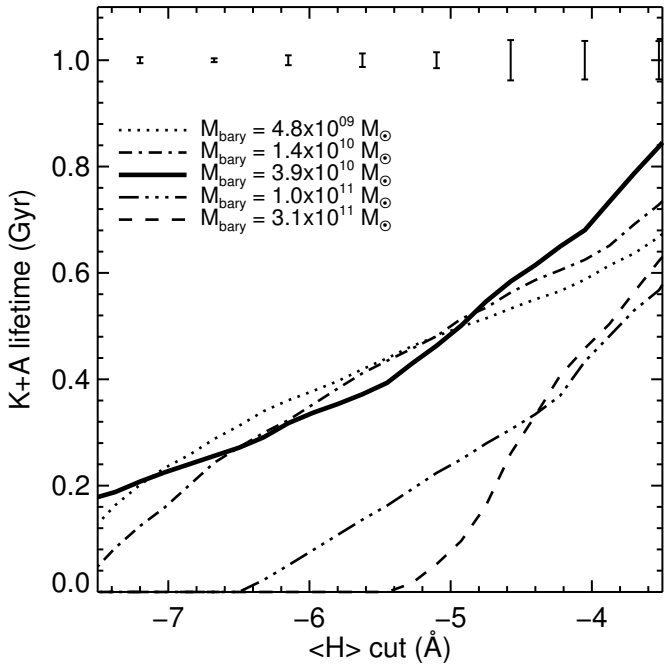

Figure 4.9.—: Similar to Figure 4.8 except we now fix the orientation (e) and initial gas fraction, but vary the total mass of the merging galaxies. The bars along the top represent the standard deviation in K+A lifetime (total length = 2σ) owing to viewing angle, averaged over this set of simulations, as shown by Figure 4.5 for single cases. Note: these bars do not represent the scatter between the curves plotted here.

such as the mass, gas fraction, and bulge fraction are correlated. However, including all the relevant coupling actually makes the results of such a study harder to interpret. By isolating these dependencies systematically in this 'one at a time' fashion, as we have done here, we hope to gain some physical insight into the real behavior of galaxies.

In the total baryon mass range $5 \times 10^9 - 5 \times 10^{10}$ $M_\odot$, the strength and duration of the post-merger K+A signature does not vary much (Figure 4.9), if anything declining slowly with larger mass. Above roughly 10^{11} $M_\odot$, the post-merger K+A lifetimes decline rapidly. This result may seem counter-intuitive because we have fixed the gas fraction and thus expect the burst fractions to be of the same order or larger. However, the K+A

features are sensitive not only to the total burst fraction, but also the detailed shape of the burst star formation history. The star formation histories of the most massive mergers we simulate are in fact characterized by an extreme burst that may be as large a fraction of total mass as the low-mass cases.

However, this extreme burst occurs primarily in the mode of a monotonic decrease of global star formation, leading to an efficient, rapid merger. The final "starburst" in these cases is significant, but not distinct enough to form a long-lived K+A galaxy. By contrast, the less massive mergers experience a burst that better resembles what we might expect for making K+A galaxies: an enhancement followed by a rapid decline in star formation.

We note that the trend of K+A lifetime at high masses does not strongly affect predictions made about the populations observed in large surveys, which will be dominated by significantly more populous lower-mass galaxies.

4.4.3 Gas Fraction

The trend as a function of gas fraction is shown in Figure 4.10. At $f_{gas,0} = 0.8$, the mean K+A lifetime as seen by our aperture is ~ 100 Myr shorter than for $f_{gas,0} = 0.4$. However, here we do not simulate many mergers with gas fractions as high as 0.8, so it is not clear if this trend will actually turn over for the galaxy population as a whole. We might expect this to happen, as extremely gas-rich merger remants have been shown to reform substantial disks in some cases (Robertson et al. 2006a; Hopkins et al. 2009e), and our result is then consistent with the picture that mergers with disky remnants experience shorter and less-robust K+A phases. As we showed in §4.3.4, a large range

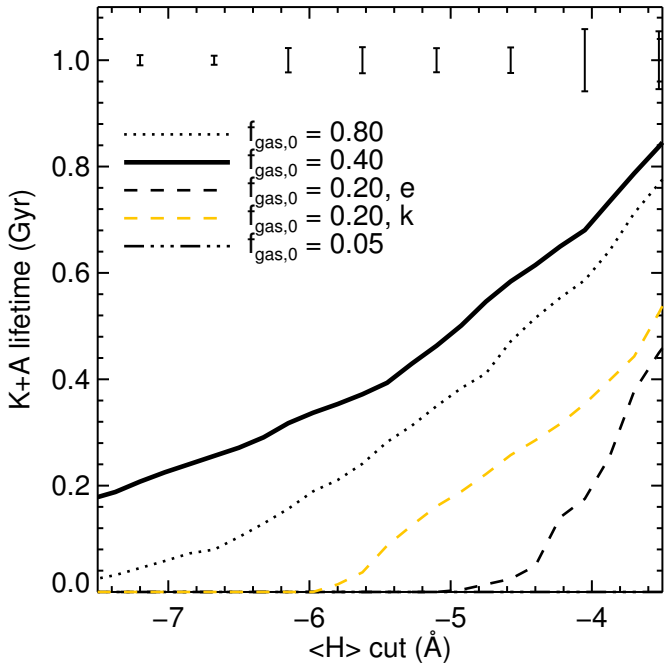

Figure 4.10.—: Similar to Figure 4.8 except we now fix the orientation (e for all and k for one case) and total mass, but vary the initial gas fractions of the progenitors. The bars along the top represent the standard deviation in K+A lifetime (total length = 2σ) owing to viewing angle, averaged over this set of simulations, as shown by Figure 4.5 for single cases. Note: these bars do not represent the scatter between the curves plotted here.

of K+A lifetimes will be seen when the gas fraction is this high, with star formation often occurring at high levels after the merger, and high dust column densities obscuring various parts of the burst/post-burst stellar populations.

When the gas fraction is lower, we recover an expected behavior. Since the gas reservoir at the time of merger defines an upper limit to the burst mass fraction, for low gas fractions at merger ($\lesssim 0.1$) the resulting starburst will not contribute enough to the spectrum to look like a strong K+A galaxy.

4.4.4 Merger Mass Ratio

Since equal-mass mergers are uncommon, we also consider a number of unequal-mass scenarios. We define the parameter μ as the ratio of the baryon mass in the more massive galaxy to the baryon mass in the less massive galaxy. In Figure 4.11, we plot the K+A lifetimes for a variety of merger mass ratios. In addition, we consider a second initial disk orientation in order to get a better idea at how this changes the results.

The K+A lifetime falls off very quickly as we increase μ: on average, three-to-one mergers live as a strong K+A (EW < -5.5Å) for $\lesssim 100$ Myr and ten-to-one mergers $\lesssim 20$ Myr (though note the high variance with viewing angle). As with equal mass mergers, different orientations introduce a strong dispersion in K+A lifetimes.

Mergers with a high mass ratio tend to make weaker starbursts (see Hernquist 1989; Hernquist & Mihos 1995; Hopkins et al. 2008d; Cox et al. 2008), owing to the mass-dependence of the response to tidal forcing (D'Onghia, E., et al. 2010), and this is reflected in the shorter mean K+A lifetimes for these scenarios. In addition, when a K+A signature is detected for a high-mass-ratio merger, it is often from a single viewing angle (out of seven), and for a single simulation snapshot at a single crossing between the galaxies (out of several). This leads to rather unpredictable behavior when the interaction is weak, likely in part because the remnants are more disky than the major merger counterparts and hence the burst population experiences greater dust attenuation from certain viewing angles. Moreover, our method of placing the spectrograph fiber on the peak of the surface brightness leads to noisy measurements as the interactions proceed. The small bursts in these interactions create stellar populations with complex three-dimensional motions and luminosities that vary rapidly with time.

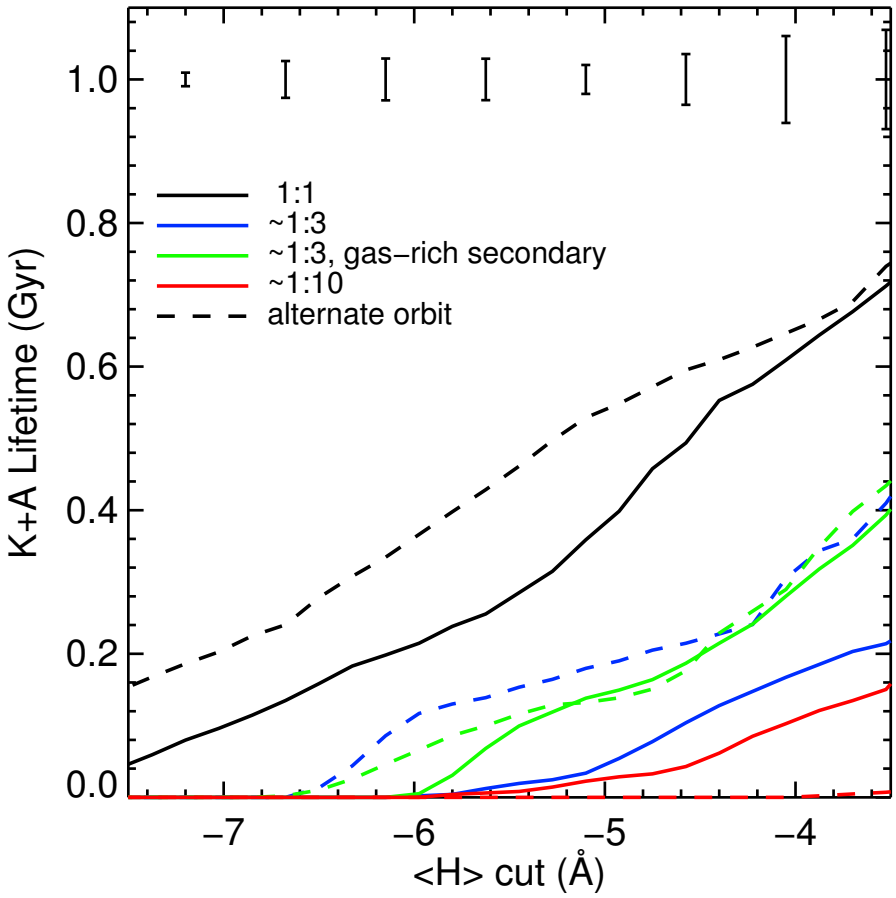

Figure 4.11.—: Similar to Figure 4.8 except we now fix the orientation (e) and initial gas fraction, but vary the mass of one galaxy to demonstrate the trend of decreasing K+A lifetime with increasing merger mass ratio (§4.4.4). Solid and dashed curves represent different initial disk orientations that lead to a strong-burst merger when the masses are equal. *Black* - 1:1 merger, companion $f_{gas,0} = 0.4$. *Blue* - 3:1 merger, companion $f_{gas,0} = 0.4$. *Green* - 3:1 merger, companion $f_{gas,0} = 0.8$. *Red* - 10:1 merger, companion $f_{gas,0} = 0.4$. In each case the more massive galaxy has a baryonic mass of $2 \times 10^{10} M_{\odot}$. Here we give all the merging galaxies bulges, so the tidal forcing owing to first passage is not sufficient to incite a K+A phase in any of them. Thus for simplicity we plot the entire evolution of the merger up to ~ 3 Gyr after first pericenter, allowing us to measure the response to multiple passages in the minor mergers. The bars along the top represent the standard deviation in K+A lifetime (total length $= 2\sigma$) owing to viewing angle, averaged over this set of simulations, as shown by Figure 4.5 for single cases. Note: these bars do not represent the scatter between the curves plotted here.

4.5 Summaries and Fitting Formulae

We show a summary of the trends with the selective parameters mass, gas fraction, and mass ratio, averaged over viewing angle and disk orientation in Figure 4.12. We will focus on our fiducial K+A cut, which is shown as the filled circles.

One conclusion to draw from this systematic study is that mergers produce a wide variety of K+A behavior, even when the gas content and structure of the progenitor disks are not changed. The lifetime of this phase is not limited to a fixed single value for all mergers of the same two disks. In particular, only gas-rich major mergers ($\gtrsim 10\%$ gas fraction at merger) of specific initial disk orientations generate a strong K+A signature ($\gtrsim 5.5$Å EW in Balmer absorption) for a substantial fraction of an A star lifetime. We find that mergers reproduce canonical estimates of K+A lifetimes of 1 Gyr (e.g. from SSPs) only when the dynamics of the merger lead to a burst that is in some sense "maximal" for producing the K+A spectral features.

This means that the dispersion in K+A lifetime for a merger, given its progenitors, is large (of order 100% in Figure 4.8). However, when comparing to a large population of galaxies at a snapshot in time, we care mostly about the estimate in the *mean* K+A lifetime for a given pair of progenitors, which is known better by a factor of 3-5 because we can average over these 15 possible spin orientations. In Figure 4.12, a bar representing the 1σ scatter owing to disk orientation is shown in the upper left corner, and the corresponding (smaller) standard 1σ error in our estimate of the mean value is shown to the right of it.

In detail, our study in §4.4.1 finds a mean K+A lifetime that is roughly a factor of

five lower than typical estimates of 0.5-1.5 Gyr: here, $T_{K+A} \approx 0.2 \pm 0.05$ Gyr. In the next section we show that this rarity of strong poststarburst mergers is consistent to within a factor of a few with nearby large-volume spectroscopic surveys.

For convenience, we provide example analytic approximations to our general trends that are plotted as the solid black curves in Figure 4.12.

As a function of baryonic mass M above roughly $10^9 M_\odot$, we find that the mean K+A lifetimes for our fiducial selection cut (-5.5Å) follow an exponential:

$$T_M(M_{baryon}) = 0.2 \ \exp\left(-\frac{M_{baryon}}{10^{11} M_\odot}\right) \ \text{Gyr}. \tag{4.3}$$

As a function of baryonic mass ratio μ up to at least $\mu \approx 10$, they follow a power law:

$$T_\mu(\mu) = 0.2 \ \mu^{-1.5} \ \text{Gyr}. \tag{4.4}$$

Most of the simulations we present here have $f_{gas}(t_{merger}) \lesssim 0.35$, so our best-guess values are significantly uncertain beyond this regime. In the figure, we plot two options, one in which there is a turnover in the trend of K+A lifetimes with higher gas fractions, and one where it is nearly flat at higher gas fractions. As a function of gas fraction at the time of merger, the former, which provides a better fit to our simulations and is plotted as a dotted line in the bottom right panel of Figure 4.12, is approximated by a log-normal curve:

$$T_f(f_{gas}) = 0.034 \log_{10} \mathcal{N}\left(l_0, \sigma, \right) \tag{4.5}$$

$$= \frac{0.045}{x} \exp\left(-\frac{\left(\log_{10}(x) - l_0\right)^2}{2\sigma^2}\right) \text{Gyr}, \tag{4.6}$$

where $l_0 = -0.5$ and $\sigma = 0.3$. The latter option is plotted as a dashed black line in the

figure and is approximated by

$$T_f(f_{gas}) = 0.55 \ \frac{\sqrt{f_{gas} - 0.05}}{1 + f_{gas}} \ \text{Gyr}. \tag{4.7}$$

We derived these trends from a suite of simulations in which we vary only the parameter of interest in the progenitor galaxies. As we mentioned in §5.6.2, the trend with galaxy mass may be related to the fact that our more massive mergers have differing gas fractions at the time of merger coalescence. An added complication is that in real galaxies, these two properties are correlated, so we must be careful when combining these trends to ensure that we aren't mis-counting their effects. Thus, an appropriate combination of these trends may be one in which we take the gas fraction to be the driving parameter over the mass, e.g.:

$$T(f_{gas}, \mu) \approx 0.2 \ \text{Gyr} \frac{\mathrm{T_f(f_{gas})}}{0.2 \ \text{Gyr}} \frac{\mathrm{T}_\mu(\mu)}{0.2 \ \text{Gyr}}. \tag{4.8}$$

In the next section, we use these trends to estimate the K+A fraction given merger rates from an independent source.

Figure 4.12.—: Summary of K+A lifetime trends with merger mass, gas fraction, and mass ratio. This strong dependence on progenitor properties drives down the expected per-merger K+A duration, leading to better agreement between K+A abundances and independently-inferred merger rates (Figure 4.13). All points are taken from the data in Figures 4.9, 4.10, and 4.11, and the distribution of lifetimes with disk orientation from Figure 4.8 has been used to estimate the trends for the other disk pairs, assuming that the orientation is a uniform random variable selected from the 15 considered in this work. The filled circles correspond to our fiducial K+A selection cut ($\langle H \rangle \leq -5.5$Å), and the curves, which are described in Section 4.5, represent analytic approximations to these points only. The scatter in lifetime for a specific merger owing to different disk orientations is $\gtrsim 100\%$ (Figure 4.8), completely dominating the scatter owing to other physical effects such as aperture bias and viewing angle. To show this, we plot a bar representing this dominant intrinsic scatter (total length = 1σ) in the upper left of the first panel. The smaller bar placed next to it represents the standard error in the estimate of the mean K+A lifetime averaged over the spin orientations obtained by dividing the larger error bar by $\sqrt{15}$. The size of this scatter is the same to within 30% for all three selection cuts. We do not plot the scatter owing to viewing angle. In the two panels on the right, the four gas fraction cases are the same. The only difference is that we have shifted the value of f_{gas} to reflect the typical gas fraction at merger for each case (note: the $f_{gas,0} = 0.8$ case is sampled most sparsely in our simulations, and so both the K+A lifetime and $f_{gas}(t_{merger})$ are more poorly constrained).

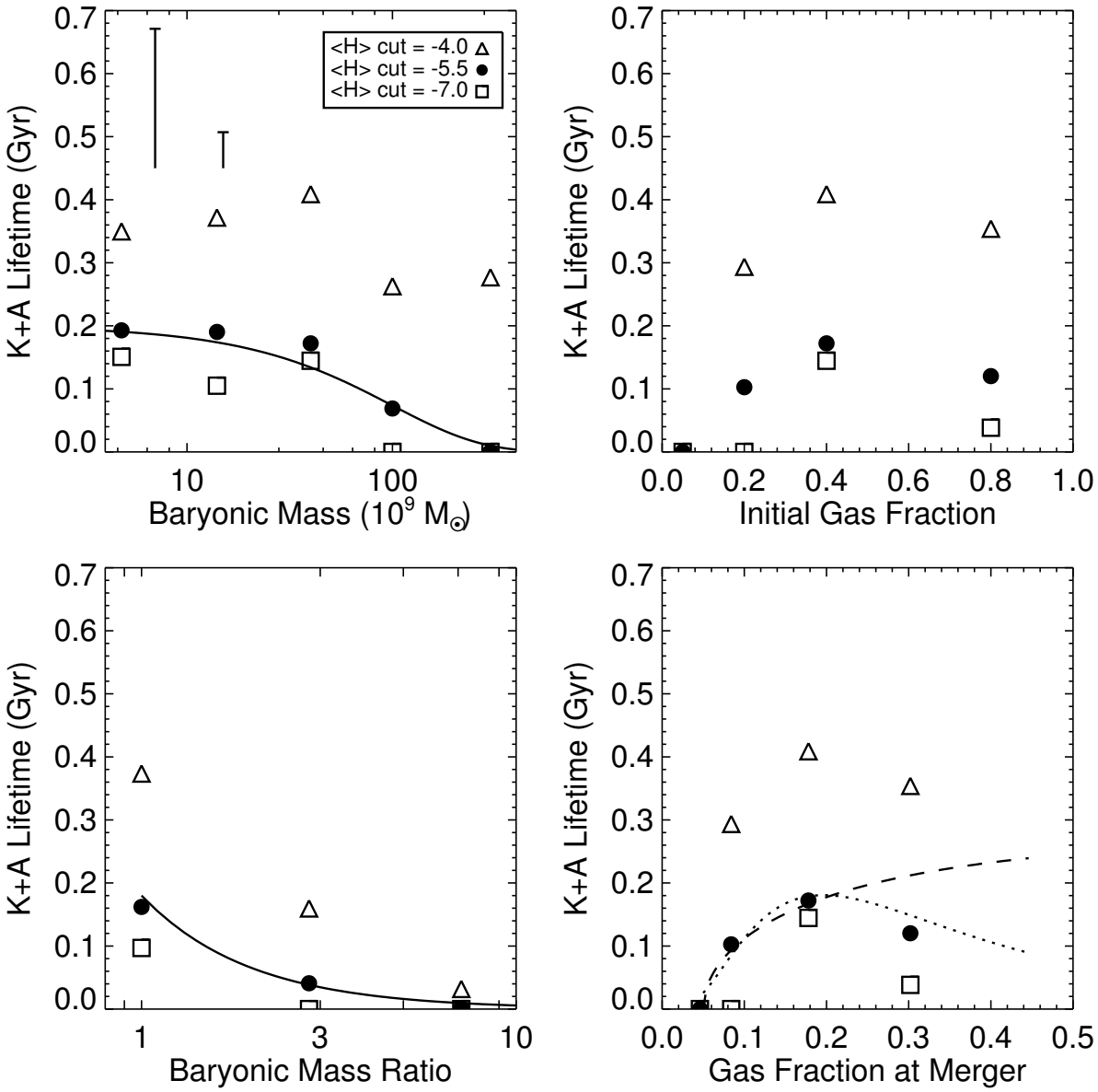

Figure 4.12.—: (Continued)

4.6 Implications for the K+A Fraction

Here we use our lifetime calculations to make a crude estimate of the fraction of all galaxies that are seen as merger-induced K+As. To calculate this number, we combine our estimated distribution of K+A lifetimes with semi-empirical merger rates. Thus we must know or estimate the following: (1) The K+A lifetime for every pair of possible interacting galaxies above some mass (flux) limit for a comparison sample, and (2) The merger rate for any given pair of these galaxies at the redshift of interest. Note that number 2 will change when the prevalent progenitor galaxy properties do, but number 1 is fixed by our calculations for a given pair of galaxies.

4.6.1 Merger Rates

For item (2), the merger rates, we use the semi-empirical models from Hopkins et al. (2010b,c). These models calculate the merger rate per galaxy per Gyr by applying empirical constraints to the halo occupation distribution (HOD) of possible merger progenitors.

We limit our analysis to merger remnants with $M_{\rm baryons} > 10^{10}$ $M_{\odot}$ and use the median rates quoted in Hopkins et al. (2010b) for this mass range, because the merger rates are significantly less certain for lower masses and the nearby spectroscopic samples have mass limits of this order.

A crude example of our calculation, undertaken in more detail in what follows, is to multiply a characteristic K+A lifetime by the merger rate. In the previous section, we found a rough mean lifetime of $\lesssim 0.2$ Gyr for major mergers. The Hopkins et al. (2010b)

models indicate that the median major ($\mu < 3$) merger rate for galaxies in this mass range is 0.04 galaxy^{-1} Gyr^{-1} at $z = 0.1$. This implies a rough K+A incidence of

$$\begin{aligned} &\approx (0.2 \text{ Gyr})(0.04 \text{ galaxy}^{-1}\text{Gyr}^{-1}) \\ &= 0.008 \text{ galaxy}^{-1}. \end{aligned}$$

Note that our K+A lifetime per merger must still be significantly overestimated, because the K+A fraction inferred from large-scale spectroscopic surveys is ~ 0.001. This is because we have not yet taken into account the trends of K+A lifetime with merger parameters, e.g. (most importantly) the merger mass ratio. Note that the canonical K+A lifetime of $\sim$ Gyr, which furthermore does not take into account the dispersion with orbital parameters, would overestimate this fraction even more significantly.

4.6.2 K+A Fraction Estimation

A more accurate calculation must take into account the trends derived in §4.5, because (for example), 3:1 mergers have a lower characteristic K+A lifetime than do 1:1 mergers. The three merger parameters we consider are the primary ones from §4.3: the total baryonic mass $M_{\rm gal}$ of the merging system, the gas fraction f_{gas} at the time of merger, and the baryonic mass ratio μ.

We define the K+A lifetime to be the time the galaxy spends with $\langle H \rangle < -5.5$Å, our fiducial cut, which is similar to the limit imposed in many observational samples. To estimate (1), ideally we should simulate a complete sample of possible mergers and apply directly our methods to each one. In §4.4 we performed these calculations for the *axes* of the three-dimensional merger parameter space that we considered, where we take the gas fraction, mass, and mass ratio as the salient properties, plus a range of disk

orientations, for a total of ≈ 40 simulations. To sample our entire space with a similar quality requires of order ~ 1000 more, so in order to reduce the computational expense, we limit ourselves to a rough approximation using the information we already have. We expect that little more would be gained by calculating the complete sample.

The general trends with each of our merger parameters are readily seen in Figure 4.12, so we make the assumption that these trends extend to the unsampled sectors of the parameter space. For a single simulation in detail, this assumption is obviously incorrect. To see this, compare the "k" orbit from Figure 4.8 to the "e" orbit for 40% gas in Figure 4.10 to the ones with 20% gas in Figure 4.10. However, for the parts of our study where we have extended the sample in larger numbers (e.g. Figure 4.11), the trends hold to within the scatter owing to viewing angle.

An example of this extrapolation was shown in Equation 4.8. For the calculation here, we also include a term expressing the mass-dependence. However, this may not be appropriate in all cases, owing to the previously-mentioned (§5.6.2) coupling between the mass-dependence and the gas fraction-dependence. Luckily, the steepness of the mass function in comparison samples renders our estimate of the K+A lifetime trend at the highest masses unimportant. If we assume instead a flat K+A lifetime curve with mass, thus assuming that mass and gas fraction are approximately uncorrelated, our K+A fraction estimates in what follows increase by at most $\sim 10\%$.

We generate a K+A fraction in the following manner:

$$f_{K+A} = \frac{N_{K+A}}{N_{gal}} = \int p(\mathbf{X})\, T(\mathbf{X})\, R(\mathbf{X})\, d\mathbf{X}, \tag{4.9}$$

where $\mathbf{X}$ represents the full space of merger parameters. $p(\mathbf{X})$ is the fraction of all merger pairs, which we estimate from observations or set by hand, represented by the specific

choice of parameters $\mathbf{X}$; this quantity has $\int p(\mathbf{X})\, d\mathbf{X} = 1$, and includes information about the observed merger mass function from Hopkins et al. (2008c), and the the gas fraction distributions at $z \sim 0.1$ and 1.0 from Lin et al. (2008).

The quantity $T(\mathbf{X})$ is the K+A lifetime derived from this work for the specific merger $\mathbf{X}$, averaged over the initial disk orientation. Where we have simulations, we use the values from Figure 4.12. Where we do not have direct simulations, we construct T by assuming that the trends in Figure 4.12 extend trivially to the untested scenarios (e.g. Equation 4.8). This introduces uncertainty into our calculation, because we cannot be certain that there is not a dramatic departure from these trends.

$R(\mathbf{X})$ is the merger rate per galaxy per gigayear from Hopkins et al. (2010b), and depends on $\mathbf{X}$ only insofar as we have ignored such dependence in choosing $p(\mathbf{X})$. We make the approximation that the universal merger rates at a given redshift depend only on $M_{\rm gal}$ and μ, but not separately on the gas fraction. Since we have chosen to consider a fixed mass range for which the merger rates are compiled, the rates we apply will depend only on μ.

The absolute merger rates for all mergers with $\mu > 10$ are about twice that for "major" mergers ($\mu > 3$) alone, but the K+A lifetimes of the major mergers are $\gtrsim 2-5$ times that for minor mergers (§4.4.4) using these definitions. Thus we might expect that the local K+A population is composed of roughly equal numbers of major and minor merger remnants.

Within the "major" merger range, our lifetime estimates are still rather different between $\mu = 1$ and $\mu = 3$, so we need an estimate of the relative size of each population. For this purpose, we simply choose two test values by hand to demonstrate the sensitivity

of our models: $N_{\mu=3} = 3N_{\mu=1}$ or $N_{\mu=3} = 20N_{\mu=1}$. This choice of major merger mass ratio distribution has an effect at a factor of ~ 2 level, because this is the corresponding ratio in the K+A lifetime calculations.

Since our lifetimes also depend strongly on f_{gas}, we need to apply an estimate of the gas fraction distribution in our mass range of interest. To calculate $p(f_{gas})$ as a function of redshift, we assume gas fraction distributions roughly consistent with observed gas-rich/gas-poor merger fractions from Lin et al. (2008). These observations are in good agreement with semi-analytic models, e.g. Khochfar & Burkert (2003), for halo masses of $\sim 10^{13} M_{\odot}$.

For $z \approx 0.1$, where observations suggest that the total mass density in the mass range of interest is split roughly equally between gas-rich disks and gas-poor ellipticals, we assume that merger progenitors are 50% ellipticals and 50% spirals, and strongly prefer gas fractions at merger that are $\lesssim 0.1$. We assume that gas-poor mergers do not form K+A galaxies (this cutoff occurs at roughly $f_{gas} = 0.05$ for our simulations). At $z \approx 1$ for these masses, the observed gas-free merger fraction is $\sim 10\%$, and gas-rich mergers account for almost 70% of interactions (mixed mergers accounting for the rest). We assume that typical galaxies at this redshift have gas fractions of 0.2 by putting 50% of mergers into this bin.

We note that the estimates from Lin et al. (2008) correspond to a mass range somewhat higher than the ones that dominate our comparison samples, so the values we take of the gas-rich merger fraction are probably somewhat conservative. In addition, the choices we make of the gas fraction bins in which to put each type of merger are meant to be reasonable, but not necessarily precise. Changes in the exact details of the gas

fraction distribution produce K+A fractions that vary within the uncertainties of other parts of our modeling. A more thorough calculation can be done using such estimates, but we leave this for a more precise study.

We interpolate between our two redshift points to plot the K+A fraction as a function of redshift in the solid black line of Figure 4.13. Such a curve should be thought of as the average merger-induced K+A fraction in all environments at a given redshift. Note that a predicted merger-induced K+A fraction below the observed one is not necessarily problematic, since there may be additional sources of K+A creation such as ram-pressure stripping or other quenching mechanisms.

The gray box represents the 0.5 dex believable range of our best-guess model. This quantity comes from uncertainty in the merger rates Hopkins et al. (2010b) in conjunction with the standard error of the mean K+A lifetimes shown in §4.5. We plot $0.0 < z < 1.2$, but we do not attempt to account for aperture bias, and as noted above, our accounting for gas fraction evolution is a crude one (and we do not account for things like bulge mass or morphological sub-type).

4.6.3 Comparison to Surveys

Above, we described our method for estimating the K+A fraction at $z = 0.1$ and $z = 1.0$. At $z \approx 0.1$, our procedure yields a K+A fraction of roughly 10^{-3}, and the K+A fraction we estimate at $z \approx 1$ is 0.7%, almost an order of magnitude higher than at $z = 0.1$.

For comparison, we plot in Figure 4.13 the K+A fraction with associated measurement uncertainty quoted from a number of spectroscopic surveys. We acknowledge the complications of this approach as pointed out by Yan et al. (2009)

and other authors, especially the fact that each survey uses different selection criteria, has different flux limits, and is affected in different ways by cosmic variance and environmental effects. For instance, the Poggianti et al. (1999) sample has a less stringent EW requirement than we consider here. Combining our models with a detailed cosmological framework, it is possible in principle to account for such effects, but we defer this more sophisticated study to future work. However, even with this basic approach we are able to reproduce some expected results as a rough check of our approach.

At $z \approx 0.1$, our models imply that a large fraction of the K+A population in large-sky surveys such as the Las Campañas Redshift Survey (LCRS, Shectman et al. 1996; Zabludoff et al. 1996) and SDSS (York et al. 2000; Goto 2007a) can be accounted for by mergers. This rough correspondence follows directly from one phenomenon: that the K+A lifetimes exhibit strong dependence on the merger scenario. The population of mergers experiences significant variation in K+A incidence that depends strongly on (at least) orbit, gas fraction, and mass ratio. As we showed above, removing these dependencies leads to a predicted K+A fraction much higher than observed.

Between $z = 0.1 - 1.0$ in the field, our example calculation demonstrates strong redshift evolution in the K+A fraction. Our curve falls somewhat below the surveys at $z \gtrsim 0.2$, though still within reason given the uncertainty in the models, and this might be expected if there is important progenitor evolution in mass, typical environment, bulge fraction, or if the evolution in typical gas fraction is more extreme than we assume. In fact, as redshift increases, we expect that the progenitor galaxies in corresponding surveys will be somewhat higher in mass and later in type than lower-redshift surveys. Both of these effects could serve to steepen the predicted curve by up to a factor of 2 each toward higher redshift. Another steepening effect may be aperture bias: in

Figure 4.6 we saw that a typical decrease in observed $\langle H \rangle$ signal between $z = 0.1$ and $z \sim 1$ (at fixed aperture size) is ≈ 1Å. The appropriate comparison is between the filled circles in Figure 4.12 and the squares (a stronger cut, which is required at higher redshift to select the same galaxies). We see that this could be an effect at the level of a few tens of percent. In addition, the other mechanisms for creating a K+A phase may account for some of this difference.

Figure 4.13.—: An estimate of the K+A fraction owing to merger-induced star-formation quenching as a function of redshift, for which we find general agreement with similarly-selected samples. This implies that a typical merger lives as a K+A galaxy for much shorter than the canonical 10^9 years, bringing the K+A-inferred merger rate up to ones estimated by other means (Hopkins et al. 2010b). The black solid line is our estimate when we assume that one-to-one mergers are three times rarer than three-to-one mergers, and is approximated by the relation $f_{\rm K+A}(t) \propto e^{2(z-0.1)}$ (red dotted curve), importantly reflecting a significant increase in K+A abundance as z increases. The dashed black line is when we set this factor equal to 20; note that this choice only leads to at most a factor of 2 difference. The gray shaded region represents roughly the 1σ confidence region of the model result, taking into account the uncertainty in the merger rates summed in quadrature with the scatter in the mean K+A lifetime from this work (each a factor of ~ 2 for a total ~ 3, or 0.5 dex). The points and error bars reflect survey data and their corresponding measurement uncertainty, with each survey using their own selection criterion. Error bars for the large local surveys LCRS and SDSS are lower limits to the uncertainty in the fraction computed as $1/\sqrt{N_{K+A}}$, and all other error bars are as supplied by the authors. All surveys have somewhat different depth limits, corresponding crudely to 10^{10} $M_\odot$ of stellar mass, and this is the cut we use in the merger rate estimates from Hopkins et al. (2010b). Where a survey is given two points, we plot both the "bright" and "faint" or total sample provided in the referenced paper. Our selection criteria mimic most closely the LCRS (Zabludoff et al. 1996) and SDSS (Goto 2007a) survey points. A weaker cut may be more appropriate for some of the surveys for which an $H\delta$ cut of ≈ 3Å was applied; for instance, Poggianti et al. (1999), since we include both their "k+a" and "a+k" classes in the plotted point. Figure 4.12 suggests that a factor of two correction to our model curve may be appropriate in this case (this would be insufficient). However, our models are much more uncertain in this regime, because a much larger class of mergers can cause such a signal, so we have focused primarily on ones that can satisfy our fiducial cut.

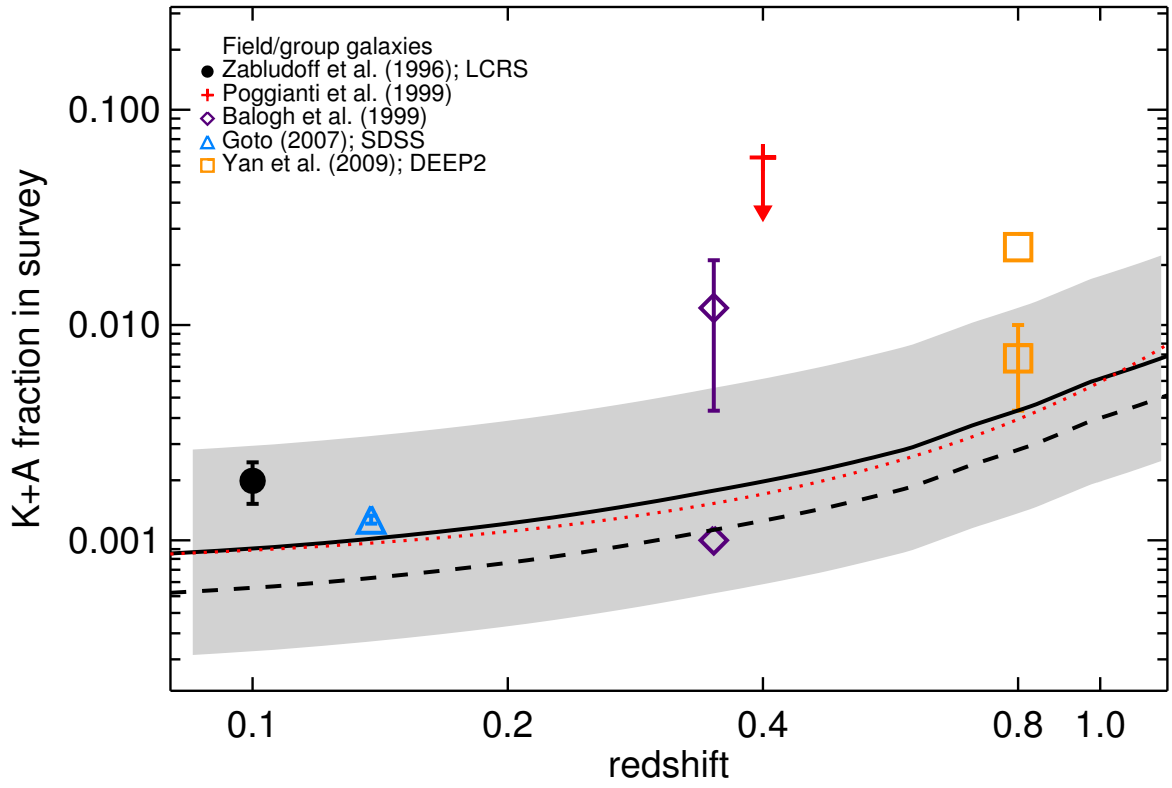

Figure 4.13.—: (Continued)

4.7 Discussion

It is believed that the K+A criteria select galaxies where star formation has recently and rapidly shut down owing to interactions with other galaxies and/or with a cluster environment. The probability of becoming a K+A galaxy is increased if the galaxy experiences a period of enhanced star formation prior to the quenching, as opposed to the rapid truncation of a low level of continuous star formation. Mergers and interactions are a natural way to create these star formation histories. We have studied this process through a large suite of three-dimensional hydrodynamic simulations coupled with the three-dimensional radiative transfer code SUNRISE, and we discuss the implications of our results in this section.

4.7.1 Poststarburst Merger Models

In combination with Wild et al. (2009), this work tested the idea that K+As arise, in many cases, via galaxy-galaxy mergers. Ultimately, measurements of K+A abundances should be reconciled with realistic models for their formation and event rates. The observed K+A abundance fraction among different samples is relatively robust insofar as the K+A selection criteria are uniform (though the lack of this uniformity is one of our uncertainties). However, realistic models for K+A events, specifically their duration, must be used in order to infer any information about the merger or event rate and hence the evolutionary context of these systems. We have demonstrated an order-of-magnitude calculation that explicitly takes this into account, specifically calculating the K+A incidence with physical merger scenario, and we showed in §4.4 that the lifetime of the K+A phase is a strong function of both merger orbit and progenitor properties.

In particular, the relative orientation of the spin vectors of the merging disks can be varied to create post-merger star formation histories with a wide variety of Balmer absorption strengths and lifetimes. This scatter with disk orientation represents a physical scatter in the mean K+A lifetime for a given pair of disks of 0.3 dex. The K+A lifetime is maximum for equal-mass mergers and for gas fractions at the time of merger between $\sim 0.1 - 0.2$, but fall of sharply at lower values. Minor mergers can also lead to a short, viewer-dependent K+A phase (§4.4.4). While major mergers produce a more robust, longer-lived K+A phase, the relative quantity of minor mergers versus major suggests that the contribution to the merger-driven K+A population may be split roughly equally between major and minor.

Thus, we find that the average maximum K+A lifetime for the merger of a given pair of disks is *at most* $\approx 0.2 \pm 0.05$ Gyr, a factor of at least several below the canonical lifetime often assumed to be ~ 1 Gyr. This is because not every merger event generates these canonical star formation histories. By allowing that not every gas-rich merger produces a K+A galaxy of order 1 Gyr, a fixed observed K+A abundance implies a greater merger rate than a calculation that assumes a lifetime of ~ 1 Gyr. For example, using a 1 Gyr duration, Quintero et al. (2004) infer a K+A event rate of order 0.01 per galaxy per gigayear at $z \sim 0.1$, a factor of several below the lower limit merger rate of ≈ 0.04 per galaxy per gigayear from Hopkins et al. (2010b), suggesting that if the latter rate is correct and the typical K+A lifetime is ~ 1 Gyr, then there are too few K+A galaxies by at least a factor of a few.

To reconcile the two, we have estimated the redshift evolution of the merger-induced K+A fraction implied by our simulations in §4.6 and Figure 4.13, using the merger rates of Hopkins et al. (2010b). For simplicity, we considered the strict selection cuts of

Zabludoff et al. (1996, e.g.), so that the observed K+A fraction at $z = 0.1$ is $\sim 10^{-3}$. The model calculation has a large scatter of ~ 0.5 dex, but we find broad agreement with large-area nearby ($z \lesssim 0.2$) spectroscopic samples that use similar selection cuts, suggesting that K+A abundances are consistent with a predominantly merger origin.

4.7.2 Implications for Merger-Induced Evolution

This result has significant implications for the physical mechanism behind the growth of bulge-dominated galaxies. For example, this lower characteristic duration per event at fixed abundance implies that a correspondingly larger number of galaxies have passed through this phase. The mean K+A lifetime of our simulations, weighted approximately to the cosmological progenitor abundances and appropriate for this selection, is ~ 0.02 Gyr per event. This implies that since $z = 1$, $\sim 40\%$ of galaxies have experienced a K+A phase, however briefly. Thus, many merger remnants spend a great deal of time outside of the traditional K+A spectral cuts, a consequence that is not too surprising, given the continuous population of galaxies in the "poststarburst spur" in Zabludoff et al. (1996); Yan et al. (2009) and hints that post-burst populations may exist outside the typical selection regions (e.g. Quintero et al. 2004; Yan et al. 2009).

Furthermore, the short-lived merger-induced K+As may be ones that experience less bulge growth than the long-lived ones. Preliminary evidence suggests that the diskiest merger remnants in our simulations also experience the shortest K+A phases, consistent with the picture put forth by, for example, Barnes (2002) and Robertson et al. (2006a), that the merger remnant of gas-dominated disks will have a greater disk component. Our limited experiments at high gas fraction showed that the K+A phase is shorter when the

gas content is large ($\gtrsim 40\%$) at the time of merger, in general agreement with the fact that the star formation halts less suddenly, or not completely, in these systems.

Hence, further study is warranted to better predict results for or interpret surveys of evolving galaxies at higher redshifts. Although gas-rich progenitors and mergers are more common at $z > 1$, we have seen that the K+A incidence is a complex function of the gas content, mass, and mass ratio of the merging pair, and the re-formation of gaseous disks will certainly play a larger role during the epoch of peak galaxy assembly at $z \gtrsim 2$. Thus care must be taken to correctly interpret poststarburst abundance measurements in upcoming higher-redshift surveys.

4.7.3 Resolving the Geometry and Dust

Our combined hydrodynamics and radiative transfer approach allows us to study in detail the physical evolution of galaxies and their components through the K+A phase. Roughly temporally coincident with a significant central starburst, SMBH accretion and feedback, and a rapidly-evolving ISM, merger-induced K+A galaxies result from violent events that are more accurately produced by fully three-dimensional physical models. Using such models, we have begun to study the effects of dust attenuation, spatial bias, and SMBH accretion on poststarburst galaxies in the context of realistic mock observations of physically-motivated simulations.

These studies fall into roughly two categories: one, understanding systematic observational effects such as aperture bias and viewing angle, and two, varying the physical setup, such as progenitor properties and models used to evolve the structure of the ISM, e.g. forming stars, accreting gas onto the SMBH, and allowing for feedback.

Since mergers lead to centrally-concentrated starbursts, we have quantified the effect of changes in the spectroscopic fiber aperture between $\approx 1 - 10$ kpc on several simulated galaxies in §4.3.6, and shown that a change of order ~ 1Å in $\langle H \rangle$ is expected. This property may distinguish merger-induced K+As from, for example, ones induced by ram-pressure stripping where smaller or inverted gradients may be expected.

Dust attenuation and viewing angle can introduce large variations in the perceived strength of K+A indicators, especially when the gas content is large. In particular, any diffuse dust that survives tends to obscure the central young stellar population and weaken the poststarburst signature. The scatter in the K+A durations induced by this effect is about three times smaller than the one owing to initial disk spin orientation §4.4.1, and the overall reduction in K+A lifetimes is an effect at the level of a few tens of percent (see Figure 4.11).

The presence of a stellar bulge suppresses the formation of poststarburst signatures caused by relatively weak perturbations such as those induced during the first passage of a merger in certain orbits (§4.3.2), and this picture is broadly consistent with K+A pair fractions from Yamauchi et al. (e.g. 2008). This effect is dominant in a small aperture of ~ 6 kpc versus the integrated spectrum. Combined with knowledge of galaxy structure such as bulge fractions, spatially-resolved observations compared to simulations such as these may provide further constraints on the properties of merger progenitors.

In some cases, the presence of AGN accretion and subsequent feedback strengthens the K+A signature of the merger remnant (Wild et al. 2009, and §4.3.7). The mergers that produce strong starbursts leading to a K+A galaxy are also ones in which much gas is funneled to the center of the coalescing remnant, so merger-induced poststarburst

galaxies are likely ones that also experienced significant AGN activity. For the simulations we consider here, the effect of AGN feedback is limited. The "shutdown" we see is dominated by simple exhaustion of the gas supply and/or feedback related to the starburst itself. This is consistent with Wild et al. (2009), who found that reducing the feedback strength from the central black hole did not substantially alter the poststarburst properties of such mergers. However, in at least one example, we find that AGN feedback produces a stronger K+A phase ($\sim$ 1Å EW enhancement) of longer duration (perhaps up to $\sim 50\%$) than simulations without. We conclude that the AGN energy disperses dust and gas remaining in the nucleus and assists in uncovering the A-star population. The systematic comparison of the K+A strength distribution to a large suite of simulations may place constraints on the strength and nature of AGN feedback.

Several modeling approximations were made in order to calculate the spectrum of simulated galaxies. These include a subresolution treatment for the H II and PDR regions surrounding young stars as well as for the state of the ISM within each resolution element. An important free parameter is $f_{\rm PDR}$, which governs the covering fraction or clearing timescale of the molecular birth clouds of young stars. We chose to use $f_{\rm PDR} = 0.3$, corresponding to a clearing timescale of $1 - 2$ Myr, as a reasonable approximation for local merger remnants, where vast quantities of molecular gas are not present. We have also chosen to use the multi-phase breakdown of the SPH gas particles to assign dust masses to either the hot phase or cold phase ISM. We assume that the attenuation of light by the cold phase ISM is captured entirely by the PDR model and so we do not use the cold phase mass to calculate additional dust attenuation. In §4.2.5, we discussed several examples where we have varied these assumptions to see their effect, which is substantial in certain cases.

4.7.4 Context of Present Simulations

In work leading up to the present, similar simulations have been used to quantitatively demonstrate that galaxy mergers contribute to the populations of $z = 0$ ellipticals (Springel et al. 2005a; Cox et al. 2006a; Hopkins et al. 2006b, 2008a), warm ultra-luminous infrared galaxies (ULIRGs) at $z \approx 0 - 1$ (Younger et al. 2009), dust-obscured galaxies (DOGs; Narayanan et al. 2010b) and submillimeter galaxies (Narayanan et al. 2009, 2010a; Hayward et al. 2011b,a) at $z \gtrsim 2$, and quasars at various redshifts (Hopkins et al. 2005a, 2006a; Hopkins & Hernquist 2006; Li et al. 2007). Here, we have shown that K+A galaxies fit within the same framework. In particular, we have studied the idea that poststarburst galaxies are predominantly remnants of galaxy-galaxy interactions. Their properties are such that they will likely evolve into passive ellipticals, and these simulations show that mergers of gas-rich disks are likely contributors to the K+A population, supporting the picture that mergers play a significant role in driving late-time galaxy evolution. Thus, the work here supports the general picture framed by e.g. Hopkins et al. (2006a, 2008c); Somerville et al. (2008) that these various phenomena are connected in an evolutionary sequence.

Additional evidence for this general scenario can be seen in the form of a fossil record preserved in the structural and kinematic properties of local early type galaxies. For example, it has recently been shown that the light profiles of gas-rich merger remnants (Hopkins et al. 2008b), ellipticals with central cusps (Hopkins et al. 2009a), and ellipticals with cores (Hopkins et al. 2009c) all show evidence of being two-component systems, with an inner relic starburst left over from a gas-rich merger (Mihos & Hernquist 1994a). These findings can additionally explain the link between the various types of elliptical

galaxies (Hopkins & Hernquist 2010b), the contribution of merger-induced starbursts to the star formation history of the Universe and the infrared background (Hopkins et al. 2010a; Hopkins & Hernquist 2010a; Hopkins et al. 2006c), and the relationships between supermassive black holes and their host galaxies (Hopkins et al. 2007a,b). The present work reinforces the conclusions derived in these studies by making an explicit connection between the immediate descendants of gas-rich mergers and the population of old elliptical galaxies.

4.8 Conclusions

We calculated rest-frame optical spectral line catalogs of binary galaxy merger remnants using 3-D Monte Carlo dust radiative transfer calculations applied to fully 3-D hydrodynamic simulations. Using these, we have studied the properties of poststarburst (K+A or E+A) galaxy models in an attempt to understand them in a context of hierarchical galaxy evolution. We summarize here our key findings:

1. We tested the hypothesis that mergers of spirals contribute meaningfully to the population of K+A galaxies. We find that realistically-simulated major merger remnants commonly satisfy traditional K+A spectral line selection cuts (§4.3), and quantified the extent to which each of a large suite of merger scenarios satisfies those cuts (§4.4).

2. The K+A lifetime is sensitive to nearly every property of the merging progenitors, including gas fraction, mass ratio, and especially the configuration of their orbit in space (§4.4.1). This follows from the fact that merger dynamics exhibit a

continuum of starburst properties, from short and violent events to more prolonged bursts.

3. Typical durations of the K+A phase as commonly defined are $\lesssim$ 0.1–0.3 Gyr for the merger of equal-mass gas-rich progenitors (§4.5), significantly shorter than the often-assumed value of $\sim$ 1 Gyr.

4. The shortness of the typical merger-induced K+A phase owes to the fact that not every merger orbit leads to a major, succinct starburst, even when certain configurations of the same progenitors do so. Thus, the canonical model of a K+A existing for about 10^9 years is appropriate only for the relatively few cases that the merger dynamics cause a sufficiently significant increase and/or sufficiently rapid cessation of star formation.

5. These results reconcile measured K+A abundances with independently-calculated merger rates (§4.6, §4.7.1). By assuming that all gas-rich mergers satisfy the K+A criteria for 1 Gyr, one underpredicts the merger/event rate by up to an order of magnitude. By accurately accounting for how the K+A lifetime depends on physical merger scenario, as we have done here and for which we provide approximate fitting formulae in §4.5, we find that the inferred merger/event rate is consistent with other estimates. Furthermore, our model estimates of the K+A abundance as a function of redshift (Figure 4.13) reflect a rapid increase from $z = 0$ to $z \sim 1$.

6. The subresolution treatment of dust attenuation remains a significant uncertainty during parts of the merger when much gas and dust is present (§4.2.5). However, we believe our choices to be reasonable for the vast majority of K+A galaxies

simulated here, because most of the time they are relatively dust-poor. The effect of dust attenuation within our chosen subresolution framework is small and characterized throughout §4.3 and §4.4, and summarized briefly in Figure 4.11 and §4.7.3.

7. The role of AGN feedback in truncating star formation to produce the K+A features in these simulations is minimal. The energy released by rapid merger-induced accretion onto the SMBH expels the now centrally-concentrated gas and dust from the merger remnant, slightly enhancing the visibility of A stars produced by the starburst, but does not alter the star formation enough to be observable in the unobscured K+A signature. However, this work focused primarily on local analogues and a single feedback model, warranting further study.

With our suite of realistic merger simulations, we have gained insight into how merger-induced poststarburst galaxies evolve and depend on their progenitors and physical models. We have described and executed a method for deriving the true poststarburst lifetimes of merger remnants and reconciled K+A abundances with independently-estimated merger event rates. Such techniques can valuably constrain the paradigm of merger-induced galaxy evolution by generating observationally-consistent predictions for the properties of evolving galaxies. For example, semi-analytic modeling, based on approximate fitting formulae such as the ones we have provided here for K+A incidence, could be used to gain insight into related questions. Future work with similar techniques is warranted to disentangle the underlying causes of galaxy evolution, constrain physical models, and to inform observations and theories of galaxy formation at ever-higher redshifts.

Specifically, the role of AGN versus star formation and gas consumption in the formation of ellipticals can be probed by varying the physics applied in large suites of merger simulations (e.g. Wild et al. 2009) and comparing them in detail to observations of the structure (Yang et al. 2008), metal abundance (Norton et al. 2001), AGN luminosity and SED (Brown et al. 2009), AGN/starburst ratios (Yuan et al. 2010), and ISM properties (Rich et al. 2010) of K+A galaxies, LIRGs, ULIRGs, and others. The complex state of the gas and stars in galaxies, mergers, and their remnants may depend on the precise nature of AGN and stellar feedback mechanisms, the details of gas recycling by stars, and the physics of the ISM, so that such observations and simulations can together provide useful constraints on the underlying physical models. For comparisons at higher redshift, mergers between more gas-dominated disks with a turbulent ISM structure can be simulated so that we may interpret correctly observations of mergers and their remnants during the epoch of peak galaxy assembly.

Chapter 5

Assembly of the Red Sequence in Infrared-Selected Galaxy Clusters from the IRAC Shallow Cluster Survey

G. Snyder, M. Brodwin, C. M. Mancone, G. R. Zeimann, S. A. Stanford, A. H. Gonzalez, D. Stern, P. R. M. Eisenhardt, M. J. I. Brown, A. Dey, B. Jannuzi, & S. Perlmutter

The Astrophysical Journal, Vol. 756, No. 114, 2011

Abstract

We present results for the assembly and star formation histories of massive ($\sim L^*$) red sequence galaxies in 11 spectroscopically confirmed, infrared-selected galaxy clusters at $1.0 < z < 1.5$, the precursors to present-day massive clusters with $M \sim 10^{15} M_{\odot}$. Using rest-frame optical photometry, we investigate evolution in the color and scatter of the red sequence galaxy population, comparing with models of possible star formation histories. In contrast to studies of central cluster galaxies at lower redshift ($z < 1$), these data are clearly inconsistent with the continued evolution of stars formed and assembled primarily at a single, much-earlier time. Specifically, we find that the colors of massive cluster galaxies at $z \approx 1.5$ imply that the bulk of star formation occurred at $z \sim 3$, whereas by $z \approx 1$ their colors imply formation at $z \sim 2$; therefore these galaxies exhibit approximately the same luminosity-weighted stellar age at $1 < z < 1.5$. This likely reflects star formation that occurs over an extended period, the effects of significant progenitor bias, or both. Our results generally indicate that massive cluster galaxy populations began forming a significant mass of stars at $z \gtrsim 4$, contained some red spheroids by $z \approx 1.5$, and were actively assembling much of their final mass during $1 < z < 2$ in the form of younger stars. Qualitatively, the slopes of the cluster color-magnitude relations are consistent with no significant evolution relative to local clusters.

5.1 Introduction

A key goal in observational cosmology is to measure the formation and assembly of cosmic structures, a history that can be traced by examining the stars in massive galaxies. The simplest model consistent with many observations is that the stars in massive early-type galaxies (ETGs) formed in a single short burst at high redshift and evolved passively (i.e., with no further star formation) thereafter. The dramatic expansion of data from high-quality wide-area galaxy surveys and deep lookback studies has permitted the rigorous testing of this picture, revealing a more complex formation and assembly history.

Present-day clusters contain a tight red sequence of galaxies, indicating early and uniform star formation histories (Bower et al. 1992). As fossil records of cluster assembly, red sequences were found to evolve nearly passively since $z \sim 1$ (Aragon-Salamanca et al. 1993; Stanford et al. 1998; Muzzin et al. 2008), suggesting negligible ongoing star formation. Their colors imply formation at $z \sim 2$ to 3, and studies at $z \sim 1$ (e.g., Blakeslee et al. 2003; Mei et al. 2006b; Lidman et al. 2008; Mei et al. 2009; Strazzullo et al. 2010) found consistency with this picture. The single short burst model predicts that the red sequences become bluer and wider nearer their formation epoch, a trend found by Hilton et al. (2009) and Papovich et al. (2010) in two clusters at $z \approx 1.5 - 1.6$.

This passive view is brought into question by some observations of clusters at $z > 1$. While Eisenhardt et al. (2008) found that the colors of cluster galaxies at $z < 1$ are consistent with the passive evolution of a group of stars formed in a short burst at $z_f = 3$, the $z > 1$ candidates favor an earlier formation. Mancone et al. (2010) found that cluster galaxies' characteristic $3.6\mu m$ and $4.5\mu m$ magnitudes (from the *Spitzer* Deep,

Wide-Field Survey (SDWFS, Ashby et al. 2009)) evolve in a manner consistent with little mass assembly at $z < 1.3$ (see also, Lin et al. 2006, Muzzin et al. 2008, Rettura et al. 2011), but are systematically fainter than the extrapolation of passive models at $z > 1.3$ (see also, Fassbender et al. 2011).

Furthermore, we now know the red sequence is a snapshot of the currently quiescent galaxies, and that galaxies evolve both on and off during formative events. Such transformations (Butcher & Oemler Jr. 1978; Dressler 1980; Tran et al. 2003; McIntosh et al. 2008) may cause the red sequence's average stellar age to evolve more slowly (van Dokkum & Franx 2001) than predicted by the single-burst model. Therefore, estimates of stellar age from the red sequence color and color dispersion (Bower et al. 1992; Demarco et al. 2010) can provide important constraints on galaxy assembly in clusters.

In this work, we report *Hubble Space Telescope* (*HST*) follow-up imaging of clusters drawn from the infrared-selected sample of Eisenhardt et al. (2008), the *Spitzer*/IRAC Shallow Cluster Survey (ISCS). This survey used near-IR imaging, an excellent proxy for stellar mass, to select structures that are the precursors to today's massive clusters (Brodwin et al. 2007). We directly study their histories by examining the red sequence galaxies in 11 spectroscopically confirmed clusters at $1.0 < z < 1.5$.

In §5.2 we describe the candidate selection and data collection, and in §5.3 we quantify the rest-frame optical color-magnitude relations. We construct simple models for their evolution in §5.4, and we compare these models with our measements in §5.5. We discuss the implications of these results in §5.6 and conclude in §5.7. Throughout this work our observed-frame magnitudes are on the AB system, but for convenience in comparing to previous work we also calculate rest-frame U-V colors on the Vega system.

We assume a flat cosmology with $\Omega_\Lambda = 0.72$ and $h = 0.71$, consistent with Larson et al. (2011, WMAP7).

5.2 Data, Reduction, and Galaxy Catalogs

5.2.1 Cluster Catalog

The *Spitzer*/IRAC Shallow Cluster Survey (ISCS; Eisenhardt et al. 2008) identified cluster candidates spanning $0.1 < z < 2$ over a 7.25 deg^2 area in the Boötes field of the NOAO Deep Wide-Field Survey (Jannuzi & Dey 1999). The clusters were identified as three-dimensional overdensities using accurate optical/IR photometric redshifts (Brodwin et al. 2006) calculated for the 4.5 μm flux-limited (8.8 μJy at 5σ) IRAC Shallow Survey (Eisenhardt et al. 2004) catalog. Thus, the clusters are selected primarily by stellar mass, largely independent of the presence of a red sequence. There are 335 ISCS cluster and group candidates, 106 of which are at $z > 1$. Over 20 clusters at $z > 1$ have now been spectroscopically confirmed with W. M. Keck Telescope and/or *HST* spectroscopy (Stanford et al. 2005, 2012; Elston et al. 2006; Brodwin et al. 2006, 2011; Eisenhardt et al. 2008, Zeimann et al. in prep., Brodwin et al. in prep.).

5.2.2 Imaging and Reduction

In this work we present sensitive, high-resolution *HST* follow-up imaging obtained from a variety of programs (GO proposal IDs 10496, 11002, 11597, and 11663) for a subset of the confirmed $z > 1$ ISCS clusters. In order to construct a rest–frame optical color

magnitude diagram with the most leverage on the galaxies' stellar ages, instrument/filter combinations were chosen to bracket the 4000Å break. Specifically, each cluster was observed in the near-infrared with the Wide Field Camera 3 (WFC3; Kimble et al. 2008) filter F160W. Optical data were taken with the Advanced Camera for Surveys (ACS; Ford et al. 1998) in filters F775W and F850LP or F814W, or with the Wide Field Planetary Camera 2 (WFPC2; Holtzman et al. 1995) filter F814W, all approximating broad I band or I+z band coverage. We provide a summary in Table 5.1.

The *HST* images were reduced using standard procedures with the MultiDrizzle software (Koekemoer et al. 2002; Fruchter et al. 2009). The WFC3/F160W imaging was obtained in a single pointing of 4x103s (dithered between each exposure) for all but one of the clusters. For cluster ISCS J1432.4+3250 ($z = 1.487$) there were two slightly overlapping pointings, each consisting of 700s of integration time in a two-dithered pattern. The native (undersampled) WFC3 0.13″ pixel scale was drizzled down to 0.065″ to better match the pixel scale of ACS/WFPC2 and to better recover the point-spread function.

The regions from which we construct CMDs are limited to the overlap between the optical and WFC3/F160W fields, $\sim$ 2 to 8 arcmin^2, corresponding to fields of view $\sim$ 0.7 to 1.5 Mpc in diameter. Therefore, all results that follow pertain only to the cluster cores, and we will refer to galaxies within $\sim$ 1 Mpc as "central". The *HST* fields for these clusters differ in total size, and so we have checked that the conclusions of this paper are unchanged when we consider only sources within a fixed 0.7 projected physical Mpc radius from the spectroscopic cluster centers.

The ACS/F814W observation of ISCS J1432.4+3250 ($z = 1.487$) is comprised of

Table 5.1. Summary of *HST* observations of ISCS clusters.

Name	R.A.	Dec.	z	CMD Area (arcmin^2)	Instrument/Filter (optical)	Depth[a] (optical)	Depth[a] (F160W)
ISCS J1429.2+3357	14:29:15.16	33:57:08.5	1.059	3.1	WFPC2/F814W	26.1	24.7
ISCS J1432.4+3332[b]	14:32:29.18	33:32:36.0	1.112	3.6	ACS/F775W	26.2	24.8
ISCS J1426.1+3403	14:26:09.51	34:03:41.1	1.136	3.3	WFPC2/F814W	26.1	24.7
ISCS J1429.2+3425[b,c]	14:29:15.16	34:25:46.4	1.162	1.7	WFPC2/F814W	26.6	24.7
ISCS J1426.5+3339	14:26:30.42	33:39:33.2	1.163	1.9	WFPC2/F814W	26.4	24.5
ISCS J1427.9+3430[c]	14:27:54.88	34:30:16.3	1.235	3.3	WFPC2/F814W	26.7	24.7
ISCS J1434.5+3427	14:34:30.44	34:27:12.3	1.243	4.4	ACS/F775W	26.1	24.5
ISCS J1429.3+3437	14:29:18.51	34:37:25.8	1.262	4.2	ACS/F850LP	26.3	24.4
ISCS J1432.6+3436	14:32:38.38	34:36:49.0	1.349	4.4	ACS/F850LP	26.0	24.8
ISCS J1433.8+3325	14:33:51.13	33:25:51.1	1.369	4.5	ACS/F850LP	26.1	24.8
ISCS J1434.7+3519	14:34:46.33	35:19:33.5	1.372	4.5	ACS/F850LP	26.1	24.8
ISCS J1438.1+3414	14:38:08.71	34:14:19.2	1.413	4.5	ACS/F850LP	26.1	24.7
ISCS J1432.4+3250	14:32:24.16	32:50:03.7	1.487	8.0	ACS/F814W	26.0	25.8

[a]5-sigma point source depth in 0.8" diameter; AB system

[b]*HST* pointing did not intersect cluster core due to guide star requirements

[c]No single identifiable CMR

8x564s exposures. The ACS/F850LP and F775W images for seven clusters were obtained as part of the *HST* Cluster Supernova Survey (PI Perlmutter, GO-10496 Dawson et al. 2009; Suzuki et al. 2012; Barbary et al. 2012a,b). The program consisted of 219 orbits targeting rich clusters at $z \gtrsim 1$, and the images comprise multiple overlapping pointings covering tens of arcmin^2. The single-pointing WFPC2/F814W images were obtained in a joint *Spitzer*/*HST* program to survey Luminous Infrared Galaxies (LIRGs) in clusters at $z \gtrsim 1$ (*HST* proposal ID 11002, *Spitzer* proposal ID 30950).

SCAMP (Bertin 2006) was applied to align the world coordinate system (WCS) of each image with the reference frame of SDWFS (itself matched to 2MASS). SWARP (Bertin et al. 2002) was used to resample the *HST* optical images to match the pixel scale of the drizzled WFC3 images and to project the images to the tangent plane. This process aligned the WFC3 and optical images so that pixels in all images for a given cluster covered precisely the same regions of the sky.

5.2.3 Photometric Catalogs

From the reduced and registered images, we measure fixed-aperture photometry using Source Extractor (SE; Bertin & Arnouts 1996) in dual-image mode with sources detected in the WFC3/F160W images. For comparison we compute colors using aperture diameters of 0.4″ to 1.5″, and choose 0.8″ for our default color as a reasonable balance between preventing interference in our crowded fields and intersecting a physically representative portion of each galaxy. We also constructed colors using galaxy-specific apertures scaled to the half-light radius. We manually inspected the CMRs made with each aperture, and found little change in the appearance and location of the red

sequences. Our results are thus insenstive to our choice of photometric aperture. We use SE's MAG_AUTO in the F160W band as an approximate total magnitude for our CMRs.

Differences in ETG color profiles may cause a bias in CMR properties owing to our fixed-aperture color photometry. The aperture tests described above suggest that the intrinsic widths of the color distributions dominate this bias for most galaxies. Furthermore, in what follows we assume that the slope of the rest-frame CMR matches that of the Coma cluster, in which the slope was measured (Eisenhardt et al. 2007) in an aperture corresponding to a nearly identical physical scale as the one used herein. If high-redshift ellipticals form the cores of present-day ETGs (e.g., as suggested by the measurements of Trujillo et al. 2011), then we expect minimal bias owing to this effect.

Our photometric uncertainties are dominated by sky shot noise, which we estimate in each image from the distribution of fluxes through 5000 randomly-placed apertures with a diameter matched to our catalogs. The flux distribution is to a good approximation normal except for the sources contaminating the positive half. We compute the background level $\sigma_{\rm sky}$ by fitting a normal distribution to the negative half. We verified this procedure by confirming that it produces the correct scaling in photometric scatter of sources detected in the sets of dither images before making the final stack.

We calculated the standard completeness of the WFC3/F160W-selected catalogs by generating artificial objects with known total magnitude and $R^{1/4}$ light profiles where R_e is distributed as a Rayleigh function with $\sigma_{R_e} = 3.5$ pixels (~ 0.23 arcseconds, or ~ 2 Kpc at $z = 1.5$), matching well the observed SE-derived R_e distribution for sources in these fields. We found that the WFC3/F160W-detected catalogs for each cluster

are more than 90% complete at an AB magnitude of 23.5, and every field is roughly 97% complete at $H^*(z) + 1.5$, which is approximately $H = 22$–23 for these redshifts. $H^*(z) + 1.5$ is the magnitude cut we impose for the CMR analysis presented in this work (Section 5.3.2).

5.3 Color-Magnitude Relations

We aim to study the star formation epoch of ETGs on the red sequences for our $z > 1$ cluster sample using the color and color scatter of the red sequence CMRs, which are identified using morphological classification and color selection techniques. The color and scatter of a CMR serve as proxies of the formation history of the galaxies that comprise it. The simplest physical parameters that they probe is the average formation time or age of the galaxies' stars. If the galaxies formed separately in short bursts over a period of time, then the color scatter will be inversely proportional to the time since they stopped forming, whereas if they formed in a synchronized fashion, then the scatter between galaxies may be always small. Since this is true regardless of their average age (and hence average color), then we are motivated to measure both color and scatter in order to better constrain the history of these galaxies.

5.3.1 Morphological Classification

Visual inspection of the individual galaxies in the F160W-selected catalogs was carried out by one of us (S. A. S.) using the WFC3 images. T-types (RC3; de Vaucouleurs et al. 1991) were assigned where possible to all objects down to $F160W = 23.5$. If the

object was too faint to accurately classify, too close to a bright star, or affected by bad data, no morphology was assigned. In all other cases an attempt was made to determine the T-type on the scale ranging from -5 for a giant elliptical, to 10 for an irregular galaxy. In addition, information was recorded on the environment of the object, if it was compact or appeared inclined to the line of sight, and if it appeared to be interacting with any neighboring objects.

Quantitative measurements of galaxy shapes were made by fitting a single Sérsic profile to every object in the F160W-selected catalogs. The fitting was done with GALFIT (Peng et al. 2010a), and GALAPAGOS (Häuß ler et al. 2011) was employed to automate the task of running GALFIT. GALFIT does two dimensional fitting and can fit an arbitrary number of models to any image while accounting for the image's point spread function. GALAPAGOS automates the task of running GALFIT by generating first–guess Sérsic parameters from an SE run, measuring the sky for each galaxy, deciding when to simultaneously fit nearby galaxies, and deciding when to subtract off brighter objects that might bias a fit. It then uses GALFIT to fit a single Sérsic profile to every object in the image and builds a catalog of the results.

In Figure 5.1 we present a comparison of the visual and quantitative morphologies in CMDs of two clusters that span the redshift range of our sample. The early–type CMRs resulting from these methods are qualitatively quite similar in these two clusters, as well as in the rest of our sample, and lead to quantitatively similar results. For clarity we therefore present the remainder of our CMDs using only the visual T-types, but for completeness retain a comparison with the quantitive morphologies in Figures 5.1 and 5.6 and in several tables.

Figure 5.1.—: Comparison between morphological selection techniques for clusters ISCS J1429.2+3357 ($z = 1.059$) and ISCS J1438.1+3414 ($z = 1.413$). We identify objects in the top and bottom panel based on visually-classified and automated morphologies, respectively (§5.3.1). The black dotted lines show the CMR calculated from the Coma cluster (Eisenhardt et al. 2007) and evolved (assuming a single short burst at $z_f = 3$) to the observed redshift. We plot a vertical dotted line at $H = H^* + 1.5$, representing the magnitude selection limit we apply in Section 5.3.2. Gray crosses represent all spectroscopically confirmed cluster members currently known that are covered by the *HST* images and that fall within the color-magnitude ranges of the CMD. An updated description of the spectroscopy will be presented by Zeimann et al. (in prep.) and Brodwin et al. (in prep.). Where visible in the upper right corners, the diagonal blue dashed lines approximate the boundary of the 5σ color and F160W magnitude measurements. For ISCS J1438.1+3414 ($z = 1.413$), we note the presence of many early-type galaxies ~ 1 magnitude blueward of the identified cluster red sequence. Several of these objects are part of a foreground structure evident in the photometric redshifts of the ISCS catalog, and are offset from the spectroscopic cluster center by ~ 1 arcminute. Therefore we believe those relatively blue early-type galaxies are interlopers. We find that both morphology classification schemes yield similar CMRs for all of our clusters, so we present the CMDs in Figure 5.2, 5.3, and 5.4 using only the visual typing, and analyze them in Figure 5.4.

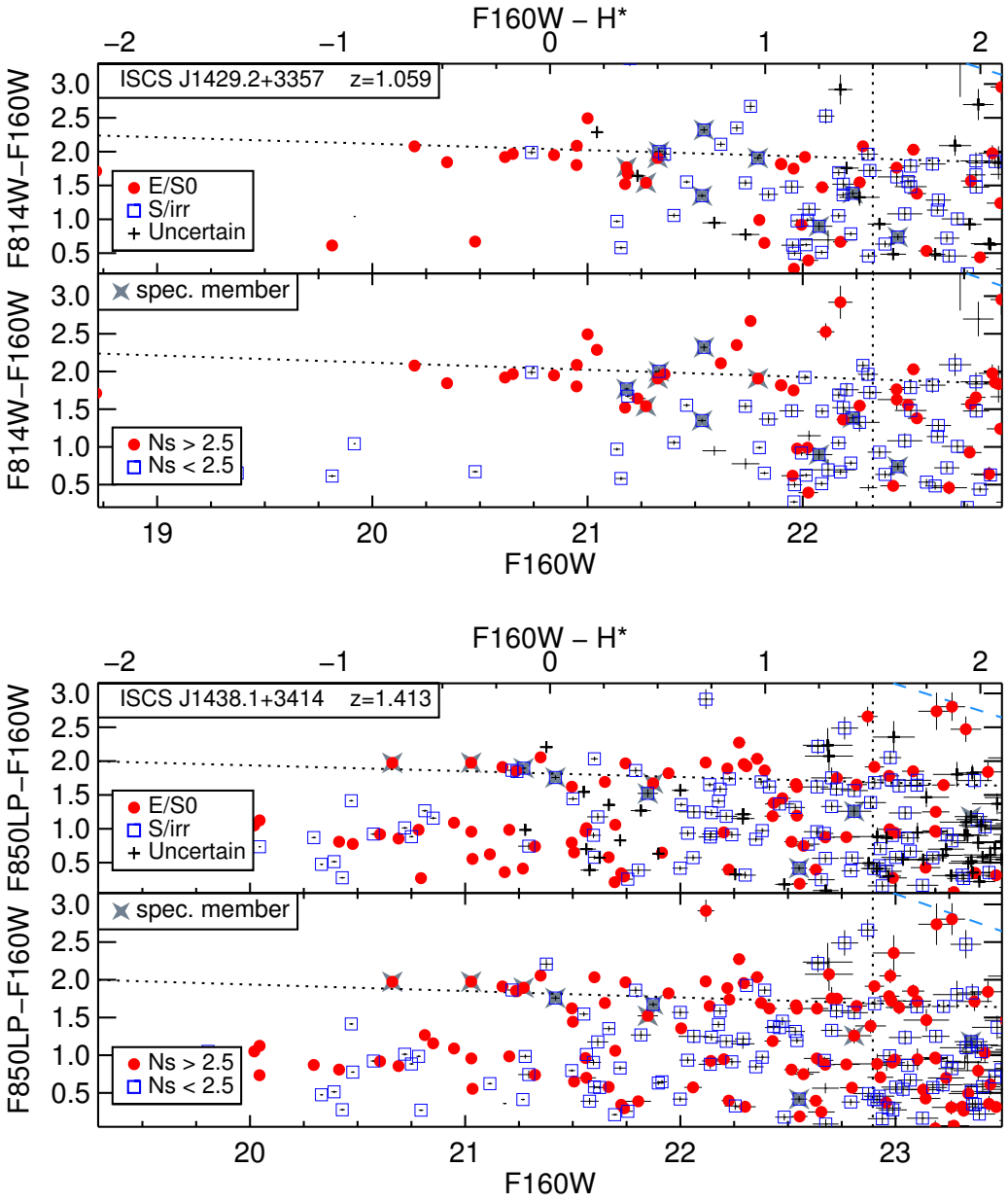

Figure 5.1.—: (Continued)

5.3.2 Red Sequence Selection

We use the colors, magnitudes, morphological classifications, and available spectroscopy to identify early–type members of the red sequence in each cluster. Multi–band photometric redshifts, which are not considered in this work, are available for only a small fraction of the galaxies selected in the WFC3/F160W images, because these *HST*-based catalogs are dominated by fainter galaxies in fields too crowded for reliable ground-based photometry.

The basic observables, the CMDs for 13 clusters, are presented in Figures 5.2 and 5.3. In each panel we plot the Coma CMR (Eisenhardt et al. 2007) evolved to the appropriate redshift (see Section 5.4 for details).

In ISCS J1429.2+3425 ($z = 1.162$) and ISCS J1427.9+3430 ($z = 1.235$), shown in Figure 5.3, there exist multiple known structures at different redshifts in the *HST* field of view. Moreover, the intersection between the WFC3/F160W image of ISCS J1429.2+3425 ($z = 1.162$) and its WFPC2/F814W image is small and does not include an identifiable CMR. To avoid a possible bias from including projected large scale structure, as opposed to massive, collapsed clusters, we omit these two clusters from our analysis. It is possible that one or two other members of the 11 remaining clusters are similar outliers, but lacking such evidence at present, we cannot confidently omit them from our analysis.

For the clusters with a clear red sequence, the rest-frame CMR slope is within 10% of that in Coma, while the color zeropoint and scatter clearly vary. The shallow slope of the CMR has been found to be nearly constant with redshift (Kodama & Arimoto 1997), and thus has been interpreted as evidence for a uniformly old sequence in mass and

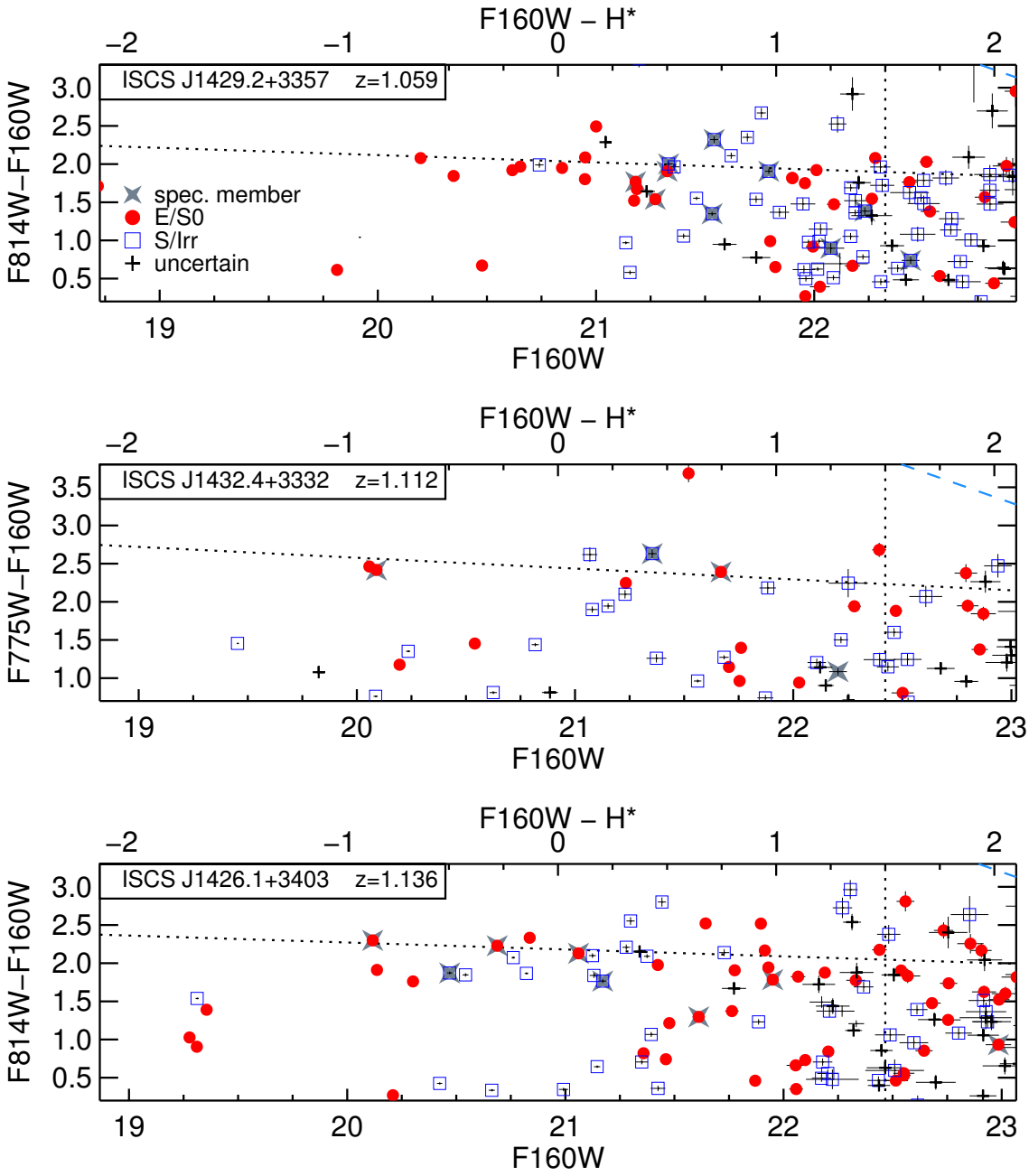

Figure 5.2.—: CMDs for our cluster sample, in ascending redshift order. These graphs follow the same formatting as the top panels of the two CMDs in Figure 5.1, where plot symbols represent the visual classification system of Section 5.3.1.

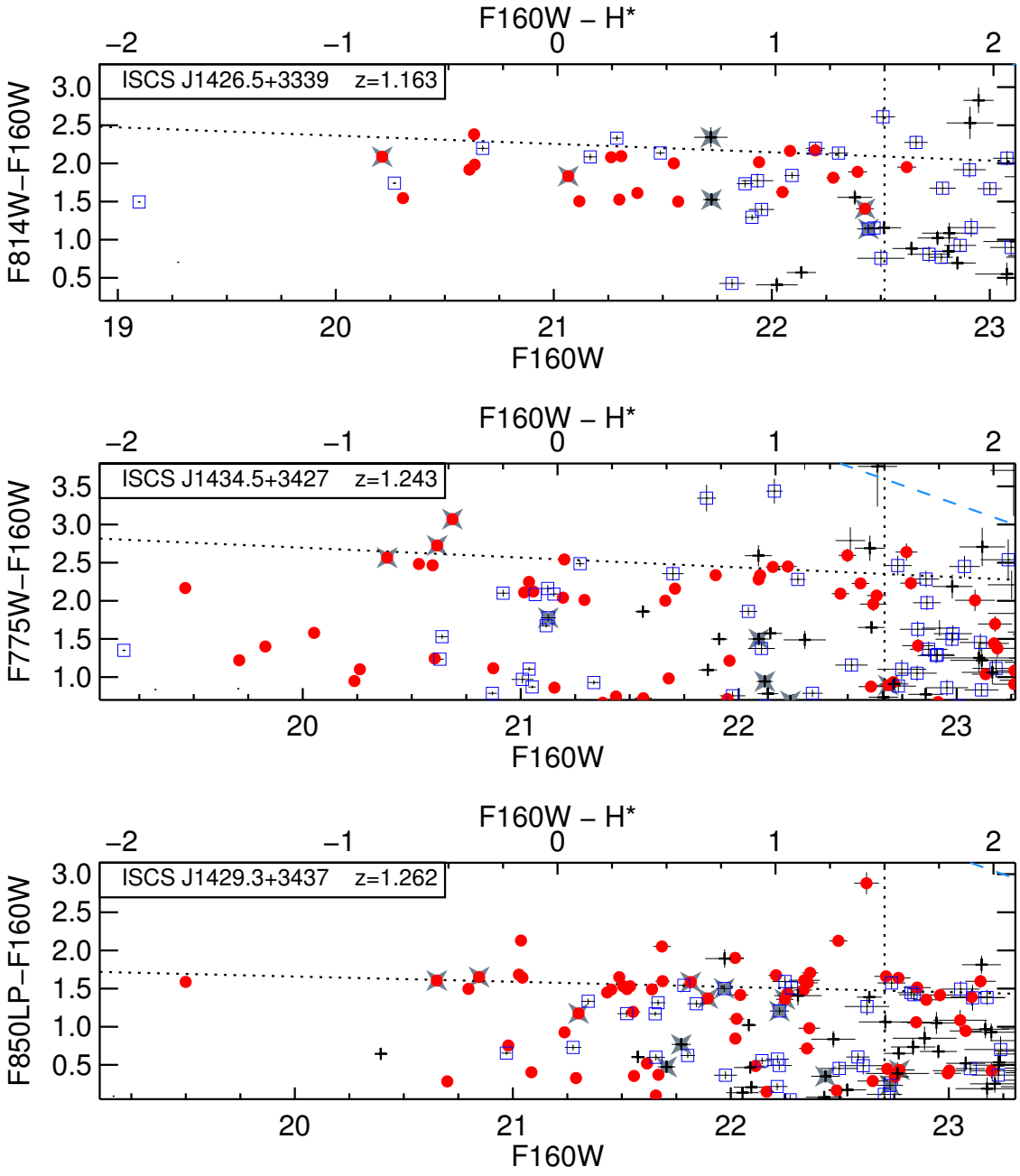

Figure 5.2.—: (Continued)

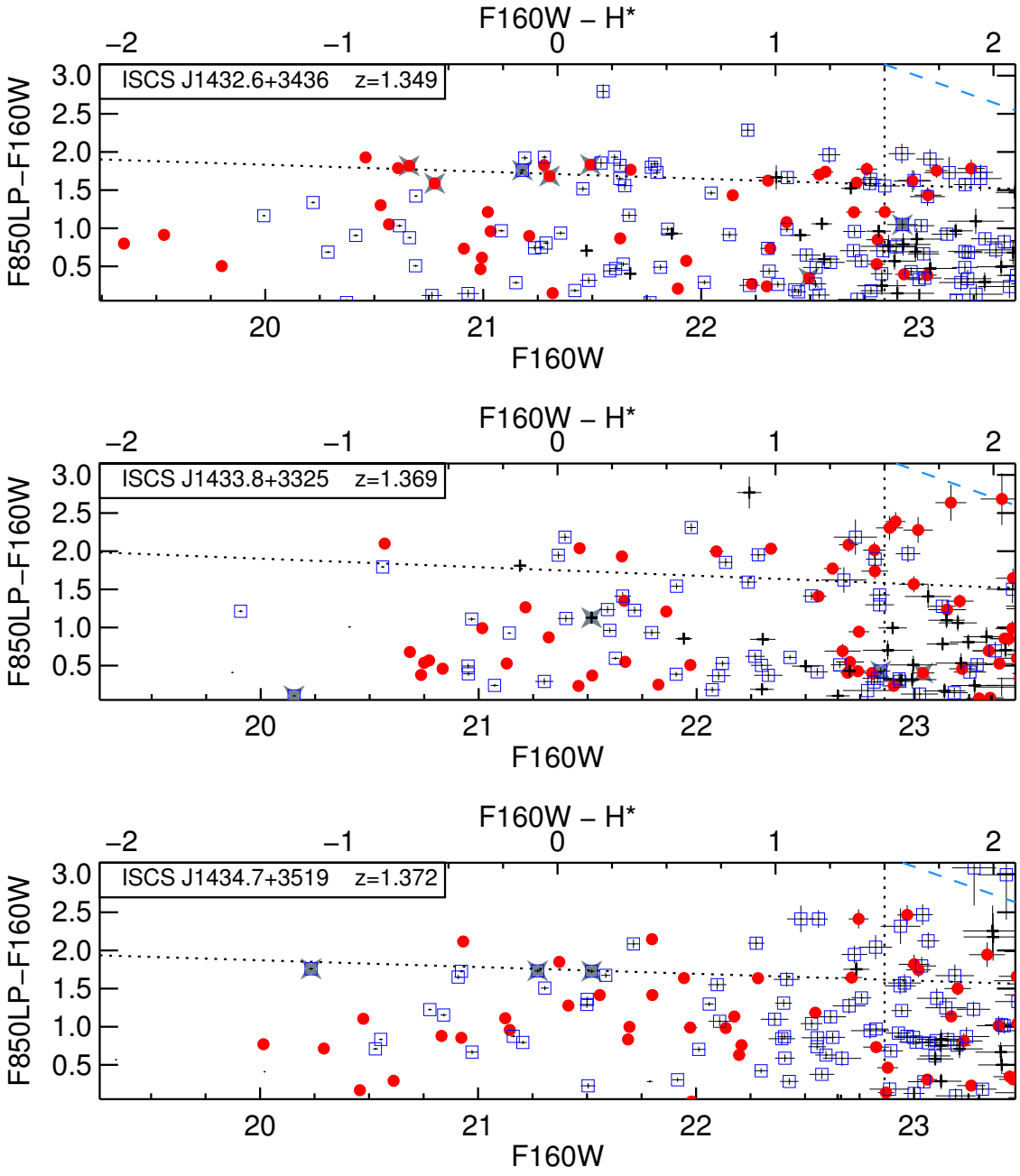

Figure 5.2.—: (Continued)

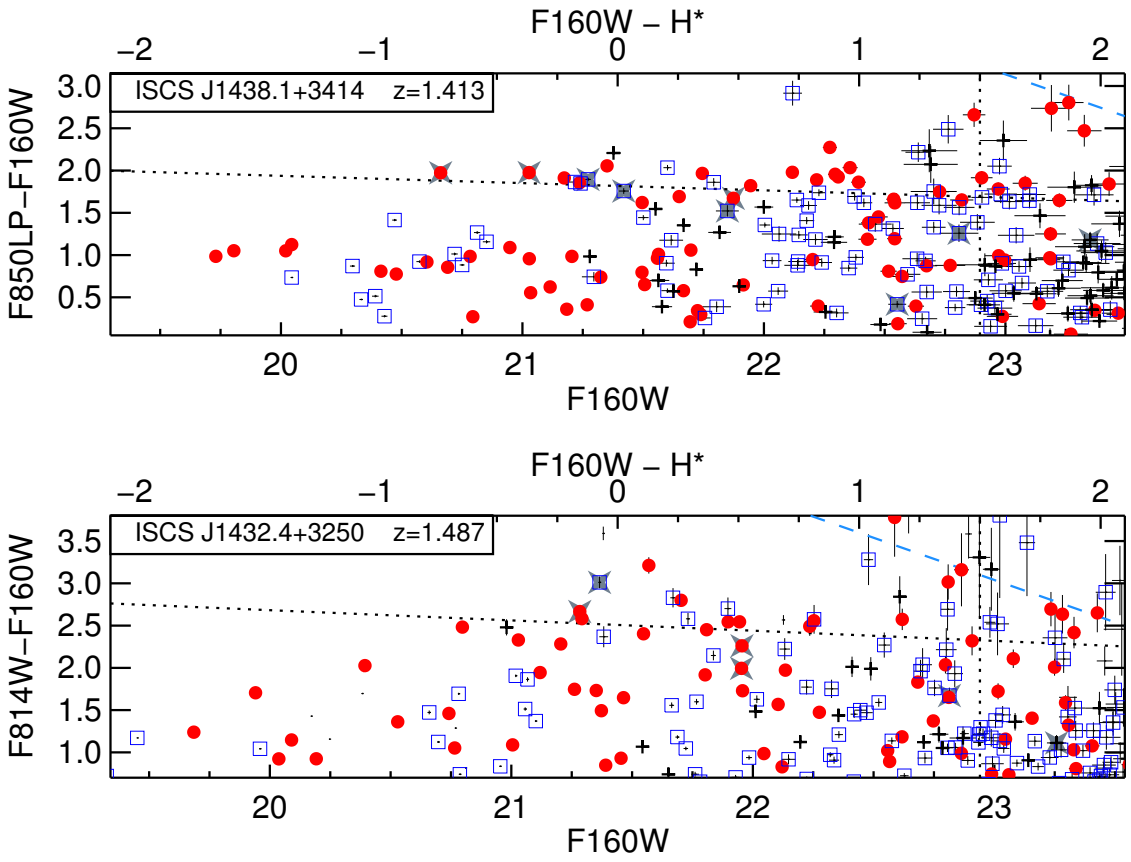

Figure 5.2.—: (Continued)

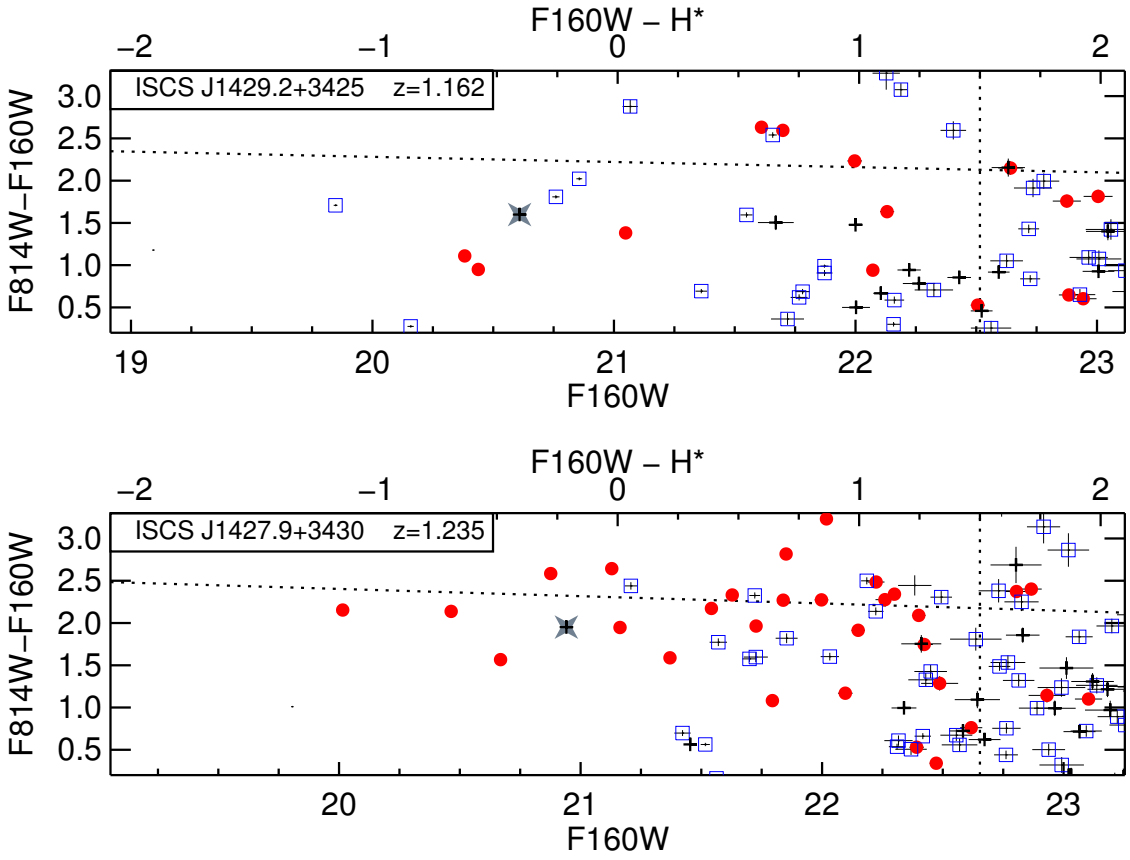

Figure 5.3.—: CMDs of two clusters for which there are known structures at different but similar ($z \sim 1$) redshifts. The symbols are the same as in Figure 5.2. In order to avoid potential confusion owing to multiple red sequences, these two clusters are not used in the subsequent analyses.

metallicity (e.g., Larson 1974), and not one based on galaxy age. If the tilted CMR is entirely the result of a mass-metallicity relation with a similar slope from $z = 2$ to 0 (as implied by the results of e.g., Erb et al. 2006; Brooks et al. 2007), then we do not expect cosmic evolution in the CMR slope so long as we can satisfactorily select galaxies that satisfy this relation. In what follows we fix the CMR slope in each cluster's rest frame, treating it as independent of age, and consider only measurements of the color zeropoint and scatter. We will discuss possible deviations from this assumption as needed.

We isolate CMRs in the 11 clusters using the following procedure. First, we subtract from every galaxy's color our fiducial Coma CMR model (a single stellar population formed in an instantaneous burst at $z_f = 3$). We plot the resulting quantity Δ, in magnitudes, in Figure 5.4. For all clusters except ISCS J1426.5+3339 ($z = 1.163$), we define a red sequence galaxy (RSG) as having and $\Delta_{z_f} - 0.25 < \Delta < 0.75$, where Δ_{z_f} is the color difference between our $z_f = 3$ assumption and a single stellar population formed at redshift z_f. We use $z_f = 2$ to set this lower limit on Δ instead of $z_f = 3$ in order to successfully select red sequences that may have formed more recently. This Δ range is chosen as a reasonable balance between including member RSGs and excluding blue interlopers or late-type members that are not on the cluster's red sequence. This range of Δ, within which we select the RSGs, is listed for each cluster in Table 5.2; in all cases this is $\gtrsim 1.2$ magnitudes. Except for ISCS J1426.5+3339 ($z = 1.163$), which has a very blue red sequence, this range cleanly selects the RSGs, and in particular the one composed of ETGs, that are visually identifiable in Figures 5.1-5.2. For ISCS J1426.5+3339 ($z = 1.163$), we have manually modified the color selection region to identify the RS: $\Delta_2 - 0.5 < \Delta < 0.75$. It is unclear why ISCS J1426.5+3339 ($z = 1.163$) appears so much younger than other clusters at similar redshifts, though we have verified that our

conclusions are unchanged if we omit it from our analysis.

Next, we define the cluster RSGs as galaxies brighter than $H^*(z) + 1.5$ and selected by the above color criteria, where $H^*(z)$ is calculated by evolving the characteristic brightness for Coma (de Propris et al. 1998) to the cluster's observed redshift, assuming the galaxies formed in a single short burst at $z_f = 3$. Some of the RSGs selected in this way are spectroscopically confirmed cluster members, and we plot these as gray stars in all CMDs. However, most do not have accompanying spectroscopic or photometric redshift information, and so the RSG samples may suffer from interloper contamination. In addition to the sample of all RSGs, we analyze two samples drawn from them to identify likely ETGs: visually-selected E's or S0's as defined in Section 5.3.1, and quantitatively-selected ETGs with $n_S > 2.5$. The latter choice is reasonably consistent with selecting bulge-dominated objects (Simard et al. 2011), as well as visually-typed E and S0 galaxies (Simard et al. 2009).

Finally, to limit the influence of interlopers that are extreme outliers from the cluster's red sequence, we drop galaxies from the final ETG or RSG catalog that are further than two median absolute deviations in color from their Δ zeropoint, as measured below. Table 5.2 lists the number of galaxies satisfying our red sequence selections, as well as the median color uncertainty (for the sample of all RSGs) in the observed bands.

5.3.3 Color Zeropoints and Scatters

For each of the three ETG or RSG samples defined above, we measure the color zeropoint and intrinsic scatter, and their associated uncertainties, applying the biweight estimates of location and scale (Mosteller & Tukey 1977; Beers et al. 1990) for the zeropoint

Table 5.2. Number of cluster red sequence galaxies.

Name	z	Δ width[a]	Number on CMR Vis. ETGs	Number on CMR Quant. ETGs	Number on CMR All RSGs	Spectroscopic Members[b] WFC3 Catalog	Spectroscopic Members[b] All RSGs	median $\sigma_{\rm phot}$ All RSGs
ISCS J1429.2+3357	1.059	1.19	13	16	26	10	5	0.04
ISCS J1432.4+3332	1.112	1.25	5	7	11	6	3	0.05
ISCS J1426.1+3403	1.136	1.24	15	20	30	8	6	0.03
ISCS J1426.5+3339	1.163	1.76	18	12	39	6	6	0.04
ISCS J1434.5+3427	1.243	1.25	19	19	27	10	3	0.05
ISCS J1429.3+3437	1.262	1.22	23	21	33	13	8	0.04
ISCS J1432.6+3436	1.349	1.24	12	16	27	7	5	0.05
ISCS J1433.8+3325	1.369	1.24	9	9	24	6	0	0.07
ISCS J1434.7+3519	1.372	1.24	10	14	27	3	3	0.04
ISCS J1438.1+3414	1.413	1.19	20	25	43	10	7	0.04
ISCS J1432.4+3250	1.487	1.24	15	13	33	6	4	0.10[c]

[a]Color width in magnitudes used to define the RSG selection region; see Section 5.3.2.

[b]Spectroscopy for parts of this sample were described by Stanford et al. (2005); Elston et al. (2006); Brodwin et al. (2006, 2011); Eisenhardt et al. (2008). Updated membership identification, including those confirmed with the *HST* WFC3 grism, will be described by Zeimann et al. (in prep.) and Brodwin et al. (in prep.).

[c]Although this cluster has the deepest WFC3/F160W image in the sample, its red sequence galaxies are fainter (and redder), leading to a high average color uncertainty.

location Δ_0 and scatter about this location σ_Δ. These two measurements define our CMR for each subsample. We calculate the color C_0 at $H^*(z)$ by adding back to Δ_0 the previously-subtracted fiducial $z_f = 3$ CMR model, and the intrinsic scatter $\sigma_{\rm int}$ by subtracting in quadrature the median photometric error from the biweight scale estimate σ_Δ of the sample in question.

Uncertainties are derived from 1000 bootstrap resamplings, from which we measure the scale of the resulting C_0 and $\sigma_{\rm int}$ distributions using the median absolute deviation (MAD). Specifically, $\sigma_C = S_{\rm MAD} = {\rm MAD}/0.6745$, since a normally-distributed quantity will have MAD $= 0.6745\sigma$. Where the samples overlap, our measurements of σ_{U-V} are consistent with those measured by Meyers et al. (2012), except for ISCS J1438.1+3414 ($z = 1.413$). At $z \gtrsim 1.3$, the addition of the *HST* WFC3/F160W data permits an improved k-correction, and so we believe the present calculation to be reliable.

For each cluster we present C_0, σ_C, and their uncertainties in Table 5.3. The observed-band $\sigma_{\rm int}$ values are all significantly smaller than ≈ 0.6 magnitudes, which is the value we would expect to measure if there were no overdensity (e.g., no red sequence) inside the Δ selection region. This implies that our measurements are driven by the real red sequences and are not an artifact of our color selection choices (Table 5.2).

Figure 5.4.—: CMD residuals from $z_f = 3$ model and subsequent analysis for each cluster, in ascending redshift order. We restrict attention to elliptical and S0 galaxies satisfying the color and magnitude cuts of Section 5.3.2. All RSGs and the visually-selected ETG subsample are plotted as gray and black filled circles, respectively. We plot a vertical dotted line at $H = H^* + 1.5$, representing the magnitude selection limit we apply in Section 5.3.2. The location and scale measurements are shown as pairs of horizontal lines centered on the final measured Δ_0 zeropoint value and spaced to surround the one-sigma region defined by the final measured $\sigma_{\rm int}$ scatter value. The blue solid lines correspond to the scatter of the subsample containing all RSGs, and the red solid lines correspond to scatter in the visual ETG subsample. Histograms are tabulated for each subsample on the right of each CMD, and include dashed black lines to show the color selection region set in Section 5.3.2.

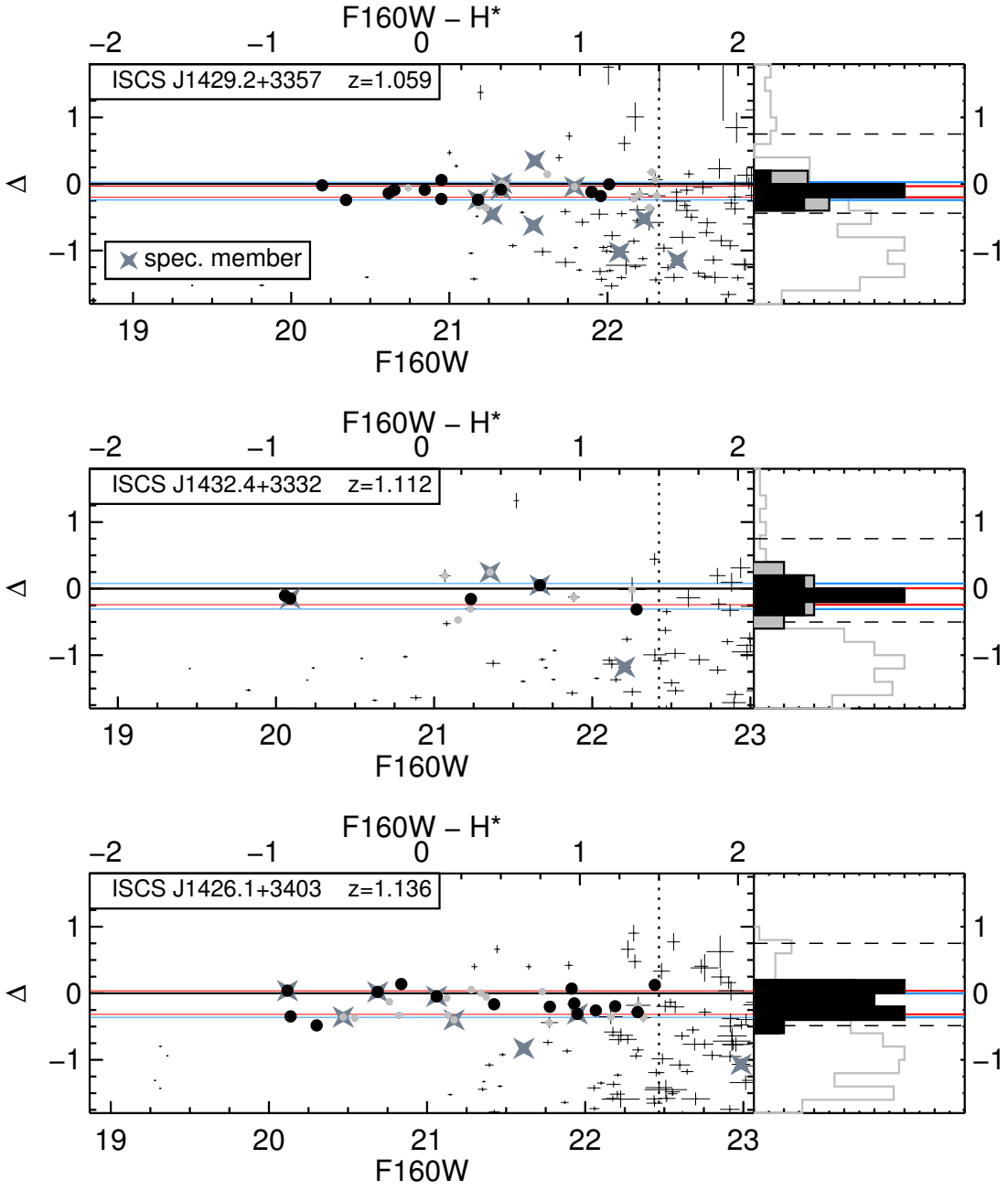

Figure 5.4.—: (Continued)

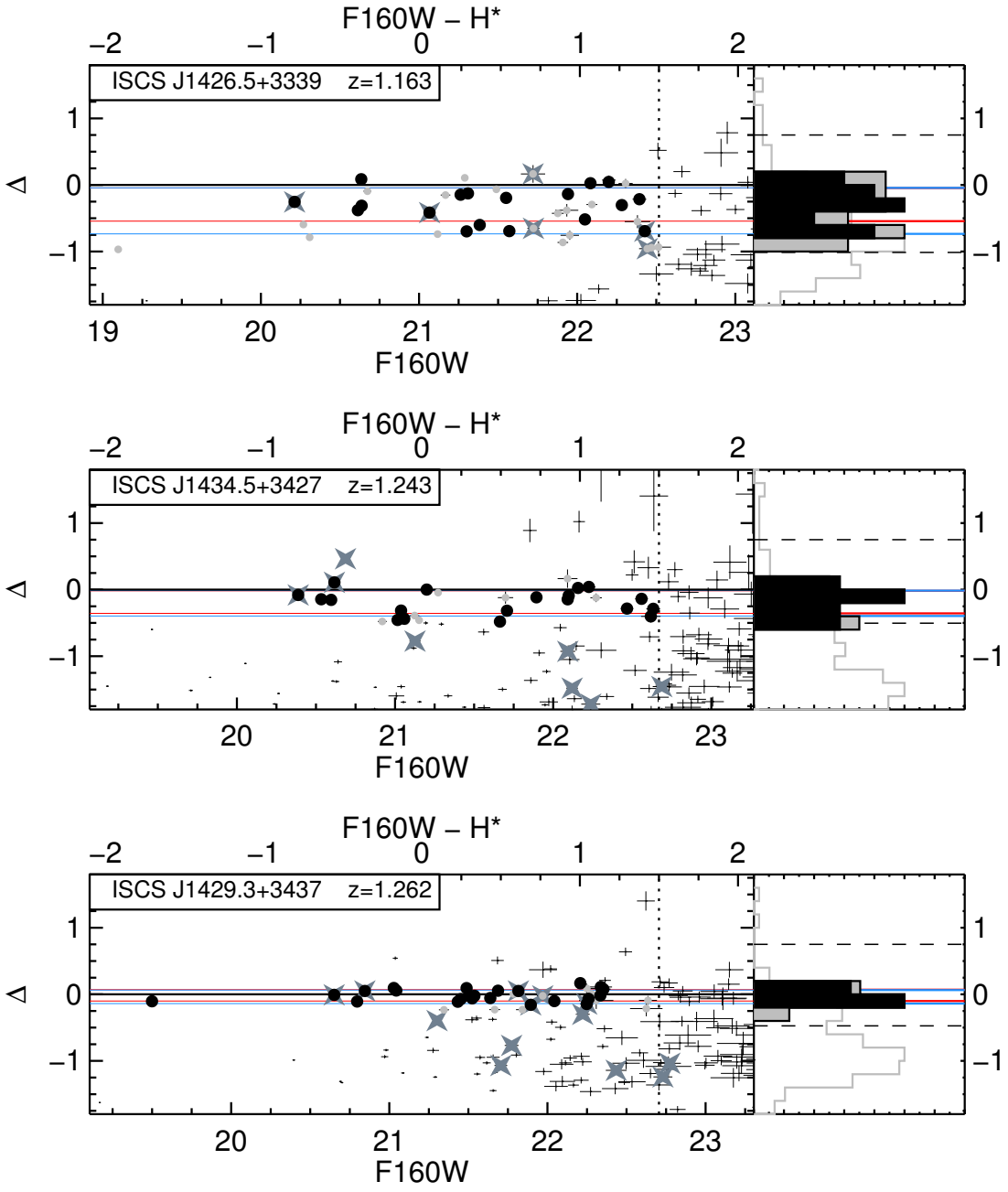

Figure 5.4.—: (Continued)

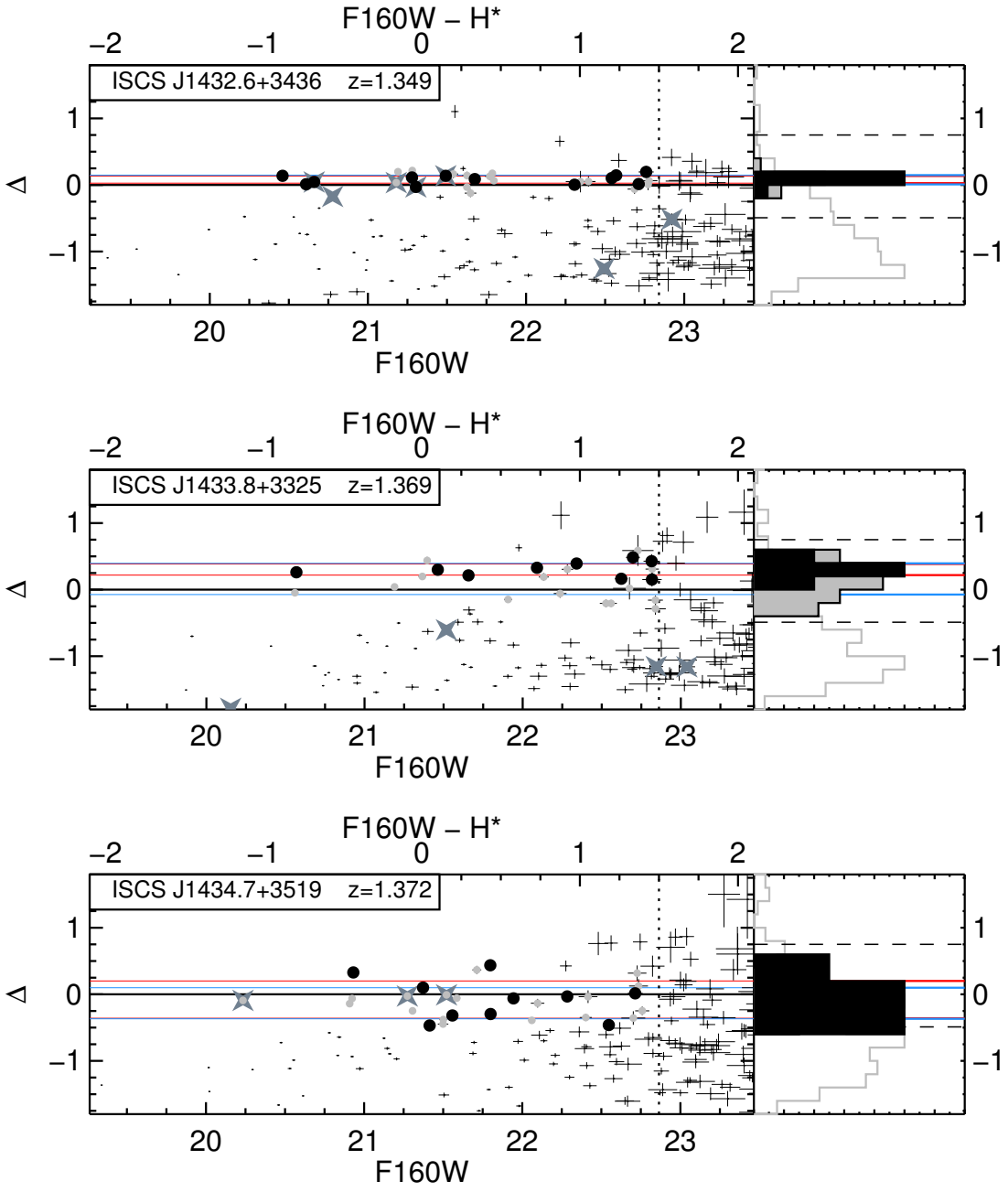

Figure 5.4.—: (Continued)

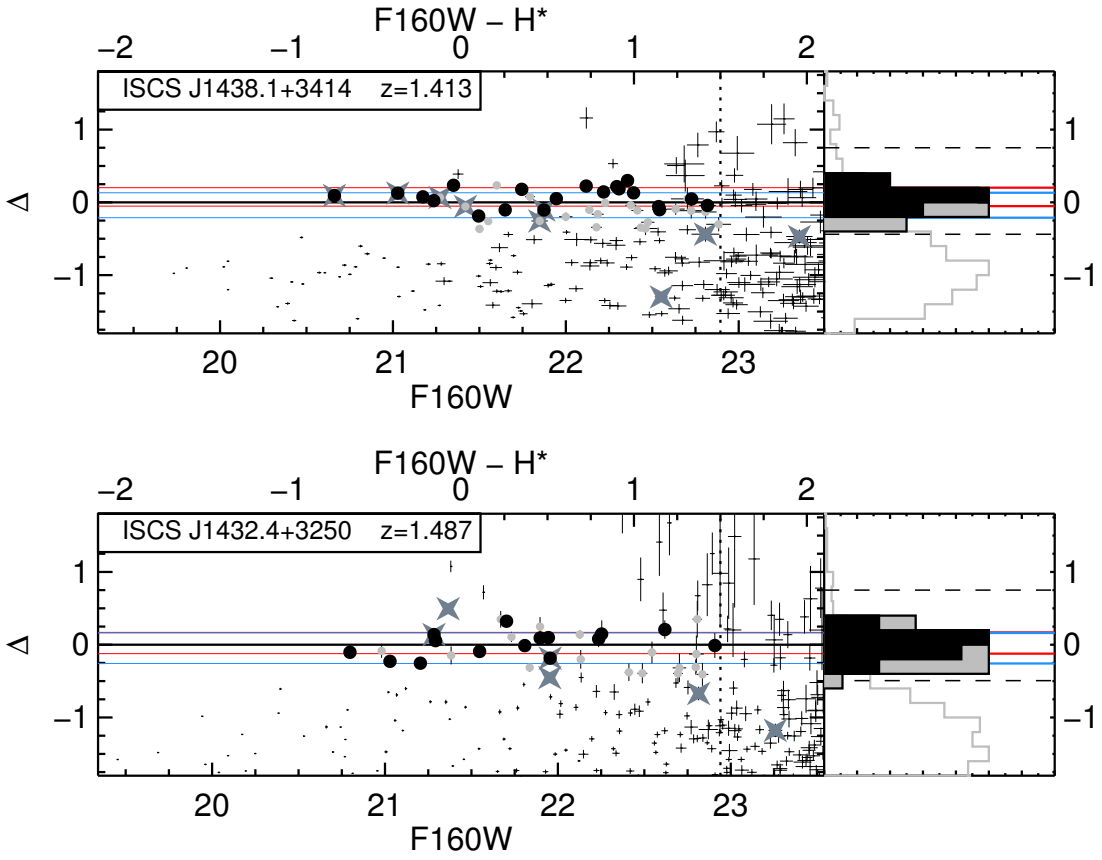

Figure 5.4.—: (Continued)

Table 5.3. Cluster red sequence color zeropoints and color scatters.

Name	z	Observed bands			Rest-frame U-V		
		Vis. ETGs	Quant. ETGs	All RSGs	Vis. ETGs	Quant. ETGs	All RSGs
				Color Zeropoint, C_0			
ISCS J1429.2+3357	1.059	1.92 ± 0.03	1.93 ± 0.03	1.93 ± 0.03	1.03 ± 0.03	1.04 ± 0.03	1.04 ± 0.03
ISCS J1432.4+3332	1.112	2.33 ± 0.05	2.32 ± 0.06	2.33 ± 0.06	1.05 ± 0.04	1.04 ± 0.05	1.05 ± 0.04
ISCS J1426.1+3403	1.136	2.04 ± 0.05	2.00 ± 0.04	2.00 ± 0.04	1.02 ± 0.05	0.99 ± 0.04	0.99 ± 0.03
ISCS J1426.5+3339	1.163	1.95 ± 0.07	1.85 ± 0.10	1.87 ± 0.06	0.91 ± 0.06	0.82 ± 0.08	0.84 ± 0.05
ISCS J1434.5+3427	1.243	2.35 ± 0.05	2.27 ± 0.04	2.34 ± 0.04	0.94 ± 0.04	0.88 ± 0.03	0.93 ± 0.03
ISCS J1429.3+3437	1.262	1.56 ± 0.02	1.53 ± 0.02	1.54 ± 0.02	1.05 ± 0.02	1.01 ± 0.02	1.02 ± 0.02
ISCS J1432.6+3436	1.349	1.79 ± 0.03	1.81 ± 0.02	1.79 ± 0.02	1.12 ± 0.02	1.14 ± 0.02	1.12 ± 0.02
ISCS J1433.8+3325	1.369	2.05 ± 0.04	2.01 ± 0.05	1.91 ± 0.06	1.33 ± 0.04	1.29 ± 0.05	1.20 ± 0.06
ISCS J1434.7+3519	1.372	1.68 ± 0.10	1.71 ± 0.08	1.62 ± 0.05	0.97 ± 0.10	1.00 ± 0.07	0.91 ± 0.05
ISCS J1438.1+3414	1.413	1.89 ± 0.04	1.85 ± 0.03	1.78 ± 0.03	1.11 ± 0.03	1.07 ± 0.03	1.00 ± 0.03
ISCS J1432.4+3250	1.487	2.53 ± 0.05	2.49 ± 0.06	2.46 ± 0.05	1.01 ± 0.04	0.97 ± 0.04	0.95 ± 0.03
				Color Scatter, $\sigma_{\rm int}$			
ISCS J1429.2+3357	1.059	0.08 ± 0.02	0.12 ± 0.03	0.13 ± 0.02	0.08 ± 0.02	0.11 ± 0.03	0.12 ± 0.02
ISCS J1432.4+3332	1.112	0.12 ± 0.02	0.20 ± 0.07	0.19 ± 0.05	0.09 ± 0.02	0.15 ± 0.05	0.14 ± 0.03
ISCS J1426.1+3403	1.136	0.18 ± 0.03	0.17 ± 0.02	0.18 ± 0.02	0.15 ± 0.02	0.14 ± 0.02	0.16 ± 0.01
ISCS J1426.5+3339	1.163	0.25 ± 0.03	0.30 ± 0.06	0.35 ± 0.03	0.21 ± 0.03	0.26 ± 0.05	0.29 ± 0.02
ISCS J1434.5+3427	1.243	0.17 ± 0.02	0.17 ± 0.02	0.19 ± 0.02	0.13 ± 0.02	0.13 ± 0.01	0.14 ± 0.02
ISCS J1429.3+3437	1.262	0.09 ± 0.01	0.09 ± 0.01	0.10 ± 0.01	0.09 ± 0.01	0.09 ± 0.01	0.10 ± 0.01
ISCS J1432.6+3436	1.349	0.05 ± 0.01	0.06 ± 0.01	0.07 ± 0.01	0.05 ± 0.01	0.06 ± 0.01	0.07 ± 0.01
ISCS J1433.8+3325	1.369	0.08 ± 0.02	0.06 ± 0.04	0.24 ± 0.03	0.08 ± 0.02	0.06 ± 0.03	0.22 ± 0.03

Table 5.3—Continued

Name	z	Observed bands			Rest-frame U-V		
		Vis. ETGs	Quant. ETGs	All RSGs	Vis. ETGs	Quant. ETGs	All RSGs
ISCS J1434.7+3519	1.372	0.28 ± 0.06	0.29 ± 0.04	0.23 ± 0.03	0.27 ± 0.05	0.28 ± 0.04	0.22 ± 0.03
ISCS J1438.1+3414	1.413	0.13 ± 0.02	0.12 ± 0.02	0.17 ± 0.02	0.12 ± 0.02	0.11 ± 0.01	0.16 ± 0.02
ISCS J1432.4+3250	1.487	0.15 ± 0.03	0.13 ± 0.04	0.21 ± 0.02	0.10 ± 0.02	0.10 ± 0.03	0.15 ± 0.02

5.4 Simple Models of Color and Scatter

To associate the measured CMRs with formation epochs, we compute grids of model colors in our observed passbands using the models of Bruzual & Charlot (2003, 2007 version). Each model galaxy forms its stars in a single exponentially-decaying burst with a timescale of $\tau = 0.1$ Gyr and evolves passively thereafter until it is observed. We will label these models our "short-burst stellar population" (sbSP) models, whose evolution after a few hundred Myr is very similar to that of a simple stellar population (SSP). To construct the grids we use the EZGal code of Mancone & Gonzalez (2012)[1], focusing on solar-metallicity stellar populations drawn from a Chabrier (2003) initial mass function (IMF), using formation epochs evenly spaced in time between $z_f = 1.8$ and $z_f = 10$.

For ease of comparison to other work, we convert our measured quantities to the rest-frame UBV filter set following Mei et al. (2006b) using these models. First, we evolve a set of sbSP models with varying metallicity and formation redshift down to each cluster's redshift. Then we fit the relation $(i - H)_z = a + b(U - V)_0$ to estimate the parameters a and b. The slope b is used to derive the rest-frame color scatter given an observed color scatter; specifically, $\sigma_{UV} = \sigma_{iH}/b$. We also use these relations to compute the slope of the Coma CMR (Eisenhardt et al. 2007) as it would be observed in the *HST* bands at these redshifts; these were used for selecting red sequences in Section 5.3.2. We visually inspected the linear fits and found good agreement in all cases. We also performed the analysis of Section 5.5 using the colors as-observed and using only directly comparable models at the appropriate redshifts. We found that our results are identical in both cases, confirming the validity of the conclusions based on the

[1]http://www.baryons.org/ezgal/

k-corrected rest-frame colors.

We construct model red sequence ETG color scatters following previous studies (Papovich et al. 2010; Hilton et al. 2009; Mei et al. 2009, and references therein). We consider the simplest models in which the dispersion in optical ETG color for a single model set depends on the redshift at which star formation ceased, $z_{\rm end}$. Prior to $z_{\rm end}$, our models assume that cluster galaxies form uniformly in time starting at $z_0 = 10$. In practice, for each stellar IMF and metallicity we draw 10^5 individual galaxy models with random formation times between z_0 and $z_{\rm end}$ and evolve them to each cluster's observed redshift. We then compute three quantities: the color dispersion and median color using the biweight scale and location estimators (Beers et al. 1990), and the luminosity-weighted average formation time, which we label $\langle z_f \rangle$, a typical (star-)formation redshift. The epochs $z_{\rm end}$ and $\langle z_f \rangle$ describe these galaxies' last major star-forming episode, the nature and timing of which we seek to trace. In what follows we denote this set of models as our "constant SFR" (cSFR) models.

To compare the color zeropoints between the observed clusters and model galaxies, we measure the color of the observed red sequence at the characteristic brightness, $H^*(z_{\rm obs})$, that we evolve from the value in Coma (de Propris et al. 1998). We assume each model galaxy has the same mass, and thus refer to all CMR quantities as those measured at $H^*(z_{\rm obs})$. A galaxy luminosity function evolving by ~ 0.5 magnitudes in the fashion of Mancone et al. (2010) will only mildly affect our interpretation of their stellar populations. Specifically, the comparison between observed and model color depends only weakly on the magnitude at which we compute numerical values of the colors from the derived CMRs. This owes to the CMR slopes in our observed bands being shallow (≈ -0.1), so a 0.5 magnitude shift in the value of H^* alters our derived $U - V$ colors

by only ≈ 0.03 magnitudes. To recover the results we obtain in Section 5.5 with a fixed formation epoch, H^* must increase by $\gtrsim 3$ magnitudes between $z \approx 1.5$ and $z \approx 1$, a change we believe is too large. We conclude that this effect may slightly bias our color measurements to the red but it does not change our qualitative results.

The true star formation and assembly histories of ETGs, as observed in cluster cores over time, are likely to be rather complex. Previous studies showed that these sbSP and cSFR models do not fully explain the evolution of the colors of cluster galaxies. However, they represent valuable parametrizations of the observed CMRs, allowing for comparisons to previous work and direct, if approximate, estimation of ETG stellar population ages without the need for a complete specification of their varied histories. Therefore the above models will be applied as the initial framework for analyzing our results.

5.5 Results

5.5.1 Color and Scatter Evolution

We compile the measured colors and scatters of cluster CMRs in Table 5.3, and plot them in Figure 5.5. We also plot the associated sbSP and cSFR models, where for the latter we have utilized the parameter $z_{\rm end}$ rather than a weighted formation redshift $\langle z_f \rangle$ because for a given model $\langle z_f \rangle$ depends on the observation redshift. Thus the cSFR models plotted correspond to fixed histories, where star formation continues uniformly in time and ceases at $z_{\rm end}$.

In the top two rows of Figure 5.5, we see that the rest-frame $U - V$ colors of cluster RSGs are nearly constant across the redshift range 1 to 1.5, in contrast to any of the model stellar populations that redden monotonically with time. The color scatters in the bottom row of Figure 5.5 reflect the same physical scenario: the rest-frame $\sigma(U - V)$ is nearly constant (or slightly declining) with increasing redshift, while the scatter increases monotonically in cSFR models.

We checked several other stellar population models (Maraston 2005; Conroy et al. 2009; Conroy & Gunn 2010) and parameter choices (metallicity, IMF, SFH) and found similar results. Models with $\sim 0.4Z_{\odot}$ can reproduce the flat $(U - V)_0 \sim 1$ trend at these redshifts, but *cannot* account for a flat or declining color scatter trend, nor for the colors of $z < 1$ giant cluster galaxies (Aragon-Salamanca et al. 1993; Stanford et al. 1998).

Several clusters are outliers to the median trends observed in these figures, and will be discussed in more detail in Sections 5.5.4 and 5.6. These general trends imply that we are not approaching the primary epoch of star formation in the centers of these clusters, and/or that their formation histories were not as simple as those assumed by the simplest models. Colors of the CMRs are redder than, and the color scatters smaller than the simplest sbSP or cSFR estimates in which the CMRs get bluer and wider as one approaches their primary formation epoch.

5.5.2 Effect of Morphology Selection

We demonstrate the effect of the morphology cut on both colors and scatters in Figure 5.6. At $z > 1.3$, the colors of morphologically-selected ETGs are slightly redder than the full red sequences at the same redshift. This might reflect the canonical in-situ

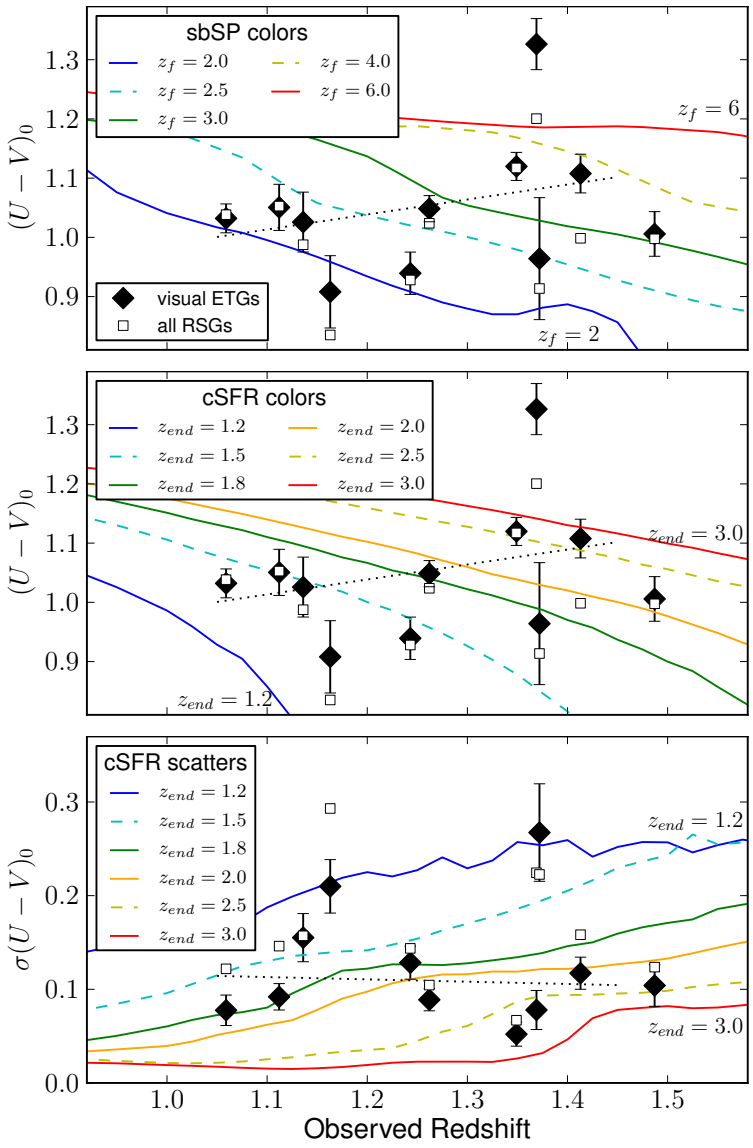

Figure 5.5.—: Rest frame colors and scatters of our clusters' CMRs, with associated models. The top, middle, and bottom figures compare our measurements against the sbSP color, cSFR color, and cSFR color scatter models, respectively (Section 5.4). Here we employ visual morphological classification for the solid black diamonds and show the results for the entire RSG subsample as the open squares. For clarity, in this and later figures we only plot error bars for the morphologically-selected sample (black diamonds) and not the entire RSG subsample – they are similar in magnitude and both are listed in Tables 5.3-5.5. We plot a linear fit to the data in each panel as dotted black lines. There is a clear disagreement between the continued evolution of any single sbSP or cSFR model and the observed CMR trends.

progenitor bias as described in van Dokkum & Franx (2001), where galaxies drop out of the ETG sample at higher redshift because they are continually being transformed and as such are not necessarily identified as ETGs in a cluster's progenitor. Progenitor bias, or a similar effect, may provide a natural explanation for the seemingly unintuitive way that the red sequences remain narrow and red, a scenario we consider further in Section 5.6. The rate of transformations inside the cluster center appears to have slowed by $z < 1.3$, lending additional evidence that above $z \approx 1.3$ we are beginning to see the late stages of evolution by the giant cluster galaxies.

The change in U-V color owing to this effect is approximately 0.1 magnitudes, and is therefore insufficient to explain the entirety of the deviation we see from any one sbSP in Figure 5.5, leaving the colors and scatters roughly constant across the redshift range. In this series of figures (Figures 5.5, 5.6, 5.7, and 5.8) we plot the entire RSG sample as unfilled black squares to demonstrate the (typically inconsequential) difference from the morphologically-selected ETG sample. We conclude that the cluster ETG samples are growing across the entire range $1 < z < 1.5$ by the incorporation of younger RSGs that are missed in the samples at higher redshift, not only because they were star forming (and hence still growing) or disk-like in the centers at $z > 1.3$, but also because RSGs/ETGs that grow or enter the central region have younger stars than those previously present.

5.5.3 Inferred (Simple) Star Formation Epochs

Although the simple models of Section 5.4 may not reflect the *evolving* stellar populations of the ISCS clusters, we can nevertheless gain some insight by fitting the individual formation redshift for each cluster. Using the sbSP and cSFR models, we interpret the

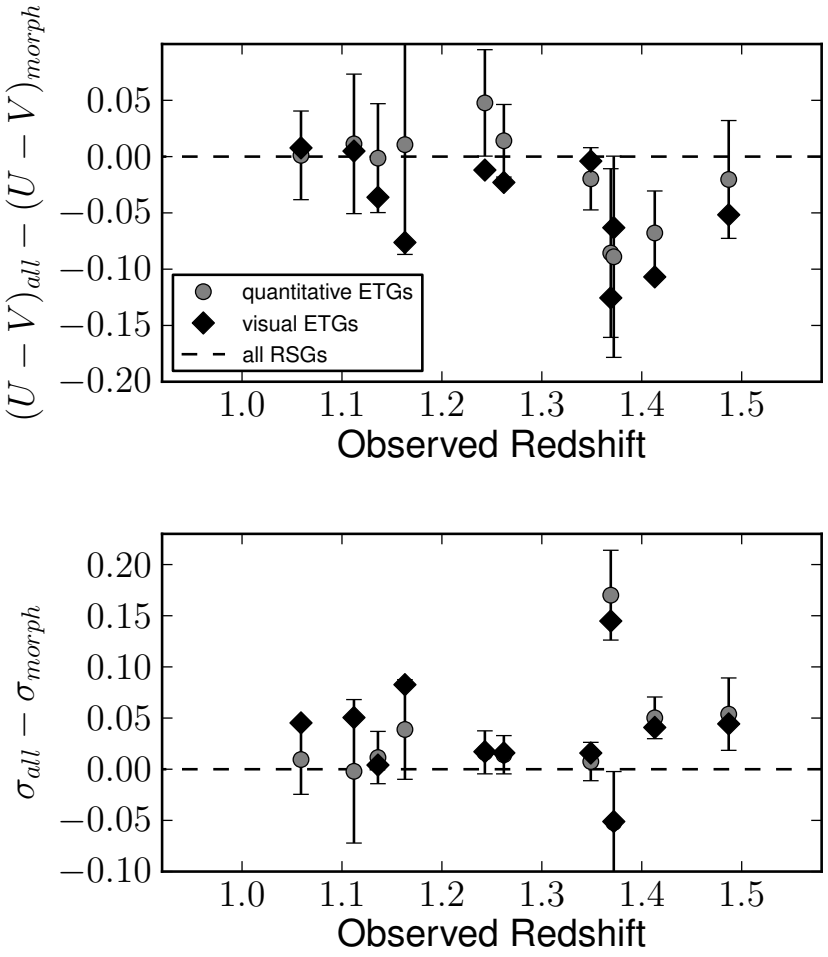

Figure 5.6.—: Demonstration of the effect of our morphological selection, in terms of colors (top) and scatters (bottom). Here we plot the change in measured CMR quantities when we turn off our morphology cut. In the top panel, a negative number occurs when the CMR of ETGs is on average redder than CMR of all RSGs in the cluster. In the bottom panel, a positive number occurs when the CMR of ETGs is on average narrower than the CMR of all RSGs in the cluster. Although weakly, the data imply the existence of bluer/younger non-ETGs on the red sequence in clusters above $z \sim 1.3$. One interpretation of this trend is as evidence of ongoing morphological transformations of relatively young late-type galaxies into cluster ellipticals. However, these in-situ color differences do not account for all evolution in the median formation epoch seen in Figure 5.5. Therefore, a significant fraction of ETG luminosity at $z \sim 1$ was assembled from outside the cluster cores (or at least, outside the ETGs' progenitors) since $z \sim 1.5$, and composed of relatively younger stellar populations.

derived ages as the average time elapsed since the last major epoch of star formation in the galaxies currently making up the red sequence.

The trends of §5.5.1 imply a tight positive correlation between a cluster's observed redshift and its inferred star formation epoch. Below $z \approx 1.3$, these cluster RSGs resemble a single burst with $\langle z_f \rangle \approx 2.0$ (or $z_{\rm end} \approx 1.5$), while higher-redshift clusters have $\langle z_f \rangle \gtrsim 3.0$ ($z_{\rm end} \gtrsim 2.0$). We plot these fitted values in Figure 5.7. Error bars are calculated by fitting the endpoints of the one-sigma color and scatter ranges in the same manner. These data are compiled in Table 5.4. *In the lower-redshift subsample, no clusters exist that are the evolutionary continuation of clusters at higher z along the cSFR or sbSP tracks.*

Figure 5.8 and Table 5.5 show the same information, but converted into stellar ages, which we interpret as the average time since the last major star-formation epoch for galaxies on the red sequence. These trends are qualitatively similar regardless of the property-model combination applied, sbSP color, cSFR color, or cSFR scatter. The scatter measurements in the bottom panel of Figures 5.7 and 5.8 show the same general trend with redshift as the median color measurements of the top two panels: clusters in this sample at higher redshift indicate an earlier formation epoch. Therefore the time elapsed since the last major star forming eposide appears roughly constant, yielding a luminosity-weighted average age of $\approx 2.3 \pm 0.6$ Gyr, consistent with the timescales inferred from rest-frame optical color scatters by Meyers et al. (2012) using the models of van Dokkum & Franx (2001) for seven of these clusters.

Numerically, the best-fit ages show a large scatter, ~ 0.5 to 1 Gyr, between when they are based on the scatter and when based on median color. It may be that the

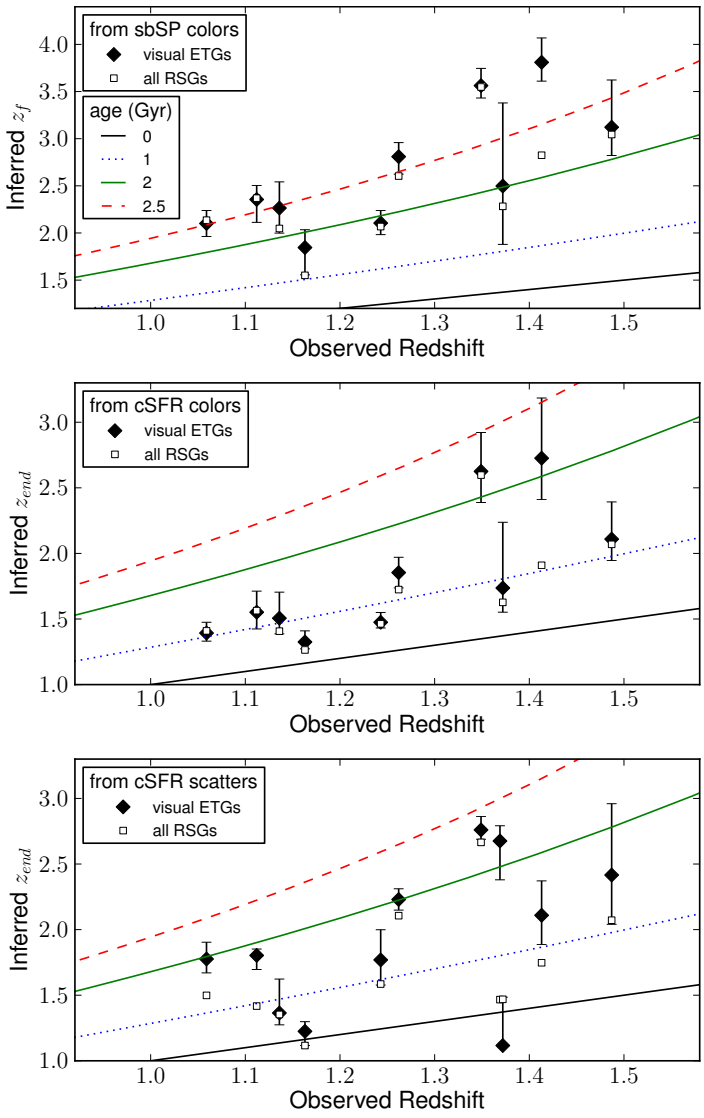

Figure 5.7.—: Inferred formation redshifts, corresponding to the same rows as Figure 5.5. The values in the top, middle, and bottom figures are inferred from our sbSP color, cSFR color, and cSFR color scatter models, respectively (Section 5.4). Here we employ visual morphological classification for the solid black diamonds and show the results for the entire RSG subsample as the open squares. Cluster ISCS J1433.8+3325 ($z = 1.369$) does not appear in the top two panels (nor in the visual ETG sample in the bottom panel) because its CMR color indicates $z_f > 6$ ($z_{\rm end} > 4$). In all cases, the inferred red sequence formation epoch is later in lower-redshift clusters, suggesting a combination of ongoing accretion of younger stars by the massive cluster galaxies during this epoch and/or formation of younger cluster ETGs. This extends the results found by, e.g., Mei et al. (2009) and Jaffé et al. (2011) that the formation redshift inferred by SSPs increases with redshift.

simple star formation histories we assumed were inadequate. For example, at a fixed red sequence color (and hence "age"), the color scatter between red sequence members can be made arbitrarily small by increasing the extent to which their star formation histories are correlated. Thus one possibility is that the formation histories of galaxies in some clusters are more uniform than others.

Table 5.4. Inferred CMR formation epochs.

Name	z	$\langle z_f \rangle$ Vis. ETGs	$\langle z_f \rangle$ Quant. ETGs	$\langle z_f \rangle$ All RSGs	$z_{\rm end}$ Vis. ETGs	$z_{\rm end}$ Quant. ETGs	$z_{\rm end}$ All RSGs
			From sbSP Colors				
ISCS J1429.2+3357	1.059	$2.10^{+0.14}_{-0.14}$	$2.12^{+0.17}_{-0.18}$	$2.15^{+0.14}_{-0.15}$	···	···	···
ISCS J1432.4+3332	1.112	$2.36^{+0.15}_{-0.25}$	$2.28^{+0.21}_{-0.27}$	$2.38^{+0.15}_{-0.28}$	···	···	···
ISCS J1426.1+3403	1.136	$2.24^{+0.28}_{-0.24}$	$2.05^{+0.20}_{-0.13}$	$2.04^{+0.18}_{-0.12}$	···	···	···
ISCS J1426.5+3339	1.163	$1.85^{+0.19}_{-0.29}$	$1.54^{+0.29}_{-0.04}$	$1.55^{+0.23}_{-0.02}$	···	···	···
ISCS J1434.5+3427	1.243	$2.10^{+0.14}_{-0.12}$	$1.89^{+0.13}_{-0.22}$	$2.07^{+0.11}_{-0.11}$	···	···	···
ISCS J1429.3+3437	1.262	$2.81^{+0.15}_{-0.19}$	$2.50^{+0.19}_{-0.15}$	$2.62^{+0.17}_{-0.17}$	···	···	···
ISCS J1432.6+3436	1.349	$3.57^{+0.21}_{-0.14}$	$3.67^{+0.25}_{-0.13}$	$3.55^{+0.12}_{-0.10}$	···	···	···
ISCS J1433.8+3325[a]	1.369	> 6	> 6	$8.86^{+0.91}_{-5.03}$	···	···	···
ISCS J1434.7+3519	1.372	$2.54^{+0.88}_{-0.64}$	$2.71^{+0.72}_{-0.39}$	$2.27^{+0.21}_{-0.39}$	···	···	···
ISCS J1438.1+3414	1.413	$3.79^{+0.23}_{-0.19}$	$3.56^{+0.15}_{-0.27}$	$2.82^{+0.30}_{-0.19}$	···	···	···
ISCS J1432.4+3250	1.487	$3.14^{+0.49}_{-0.30}$	$2.84^{+0.37}_{-0.22}$	$2.73^{+0.20}_{-0.16}$	···	···	···
			From cSFR Colors				
ISCS J1429.2+3357	1.059	$2.17^{+0.16}_{-0.10}$	$2.19^{+0.21}_{-0.15}$	$2.21^{+0.19}_{-0.11}$	$1.39^{+0.09}_{-0.06}$	$1.41^{+0.11}_{-0.09}$	$1.42^{+0.10}_{-0.07}$
ISCS J1432.4+3332	1.112	$2.44^{+0.25}_{-0.24}$	$2.33^{+0.34}_{-0.20}$	$2.46^{+0.31}_{-0.26}$	$1.56^{+0.16}_{-0.14}$	$1.50^{+0.20}_{-0.12}$	$1.57^{+0.19}_{-0.15}$
ISCS J1426.1+3403	1.136	$2.31^{+0.32}_{-0.17}$	$2.17^{+0.15}_{-0.10}$	$2.17^{+0.13}_{-0.09}$	$1.49^{+0.19}_{-0.11}$	$1.41^{+0.09}_{-0.06}$	$1.41^{+0.08}_{-0.05}$
ISCS J1426.5+3339	1.163	$2.01^{+0.17}_{-0.10}$	$1.88^{+0.11}_{-0.08}$	$1.89^{+0.09}_{-0.06}$	$1.33^{+0.09}_{-0.06}$	$1.25^{+0.07}_{-0.03}$	$1.26^{+0.04}_{-0.03}$
ISCS J1434.5+3427	1.243	$2.22^{+0.13}_{-0.08}$	$2.11^{+0.07}_{-0.08}$	$2.21^{+0.08}_{-0.08}$	$1.48^{+0.07}_{-0.05}$	$1.40^{+0.03}_{-0.04}$	$1.46^{+0.06}_{-0.05}$
ISCS J1429.3+3437	1.262	$2.84^{+0.20}_{-0.19}$	$2.53^{+0.19}_{-0.10}$	$2.64^{+0.18}_{-0.13}$	$1.84^{+0.13}_{-0.11}$	$1.68^{+0.10}_{-0.06}$	$1.73^{+0.10}_{-0.07}$
ISCS J1432.6+3436	1.349	$3.89^{+0.45}_{-0.30}$	$4.16^{+0.39}_{-0.34}$	$3.85^{+0.30}_{-0.22}$	$2.62^{+0.34}_{-0.25}$	$2.83^{+0.33}_{-0.26}$	$2.59^{+0.23}_{-0.18}$
ISCS J1433.8+3325[a]	1.369	> 6	> 6	$8.87^{+0.23}_{-4.50}$	> 6	> 6	$9.22^{+0.55}_{-6.23}$

Table 5.4—Continued

Name	z	$\langle z_f \rangle$ Vis. ETGs	$\langle z_f \rangle$ Quant. ETGs	$\langle z_f \rangle$ All RSGs	$z_{\rm end}$ Vis. ETGs	$z_{\rm end}$ Quant. ETGs	$z_{\rm end}$ All RSGs
ISCS J1434.7+3519	1.372	$2.63^{+0.79}_{-0.33}$	$2.75^{+0.70}_{-0.32}$	$2.40^{+0.19}_{-0.12}$	$1.76^{+0.51}_{-0.19}$	$1.84^{+0.46}_{-0.19}$	$1.62^{+0.11}_{-0.07}$
ISCS J1438.1+3414	1.413	$3.98^{+0.54}_{-0.39}$	$3.52^{+0.29}_{-0.26}$	$2.82^{+0.30}_{-0.13}$	$2.69^{+0.42}_{-0.30}$	$2.34^{+0.22}_{-0.17}$	$1.91^{+0.17}_{-0.09}$
ISCS J1432.4+3250	1.487	$3.16^{+0.36}_{-0.30}$	$2.87^{+0.34}_{-0.17}$	$2.80^{+0.14}_{-0.14}$	$2.13^{+0.26}_{-0.18}$	$1.96^{+0.21}_{-0.12}$	$1.90^{+0.11}_{-0.09}$
			From cSFR Scatters				
ISCS J1429.2+3357	1.059	$2.81^{+0.17}_{-0.14}$	$2.44^{+0.26}_{-0.23}$	$2.39^{+0.18}_{-0.19}$	$1.77^{+0.12}_{-0.09}$	$1.54^{+0.17}_{-0.12}$	$1.51^{+0.10}_{-0.10}$
ISCS J1432.4+3332	1.112	$2.79^{+0.12}_{-0.12}$	$2.27^{+0.54}_{-0.49}$	$2.21^{+0.43}_{-0.31}$	$1.77^{+0.09}_{-0.07}$	$1.47^{+0.32}_{-0.28}$	$1.43^{+0.25}_{-0.19}$
ISCS J1426.1+3403	1.136	$2.13^{+0.41}_{-0.17}$	$2.27^{+0.33}_{-0.21}$	$2.12^{+0.19}_{-0.10}$	$1.38^{+0.24}_{-0.10}$	$1.47^{+0.19}_{-0.14}$	$1.37^{+0.12}_{-0.05}$
ISCS J1426.5+3339[a]	1.163	$1.73^{+0.22}_{-0.55}$	< 2	< 2	$1.20^{+0.09}_{-0.08}$	< 1.2	< 1.2
ISCS J1434.5+3427	1.243	$2.75^{+0.33}_{-0.34}$	$2.75^{+0.28}_{-0.32}$	$2.41^{+0.26}_{-0.12}$	$1.79^{+0.20}_{-0.20}$	$1.79^{+0.19}_{-0.19}$	$1.59^{+0.16}_{-0.08}$
ISCS J1429.3+3437	1.262	$3.40^{+0.08}_{-0.13}$	$3.39^{+0.10}_{-0.15}$	$3.24^{+0.14}_{-0.26}$	$2.23^{+0.07}_{-0.08}$	$2.22^{+0.08}_{-0.10}$	$2.12^{+0.10}_{-0.18}$
ISCS J1432.6+3436	1.349	$4.09^{+0.12}_{-0.11}$	$4.03^{+0.09}_{-0.15}$	$3.97^{+0.12}_{-0.13}$	$2.76^{+0.11}_{-0.09}$	$2.70^{+0.09}_{-0.09}$	$2.67^{+0.09}_{-0.09}$
ISCS J1433.8+3325	1.369	$3.99^{+0.16}_{-0.43}$	$4.16^{+0.37}_{-0.34}$	$2.09^{+0.17}_{-0.25}$	$2.68^{+0.12}_{-0.31}$	$2.81^{+0.33}_{-0.26}$	$1.46^{+0.07}_{-0.35}$
ISCS J1434.7+3519[a]	1.372	< 2	< 2	$2.12^{+0.19}_{-0.27}$	< 1.5	< 1.5	$1.47^{+0.09}_{-0.36}$
ISCS J1438.1+3414	1.413	$3.20^{+0.38}_{-0.39}$	$3.37^{+0.42}_{-0.27}$	$2.61^{+0.11}_{-0.12}$	$2.13^{+0.25}_{-0.23}$	$2.25^{+0.29}_{-0.20}$	$1.76^{+0.07}_{-0.07}$
ISCS J1432.4+3250	1.487	$3.60^{+0.77}_{-0.60}$	$3.81^{+0.98}_{-0.73}$	$2.79^{+0.14}_{-0.14}$	$2.43^{+0.58}_{-0.39}$	$2.58^{+0.77}_{-0.48}$	$1.89^{+0.11}_{-0.08}$

[a]In some cases, fitting resulted in seemingly unphysical parameters — e.g. galaxies formed earlier than our code permitted ($\sim 5 \times 10^8$ years) or have a negative age — in these cases we give a one-sided estimate.

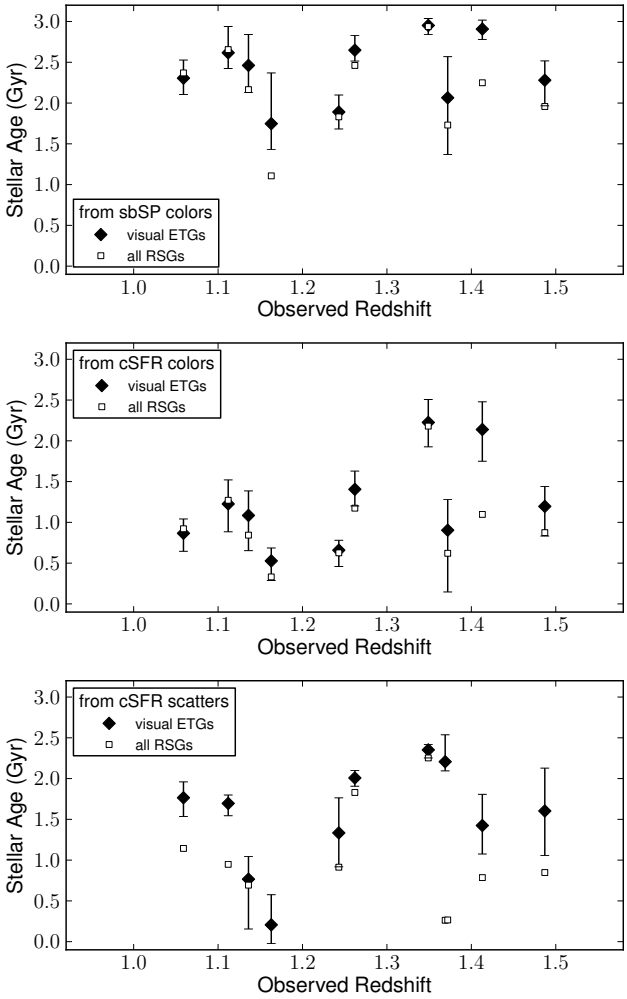

Figure 5.8.—: Inferred ages, corresponding to the same rows as Figure 5.5. The values in the top, middle, and bottom figures are inferred from our sbSP color, cSFR color, and cSFR color scatter models, respectively (Section 5.4). Here we employ visual morphological classification for the solid black diamonds and show the results for the entire RSG subsample as the open squares. Cluster ISCS J1433.8+3325 ($z = 1.369$) does not appear in the top two panels (nor in the visual ETG sample in the bottom panel) because its CMR color indicates an age $\gtrsim 4$ Gyr.

Table 5.5. Inferred CMR ages, in Gyr.

Name	z	Vis. ETGs	Quant. ETGs	All RSGs
		Stellar Age, $t_{\rm obs} - \langle t_f \rangle$, from sbSP Colors		
ISCS J1429.2+3357	1.059	$2.30^{+0.21}_{-0.23}$	$2.33^{+0.23}_{-0.29}$	$2.38^{+0.19}_{-0.23}$
ISCS J1432.4+3332	1.112	$2.66^{+0.17}_{-0.34}$	$2.57^{+0.25}_{-0.39}$	$2.69^{+0.17}_{-0.37}$
ISCS J1426.1+3403	1.136	$2.44^{+0.34}_{-0.36}$	$2.16^{+0.30}_{-0.21}$	$2.15^{+0.26}_{-0.19}$
ISCS J1426.5+3339	1.163	$1.73^{+0.33}_{-0.61}$	$1.09^{+0.61}_{-0.11}$	$1.10^{+0.49}_{-0.06}$
ISCS J1434.5+3427	1.243	$1.89^{+0.19}_{-0.19}$	$1.55^{+0.22}_{-0.43}$	$1.83^{+0.16}_{-0.17}$
ISCS J1429.3+3437	1.262	$2.66^{+0.13}_{-0.18}$	$2.34^{+0.20}_{-0.18}$	$2.47^{+0.17}_{-0.19}$
ISCS J1432.6+3436	1.349	$2.95^{+0.11}_{-0.09}$	$3.01^{+0.13}_{-0.08}$	$2.94^{+0.07}_{-0.06}$
ISCS J1433.8+3325[a]	1.369	> 3	> 3	$4.13^{+0.07}_{-1.09}$
ISCS J1434.7+3519	1.372	$2.06^{+0.74}_{-0.89}$	$2.24^{+0.56}_{-0.43}$	$1.73^{+0.26}_{-0.60}$
ISCS J1438.1+3414	1.413	$2.90^{+0.11}_{-0.10}$	$2.77^{+0.09}_{-0.17}$	$2.23^{+0.25}_{-0.18}$
ISCS J1432.4+3250	1.487	$2.30^{+0.32}_{-0.25}$	$2.06^{+0.29}_{-0.21}$	$1.95^{+0.18}_{-0.16}$
		Stellar Age, $t_{\rm obs} - t_{\rm end}$, from cSFR Colors		
ISCS J1429.2+3357	1.059	$0.86^{+0.23}_{-0.18}$	$0.90^{+0.29}_{-0.26}$	$0.93^{+0.25}_{-0.20}$
ISCS J1432.4+3332	1.112	$1.30^{+0.35}_{-0.35}$	$1.16^{+0.45}_{-0.32}$	$1.32^{+0.40}_{-0.38}$
ISCS J1426.1+3403	1.136	$1.05^{+0.43}_{-0.28}$	$0.84^{+0.23}_{-0.17}$	$0.83^{+0.21}_{-0.15}$
ISCS J1426.5+3339	1.163	$0.52^{+0.25}_{-0.17}$	$0.30^{+0.20}_{-0.10}$	$0.32^{+0.13}_{-0.08}$
ISCS J1434.5+3427	1.243	$0.66^{+0.17}_{-0.14}$	$0.47^{+0.09}_{-0.10}$	$0.63^{+0.14}_{-0.12}$
ISCS J1429.3+3437	1.262	$1.39^{+0.22}_{-0.20}$	$1.07^{+0.20}_{-0.14}$	$1.19^{+0.19}_{-0.15}$
ISCS J1432.6+3436	1.349	$2.21^{+0.32}_{-0.28}$	$2.41^{+0.27}_{-0.26}$	$2.18^{+0.23}_{-0.21}$
ISCS J1433.8+3325[a]	1.369	> 3	> 3	$4.16^{+0.04}_{-1.66}$
ISCS J1434.7+3519	1.372	$0.90^{+0.83}_{-0.41}$	$1.06^{+0.71}_{-0.39}$	$0.63^{+0.22}_{-0.16}$
ISCS J1438.1+3414	1.413	$2.11^{+0.36}_{-0.32}$	$1.72^{+0.26}_{-0.23}$	$1.07^{+0.28}_{-0.16}$
ISCS J1432.4+3250	1.487	$1.24^{+0.34}_{-0.28}$	$0.96^{+0.32}_{-0.21}$	$0.87^{+0.18}_{-0.16}$
		Stellar Age, $t_{\rm obs} - t_{\rm end}$, from cSFR Scatters		
ISCS J1429.2+3357	1.059	$1.75^{+0.22}_{-0.18}$	$1.24^{+0.38}_{-0.31}$	$1.18^{+0.24}_{-0.25}$
ISCS J1432.4+3332	1.112	$1.75^{+0.16}_{-0.14}$	$1.07^{+0.71}_{-0.82}$	$0.97^{+0.60}_{-0.54}$
ISCS J1426.1+3403	1.136	$0.76^{+0.60}_{-0.29}$	$1.00^{+0.45}_{-0.37}$	$0.74^{+0.32}_{-0.16}$
ISCS J1426.5+3339[a]	1.163	$0.12^{+0.28}_{-0.28}$	< 0.1	< 0.1
ISCS J1434.5+3427	1.243	$1.36^{+0.36}_{-0.43}$	$1.35^{+0.33}_{-0.40}$	$0.93^{+0.34}_{-0.18}$
ISCS J1429.3+3437	1.262	$2.01^{+0.09}_{-0.11}$	$1.99^{+0.11}_{-0.14}$	$1.85^{+0.14}_{-0.29}$
ISCS J1432.6+3436	1.349	$2.35^{+0.10}_{-0.08}$	$2.29^{+0.09}_{-0.09}$	$2.26^{+0.09}_{-0.09}$

Table 5.5—Continued

Name	z	Vis. ETGs	Quant. ETGs	All RSGs
ISCS J1433.8+3325	1.369	$2.21^{+0.12}_{-0.34}$	$2.34^{+0.27}_{-0.26}$	$0.25^{+0.18}_{-1.06}$
ISCS J1434.7+3519[a]	1.372	< 0.1	< 0.1	$0.27^{+0.23}_{-1.08}$
ISCS J1438.1+3414	1.413	$1.42^{+0.34}_{-0.38}$	$1.60^{+0.35}_{-0.28}$	$0.80^{+0.13}_{-0.14}$
ISCS J1432.4+3250	1.487	$1.64^{+0.57}_{-0.53}$	$1.80^{+0.65}_{-0.61}$	$0.85^{+0.18}_{-0.16}$

[a]In some cases, fitting resulted in seemingly unphysical parameters — e.g. galaxies formed earlier than our code permitted ($\sim 5 \times 10^8$ years) or have a negative age — in these cases we give a one-sided estimate.

5.5.4 Qualitative Discussion of CMR Assumption

Several additional features pertaining to cluster galaxy evolution are seen in these data. Specifically, since the cluster selection technique does not depend directly on the presence of a canonical red sequence, these CMRs have a wide variety of properties.

In nearly all cases, the cluster red sequence spans a factor of at least ~ 10 in brightness, indicating that cluster ETGs spanning the range $L \approx 0.3$ to 3 L^* are present by $z \sim 1.5$. On the other hand, we measure several clusters with very tenuous or wide RSs. ISCS J1426.5+3339 ($z = 1.163$), ISCS J1434.7+3519 ($z = 1.372$), ISCS J1433.8+3325 ($z = 1.369$), and ISCS J1432.4+3250 ($z = 1.487$) all contain an over-density of red galaxies that are near the expected red sequence color but do not define the canonical locus in color-magnitude space consistent with a single CMR of old galaxies.

Moreover, clusters ISCS J1429.2+3357 ($z = 1.059$), ISCS J1432.6+3436 ($z = 1.349$), and ISCS J1434.5+3427 ($z = 1.243$) appear to have red sequences where the red sequence is deficient in ETGs at $L < 0.3$ L^*. Furthermore, ISCS J1434.5+3427 ($z = 1.243$) and ISCS J1438.1+3414 ($z = 1.413$) have 5 to 10 RSGs at $L < L^*$ that are bluer by up to ~ 0.4 magnitudes than the most apparent CMR, comprising $\approx 30\%$ of the red sequence galaxies. We also notice a large number of early-type galaxies that are as bright and brighter than the red sequence we identified for ISCS J1438.1+3414 ($z = 1.413$), and that are ~ 1 magnitude bluer. However, they are likely interlopers based on their projected spatial offset (> 0.5 Mpc) from the cluster center and association with a known foreground structure.

Taken together with the quantitative results described above, these qualitative

properties outline a picture whereby some massive cluster ETGs (ellipticals and S0s) are in place in many clusters, but perhaps not all, by $z \approx 1.5$, with stellar populations formed at $\langle z_f \rangle > 3$. At $z \sim 1$, the stellar populations of the ETGs in this sample appear more recently formed, on average by ≈ 1 Gyr, having $\langle z_f \rangle \sim 2$.

5.6 Discussion

We analyzed the rest-frame optical CMRs of red sequence galaxies in 11 spectroscopically confirmed, infrared-selected massive galaxy clusters at $1.0 < z < 1.5$. Clustering (Brodwin et al. 2007), extended X-ray emission (Brodwin et al. 2011), weak lensing (Jee et al. 2011), and stellar masses (Eisenhardt et al. 2008) support the view that these are massive ($M \gtrsim 10^{14} M_{\odot}$) clusters and are the precursors to present-day massive ($M \sim 10^{15} M_{\odot}$) clusters. These observations thus provide a valuable window into the evolution of galaxies within the most massive halos in the universe by revealing the time during which most of their stellar mass formed and assembled from smaller pieces.

5.6.1 Star Formation Histories of Cluster Ellipticals

The present data (Figure 5.7) indicate that massive, red ETGs existed in the centers of many rich clusters by at least $z = 1.5$. Other observations suggest this is true at even higher redshifts, both in massive, mature clusters (Stanford et al. 2012) and assembling structures or "proto-clusters" (e.g., Kurk et al. 2009). The red colors of these galaxies at $z \approx 1.5$ indicate that their luminosity-weighted age is ≈ 2 to 3 Gyr (a formation epoch of $z \sim 4$), and/or that the formation of stars then present ceased by ≈ 1 Gyr prior to

their observed state ($z \sim 2.5$).

This story is reminiscent of a "monolithic collapse" (Eggen et al. 1962), whereby the stars in these galaxies formed in a single short burst at a much earlier time. Massive cluster ETGs at $z \lesssim 1$ evolve in a manner consistent with this passively-evolving model (Bower et al. 1992; Ellis et al. 1997; Stanford et al. 1998; Mancone et al. 2010), although their rest-frame optical colors are consistent with a wide variety of potential formation epochs (e.g., the first panel of Figure 5.5).

The analysis presented here connects the low-redshift cluster galaxy population to their pasts by quantifying the stellar populations in cluster galaxies over a span of 1.5 Gyr following the end of the peak star formation activity in the universe at $z \sim 2$. The measurements of Section 5.5 suggest that the characteristic ages of the total stellar populations in massive RSGs are roughly the same across this cluster sample at $1 < z < 1.5$ (Figure 5.8). This manifests as an inferred star formation epoch z_f that continues to increase with the observed cluster redshift, as found previously in samples presented by, e.g., Mei et al. (2009) and Jaffé et al. (2011).

This is explained naturally if they experience significant stellar mass assembly during this epoch, a scenario we discuss in Sections 5.6.4–5.6.7 below. Alternatively, these observations could reflect drastic changes during this epoch in the nature of the galaxies/overdensities selected for this study, a possibility we consider in Sections 5.6.2–5.6.3.

5.6.2 The Impact of Cluster Mass

One factor that might confuse our analysis is if the nature of the clusters in the ISCS sample changes significantly over the redshift range we consider, or if they are fundamentally different structures than the progenitors of today's massive clusters, as our interpretation assumes. The correlation function of ISCS cluster candidates (Brodwin et al. 2007) implies that they are predominately $M > 10^{14} M_{\odot}$ structures and likely the precursors to today's massive ($\sim 10^{15} M_{\odot}$) clusters. Furthermore, for the spectroscopically confirmed subsample considered herein, clusters with sufficiently-deep X-ray observations (Brodwin et al. 2011) are detected at a significance consistent with their being $\gtrsim 10^{14} M_{\odot}$ objects (see also, Stanford et al. 2012). Finally, shear measurements by Jee et al. (2011) for *all* of these clusters with very deep imaging from the *HST* Cluster Supernova Survey (PI Perlmutter, GO-10496; see Dawson et al. 2009) yield individual (i.e., not stacked) weak–lensing masses comfortably above $10^{14} M_{\odot}$.

This does not preclude our spectroscopic subsample from containing a small number of structures that are somehow different than the remainder of the sample (for instance see ISCS J1433.8+3325 ($z = 1.369$) and ISCS J1429.2+3425 ($z = 1.162$)). Furthermore, the expected rapid assembly of cluster-mass halos at these redshifts implies significant changes to the cluster galaxy population resulting from the incorporation of external groups via mergers, changes that might occur stochastically and lead to the outliers we observe in particular cases. Therefore the stellar-mass selection employed for this sample is effective at selecting cluster-size objects whose galaxy populations are not required to be fully evolved, permitting the analysis of a more diverse set of evolutionary paths in massive clusters. The fact that these clusters, which have similar stellar masses owing to

their selection, exhibit similar colors implies that they had similar rates of star formation in their recent pasts. This matches our conclusion that massive cluster galaxies star formation over an extended period at $1 < z < 1.5$.

5.6.3 The Effect of Reddening

Significant dust attenuation in cluster galaxies would bias our measurements toward a redder color, although we have no reason to believe that these ETGs contain an unusual amount of dust. If we posit that galaxies follow an evolutionary path from star-forming disks, through quenching, and ultimately to red-and-dead galaxies, then it is not clear that ETGs at higher redshift will have significantly more dust obscuration than those at $z \ll 1$. Meyers et al. (2012) analyzed the ETGs in a set of clusters that includes seven members of the ISCS, and found that these galaxies, some of which are on the red sequences in the present work, likely experience little dust reddening: $E(B-V) \lesssim 0.06$.

If cluster ETGs at $z \gtrsim 1.3$ are more highly obscured than their lower-redshift counterparts, but reflect the same general star formation histories (suggesting $z_f \approx 2$), then cluster galaxies would appear redder (Eisenhardt et al. 2008) and fainter (Mancone et al. 2010). Line emission may also bias the present measurements to the red, since the WFC3/F160W filter includes the $H\alpha$ line for clusters at $1.14 < z < 1.55$. However, WFC3/G141 spectra (Zeimann et al. in prep.) indicate weak $H\alpha$ emission in most of these RSGs. Furthermore, if either of these effects cause the red colors, we would expect significant variation between objects, and so the red sequence color scatters would systematically *increase* with redshift, contrary to the constant or decreasing scatters we found in Section 5.5.3.

This does not mean that dust plays no role at these redshifts. At least one cluster's CMD (ISCS J1434.5+3427 ($z = 1.243$)) contains a spectroscopically confirmed member (Wagg et al. 2012) satisfying the dust-obscured galaxy (DOG) criteria of Dey et al. (2008). In addition, some objects (spectroscopic members or otherwise) are very red members of the clusters' red sequences. If this reflects contamination of the red sequences by dusty galaxies then our colors and/or color scatters may be biased high in some cases, an effect we expect to get larger at higher redshifts owing to the increasing presence of dusty starbursts. This may also contribute to several of the outliers mentioned in Section 5.5.4.

Importantly, if dust or line emission do play a role in contaminating the red sequences or reddening cluster ETGs at $z \sim 1.5$, then it can only strengthen our conclusions that we are beginning to witness a period during which significant star formation activity recently occurred in massive central cluster galaxies.

5.6.4 Luminosity Evolution

Star formation over an extended period implies that cluster red sequences should be growing in stellar mass, and this implies evolution in the galaxy luminosity function shape or normalization, scenarios that have been explored in the ISCS by exploiting the rest-frame near-IR data obtained with *Spitzer*. Mancone et al. (2010) found that above $z \sim 1.3$, cluster galaxies are ≈ 0.5 magnitudes fainter at 3.6 and $4.5\mu m$ than one would expect from the extrapolation of their lower-redshift evolution, positing significant ongoing assembly at this epoch, leading to a rapid increase in luminosity with time. This conclusion, as well as the one consistent with the present work by Eisenhardt

et al. (2008), is based on a sample of cluster galaxies that does not apply a color or morphological selection, lending more evidence to the notion that stellar mass must be actively increasing in cluster member progenitors. Rather than the entirety of such evolution being caused by progenitor bias, we are likely witnessing the effect of real growth in the stellar mass of some cluster galaxies.

The results by Mancone et al. (2010) and Eisenhardt et al. (2008) were based on photometric cluster members within 1.5 and 1.0 projected Mpc, respectively, of the cluster candidate's center. Like we posit for the present work, those studies may track a galaxy sample that misses stellar mass that formed outside of these regions, or in galaxies not bright enough to be selected. Thus we suggest the luminosity growth in massive cluster galaxies at these redshifts is due in part to star formation that occurred over an extended period, rather than arising entirely from the merging of equally old progenitors.

5.6.5 Red Sequence Growth

Then what is the star formation and assembly history of massive cluster galaxies? The data in Figure 5.5 are consistent with each cluster's ETGs forming at a different time, as the sbSP models with $z_f = 2$ to 6 roughly bracket the observed colors. We might reasonably expect that the star formation epoch of the massive galaxies in one cluster differs from another based on the assembly history or halo mass, and that differences in this history are small enough to have damped out by $z \lesssim 1$.

However, cluster galaxies in the present sample at $1.0 < z < 1.3$ tend to be bluer than those implied by the continued passive evolution of the clusters at $z > 1.3$: any sbSP ($z_f \gtrsim 3$) that fits the high-redshift clusters is too red for the lower-redshift ones,

suggesting that the colors of massive cluster galaxies might evolve in a manner altogether different from the commonly-used simple sbSP and time-uniform composite models considered in Section 5.4. Such evolution has been observed for some time (Bell et al. 2004; Brown et al. 2007) in surveys of massive field galaxies. Additional significant growth of the massive red galaxy population occurs at $z > 1$ (Kriek et al. 2008; van Dokkum et al. 2008; Taylor et al. 2009; Whitaker et al. 2010), and this may be likely true in all environments. We therefore consider the possibility that our cluster sample selects, at least in part, a continuous evolutionary sequence that experiences star formation over an extended period leading to an increase in stellar mass on the red sequence.

Importantly, for the ETGs to reside on the red sequence and maintain a nearly-constant luminosity-weighted age as we observe, the red sequence must accrete newer stars in some fashion, making the CMR bluer than one which evolves passively. Moreover, the newer stars or galaxies must have ceased forming some time ago ($\gtrsim$ 100 Myr) in order to be considered RSGs, and must comprise a body of stellar mass that was experiencing an *increasing* star formation rate prior to its quenching. Otherwise the observed luminosity-weighted age would increase with time. Thus, these stars likely formed in gas-rich, rapidly star-forming objects that are not found in large numbers on the red sequence in the centers of their progenitor clusters. In this picture, the halting of star formation in massive cluster ETGs does not occur suddenly and absolutely in every galaxy of the final cluster, but continuously, during or after periods of significant gas accretion in objects that eventually make up the final, present-day ETGs.

With this interpretation, the CMRs of these clusters may reflect in part the ongoing growth of galaxies in the cluster centers as they accrete or form younger stars not present at a previous time, as well as the transformation from star-forming to quiescent galaxies.

The latter is the canonical in-situ progenitor bias of van Dokkum & Franx (2001), who described this effect at $z < 1$ for satellite galaxies, which exhibit remarkable constancy in their optical colors and color scatters over time. We now see this same result in massive cluster ETGs (Figure 5.5), and we showed in Section 5.5.2 that the transformations of late-type RSGs into ETGs are not sufficient to account for the entirety of the evolution we observe in the CMR formation epochs. Therefore another form of progenitor bias likely contributes, in which the red galaxy samples in the cluster centers gain stellar mass over time from outside the RSG sample in order to achieve roughly constant colors and scatters.

Contrast this result with a mass-selected field galaxy sample at comparable redshifts such as that considered by Whitaker et al. (2010), who found that the color scatter of field RSGs increases rapidly from $z = 1$ to $z = 1.5$. This likely owes to the way our sample of massive cluster galaxies were selected: we require them to exist in the center of a cluster, the bottom of a deep potential well that continuously collects significant amounts of stellar mass. We see only those galaxies and stars present there at the time we observe them, but may miss a significant amount of stellar mass that formed in massive galaxies *outside* the central ETGs at $z \lesssim 2$ to 3.

5.6.6 Models of Ongoing Assembly

We now seek an understanding of the impact of stellar mass assembly on the appearance of cluster cores over this redshift range. Previous work (e.g., van Dokkum & Franx 2001) highlighted the effect of "progenitor bias", whereby galaxies identified as ETGs or RSGs at one redshift are not selected in comparable higher or lower redshift samples. Potential

causes of this effect include the continued formation or growth of these galaxies, bursts of star formation in RSGs, and/or the transformation of star-forming disk galaxies into RSGs/ETGs via merging or other processes. Therefore we expect this and similar effects to be apparent in this sample.

As galaxies form stars, possibly merge, and eventually experience quenching as they fall into the center of the assembling halo, significant amounts of time may pass before they become incorporated into what we see as galaxies in the cluster center. Also, massive galaxies are thought to accrete a significant fraction of their stellar mass from their environment, through numerous minor mergers or smooth accretion (e.g., Kereš et al. 2005; White et al. 2007; Dekel et al. 2009; Oser et al. 2010). In this way massive galaxies experience assembly of structures that alter their average stellar population with time. If the stellar ages of the new material are different enough from those already assembled, then arbitrary paths through the space of inferred ages (through a simple proxy such as color) are possible, depending on the precise history of assembly.

In any case, the salient result of this structure growth is that the cluster cores grow in stellar mass density, a generic process for which we seek an intuitive description in terms of the quantities we measure here. A complete specification of the different star formation histories in massive structures is beyond the scope this work, yet simple models can demonstrate the key characteristics expected of galaxies that evolve in this fashion. For this purpose we apply three such models inspired by van Dokkum & Franx (2001) that differ only in the time delay between when a galaxy's stars are formed and when they are incorporated into the ETG sample. Model galaxies that have formed within Δt of the observation time are masked from the corresponding CMR model, mimicking the time before a galaxy would be identified as an ETG or RSG in the center of a cluster.

This procedure has been used previously (for example, Jaffé et al. 2011) to analyze the evolution of cluster galaxies using their red sequence colors and scatters.

This delay, and its time evolution, could represent various physical scenarios, including galaxies that experience a small burst that removes them from the red sequence, galaxies that have not yet entered the center of the cluster, and galaxies that are not bright enough to be detected in the sample. We do not apply any color cuts on these model CMRs: all model galaxies are assumed to be on the red sequence. If a particular choice of Δt leads to very blue galaxies, then the CMR model would be relatively blue on average. We could test an infinite number of choices for Δt, but our data can only reasonably constrain a small number of representative scenarios. Therefore we will test three such toy models in the hope of gaining some additional physical insight into the formation of massive cluster galaxies.

For the first two models we choose to demonstrate a constant Δt of 1.0 and 2.3 Gyr, roughly consistent with the $t_{\rm delay} \sim 2$ Gyr value found by Meyers et al. (2012) after utilizing models by van Dokkum & Franx (2001) to the optical color scatter in a subset of seven ISCS clusters. Our third model, "sudden infall", corresponds to sudden mass growth by assuming that Δt is a function of redshift, with a minimum of 200 Myr occurring at $z = 1.2$ but steeply rising to 2.3 Gyr before and after. Because galaxies that are younger than the existing RSGs are being added in large numbers to the CMR at $1.2 \lesssim z \lesssim 1.8$, this corresponds to a model red sequence that becomes bluer with time, where the amount of color variation depends on the suddenness of the assembly, the minimum delay time, as well as the closeness of the infall time to the time of peak SFR in the galaxies that eventually make up the cluster. In this case, because we track an estimate of the universal SFR, this peak occurs at $z \sim 2$ to 3.

To implement these models, we assume that each galaxy is formed in a single short burst and enters the cluster ETG sample in a first-made, first-in fashion exactly Δt after its formation. We simulate 10^5 sbSP tracks that form at a rate such that the final red sequence experienced the same star formation history in all three cases. To reduce the number of free parameters, we use models with the universal star formation history estimated by Hopkins & Beacom (2006). For simplicity we simulate only the galaxy color distribution and not the entire CMR.

These models have the beneficial features that a) the colors of the galaxy populations in higher redshift clusters are redder than one would expect given a monolithic collapse scenario with a single formation redshift, b) these colors are consistent with an earlier inferred star-formation epoch without necessarily leaving a redder descendent, and c) the final model "red sequences" have identical stellar populations, regardless of the details of their assembly history. Therefore they only reflect the consequences of (highly idealized) structure growth and do not depend on specific assumptions for the physics of star formation quenching in massive halos.

5.6.7 Colors and Scatters of Assembling Red Sequences

We plot the color and color scatter evolution of these assembly-inspired models as the gray curves in Figure 5.9. In the top panel we summarize the intrinsic U-V colors of our sample and compare it to data from the literature on clusters at $1.0 < z < 1.9$. In this panel, colors are computed relative to the Coma cluster and denoted $\Delta(U-V)_0$. The color scatters of cluster ETGs (Figure 5.9, bottom) agree largely with inferences made from their colors only, as seen in Figures 5.5, 5.7, and 5.6.

As seen in previous work, the immediate result of the delay between the galaxies' formation and their settling on the red sequence is that cluster red sequences continue to remain redder and narrower than any single sbSP or cSFR model implies, even while the red sequence is sparse or tenuous as observed in some cases (Section 5.5.4), presumably before they are fully formed.

The feature that inferred ages appear more or less constant at $z > 1$ is a natural consequence of the stars entering high-redshift ETG samples having been drawn from a history with an *increasing* star formation rate. This scenario was observed in distant galaxies ($z \gtrsim 3$) by, for example, Lee et al. (2011) and Papovich et al. (2011), suggesting that the galaxies in assembling clusters may be imprinted with this rising-SFR signature from their gas accretion epoch. In that case, for a given delay Δt, the dominant stellar population in the optical at any time resembles an sbSP formed a time Δt ago. Our third such model experiences a rapid decrease in the SF-assembly delay at $z = 1.2$, possibly mimicking the result of a dramatic enhancement to star formation in galaxies falling into the cluster, such as a merger with a star-forming group or a temporary increase in smooth gas accretion. This demonstrates one plausible effect that can make assembling CMRs bluer (or wider) for a time (cf. cluster ISCS J1426.5+3339 ($z = 1.163$)), which may be necessary or expected during this epoch. We do not claim that our data are yet able to constrain this type of model in detail, but these models do provide some evidence that such scenarios, and perhaps combinations thereof, might naturally occur in a sample like the ISCS.

Figure 5.9.—: Top: Evolution of the rest-frame U-V colors of $z > 1$ cluster galaxies, relative to Coma. Bottom: Rest-frame U-V scatters of cluster galaxies. We plot cluster data from the present work, and data compiled by Hilton et al. (2009)[a], including clusters from Blakeslee et al. (2003) and Mei et al. (2006a,b). We also include clusters CIG J0218.3-0510 (Papovich et al. 2010)[b], and two new clusters from the IRAC Deep Cluster Survey[c], IDCS 1426+3508 ($z = 1.75$; Stanford et al. 2012) and IDCS 1433+3306 ($z = 1.89$; Zeimann et al. 2012). The curves are different toy models for the stellar populations in massive ETGs at the centers of clusters. The solid red, green, and blue curves are the cSFR models corresponding to $z_{\rm end} = 3$, $z_{\rm end} = 1.8$, and $z_{\rm end} = 1.2$, which we described in Section 5.4. We show the simple alternatives of Section 5.6.6 in the gray curves: these models experience the same overall star formation histories (Hopkins & Beacom 2006), but differ in the time delay between the formation of stars in a galaxy and the time at which the galaxy becomes apparent in the cluster red sequence.

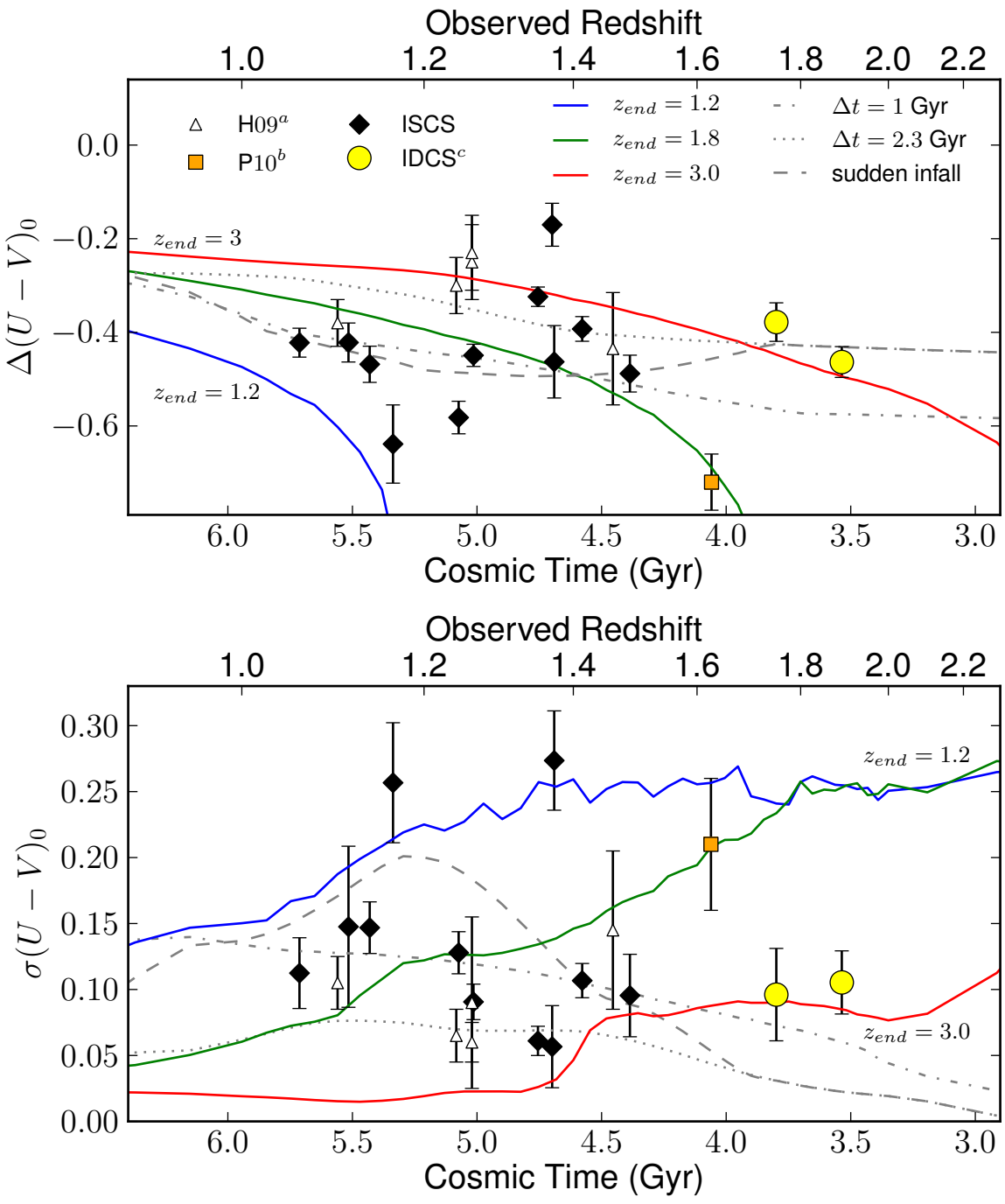

Figure 5.9.—: (Continued)

The color scatter measurements provide an additional constraint, because they reflect the extent to which the star formation episodes of the cluster ETGs (at fixed color) were correlated. We demonstrate specific variants of this in the bottom panel of Figure 5.9; the assembly-inspired models can yield the necessary slowly-varying (or increasing) color scatter as time progresses for clusters at $z > 1$. In these models, each "galaxy" is an uncorrelated sbSP formed at a random time such that the correct average SFH is borne out in a large sample. Therefore the correlation between model ETG star formation episodes reflects only the correlation implied by the underlying SFH (e.g., when it peaks, galaxies forming at that time will have correlated SFHs), and so any such scatter models could be considered as upper limits.

The model tracks we show in this work are ≈ 0.05 magnitudes bluer than clusters at $z < 1$, reflecting either a possible systematic offset in the photometric systems between the model and sample (here we merely quote the numeric values from the cited works), that cluster galaxies experience an earlier peak in their star formation than the SFH we assumed, or that massive cluster ETGs at low redshift have a slightly higher than solar metallicity.

While order-unity departures from roughly solar metallicity in cluster ETG stellar populations are inconsistent with their evolution at $z < 1$, the metallicity evolution in cluster ETG progenitors at $z \gg 1$ is unclear. The color and scatter trends we have observed here, at a fixed formation epoch ($z_f \sim 3$) using our sbSP or cSFR models, would imply that the luminosity-weighted average stellar metallicities decrease by a factor of ~ 5 during approximately 1 Gyr at $1 < z < 1.5$. This by itself is perhaps unphysical, but if it does contribute, it again implies stellar mass growth, in this idealized case owing to the incorporation of relatively low-mass (low-metallicity) galaxies. Like

our toy models at fixed metallicity but evolving average age, this scenario would suggest significant ongoing star formation near cluster cores, and assembly into cluster cores, over an extended period at $z \sim 1.5$. In reality both effects might contribute to the observed trends at this epoch, when assembling clusters contain massive galaxies (high-Z, early z_f), but grow their red sequences rapidly by incorporating or growing lower-mass (lower-Z, late z_f) galaxies (Raichoor et al. 2011).

In this work, we have not separated the elliptical versus S0 galaxy samples, and therefore the apparent evolution of the ETG population may owe to an increasing population of S0 galaxies (and not necessarily ellipticals) with time, extending the results of, e.g., Poggianti et al. (2009). Subsequent analyses will determine the evolution of the cluster galaxies' morphologies.

5.7 Conclusions

We studied sensitive, high-resolution, rest-frame optical imaging of the central regions in 13 spectroscopically confirmed infrared-selected galaxy clusters at $1 < z < 1.5$ that are plausible progenitors of today's massive clusters with $M \sim 10^{15} M_{\odot}$. In 11 of these clusters we measured the CMR of red galaxies at a color consistent with the cluster's known redshift, and subsequently we analyzed the stellar populations implied by the location and dispersion of the red sequence. We find the following:

1. Red sequences of bright galaxies are present in the centers of many clusters by $z = 1.5$. However, the properties of their CMRs indicate large cluster-to-cluster variations in the formation histories of cluster galaxies observed at a given redshift.

2. As a function of redshift from $z = 1.5$ to 1.0, the median rest-frame $U - V$ color of cluster galaxies in this sample is nearly constant at $(U - V)_0 \sim 1.0$, and the scatter about the median color is nearly constant at $\sigma_{\rm int} \sim 0.1$ magnitudes. Some clusters deviate widely from these trends, and outliers may represent contamination by dust-obscured galaxies, the evolution of galaxies through the "green valley", or red sequences that are not yet fully formed.

3. The flatness of the color and scatter trends at $1 < z < 1.5$ requires star formation histories more diverse than a single short burst in the past. These average trends are plausibly in part the result of progenitor bias, where the progenitors of lower-redshift cluster ETGs are excluded by the sample selection at higher redshifts.

4. Across this redshift range, these average colors and scatters both imply a roughly constant luminosity-weighted stellar age in the cluster RSGs, where the time since the bulk of stars formed is roughly 2 to 2.5 Gyr, and the time since star formation halted is roughly 1 to 2 Gyr.

5. A constant stellar age is a natural consequence of observing the center of an assembling halo whose final stellar population is experiencing ongoing or increasing star formation at the observed redshift. If the red sequence stars are nearly completely in place, they would reflect a small continuing star formation rate and their luminosity-weighted ages should increase with time. By contrast, at $z \sim 1.5$ our observations imply that significant current star formation is occuring that will contribute to the stellar populations of central cluster galaxies by $z \sim 1$.

6. Assuming the star formation of cluster galaxies follows that of other systems, the color and scatter trends we find are consistent with a factor of two growth in the cluster red sequences from $z = 1.5$ to 1.0.

7. These observations lend credence to the idea that the red sequence in the centers of clusters was growing rapidly at $z \sim 1.5$, where this mass assembly was likely in the form of relatively younger, smaller, and/or metal-poorer galaxies that were actively growing in their recent past.

Chapter 6

Mock Data from *ab initio* Simulations of Galaxy Formation

G. Snyder, M. Vogelsberger, P. Torrey, D. Nelson, L. Hernquist, V. Springel, in preparation

Abstract

Numerous processes affect the appearance of galaxies, such as feedback from active galactic nuclei and stars, galaxy interactions, gas accretion, and the evolution of disks. While small-scale, very high-resolution simulations are essential for verifying physical models for such processes, large-scale calculations of their effects in entire populations are required to comprehensively compare galaxy formation theory with data. To directly enable such comparisons, we begin to build a large suite of high-resolution mock images based on cosmological simulations performed with the moving mesh code

Arepo. These are the largest and most accurate continuous-volume hydrodynamical simulations of galaxy formation run to date, tracing the formation of thousands of Milky Way-like objects on physical scales comparable to the resolving power of the *Hubble Space Telescope* (*HST*). Model images of their assembly process will constitute a timely and definitive tool to advance two key goals of observational cosmology: linking the building blocks of galaxies across cosmic time, and understanding the implications of galaxy morphology and structure. Therefore this model dataset is ideally suited to enhance results from, for example, *HST* Treasury and Archival Legacy surveys, the Ultra Deep Fields, and the Frontier Fields. Since such simulations also predict the state and distribution of gas, our techniques could be extended to inform deep multi-wavelength studies utilizing the *Chandra X-ray Observatory* and the *Atacama Large Millimeter/submillimeter Array* (*ALMA*). To increase the science return from these valuable projects, we will publicly release our model images. With this dataset, we will directly study how galaxy colors, morphologies, and structures evolve and depend on feedback, interactions, and environments, and aim to provide a tool that can usher in a new era of comprehensive interpretations of high redshift galaxy data.

6.1 Background

The field of galaxy evolution benefits from copious high quality observational data. However, many aspects of galaxy formation remain poorly understood. What sets galaxy structure? How does feedback from stars and active galactic nuclei (AGN) impact the evolution of these structures? How or why does environment matter at different epochs? How do baryons get into and out of galaxies? Such questions are difficult to answer

owing to the inability to directly follow the evolution of observed sources in time, and to limitations in our ability to calculate the physical processes affecting galaxies.

Advances in computational methods have led to crucial progress against these challenges. Today, the formation and resulting impact of individual star clusters are modeled in galaxy-wide simulations, and entire universes are modeled by combining gigaparsec-scale dark matter simulations with semi-analytic modeling, in which toy models of galaxy formation are computed in post-processing, or subhalo abundance matching, in which galaxy statistics are matched with dark matter halo catalogs.

These approaches are essential for verifying the physics acting on galaxies on small and large scales. However, large-scale calculations are not detailed enough to model internal galaxy structures, and small-scale calculations are not broad enough to simultaneously capture the range of galaxy populations and environments. In particular, neither approach can extract all information from surveys of galaxy morphology and structure. Meanwhile, the amount of such data that is readily available has greatly increased from projects such as the Sloan Digital Sky Survey (SDSS), and it will continue to increase from future projects such as the Large Synoptic Survey Telescope (LSST). Additionally, the community continues to invest significantly in space-based surveys of very distant ($z > 1$) galaxies.

Realizing the greatest return of these datasets requires cosmological simulations with sufficient dynamic range to directly follow dark matter, stars, and gas in entire galaxy populations. Recently, rapid progress has been made toward this elusive goal by appreciating the need for significant feedback to regulate star formation and by overcoming challenges with numerical methods. Now, hydrodynamical simulations can

form realistic galaxies from cosmological initial conditions, and large calculations of this type can soon be the foundation of new, more complete ways to study distant galaxies.

In this chapter, we develop methods to efficiently produce and analyze "mock data" from large continuous-volume cosmological hydrodynamical simulations. Small-scale calculations of this type have been a valuable tool to analyze galaxy evolution (Scannapieco et al. 2010; Wuyts et al. 2010; Guedes et al. 2011), and we have applied isolated merger simulations to explore elliptical galaxy formation in Chapters 3 and 4, but our goal now is to develop a full-scale "mock observatory" based on accurate simulations of the formation of galaxies in thousands of cubic megaparsecs. In Section 6.2 we summarize the hydrodynamical simulations we analyze, and in Section 6.3 we describe the data products we generate with the hope of exploring from an observational perspective.

6.2 Arepo Simulations

This work is based on a suite of cosmological simulations performed with the Arepo code of Springel (2010). Arepo combines an efficient gravity solver with cell-based hydrodynamics in which the mesh moves with the fluid. A series of studies (Vogelsberger et al. 2012; Sijacki et al. 2012; Kereš et al. 2012) have verified Arepo's promising performance on cosmological hydrodynamics. Torrey et al. (2012b) showed, for a given computing time, Arepo yields larger galaxy disks that are more likely to survive in a cosmological environment than previous methods. Nelson et al. (2013) used Arepo to study the thermodynamics of cosmological gas accretion, pressuring the conventional picture derived from previous generations of simulations that "cold flows" dominate the

early formation of galaxies.

These initial results led to revised treatments for the physics of galaxy formation, including star formation, gas cooling, stellar and AGN feedback, super-massive black hole (SMBH) growth, chemical enrichment, and gas recycling (M. Vogelsberger et al. in prep.). These Arepo simulations of cosmological galaxy formation now match a number of observational statistics across cosmic time (P. Torrey et al. in prep.), including the star formation history of the universe, the galaxy stellar mass function, the galaxy mass-metallicity relation, and the stellar mass-halo mass relation. These issues are explored in a series of $(25/h \text{ Mpc})^3$ simulations which constitute the initial thrust of our analysis.

Forthcoming larger calculations motivate the developmental work presented in this chapter. For example, the *Illustris* project (M. Vogelsberger et al. in prep.) comprises three $(75/h \text{ Mpc})^3$ calculations of increasing complexity, including one with the full best-matching physics. Resolved on sub-kiloparsec scales, the *Illustris* simulation has the greatest dynamic range ever for such a large-volume cosmological hydrodynamical simulation. Therefore it is expected to constitute a valuable reference to our understanding of galaxy formation, one which can be contrasted with observations in direct new ways.

6.3 Data Analysis Pipelines

The $(75/h \text{ Mpc})^3$ *Illustris* simulation forms over $\sim$ 10,000 galaxies that are more than $\sim 10\%$ the mass of the Milky Way (stellar masses $M_* \gtrsim 10^{10} M_\odot$), and their evolution is

output at each of 136 cosmic times at $0 < z < 40$. The $(25/h \text{ Mpc})^3$ calculations will comprise of order ~ 12 simulations with varying resolution and physics settings. These represent a significant quantity of theoretical data (~ 100 TB) that we seek to analyze in post-processing to create mock catalogs. In addition to suites of rest-frame model photometry derived directly from the simulation outputs, we use the code SUNRISE (Jonsson 2006) to compile stellar population and AGN model SEDs and produce observed-frame images in arbitrary filters. In this section, we briefly describe these two modes of producing mock images. The long-term vision is to enable users to rapidly create customized models, a significant data processing challenge when applied to simulations as large as in the *Illustris* project.

6.3.1 Subhalo Image Catalogs

Simple photometric quantities are saved in the simulation outputs. Collisionless star particles form stochastically out of cold gas according to the SF law prescribed in the simulations, and enrich the surrounding ISM with metals according to a newly developed chemistry model (M. Vogelsberger et al. in prep.) derived from several sources, including Leitherer et al. (1999). Each star particle retains knowledge of its formation time and metal content, from which its rest-frame luminosity is assigned in each of eight chosen filters according to the stellar population synthesis models of (Bruzual & Charlot 2003). These simulations store rest-frame U, B, V, K magnitudes (Johnson & Morgan 1953), and g, r, i, z magnitudes (Fukugita et al. 1996). These quantities are stored on disk for immediate post-processing analyses. In principle, arbitrary such syntheses (which are less efficient) can be conducted from knowlege of the stars' age and metallicity

(and optionally, dust in the ISM); we also prepare such a pipeline in the following Section 6.3.2.

Dark matter halos are initially identified using the SUBFIND algorithm (Springel et al. 2001), generating a highly efficient catalog of galaxies' particles saved in such a way that minimizes unnecessary data access and computing. For each halo, we project the pre-stored photometric quantities onto a chosen set of viewing directions, including seven random directions that are the same for all halos, plus two based on the angular momentum of the galaxy's stars: one "face on" and the other "edge on". Star particles are assumed to be star clusters Normally distributed in radius, with a standard deviation equal to one half the smoothing length of the collisionless particle (cite definition of this). Each "star cluster" is sampled with 128 random points.

These projections are saved to disk as a suite of FITS images with associated metadata, including catalog identifiers, camera geometry, halo mass, stellar mass, and other physical quantities. For the $(25/h \text{ Mpc})^3$ boxes, we generate ~ 10 images for each of the 10^3 most massive halos at each simulation output time. Having of order ~ 100 outputs, a $(25/h \text{ Mpc})^3$ simulation yields $\sim 10^6$ images that can be linked across cosmic time to analyze the evolution of galaxies. The *Illustris* project will yield $\sim 5 \times 10^7$ such images.

6.3.2 Lightcones and Mock Imaging with Sunrise

In a parallel effort, we generate mock survey fields from the simulations, making use of their periodic boundary conditions and constant comoving volume. In brief, this involves remapping the cubic simulation volume to a shape that preserves large-scale structure

information but can more flexibly mimic observation geometries. Several authors have published techniques for accomplishing this remapping (Blaizot et al. 2005; Kitzbichler & White 2007; Carlson & White 2010), either with a single simulation output or replacing distant volume with the output from an earlier cosmic time. This latter approach can be used to define "lightcones" in which the properties of galaxies evolve roughly as they would be "observed".

Such a "mock observatory" effort (Lemson 2006; Overzier et al. 2012) has been undertaken by the Virgo Consortium based on dark matter-only simulations with semi-analytic modeling of the galaxy population. However, given the rapidly increasing availability of computational resources and advances in numerical techniques, much more direct comparisons can be based on high-resolution self-consistent hydrodynamical simulations in which the effects of galaxy physics are explicit. In particular, such models can make detailed predictions that could be constrained by spatially and spectrally resolved observations across a wide range of cosmic times.

In this work, we explore simple proofs of concept to apply this technique to hydrodynamical simulations. In brief, we first define a lightcone in comoving units, replicate the simulation volume a number of times to fill the lightcone, and then vary the output time used to fill the volume as a function of comoving distance. Then, we directly convert the physical information in the simulation at each cosmic time into customized mock observations. We do this using the SUNRISE code (Jonsson 2006; Jonsson et al. 2010), which creates projections into pre-defined "cameras", performs optional dust radiative transfer, and integrates the final emission in arbitrary filter bands assuming the appropriate redshift. In this way, we directly link theory with data.

In Figure 6.1, we present a mock *HST* image of our default lightcone definition. This default follows (Kitzbichler & White 2007), in which we choose two integers $(n, m) = (11, 10)$ that set the viewing direction from the origin of the cubic simulation volume, defined

$$\hat{u}_3 = |(n, m, nm)|.$$

The angular field of view of the camera, is set to

$$\frac{1}{mn^2} \text{ radians} \approx 2.8 \text{ arcmin}.$$

We trace a line along $\hat{u}_3$ until it exits the first simulation volume and enters the next periodic replication, and repeat this until the desired comoving distance is reached. If the comoving distance traveled is such that a simulation output exists at a redshift appropriate for the distance to the midpoint of the next segment, this new replication is assumed to use this new output (from an earlier cosmic time). The viewing direction vector and angular field of view are such that the lightcone will trace out a unique comoving volume up to nm replications. For a box size L, this unique volume is $V_0 \approx L^3/3$. For our $(25/h \text{ Mpc})^3$ simulations and $(n, m) = (11, 10)$ (shown here) this produces a lightcone subtending a unique volume from $z = 0$ to $z \sim 1.2$. In our examples, we allow the comoving volume to repeat and continue tracing the lightcone to $z = 12$. In this way, the same comoving is repeated ~ 3 times, but at very different cosmic times, creating an image that looks reasonably realistic. We refer the reader to the literature for more details of this procedure (Blaizot et al. 2005; Kitzbichler & White 2007; Henriques et al. 2012; Overzier et al. 2012).

Given the above geometry, we produce a catalog of camera definitions (one for each replication) in physical coordinates, and extract a minimal simulation volume

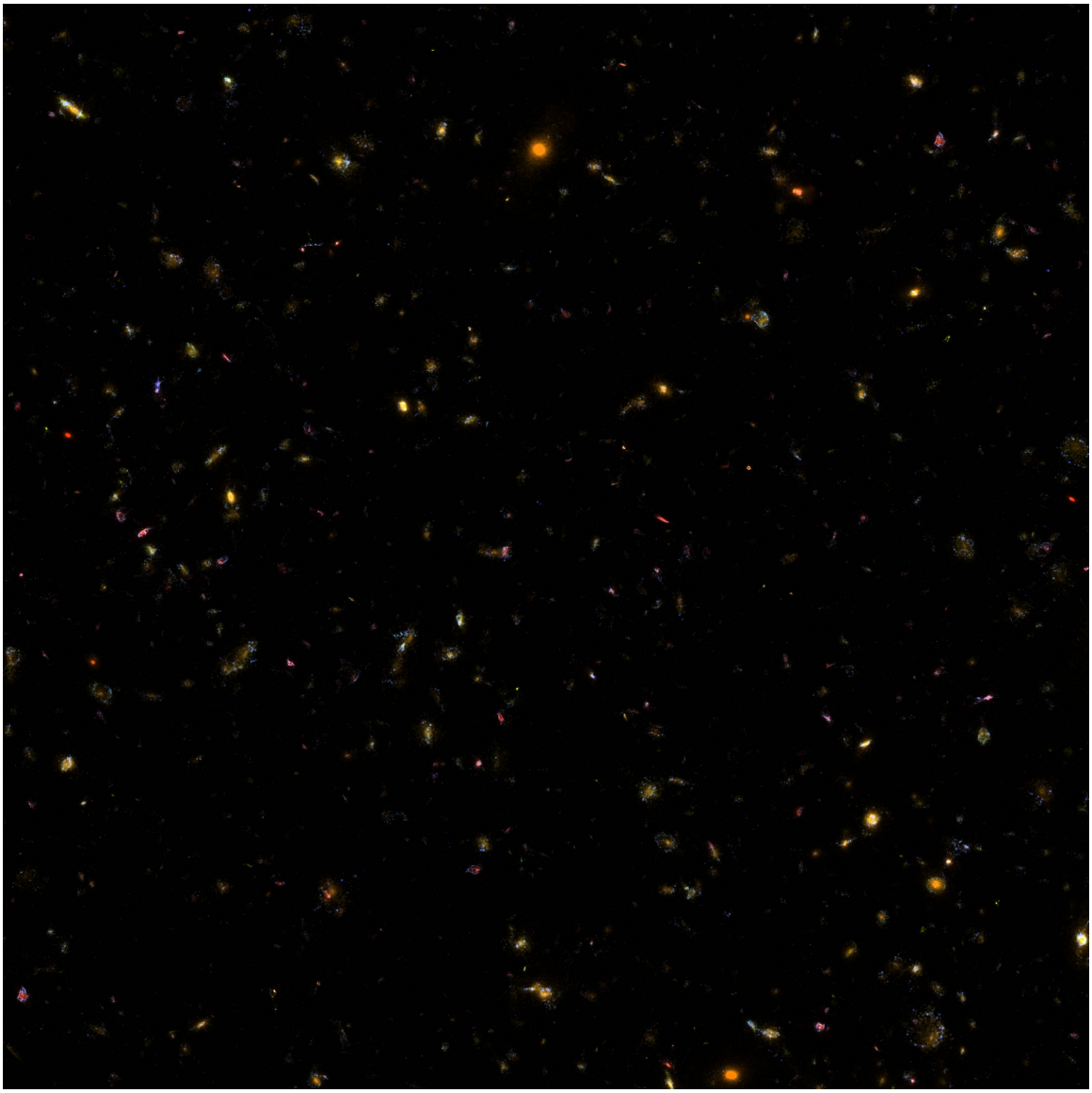

Figure 6.1.—: A 2.8 arcmin × 2.8 arcmin mock "ultra deep field", a false color image based on *HST* ACS and WFC3 filters F435W (blue), F850LP (green), and F160W (red), using the scaling recommendations of Lupton et al. (2004). We derived this image from a $(25/h$ Mpc$)^3$ hydrodynamical simulation run for the *Illustris* project (M. Vogelsberger et al. in prep.) with the final best-fitting physics prescription and physical resolution ($\sim$1 comoving kpc). We created these mock images using lightcone-building techniques (e.g., Kitzbichler & White 2007; Henriques et al. 2012) and the code SUNRISE (Jonsson 2006), assuming the empirical dust attenuation law of Charlot & Fall (2000). This example represents a tiny fraction ($\lesssim 0.1\%$) of the galaxy information modeled by the *Illustris* project. These simulations produce a striking diversity in galaxy morphology similar to those observed (see Figure 6.5).

around the lightcone for input to SUNRISE. We apply Starburst99 stellar population models (Leitherer et al. 1999) with variable metallicity, but at present we do not use any information about dust in the ISM. In these tests, star particles are assumed to be star clusters with a size equal to the minimum physical gravitational softening length. However, given the widely adaptive resolution of these simulations, a more appropriate size definition, such as the one we use for the catalogs of Section 6.3.1, should be implemented in the future.

We redshift and dim the images appropriately for the comoving distance along the lightcone. This redshift is independent of (but similar to) the redshift of the simulation output. The image field of view is fixed in comoving units but appropriately varied in physical units according to the angular diameter distance. Finally, we add the ~ 300 images in each of our chosen bands. Initially, we produce mock images in filters used by *HST*'s ACS and WFC3-IR cameras as well as *JWST*'s NIRCAM.

We implement simple extinction laws (e.g., Charlot & Fall 2000), which we demonstrate in Figure 6.2, but sophisticated explorations of this issue are tenable. Ultimately, the resolving power of such large-volume simulations will increase with available computing power, and in several years it is expected to be feasible to exploit this improved resolution to perform dust radiative transfer calculations (e.g., Jonsson et al. 2010), thus self-consistently predicting dust attenuation and emission as in Chapters 3 and 4, with galaxies formed in similar volumes. We aim to prepare for this eventuality.

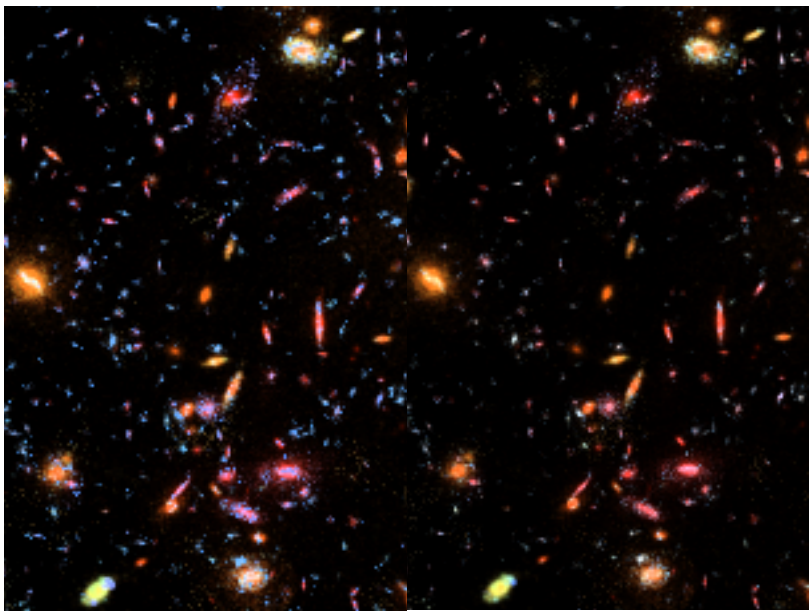

Figure 6.2.—: *left:* Unattenuated Starburst99 stellar populations. *right:* Same image using the recommended attenuation of starlight by dust in the diffuse and star-forming ISM from Charlot & Fall (2000). Since current simulations predict the metal content in the ISM, in principle a number of different models of dust chemistry could be tested using these calculations.

6.4 Initial Applications

1. **Combining physical and observed quantities.** Knowledge about a given galaxy is limited owing to our observational perspective. However, simulations of this type can allow researchers to explore the physical properties of selected galaxies (given the physics assumed), such as how they depend on viewing angle or local environment and how assumptions like dust content, AGN strength, and stellar populations affect their conclusions. Figure 6.3 presents an example application: identifying the stellar mass associated with an assembling group. This is a key uncertainty for studies such as in Chapter 5 (e.g., Snyder et al. 2012b; Rudnick et al. 2012) where stellar mass growth is difficult to infer directly; these

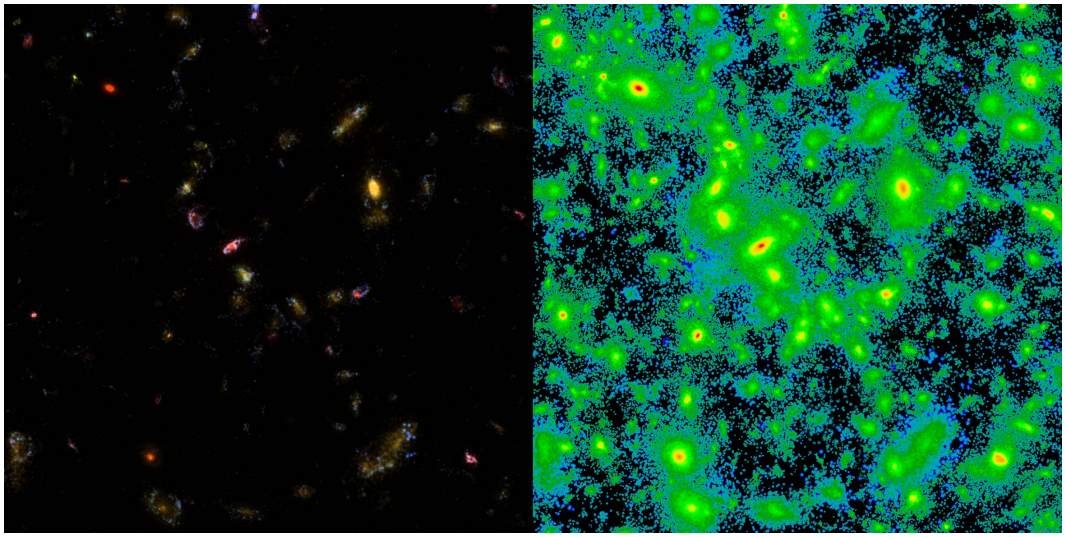

Figure 6.3.—: *left:* Roughly 1 arcmin cutout from Figure 6.1 showing an apparent structure of galaxies at $z \gtrsim 1$. *right:* The same region colored by stellar mass surface density. The scaling is logarithmic with a rainbow colormap. By modeling full observations, objects can be selected from the left panel and their properties measured using quantities in the right panel. An example application is to directly evaluate the hypothesis we put forward in Chapter 5 that the color evolution of galaxies in massive halos is a consequence of ongoing stellar mass growth combined with progenitor bias.

simulations can predict the structure and colors of galaxies in such a scenario and therefore constrain models for this assembly process.

2. **Comparing simulation results.** The data produced by suites of hydrodynamical simulations can occupy tens to hundreds of terabytes. Therefore, by converting such simulations into limited suites of mock images, we can "compress" their results into much more manageable and inexpensive forms. In Figure 6.4 we demonstrate a striking visual, and potentially "observable", difference between the Gadget (Springel 2005) and Arepo (Springel 2010). Alternatively, with sufficient resources, fully customizable image databases could be constructed with these techniques.

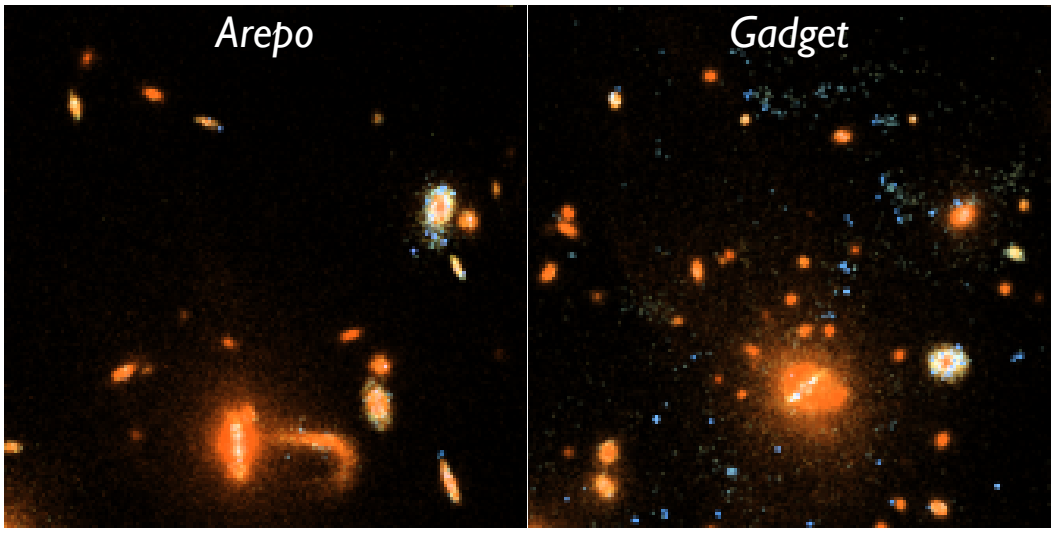

Figure 6.4.—: Comparison of the same $\sim 10^{13} M_{\odot}$ halo simulated with GADGET and AREPO (Vogelsberger et al. 2012; Kereš et al. 2012; Sijacki et al. 2012), demonstrating very obvious differences between the two mock observations. In GADGET, the halo forms a larger number of satellite galaxies that are more axisymmetric (rounder) than their AREPO counterparts. Additionally, there is star-forming gas found in the intracluster regions, likely the result of spurious gas clumps known to result from numerical artifacts with the standard formulation of SPH in GADGET (Torrey et al. 2012b).

3. **The effect of feedback.** In Figure 6.5 we present a direct comparison of three simulated images with the *HST* ACS Ultra Deep Field (Beckwith et al. 2006). The three simulated images use successively more refined feedback prescriptions (M. Vogelsberger et al. in prep.) and demonstrate the need for ejective stellar feedback in low mass systems and AGN feedback in high mass systems in order to roughly match the color, size, and morphology of observed galaxies (in this case, at $z \lesssim 1$). For this image we use the Charlot & Fall (2000) attenuation law, and the results from Figure 6.2 highlight the importance of this correction.

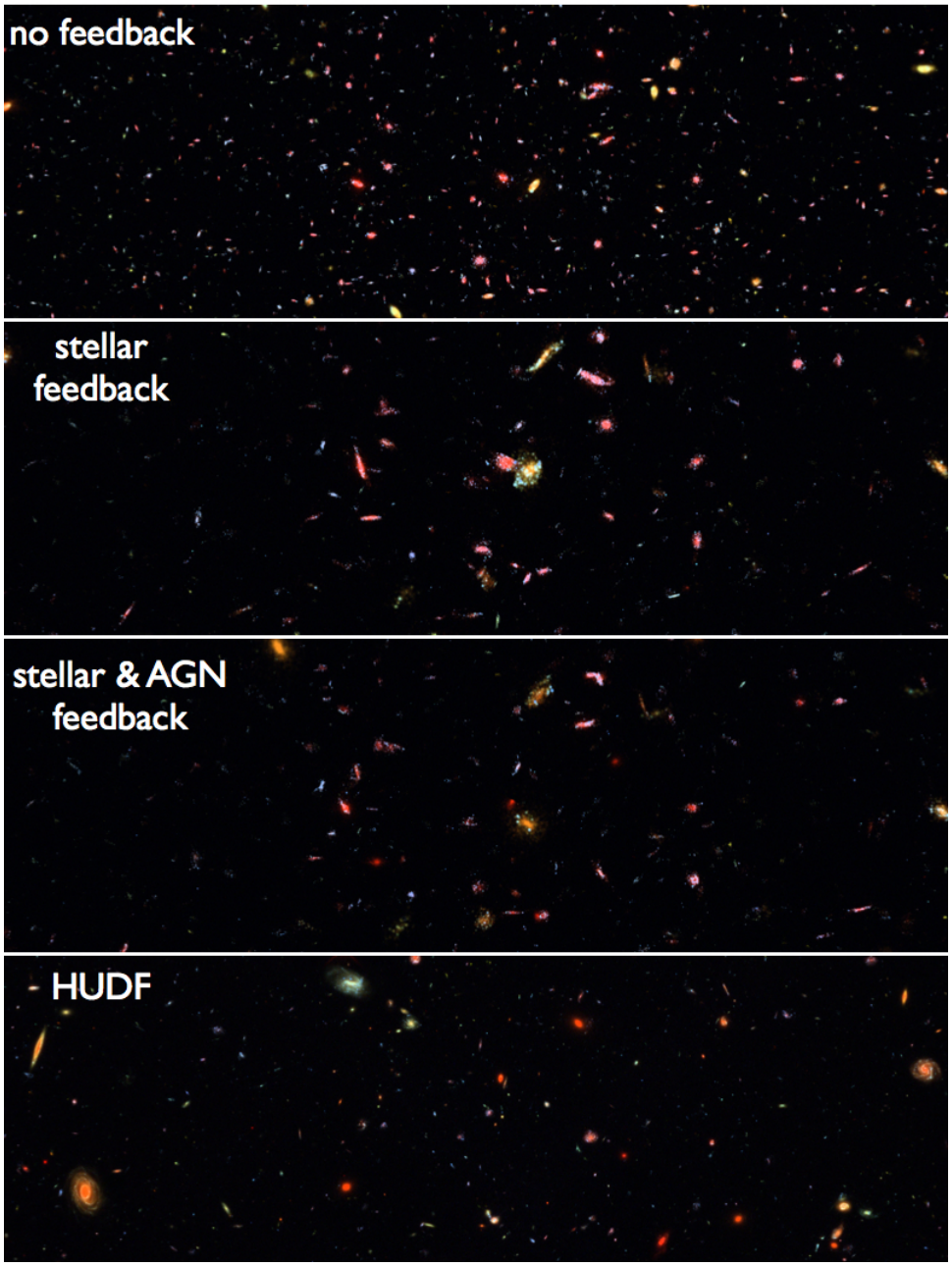

Figure 6.5.—: Direct comparison of a $\sim 3 \times 1$ arcmin region from the *HST* ACS Ultra Deep Field (bottom; Beckwith et al. 2006) to mock fields from low-resolution test simulations (top three; M. Vogelsberger et al. in prep.) in which stellar and AGN feedback prescriptions are added from top to bottom. The full physics prescription produces galaxies with an overall size, color, and morphology distribution broadly matching those observed, including several red-and-dead ellipticals.

6.5 Anticipated Results

Our primary goal is to comprehensively compare data to model predictions. To do so, we are developing a blueprint by which a fully customizable model server could be constructed based on large hydrodynamical simulations of galaxy formation. This will be a necessary step to realize the full benefit of ever-larger theoretical and observational archives. Ultimately, we will publicly release our model images with the goal of enabling novel ways to interpret observations of galaxies across cosmic time. Here we identify three future projects that we aim to enable in this way:

1. **Tracing the build-up of galaxies.** Ultimately, arbitrary remappings and lightcones (Section 6.3.2) are planned based on the $(75/h\ \mathrm{Mpc})^3$ *Illustris* simulation. For example, with $(75/h\ \mathrm{Mpc})^3$, this procedure can produce a fully self-consistent (no volume repeated) "ultra deep field" (Beckwith et al. 2006), and with moderate repetition (at well-separated epochs) can produce fields $\sim 100\ \mathrm{arcmin}^2$, comparable with the widest very-deep *HST* surveys to date. These could then be used to determine the consequences of different selection criteria and contamination or confusion. Additionally, we can evaluate the histories and futures of simulated galaxies that appear to be evolving between star-forming and quiescent (cf. Snyder et al. 2011a). Moreover, researchers can then relate such samples over cosmic time, opening the time domain with three-dimensional models for how the building blocks of galaxies appear in the distant universe. In Figure 6.6, we examine a $z \sim 10$ object that appears to be behind a very low-mass $z \sim 6$ interloper.

2. **Calibrating merger rates.** The galaxy merger rate is of fundamental importance for our understanding of galaxy evolution. However, it is notoriously difficult to measure from observations, since it is impossible to watch galaxies evolve over time. Hydrodynamical simulations have been used to calibrate the timescale of merger signatures in a wide variety of contexts (Lotz et al. 2008, 2010; Snyder et al. 2011a; Hayward et al. 2013), and the *Illustris* project is well-poised to extend these techniques to $z > 3$ in combination with *HST* and *JWST*. Resolved at sub-kiloparsec comoving scales, the *Illustris* simulation easily resolves the structure of bright galaxies at $z > 2$, predicting the appearance of a wide population of galaxies in their full cosmological context. Idealized merger rates are calculated by V. Rodriguez-Gomez et al. (in prep.), and our mock images could be used to identify the most efficient method to measure the physical merger rate.

3. **Understanding environment dependence.** The *Illustris* project can probe halo masses up to a few times $10^{14} M_{\odot}$ (at $z = 0$), the largest range of galaxy environments in a hydrodynamical simulation to date. We will simulate selection and observations of assembling halos (c.f., Eisenhardt et al. 2008; Mancone et al. 2010; Snyder et al. 2012b), including merger rate indicators, with the hope of clearly understanding issues such as stellar mass growth and progenitor bias in galaxy populations that are rapidly evolving and whose physical time evolution is difficult to characterize.

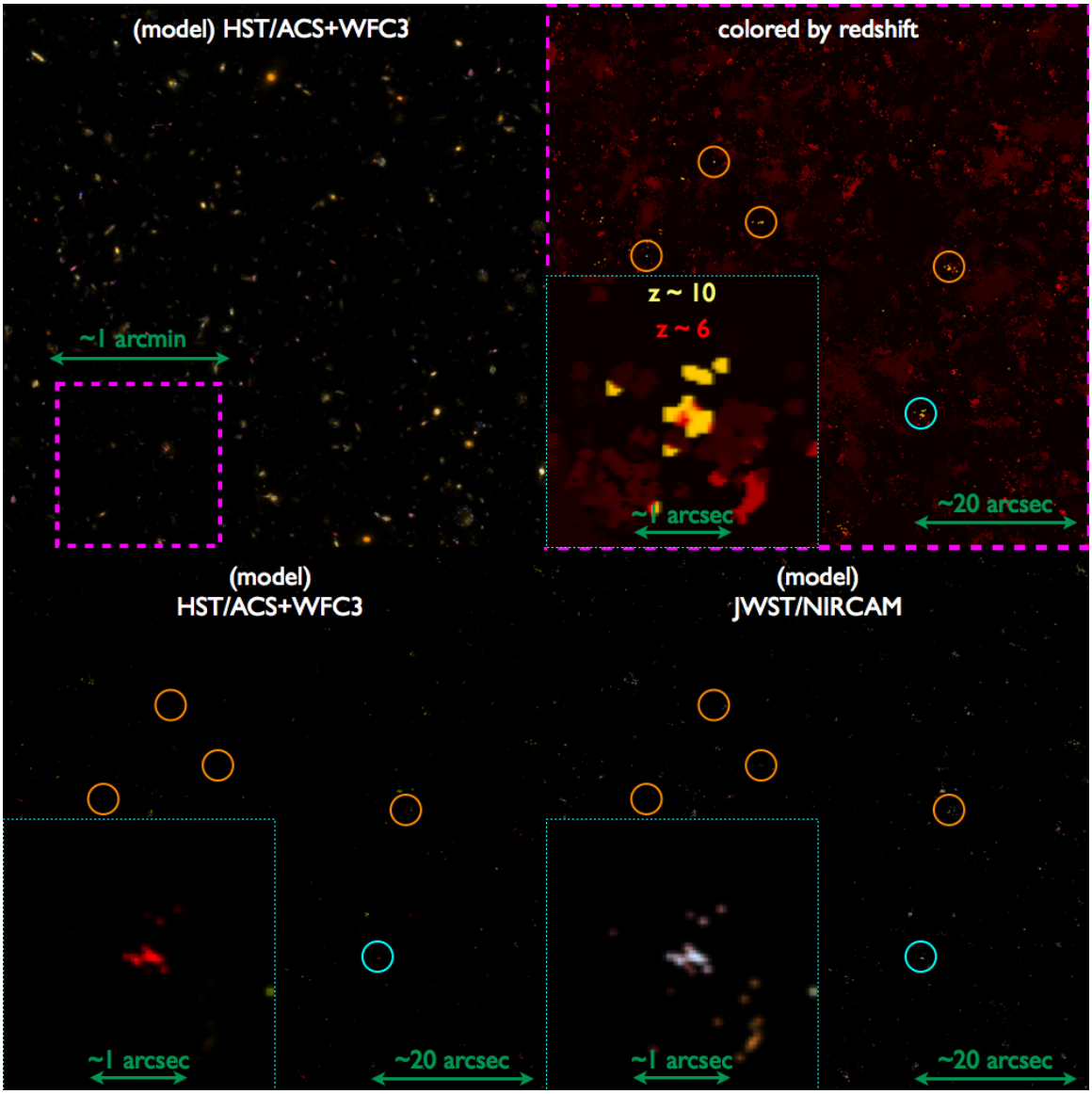

Figure 6.6.—: An exploration of high-redshift objects in the mock data. *top left:* The mock image from Figure 6.1 with a $\sim$ 1 arcmin cutout in dashed pink lines. The remaining three quadrants zoom in to this region. *top right:* The zoomed cutout region colored by the luminosity-weighted redshift of the sources contributing to each pixel. Dark red colors are $z \lesssim 4$, bright red is $z \sim 6$, and yellow-white is $z \sim 10$ to 12. We identify five such objects with circles; in the lower left corner of the quadrant, we zoom onto the bottom-right (blue) circled object. This highly zoomed inset spans $\sim$ 4 arcseconds. *bottom left:* Same regions as shown in the top right, now in the same *HST* filters (F435W, F850LP, F160W) as the top left image, where all sources at $z < 6$ have been subtracted. *bottom right:* same, but with a false-color NIRCAM image in F200W, F277W, and F444W.

Conclusions and Future Directions

This thesis constrained galaxy evolution questions using various methods, including SED modeling of merger-induced evolution, interpreting high-spatial-resolution observations of cluster galaxies within the context of the cosmic web, and producing mock data from the largest and most accurate cosmological hydrodynamical simulations. Here I summarize the main conclusions and highlight directions for future projects.

Black Hole — Bulge Relations

Correlations between galaxies' bulge properties and the mass of their supermassive black holes (SMBHs) represent a fossil record of their formation, during which star formation and SMBH accretion were triggered, followed possibly by feedback, BH self-regulation, and quenching. In Chapter 2, I analyzed the relation between the mass of the central supermassive black hole (M_{BH}) and the number of globular clusters (N_{GC}) in nearby ellipticals (Burkert & Tremaine 2010). I considered this relation in the context of the black hole fundamental plane (BHFP), a multi-variable correlation between the mass of the SMBH and galaxy properties that supports a feedback-regulated model in which the bulge binding energy is most important. We argued that the relatively small scatter of

the M_{BH}-N_{GC} relation, which suggests an unlikely causal link, owes instead to the mutual residual correlations of M_{BH} and N_{GC} with stellar mass at fixed velocity dispersion; further evidence for this claim was subsequently found by Rhode (2012). This implies that N_{GC} correlates with the binding energy of ellipticals and bulges, raising the question of why it should so closely trace their formation. Moreover, it is still an open challenge to understand the formation of globular cluster systems, owing in part to numerical challenges with common hydrodynamics techniques (see e.g., Torrey et al. 2012b, for examples). Another potential application of the Arepo code is to test whether the link between the SMBH and globular cluster systems in ellipticals is indeed indirect, and new data will test the BH-bulge correlations in galaxies at higher (McConnell et al. 2011) and lower (Greene et al. 2010) masses.

The Formation Sequence of Elliptical Galaxies

In the bulk of this thesis, I studied three successive stages in the formation of massive ($\sim L^*$) ellipticals: starburst, transition object, and red sequence galaxy. In Chapters 3 and 4, I evaluated the predicted evolution of star formation and AGN activity in mergers, focusing on how such processes play out in a broad range of observations. To do so, I combined hydrodynamical calculations of individual galaxy mergers with dust radiative transfer. In Chapter 5, I analyzed the rest-frame optical colors of red sequence galaxies in infrared-selected clusters using images from the *Hubble Space Telescope*.

Mid-Infrared Diagnostics of Starbursts: Major starbursts are thought to be the formative event of most elliptical galaxies. In Chapter 3, I analyzed diagnostics used to disentangle AGN emission and star formation in starbursts such as ultraluminous

infrared galaxies (ULIRGs), focusing on the effects of galaxy dust on mid-infrared features such as $9.7\mu m$ silicate absorption, PAH emission, and SED slope. I calculated their behavior as a function of time, viewing angle, dust model, AGN spectrum, and AGN strength in a small number of merger simulations meant to span a wide range of obscuration levels in ULIRGs. Although this technique satisfactorily represents the spread in observed SEDs (e.g., Veilleux et al. 2009), none of these indicators unambiguously estimate the AGN luminosity fraction: some identify unobscured AGN where the torus emission is observed directly, while others indicate much more highly obscured AGN. I proposed a testable JWST-accessible combination of these infrared features that simultaneously constrains the AGN fraction and dust grain model for a wide range of obscuration.

Transition Objects: After a starburst, the remnant can evolve rapidly in gas and dust content, which may be heated or expelled, and in the appearance of stellar populations, which may evolve quickly or slowly depending on their formation history. Here, I modeled merger remnants while they are transitioning out of the starburst phase and onto the red sequence, including "poststarburst" (or "K+A" or "E+A") galaxies, in which there are many young (A-type) stars but no star formation. Since the lifetime of A stars is ~ 1 Gyr, it was thought this should be the duration of galaxies' poststarburst phase. However, this assumption implies a gas-rich merger rate up to ten times lower than other estimates because the K+A abundance is so low. To examine this, in Chapter 4, I built mock spectral line catalogs to select and analyze poststarburst galaxies from simulated merger remnants. I calculated the spatially resolved optical spectrum at each time using the dust radiative transfer code Sunrise, extracted the spectrum falling within the SDSS fiber size for $z = 0.1$, and measured their Balmer absorption and [O II]

emission to select poststarburst galaxies in a manner identical to observational surveys. I showed that the K+A duration depends strongly on merger scenario, dramatically reducing the appropriate average lifetime to assume. I combined this result with external estimates of the merger rate to resolve the alleged local underabundance of poststarburst galaxies and estimate their increasing number density with redshift.

A natural extension is to generalize to more easily identifiable "green valley" (GV) galaxies (Strateva et al. 2001), having colors between the blue cloud and red sequence, to predict the expected contribution from mergers. AGN are observationally linked to the GV (e.g., Schawinski et al. 2010), but whether they are the cause of large-scale evolution in the host is unclear. While feedback may be needed to redden the remnant (Springel et al. 2005a), it may not be needed to produce a GV galaxy with lingering AGN activity. A suite of high-resolution simulations can be used to build a library of spatially resolved optical photometry and spectroscopy, with which we could compare the impact of different feedback models to survey statistics (e.g., Mendez et al. 2011) and IFU observations (e.g., Swinbank et al. 2011) of transition objects. Initial work toward this goal includes making mock IFU maps for comparison with ULIRG observations (Rothberg & Fischer 2010), comparing the green valley and poststarburst stage in merger models (Snyder et al. 2012a), and testing the data-intensive kinematics module in SUNRISE.

Alternatively, the moderate-resolution simulations comprising Chapter 6 can be used as a new starting point to capture the diversity of interactions and mergers in a given volume, overcoming a time-consuming challenge from Chapters 3 and 4. For example, the appearance of merger remnants derived from high or very high resolution simulations could be summarized by basic trends and used to predict statistics of the

full galaxy population modeled in a cosmological context. A first application is to select transition objects directly from these cosmological simulation databases, connect them to their progenitors and descendents, and quantify the triggers responsible for driving their evolution.

Formation of the Red Sequence in Clusters: Ultimately, ellipticals enter the red sequence from 10^7 to several 10^9 years after the bulk of their stars formed. The location and scatter of the red sequence in galaxy clusters can be used to diagnose the timing and duration of this star formation. In Chapter 5, I studied *HST* imaging of infrared-selected galaxy clusters at $1 < z < 1.5$, investigating evolution in the color and scatter of the $L \sim L^*$ red sequence galaxy (RSG) population to constrain their star formation histories. Additional results of this work were presented by Stanford et al. (2012) and Zeimann et al. (2012), in which we characterized the optical colors of galaxies in two of the most distant spectroscopically confirmed rich clusters ($z = 1.75$ and $z = 1.89$). We found that the RSGs exhibit approximately the same average luminosity-weighted stellar age across $1 < z < 2$, which implies significant ongoing star formation and progenitor bias, likely the result of a significant quantity of younger stars and galaxies entering the red sequence selection over time. This represents the first direct evidence of ongoing massive elliptical formation in a large uniform sample of precursors to present-day massive clusters. Combined with other studies (e.g., Martini et al. 2009; Galametz et al. 2009; Mancone et al. 2010), this implies a period of vigorous activity and stellar mass assembly by massive cluster galaxies at $z > 1.5$ that ends by $z = 1$ (Muzzin et al. 2012). Brodwin et al. (in prep.) show that the star formation in these central cluster galaxies came to a rapid halt during $1 < z < 1.5$, suggesting a stochastic and sudden quenching mechanism consistent with merger-induced AGN feedback scenarios.

Mock Data from Hydrodynamical Simulations

In Chapter 6, I developed tools to analyze cosmological hydrodynamical simulations from an observational perspective. I tested techniques to build mock *HST* Ultra Deep Fields using a pipeline designed to implement the dust radiative transfer code SUNRISE (Jonsson 2006) in a cosmologically consistent context. I also designed a dual-purpose analysis of this type of simulation to simultaneously construct mock survey fields and model SEDs and images of all individual subhalos. In our next step, we will analyze simulated ultra deep fields and begin to model the photometric evolution of galaxies from the *Illustris* Project, which calculates the cosmological assembly of thousands of Milky-Way mass galaxies using the moving-mesh code AREPO (Springel 2010). We will use these mock data to infer basic consequences of the intrinsically complex heirarchical assembly of galaxies, and to release model images and SEDs for use by the entire community. Another forthcoming application is to add simulated images to the Galaxy Zoo Project, which can then be classified and studied by citizen scientists.

As computational resources expand along with survey datasets, it will become essential to bring the most expensive simulations into a form that can be tested efficiently by the community. Such a database could serve as a stepping stone to petabyte-scale simulation databases that will be invaluable for direct comparisons to data in this era of expanding astronomical surveys. Following the success of readily available models for the evolution of stellar populations, dark matter structure growth, and galaxy semi-analytics, a hydrodynamical "mock observatory" could represent a tool to initiate an era in which all available data – spatially and spectrally resolved, across wavelength regimes and cosmic time – is brought to bear simultaneously to understand the history of galaxies.

References

Ahn, C. P., et al. 2012, ApJS, 203, 21

Aird, J., et al. 2012, ApJ, 746, 90

Akritas, M., & Bershady, M. 1996, ApJ, 470, 706

Allen, M., Groves, B., Dopita, M., Sutherland, R., & Kewley, L. 2008, ApJS, 178, 20

Aller, M., & Richstone, D. 2007, ApJ, 665, 120

Aragon-Salamanca, A., Ellis, R., Couch, W., & Carter, D. 1993, MNRAS, 262, 764

Armus, L., et al. 2006, ApJ, 640, 204

—. 2007, ApJ, 656, 148

Ashby, M., et al. 2009, ApJ, 701, 428

Babu, G. J., & Rao, C. R. 1993, Handbook of Statistics, Vol. 9 (Amsterdam: Elsevier Science), 627–659

Balogh, M., Morris, S., Yee, H., Carlberg, R., & Ellingson, E. 1999, ApJ, 527, 54

Barbary, K., et al. 2012a, ApJ, 745, 32

—. 2012b, ApJ, 745, 31

Barnes, J. 1992, ApJ, 393, 484

—. 2002, MNRAS, 333, 481

Barnes, J., & Hernquist, L. 1991, ApJ, 370, L65

—. 1996, ApJ, 471, 115

Bauer, F., Yan, L., Sajina, A., & Alexander, D. 2010, ApJ, 710, 212

Beckwith, S. V. W., et al. 2006, AJ, 132, 1729

Beers, T., Flynn, K., & Gebhardt, K. 1990, AJ, 100, 32

Behroozi, P. S., Wechsler, R. H., & Conroy, C. 2012, eprint arXiv:1207.6105

Bell, E., et al. 2004, ApJ, 608, 752

Belloni, P., Bruzual, A., Thimm, G., & Roser, H.-J. 1995, A&A, 297, 61

Bender, R., Doebereiner, S., & Moellenhoff, C. 1988, A&AS, 74, 385

Benson, A. J. 2012, New Astronomy, 17, 175

Berger, M., & Colella, P. 1989, Journal of Computational Physics, 82, 64

Bertin, E. 2006, in Astronomical Society of the Pacific Conference Series, Vol. 351, Astronomical Data Analysis Software and Systems XV, ed. C. Gabriel, C. Arviset, D. Ponz, & S. Enrique, 112

Bertin, E., & Arnouts, S. 1996, A&AS, 117, 393

Bertin, E., Mellier, Y., Radovich, M., Missonnier, G., Didelon, P., & Morin, B. 2002, in Astronomical Society of the Pacific Conference Series, Vol. 281, Astronomical Data Analysis Software and Systems XI, ed. D. A. Bohlender, D. Durand, & T. H. Handley, 228

Binette, L., Dopita, M., Dodorico, S., & Benvenuti, P. 1982, A&A, 115, 315

Birnboim, Y., Dekel, A., & Neistein, E. 2007, MNRAS, 380, 339

Blaizot, J., Wadadekar, Y., Guiderdoni, B., Colombi, S. T., Bertin, E., Bouchet, F. R., Devriendt, J. E. G., & Hatton, S. 2005, MNRAS, 360, 159

Blake, C., et al. 2004, MNRAS, 355, 713

Blakeslee, J. 1999, AJ, 118, 1506

Blakeslee, J., et al. 2003, ApJ, 596, L143

Blanton, M. R., et al. 2003, ApJ, 594, 186

Bournaud, F., et al. 2011, ApJ, 730, 4

Bouwens, R. J., Illingworth, G. D., Franx, M., & Ford, H. 2007, ApJ, 670, 928

Bower, R., Lucey, J., & Ellis, R. 1992, MNRAS, 254, 601

Boylan-Kolchin, M., Springel, V., White, S. D. M., Jenkins, A., & Lemson, G. 2009, Monthly Notices of the Royal Astronomical Society, 398, 1150

Brammer, G., et al. 2009, ApJ, 706, L173

Brammer, G. B., et al. 2011, ApJ, 739, 24

Brandl, B., et al. 2006, ApJ, 653, 1129

Brodwin, M., Gonzalez, A., Moustakas, L., Eisenhardt, P., Stanford, S., Stern, D., & Brown, M. 2007, ApJ, 671, L93

Brodwin, M., et al. 2006, ApJ, 651, 791

—. 2011, ApJ, 732, 33

Brooks, A., Governato, F., Booth, C., Willman, B., Gardner, J., Wadsley, J., Stinson, G., & Quinn, T. 2007, ApJ, 655, L17

Brown, M., Dey, A., Jannuzi, B., Brand, K., Benson, A., Brodwin, M., Croton, D., & Eisenhardt, P. 2007, ApJ, 654, 858

Brown, M., et al. 2009, ApJ, 703, 150

Bruzual, G., & Charlot, S. 2003, MNRAS, 344, 1000

Burkert, A., & Silk, J. 2001, ApJ, 554, L151

Burkert, A., & Tremaine, S. 2010, ApJ, 720, 516

Bush, S., Cox, T., Hayward, C., Thilker, D., Hernquist, L., & Besla, G. 2010a, ApJ, 713, 780

Bush, S. J., Cox, T. J., Hayward, C. C., Thilker, D., Hernquist, L., & Besla, G. 2010b, ApJ, 713, 780

Butcher, H., & Oemler Jr., A. 1978, ApJ, 219, 18

Caputi, K., et al. 2007, ApJ, 660, 97

Carlson, J., & White, M. 2010, ApJS, 190, 311

Chabrier, G. 2003, PASP, 115, 763

Chakrabarti, S., Cox, T. J., Hernquist, L., Hopkins, P. F., Robertson, B., & Matteo, T. D. 2007, ApJ, 658, 840

Chang, T.-C., van Gorkom, J., Zabludoff, A., Zaritsky, D., & Mihos, J. 2001, AJ, 121, 1965

Charlot, S., & Fall, S. M. 2000, ApJ, 539, 718

Coe, D., et al. 2013, ApJ, 762, 32

Cole, S., Lacey, C., Baugh, C., & Frenk, C. 2000, MNRAS, 319, 168

Conroy, C., & Gunn, J. 2010, ApJ, 712, 833

Conroy, C., Gunn, J., & White, M. 2009, ApJ, 699, 486

Conroy, C., White, M., & Gunn, J. E. 2010, The Astrophysical Journal, 708, 58

Conselice, C. J., Bershady, M. A., Dickinson, M., & Papovich, C. 2003, The Astronomical Journal, 126, 1183

Côté, P., et al. 2004, ApJS, 153, 223

Couch, W., & Sharples, R. 1987, MNRAS, 229, 423

Cox, T. 2004, PhD thesis, University of California, Santa Cruz, United States – California

Cox, T., Dutta, S., Di Matteo, T., Hernquist, L., Hopkins, P., Robertson, B., & Springel, V. 2006a, ApJ, 650, 791

Cox, T., Jonsson, P., Primack, J., & Somerville, R. 2006b, MNRAS, 373, 1013

Cox, T., Jonsson, P., Somerville, R., Primack, J., & Dekel, A. 2008, MNRAS, 384, 386

Croton, D., et al. 2006, MNRAS, 365, 11

Dale, D., et al. 2006, ApJ, 646, 161

—. 2007, ApJ, 655, 863

Dasyra, K. M., et al. 2009, ApJ, 701, 1123

Dawson, K., et al. 2009, AJ, 138, 1271

de Propris, R., Eisenhardt, P., Stanford, S., & Dickinson, M. 1998, ApJ, 503, L45

de Vaucouleurs, G., de Vaucouleurs, A., Corwin Jr., H., Buta, R., Paturel, G., & Fouque, P. 1991, Third Reference Catalogue of Bright Galaxies (Springer-Verlag)

Dekel, A., & Birnboim, Y. 2006, MNRAS, 368, 2

Dekel, A., Sari, R., & Ceverino, D. 2009, ApJ, 703, 785

Demarco, R., et al. 2010, ApJ, 725, 1252

Dey, A., et al. 2008, ApJ, 677, 943

Di Matteo, T., Springel, V., & Hernquist, L. 2005, Nature, 433, 604

Dole, H., et al. 2006, A&A, 451, 417

D'Onghia, E., et al. 2010, ApJ, submitted

Donley, J. L., et al. 2012, The Astrophysical Journal, 748, 142

Dopita, M., et al. 2005, ApJ, 619, 755

Draine, B., & Li, A. 2007, ApJ, 657, 810

Draine, B. T. 2003, ARA&A, 41, 241

Draine, B. T., & Li, A. 2001, ApJ, 551, 807

Draine, B. T., et al. 2007, ApJ, 663, 866

Dressler, A. 1980, ApJ, 236, 351

Dressler, A. 1987, in Nearly Normal Galaxies. From the Planck Time to the Present, ed. S. Faber, 276–289

Dressler, A., & Gunn, J. 1983, ApJ, 270, 7

Dressler, A., & Gunn, J. 1990, in Astronomical Society of the Pacific Conference Series, Vol. 10, Evolution of the Universe of Galaxies, ed. R.∼G.∼Kron, 200–208

Dwek, E. 1998, ApJ, 501, 643

Eggen, O., Lynden-Bell, D., & Sandage, A. 1962, ApJ, 136, 748

Eisenhardt, P., De Propris, R., Gonzalez, A., Stanford, S., Wang, M., & Dickinson, M. 2007, ApJS, 169, 225

Eisenhardt, P., et al. 2004, ApJS, 154, 48

—. 2008, ApJ, 684, 905

Eisenhardt, P. R. M., et al. 2012, ApJ, 755, 173

Ellis, R., Smail, I., Dressler, A., Couch, W., Oemler Jr., A., Butcher, H., & Sharples, R. 1997, ApJ, 483, 582

Ellis, R. S., et al. 2013, ApJ, 763, L7

Elmegreen, D., Elmegreen, B., Ravindranath, S., & Coe, D. 2007, ApJ, 658, 763

Elston, R., et al. 2006, ApJ, 639, 816

Erb, D., Shapley, A., Pettini, M., Steidel, C., Reddy, N., & Adelberger, K. 2006, ApJ, 644, 813

Faber, S., et al. 2007, ApJ, 665, 265

Fabricant, D., McClintock, J., & Bautz, M. 1991, ApJ, 381, 33

Fadda, D., et al. 2010, ApJ, 719, 425

Fall, S. M., & Efstathiou, G. 1980, MNRAS, 193, 189

Fassbender, R., et al. 2011, A&A, 527, L10

Faucher-Giguère, C.-A., Lidz, A., Zaldarriaga, M., & Hernquist, L. 2009, ApJ, 703, 1416

Fazio, G., et al. 2004, ApJS, 154, 10

Feoli, A., & Mancini, L. 2009, ApJ, 703, 1502

Ferrarese, L., & Merritt, D. 2000, ApJ, 539, L9

Ford, H., et al. 1998, in Society of Photo-Optical Instrumentation Engineers (SPIE) Conference Series, Vol. 3356, Society of Photo-Optical Instrumentation Engineers (SPIE) Conference Series, ed. P. Y. Bely & J. B. Breckinridge, 234–248

Förster Schreiber, N. M., et al. 2009, ApJ, 706, 1364

Fruchter, A., Sosey, M., Hack, W., Dressel, L., Koekemoer, A. M., Mack, J., Mutchler, M., & Pirzkal, N. 2009, The MultiDrizzle Handbook, version 3.0, (Baltimore, STScI) (Baltimore: STScI)

Fukugita, M., Ichikawa, T., Gunn, J. E., Doi, M., Shimasaku, K., & Schneider, D. P. 1996, AJ, 111, 1748

Galametz, A., et al. 2009, ApJ, 694, 1309

Gebhardt, K., et al. 2000, ApJ, 539, L13

Genzel, R., et al. 1998, ApJ, 498, 579

Georgantopoulos, I., et al. 2011, A&A, 531, A116

Gingold, R., & Monaghan, J. 1977, MNRAS, 181, 375

Gordon, K., & Clayton, G. 1998, ApJ, 500, 816

Gordon, K. D., Calzetti, D., & Witt, A. N. 1997, ApJ, 487, 625

Gordon, K. D., Clayton, G. C., Misselt, K. A., Landolt, A. U., & Wolff, M. J. 2003, ApJ, 594, 279

Goto, T. 2007a, MNRAS, 381, 187

—. 2007b, MNRAS, 377, 1222

Goto, T., Kawai, A., Shimono, A., Sugai, H., Yagi, M., & Hattori, T. 2008, MNRAS, 386, 1355

Graham, A., Erwin, P., Caon, N., & Trujillo, I. 2001, ApJ, 563, L11

Greene, J., et al. 2010, ApJ, 721, 26

Groves, B., Dopita, M., & Sutherland, R. 2004, ApJS, 153, 9

Groves, B., Dopita, M., Sutherland, R., Kewley, L., Fischera, J., Leitherer, C., Brandl, B., & van Breugel, W. 2008, ApJS, 176, 438

Guedes, J., Callegari, S., Madau, P., & Mayer, L. 2011, ApJ, 742, 76

Guhathakurta, P., & Draine, B. T. 1989, ApJ, 345, 230

Gültekin, K., et al. 2009, ApJ, 698, 198

Gunn, J., & Gott, J. 1972, ApJ, 176, 1

Harris, G., & Harris, W. 2011, MNRAS, 410, 2347

Harris, W., & van den Bergh, S. 1981, AJ, 86, 1627

Häuß ler, B., Barden, M., Bamford, S., & Rojas, A. 2011, in Astronomical Society of the Pacific Conference Series, Vol. 442, Astronomical Society of the Pacific Conference Series, ed. I. Evans, A. Accomazzi, D. J. Mink, & A. H. Rots, 155

Hayward, C., Kereš, D., Jonsson, P., Narayanan, D., Cox, T., & Hernquist, L. 2011a, ApJ, 743, 159

Hayward, C., Narayanan, D., Jonsson, P., Cox, T., Kereš, D., Hopkins, P., & Hernquist, L. 2011b, in ASP Conf. Ser. 440, Have Observations Revealed a Variable Upper End of the Initial Mass Function?, ed. M. Treyer, T. Wyder, J. Neill, M. Seibert, & J. Lee (San Francisco, CA: ASP), 369

Hayward, C. C., Jonsson, P., Kereš, D., Magnelli, B., Hernquist, L., & Cox, T. J. 2012, MNRAS, 424, 951

Hayward, C. C., Narayanan, D., Keres, D., Jonsson, P., Hopkins, P. F., Cox, T. J., & Hernquist, L. 2013, MNRAS, 428, 2529

Henriques, B. M. B., White, S. D. M., Lemson, G., Thomas, P. A., Guo, Q., Marleau, G.-D., & Overzier, R. A. 2012, MNRAS, 421, 2904

Hernquist, L. 1989, Nature, 340, 687

—. 1990, ApJ, 356, 359

Hernquist, L., & Katz, N. 1989, ApJS, 70, 419

Hernquist, L., & Mihos, J. 1995, ApJ, 448, 41

Hickox, R. C., et al. 2012, MNRAS, 421, 284

Hilton, M., et al. 2009, ApJ, 697, 436

Hoffman, L., Cox, T., Dutta, S., & Hernquist, L. 2009, ApJ, 705, 920

Hoffman, L., Cox, T. J., Dutta, S., & Hernquist, L. 2010, ApJ, 723, 818

Holtzman, J., Burrows, C., Casertano, S., Hester, J., Trauger, J., Watson, A., & Worthey, G. 1995, PASP, 107, 1065

Hönig, S. F., Beckert, T., Ohnaka, K., & Weigelt, G. 2006, A&A, 452, 459

Hönig, S. F., Kishimoto, M., Gandhi, P., Smette, A., Asmus, D., Duschl, W., Polletta, M., & Weigelt, G. 2010, A&A, 515, A23

Hopkins, A., & Beacom, J. 2006, ApJ, 651, 142

Hopkins, P., Cox, T., Dutta, S., Hernquist, L., Kormendy, J., & Lauer, T. 2009a, ApJS, 181, 135

Hopkins, P., Cox, T., Kereš, D., & Hernquist, L. 2008a, ApJS, 175, 390

Hopkins, P., Cox, T., Younger, J., & Hernquist, L. 2009b, ApJ, 691, 1168

Hopkins, P., & Hernquist, L. 2006, ApJS, 166, 1

—. 2010a, MNRAS, 402, 985

—. 2010b, MNRAS, 407, 447

Hopkins, P., Hernquist, L., Cox, T., Di Matteo, T., Martini, P., Robertson, B., & Springel, V. 2005a, ApJ, 630, 705

Hopkins, P., Hernquist, L., Cox, T., Di Matteo, T., Robertson, B., & Springel, V. 2006a, ApJS, 163, 1

Hopkins, P., Hernquist, L., Cox, T., Dutta, S., & Rothberg, B. 2008b, ApJ, 679, 156

Hopkins, P., Hernquist, L., Cox, T., & Kereš, D. 2008c, ApJS, 175, 356

Hopkins, P., Hernquist, L., Cox, T., Robertson, B., & Krause, E. 2007a, ApJ, 669, 45

—. 2007b, ApJ, 669, 67

Hopkins, P., Hernquist, L., Cox, T., Robertson, B., & Springel, V. 2006b, ApJS, 163, 50

Hopkins, P., Hernquist, L., Cox, T., Younger, J., & Besla, G. 2008d, ApJ, 688, 757

Hopkins, P., Hernquist, L., Martini, P., Cox, T., Robertson, B., Di Matteo, T., & Springel, V. 2005b, ApJ, 625, L71

Hopkins, P., Lauer, T., Cox, T., Hernquist, L., & Kormendy, J. 2009c, ApJS, 181, 486

Hopkins, P., Murray, N., & Thompson, T. 2009d, MNRAS, 398, 303

Hopkins, P., & Quataert, E. 2010, MNRAS, 407, 1529

Hopkins, P., Richards, G., & Hernquist, L. 2007c, ApJ, 654, 731

Hopkins, P., Richards, G. T., & Hernquist, L. 2007d, ApJ, 654, 731

Hopkins, P., Somerville, R., Hernquist, L., Cox, T., Robertson, B., & Li, Y. 2006c, ApJ, 652, 864

Hopkins, P., Younger, J., Hayward, C., Narayanan, D., & Hernquist, L. 2010a, MNRAS, 402, 1693

Hopkins, P., et al. 2009e, MNRAS, 397, 802

—. 2010b, ApJ, 715, 202

Hopkins, P. F., Cox, T. J., Hernquist, L., Narayanan, D., Hayward, C. C., & Murray, N. 2013, MNRAS, 430, 1901

Hopkins, P. F., Hayward, C. C., Narayanan, D., & Hernquist, L. 2012a, MNRAS, 420, 320

Hopkins, P. F., Hernquist, L., Hayward, C. C., & Narayanan, D. 2012b, MNRAS, 425, 1121

Hopkins, P. F., et al. 2004, AJ, 128, 1112

—. 2010c, ApJ, 724, 915

Houck, J., et al. 2004, in Society of Photo-Optical Instrumentation Engineers (SPIE) Conference Series, Vol. 5487, Society of Photo-Optical Instrumentation Engineers (SPIE) Conference Series, ed. J.C.Mather, 62–76

Houck, J., et al. 2005, ApJ, 622, L105

Houck, J. R., et al. 1984, ApJ, 278, L63

Hubble, E. 1926, ApJ, 64, 321

Huchra, J., Davis, M., Latham, D., & Tonry, J. 1983, ApJS, 52, 89

Hunter, J. D. 2007, Computing In Science & Engineering, 9, 90

Imanishi, M., Nakagawa, T., Ohyama, Y., Shirahata, M., Wada, T., Onaka, T., & Oi, N. 2008, Publications of the Astronomical Society of Japan, 60, 489

Jaffé, Y., Aragón-Salamanca, A., De Lucia, G., Jablonka, P., Rudnick, G., Saglia, R., & Zaritsky, D. 2011, MNRAS, 410, 280

Jannuzi, B., & Dey, A. 1999, in Astronomical Society of the Pacific Conference Series, Vol. 191, Photometric Redshifts and the Detection of High Redshift Galaxies, ed. R. Weymann, L. Storrie-Lombardi, M. Sawicki, & R. Brunner, 111

Jee, M., et al. 2011, ApJ, 737, 59

Jogee, S., et al. 2009, The Astrophysical Journal, 697, 1971

Johansson, P., Naab, T., & Burkert, A. 2009, ApJ, 690, 802

Johnson, H., & Morgan, W. 1953, ApJ, 117, 313

Jonsson, P. 2006, MNRAS, 372, 2

Jonsson, P., Groves, B., & Cox, T. 2010, MNRAS, 403, 17

Juneau, S., Dickinson, M., Alexander, D. M., & Salim, S. 2011, ApJ, 736, 104

Katz, N., Weinberg, D. H., & Hernquist, L. 1996, ApJS, 105, 19

Kaviraj, S., Kirkby, L., Silk, J., & Sarzi, M. 2007, MNRAS, 382, 960

Kennicutt, R. C. 1998, ApJ, 498, 541

Kennicutt Jr., R. 1998, ARA&A, 36, 189

Kereš, D., & Hernquist, L. 2009, ApJ, 700, L1

Kereš, D., Katz, N., Weinberg, D., & Davé, R. 2005, MNRAS, 363, 2

Kereš, D., Vogelsberger, M., Sijacki, D., Springel, V., & Hernquist, L. 2012, MNRAS, 425, 2027

Khochfar, S., & Burkert, A. 2003, ApJ, 597, L117

Kimble, R., MacKenty, J., O'Connell, R., & Townsend, J. 2008, in Society of Photo-Optical Instrumentation Engineers (SPIE) Conference Series, Vol. 7010, Society of Photo-Optical Instrumentation Engineers (SPIE) Conference Series

Kirkpatrick, A., et al. 2013, ApJ, 763, 123

Kitzbichler, M. G., & White, S. D. M. 2007, MNRAS, 376, 2

Klypin, A. A., Trujillo-Gomez, S., & Primack, J. 2011, ApJ, 740, 102

Kocevski, D. D., et al. 2012, ApJ, 744, 148

Kodama, T., & Arimoto, N. 1997, A&A, 320, 41

Koekemoer, A., Fruchter, A., Hook, R., & Hack, W. 2002, in The 2002 HST Calibration Workshop : Hubble after the Installation of the ACS and the NICMOS Cooling System, ed. S. Arribas, A. Koekemoer, & B. Whitmore, 337

Kormendy, J., Fisher, D., Cornell, M., & Bender, R. 2009, ApJS, 182, 216

Kormendy, J., & Richstone, D. 1995, ARA&A, 33, 581

Kriek, M., van der Wel, A., van Dokkum, P., Franx, M., & Illingworth, G. 2008, ApJ, 682, 896

Kroupa, P. 2001, MNRAS, 322, 231

Kundu, A., & Whitmore, B. 2001, AJ, 121, 2950

Kurk, J., et al. 2009, A&A, 504, 331

Lacy, M., Sajina, A., Petric, A. O., Seymour, N., Canalizo, G., Ridgway, S. E., Armus, L., & Storrie-Lombardi, L. J. 2007, ApJ, 669, L61

Laor, A., & Draine, B. T. 1993, ApJ, 402, 441

Larson, D., et al. 2011, ApJS, 192, 16

Larson, R. 1974, MNRAS, 169, 229

Larson, R., Tinsley, B., & Caldwell, C. 1980, ApJ, 237, 692

Lauer, T., et al. 2007, ApJ, 664, 226

Laurent, O., Mirabel, I., Charmandaris, V., Gallais, P., Madden, S., Sauvage, M., Vigroux, L., & Cesarsky, C. 2000, A&A, 359, 887

Lavery, R., & Henry, J. 1988, ApJ, 330, 596

Le Floc'h, E., et al. 2005, ApJ, 632, 169

Lee, K.-S., et al. 2011, ApJ, 733, 99

Leitherer, C., et al. 1999, ApJS, 123, 3

Lemson, G. 2006, ArXiv astro-ph/0608019

Levenson, N., Heckman, T., Krolik, J., Weaver, K., & Życki, P. 2006, ApJ, 648, 111

Levenson, N., Sirocky, M., Hao, L., Spoon, H., Marshall, J., Elitzur, M., & Houck, J. 2007, ApJ, 654, L45

Li, A., & Draine, B. T. 2001, ApJ, 554, 778

Li, Y., et al. 2007, ApJ, 665, 187

—. 2008, ApJ, 678, 41

Lidman, C., et al. 2008, A&A, 489, 981

Lin, L., et al. 2008, ApJ, 681, 232

Lin, Y.-T., Mohr, J., Gonzalez, A., & Stanford, S. 2006, ApJ, 650, L99

Lotz, J., Jonsson, P., Cox, T., & Primack, J. 2008, MNRAS, 391, 1137

—. 2010, MNRAS, 404, 575

Lotz, J. M., Jonsson, P., Cox, T. J., Croton, D., Primack, J. R., Somerville, R. S., & Stewart, K. 2011, ApJ, 742, 103

Lucy, L. 1977, AJ, 82, 1013

Lupton, R., Blanton, M. R., Fekete, G., Hogg, D. W., OMullane, W., Szalay, A., & Wherry, N. 2004, PASP, 116, 133

Lutz, D., Maiolino, R., Spoon, H., & Moorwood, A. 2004, A&A, 418, 465

Lutz, D., Spoon, H., Rigopoulou, D., Moorwood, A., & Genzel, R. 1998, ApJ, 505, L103

Lutz, D., et al. 1996, A&A, 315, L137

Magnelli, B., Elbaz, D., Chary, R., Dickinson, M., Le Borgne, D., Frayer, D., & Willmer, C. 2011, A&A, 528, A35

Magorrian, J., et al. 1998, AJ, 115, 2285

Mancone, C., Gonzalez, A., Brodwin, M., Stanford, S., Eisenhardt, P., Stern, D., & Jones, C. 2010, ApJ, 720, 284

Mancone, C. L., & Gonzalez, A. H. 2012, Publications of the Astronomical Society of the Pacific, 124, 606

Maraston, C. 2005, MNRAS, 362, 799

Marchesini, D., van Dokkum, P. G., Förster Schreiber, N. M., Franx, M., Labbé, I., & Wuyts, S. 2009, ApJ, 701, 1765

Marconi, A., & Hunt, L. 2003, ApJ, 589, L21

Martini, P., Sivakoff, G. R., & Mulchaey, J. S. 2009, ApJ, 701, 66

McConnell, N., Ma, C.-P., Graham, J., Gebhardt, K., Lauer, T., Wright, S., & Richstone, D. 2011, ApJ, 728, 100

McElroy, D. 1995, ApJS, 100, 105

McIntosh, D., Guo, Y., Hertzberg, J., Katz, N., Mo, H., van den Bosch, F., & Yang, X. 2008, MNRAS, 388, 1537

McLaughlin, D. 1999, AJ, 117, 2398

—. 2000, ApJ, 539, 618

Mei, S., et al. 2006a, ApJ, 639, 81

—. 2006b, ApJ, 644, 759

—. 2009, ApJ, 690, 42

Mendez, A., Coil, A., Lotz, J., Salim, S., Moustakas, J., & Simard, L. 2011, ApJ, 736, 110

Messias, H., Afonso, J., Salvato, M., Mobasher, B., & Hopkins, A. 2012, ApJ, 754, 120

Meyers, J., et al. 2012, ApJ, 750, 1

Mihos, J., & Hernquist, L. 1994a, ApJ, 437, L47

—. 1994b, ApJ, 431, L9

—. 1996, ApJ, 464, 641

Morrison, R., & McCammon, D. 1983, ApJ, 270, 119

Mosteller, F., & Tukey, J. 1977, Data analysis and regression. A second course in statistics (Addison-Wesley, Reading, MA)

Moster, B. P., Somerville, R. S., Maulbetsch, C., van den Bosch, F. C., Macciò, A. V., Naab, T., & Oser, L. 2010, ApJ, 710, 903

Muzzin, A., Wilson, G., Lacy, M., Yee, H., & Stanford, S. 2008, ApJ, 686, 966

Muzzin, A., et al. 2012, ApJ, 746, 188

Narayanan, D., Cox, T., Hayward, C., Younger, J., & Hernquist, L. 2009, MNRAS, 400, 1919

Narayanan, D., Hayward, C., Cox, T., Hernquist, L., Jonsson, P., Younger, J., & Groves, B. 2010a, MNRAS, 401, 1613

Narayanan, D., et al. 2010b, MNRAS, 407, 1701

Navarro, J. F., Mosconi, M. B., & Garcia Lambas, D. 1987, Monthly Notices of the Royal Astronomical Society (ISSN 0035-8711), 228, 501

Nelson, D., Vogelsberger, M., Genel, S., Sijacki, D., Keres, D., Springel, V., & Hernquist, L. 2013, MNRAS, 429, 3353

Nenkova, M., Sirocky, M., Nikutta, R., Ivezić, v., & Elitzur, M. 2008, ApJ, 685, 160

Norton, S., Gebhardt, K., Zabludoff, A., & Zaritsky, D. 2001, ApJ, 557, 150

Oemler, A. 1974, ApJ, 194, 1

Oesch, P. A., et al. 2013, eprint arXiv:1301.6162

Oser, L., Naab, T., Ostriker, J. P., & Johansson, P. H. 2012, ApJ, 744, 63

Oser, L., Ostriker, J., Naab, T., Johansson, P., & Burkert, A. 2010, ApJ, 725, 2312

O'Shea, B. W., Bryan, G., Bordner, J., Norman, M. L., Abel, T., Harkness, R., & Kritsuk, A. 2004, eprint arXiv:astro-ph/0403044

Overzier, R., Lemson, G., Angulo, R. E., Bertin, E., Blaizot, J., Henriques, B. M. B., Marleau, G.-D., & White, S. D. M. 2012, MNRAS, 428, 778

Page, M. J., et al. 2012, Nature, 485, 213

Papovich, C., Finkelstein, S., Ferguson, H., Lotz, J., & Giavalisco, M. 2011, MNRAS, 412, 1123

Papovich, C., et al. 2010, ApJ, 716, 1503

Paturel, G., Petit, C., Prugniel, P., Theureau, G., Rousseau, J., Brouty, M., Dubois, P., & Cambrésy, L. 2003, A&A, 412, 45

Peng, C., Ho, L., Impey, C., & Rix, H.-W. 2010a, AJ, 139, 2097

Peng, E., et al. 2008, ApJ, 681, 197

Peng, Y.-j., et al. 2010b, ApJ, 721, 193

Pier, E., & Krolik, J. 1992, ApJ, 401, 99

Poggianti, B., Smail, I., Dressler, A., Couch, W., Barger, A., Butcher, H., Ellis, R., & Oemler, A. 1999, ApJ, 518, 576

Poggianti, B., et al. 2009, ApJ, 693, 112

Pope, A., et al. 2008, ApJ, 689, 127

Pracy, M., Kuntschner, H., Couch, W., Blake, C., Bekki, K., & Briggs, F. 2009, MNRAS, 396, 1349

Press, W., Flannery, B., & Teukolsky, S. 1986, Numerical recipes. The art of scientific computing (Cambridge: University Press, 1986)

Quintero, A., et al. 2004, ApJ, 602, 190

Raichoor, A., et al. 2011, ApJ, 732, 12

Rees, M., & Ostriker, J. 1977, MNRAS, 179, 541

Rees, M. J. 1984, ARA&A, 22, 471

Rees, M. J., Silk, J. I., Werner, M. W., & Wickramasinghe, N. C. 1969, Nature, 223, 788

Rettura, A., et al. 2011, ApJ, 732, 94

Rhode, K. L. 2012, AJ, 144, 154

Rich, J., Dopita, M., Kewley, L., & Rupke, D. 2010, ApJ, 721, 505

Richards, G., et al. 2006a, ApJS, 166, 470

Richards, G. T., et al. 2006b, AJ, 131, 2766

Rigopoulou, D., Spoon, H., Genzel, R., Lutz, D., Moorwood, A., & Tran, Q. 1999, AJ, 118, 2625

Robertson, B., Bullock, J., Cox, T., Di Matteo, T., Hernquist, L., Springel, V., & Yoshida, N. 2006a, ApJ, 645, 986

Robertson, B., Hernquist, L., Cox, T., Di Matteo, T., Hopkins, P., Martini, P., & Springel, V. 2006b, ApJ, 641, 90

Robertson, B., Yoshida, N., Springel, V., & Hernquist, L. 2004, ApJ, 606, 32

Rothberg, B., & Fischer, J. 2010, ApJ, 712, 318

Rothberg, B., & Joseph, R. 2004, AJ, 128, 2098

Roussel, H., Helou, G., Beck, R., Condon, J., Bosma, A., Matthews, K., & Jarrett, T. 2003, ApJ, 593, 733

Rudnick, G., Tran, K.-V., Papovich, C., Momcheva, I., & Willmer, C. 2012, ArXiv e-prints

Sajina, A., Spoon, H., Yan, L., Imanishi, M., Fadda, D., & Elitzur, M. 2009, ApJ, 703, 270

Sajina, A., Yan, L., Fadda, D., Dasyra, K., & Huynh, M. 2012, ApJ, 757, 13

Sajina, A., Yan, L., Lacy, M., & Huynh, M. 2007, ApJ, 667, L17

Sanders, D., & Mirabel, I. 1996, ARA&A, 34, 749

Sanders, D., Soifer, B., Elias, J., Madore, B., Matthews, K., Neugebauer, G., & Scoville, N. 1988, ApJ, 325, 74

Scannapieco, C., Gadotti, D., Jonsson, P., & White, S. 2010, MNRAS, L99

Schawinski, K., et al. 2010, ApJ, 711, 284

Schulz, S., & Struck, C. 2001, MNRAS, 328, 185

Schweitzer, M., et al. 2006, ApJ, 649, 79

Schweizer, F. 1980, ApJ, 237, 303

Shectman, S., Landy, S., Oemler, A., Tucker, D., Lin, H., Kirshner, R., & Schechter, P. 1996, ApJ, 470, 172

Siebenmorgen, R., Haas, M., Krügel, E., & Schulz, B. 2005, Astronomy and Astrophysics, 436, L5

Sijacki, D., Vogelsberger, M., Kereš, D., Springel, V., & Hernquist, L. 2012, MNRAS, 424, 2999

Silk, J. 1968, ApJ, 151, 459

Silk, J., & Rees, M. 1998, A&A, 331, L1

Simard, L., Mendel, J., Patton, D., Ellison, S., & McConnachie, A. 2011, ApJS, 196, 11

Simard, L., et al. 2009, A&A, 508, 1141

Smith, J., et al. 2007, ApJ, 656, 770

Snyder, G., Cox, T., Hayward, C., Hernquist, L., & Jonsson, P. 2011a, ApJ, 741, 77

Snyder, G., Hopkins, P., & Hernquist, L. 2011b, ApJ, 728, L24

Snyder, G. F., Cox, T. J., Hayward, C. C., Hernquist, L., & Jonsson, P. 2012a, Proceedings of the International Astronomical Union, 7, 193

Snyder, G. F., Hayward, C. C., Sajina, A., Jonsson, P., Cox, T. J., Hopkins, P. F., Hernquist, L., & Lan, Y. 2013, ArXiv astro-ph/1210.6347, ApJ in press

Snyder, G. F., et al. 2012b, ApJ, 756, 114

Somerville, R., Hopkins, P., Cox, T., Robertson, B., & Hernquist, L. 2008, MNRAS, 391, 481

Spitler, L., & Forbes, D. 2009, MNRAS, 392, L1

Spitler, L., Forbes, D., Strader, J., Brodie, J., & Gallagher, J. 2008, MNRAS, 385, 361

Spoon, H., Marshall, J., Houck, J., Elitzur, M., Hao, L., Armus, L., Brandl, B., & Charmandaris, V. 2007, ApJ, 654, L49

Spoon, H. W. W., et al. 2004, ApJS, 154, 184

Springel, V. 2005, MNRAS, 364, 1105

—. 2010, MNRAS, 401, 791

Springel, V., Di Matteo, T., & Hernquist, L. 2005a, ApJ, 620, L79

—. 2005b, MNRAS, 361, 776

Springel, V., & Hernquist, L. 2002, MNRAS, 333, 649

—. 2003, MNRAS, 339, 289

Springel, V., White, S. D. M., Tormen, G., & Kauffmann, G. 2001, MNRAS, 328, 726

Springel, V., et al. 2005c, Nature, 435, 629

Stanford, S., Eisenhardt, P., & Dickinson, M. 1998, ApJ, 492, 461

Stanford, S., et al. 2005, ApJ, 634, L129

Stanford, S. A., et al. 2012, ApJ, 753, 164

Stern, D., et al. 2005, ApJ, 631, 163

—. 2012, ApJ, 753, 30

Strateva, I., et al. 2001, AJ, 122, 1861

Strazzullo, V., et al. 2010, A&A, 524, A17

Sturm, E., Lutz, D., Tran, D., Feuchtgruber, H., Genzel, R., Kunze, D., Moorwood, A., & Thornley, M. 2000, A&A, 358, 481

Sturm, E., et al. 2006, ApJ, 653, L13

Surace, J. A., & Sanders, D. B. 1999, ApJ, 512, 162

Surace, J. A., Sanders, D. B., & Evans, A. S. 2000, ApJ, 529, 170

Sutherland, R., & Dopita, M. 1993, ApJS, 88, 253

Suzuki, N., et al. 2012, ApJ, 746, 85

Swinbank, A., Balogh, M., Bower, R., Zabludoff, A., Lucey, J., McGee, S., Miller, C., & Nichol, R. 2011, MNRAS, 2050

Tacconi, L. J., et al. 2010, Nature, 463, 781

Targett, T. A., et al. 2012, ArXiv astro-ph/1208.3464

Taylor, E., et al. 2009, ApJ, 694, 1171

Teyssier, R., Chapon, D., & Bournaud, F. 2010, arXiv:1006.4757

Tinsley, B. 1968, ApJ, 151, 547

Toomre, A. 1977, in Evolution of Galaxies and Stellar Populations, ed. B. M. Tinsley & R. B. Larson, 401

Toomre, A., & Toomre, J. 1972, ApJ, 178, 623

Torrey, P., Cox, T. J., Kewley, L., & Hernquist, L. 2012a, ApJ, 746, 108

Torrey, P., Vogelsberger, M., Sijacki, D., Springel, V., & Hernquist, L. 2012b, MNRAS, 427, 2224

Tran, K.-V., Franx, M., Illingworth, G., Kelson, D., & van Dokkum, P. 2003, ApJ, 599, 865

Tran, Q., et al. 2001, ApJ, 552, 527

Tremaine, S., et al. 2002, ApJ, 574, 740

Tremonti, C., Moustakas, J., & Diamond-Stanic, A. 2007, ApJ, 663, L77

Trujillo, I., Ferreras, I., & de La Rosa, I. 2011, MNRAS, 415, 3903

van Dokkum, P., & Franx, M. 2001, ApJ, 553, 90

van Dokkum, P., et al. 2008, ApJ, 677, L5

van Gorkom, J. 2004, in Clusters of Galaxies: Probes of Cosmological Structure and Galaxy Evolution, ed. J. S. Mulchaey, A. Dressler, & A. Oemler, 305

Veilleux, S., et al. 2009, ApJS, 182, 628

Vergani, D., et al. 2010, A&A, 509, A42

Vijh, U. P., Witt, A. N., & Gordon, K. D. 2003, ApJ, 587, 533

Vogelsberger, M., Sijacki, D., Kereš, D., Springel, V., & Hernquist, L. 2012, MNRAS, 425, 3024

Vollmer, B., Cayatte, V., Balkowski, C., & Duschl, W. 2001, ApJ, 561, 708

Wagg, J., et al. 2012, ApJ, 752, 91

Wechsler, R. H., Somerville, R. S., Bullock, J. S., Kolatt, T. S., Primack, J. R., Blumenthal, G. R., & Dekel, A. 2001, ApJ, 554, 85

Weingartner, J., & Draine, B. 2001, ApJ, 548, 296

Werner, M., et al. 2004, ApJS, 154, 1

Whitaker, K., et al. 2010, ApJ, 719, 1715

White, M., Zheng, Z., Brown, M., Dey, A., & Jannuzi, B. 2007, ApJ, 655, L69

White, S. D. M., Frenk, C. S., Davis, M., & Efstathiou, G. 1987, The Astrophysical Journal, 313, 505

Wild, V., Walcher, C., Johansson, P., Tresse, L., Charlot, S., Pollo, A., Le Fèvre, O., & de Ravel, L. 2009, MNRAS, 395, 144

Witt, A. N., Thronson, H. A., & Capuano, J. M. 1992, ApJ, 393, 611

Wright, G., et al. 2004, in Society of Photo-Optical Instrumentation Engineers (SPIE) Conference Series, Vol. 5487, Society of Photo-Optical Instrumentation Engineers (SPIE) Conference Series, ed. J. Mather, 653–663

Wu, J., et al. 2012, ApJ, 756, 96

Wu, Y., Charmandaris, V., Hao, L., Brandl, B., Bernard-Salas, J., Spoon, H., & Houck, J. 2006, ApJ, 639, 157

Wuyts, S., Cox, T., Hayward, C., Franx, M., Hernquist, L., Hopkins, P., Jonsson, P., & van Dokkum, P. 2010, ApJ, 722, 1666

Wuyts, S., Franx, M., Cox, T., Hernquist, L., Hopkins, P., Robertson, B., & van Dokkum, P. 2009a, ApJ, 696, 348

Wuyts, S., et al. 2009b, ApJ, 700, 799

Yamauchi, C., Yagi, M., & Goto, T. 2008, MNRAS, 390, 383

Yan, L., et al. 2007, ApJ, 658, 778

Yan, R., et al. 2009, MNRAS, 398, 735

Yang, X., Mo, H., & van den Bosch, F. 2009, ApJ, 695, 900

Yang, Y., Zabludoff, A., Zaritsky, D., & Mihos, J. 2008, ApJ, 688, 945

York, D., et al. 2000, AJ, 120, 1579

Younger, J., Hayward, C., Narayanan, D., Cox, T., Hernquist, L., & Jonsson, P. 2009, MNRAS, 396, L66

Younger, J., Hopkins, P., Cox, T., & Hernquist, L. 2008, ApJ, 686, 815

Yuan, T.-T., Kewley, L., & Sanders, D. 2010, ApJ, 709, 884

Zabludoff, A., Zaritsky, D., Lin, H., Tucker, D., Hashimoto, Y., Shectman, S., Oemler, A., & Kirshner, R. 1996, ApJ, 466, 104

Zaritsky, D., Kennicutt Jr., R., & Huchra, J. 1994, ApJ, 420, 87

Zeimann, G. R., et al. 2012, ApJ, 756, 115